Influence of inlet acoustic boundary condition on large amplitude combustion instabilities : design of a robust impedance control system

Nicolas Tran

Ecole Centrale Paris

THESE

présentée par

Nicolas TRAN

pour l'obtention du

GRADE de DOCTEUR

Formation doctorale : Energétique

Laboratoire d'accueil : Laboratoire d'Énergétique Moléculaire et Macroscopique, Combustion (EM2C) du CNRS et de l'ECP

Influence de la condition limite acoustique amont sur les instabilités de combustion de grande amplitude : Conception d'un système robuste de contrôle d'impédance.

Soutenance le 03 avril 2009

Jury :

Candel	S.	Directeur de thèse
Ducruix	S.	
Gervais	Y.	Président
Hirschberg	A.	Rapporteur
Nicoud	F.	Rapporteur
Nottin	C.	
Schuller	T.	

Ecole Centrale des Arts et Manufactures
Grand Établissement sous tutelle
du Ministère de l'Éducation Nationale
Grande Voie des Vignes
92295 Châtenay-Malabry Cedex
Tél : 33 (1) 41 13 10 00
Télex : 634 991 F EC PARIS

Laboratoire d'Énergétique Moléculaire et Macroscopique, Combustion (E.M2.C.)
UPR 288, CNRS et Ecole Centrale Paris
Tél : 33 (1) 41 13 10 31
Fax : 33 (1) 47 02 80 35

2009ECAP0013

Remerciements

Je tiens tout d'abord à remercier MM. Sébastien Ducruix et Thierry Schuller de m'avoir fait confiance tout au long de ces trois et quelques années, de m'avoir laissé la liberté de faire des erreurs et la latitude de proposer et d'essayer dans tous les aspects rencontrés, donc de m'avoir initié à la recherche d'une manière agréable et efficace. Leur encadrement et leur amitié m'ont été très précieux. Je remercie M. Sébastien Candel d'avoir été un directeur de thèse disponible et d'excellent conseils.
Je remercie M. Yves Gervais d'avoir présider mon jury de thèse, et MM. M. Hirschberg et F. Nicoud d'avoir été de pointilleux rapporteurs.
Le soutien clair de la Fondation EADS au projet de recherche a été une aide précieuse durant ce travail de thèse, et je souhaite remercier M. Christophe Nottin d'avoir été un référent actif qui a encouragé l'équipe en lui témoignant sa confiance tout au long de la progression des travaux. Je le remercie d'avoir participé au jury de soutenance.
Ce travail a été réalisé au laboratoire EM2C, à l'Ecole Centrale Paris et je souhaite en remercier la direction et tous les membres pour leur accueil et ces trois années riches en rencontre, en échanges et en événements à photographier. Je tiens à remercier D. Durox pour sa patience et tous ses conseils. Merci à P. Scoufflaire pour son soutien à la mise en place de la PIV haute cadence. Un grand merci a toute l'équipe technique qui m'a été un soutien quotidien et a permis la mise en place des installations expérimentales. Merci donc à Yannick et Erika, toujours capables de réaliser des pièces pour la veille, à Samira pour avoir toujours bien fait passer le courant, et à Jérome pour ses bonnes idées et ses astuces multiples. Merci à Virginie et Anne-Cécile d'avoir traité toutes mes commandes et mes ordres de mission. Merci aussi à l'équipe de l'Ecole Doctorale de l'ECP, et en particulier Géraldine Carbonel.
Je tiens à remercier l'équipe du Cerfacs avec laquelle nous avons travaillé et notamment Mathieu Leyko pour ces intéressantes confrontations expérimental- numérique.
Merci enfin à tous mes compagnons de parcours grâce auxquels l'ambiance fut toujours au beau fixe. Un grand merci à la plus valeureuse d'entre eux, Séverine, pour ces épiques montages d'installation. Merci aux coureurs du dimanche Deanna, Anne, Laetitia et Jean Michel et à mes cobureaux Patrick et Corine. Enfin un mot d'encouragement pour Ammar avec qui j'ai eu le plaisir de travailler pendant sa première année.
Merci à ma famille sans qui je ne serais point là.

Ce projet de recherche a été financé en partie par la Fondation d'entreprise EADS dans le cadre du projet "Towards Predictive Numerical Simulations of Advanced Combustors: Experiments and Modeling of Instabilities in Acoustically Controlled Combustion Chambers".
This work is supported by the EADS Corporate Research Foundation in the frame of the project "Towards Predictive Numerical Simulations of Advanced Combustors: Experiments and Modeling of Instabilities in Acoustically Controlled Combustion Chambers".

Résumé

Ce travail s'inscrit dans le cadre de l'étude des instabilités de combustion couramment observées dans une grande variété d'installations, des fours industriels aux turbines à gaz terrestres ou aéronautiques. Les contraintes économiques, environnementales et sociétales de ces vingt dernières années, notamment dans les domaines de l'énergie et des transports, ont débouché sur le développement de nouvelles technologies faisant intervenir la combustion pauvre et prémélangée. Ce mode de combustion à partir d'un mélange homogène conduit à des températures de flamme plus faibles qui permettent de réduire les émissions d'oxydes d'azote tout en limitant la production d'oxydes de carbone. Pour autant, la combustion pauvre prémélangée présente le désavantage d'être sensible à toute forme de couplage notamment acoustique, menant à des instabilités de combustion. Ces instabilités limitent les performances et les plages de fonctionnement des systèmes de combustion. Elles provoquent en effet des oscillations de pression dans les systèmes, génèrent des flux de chaleurs élevés aux parois, peuvent conduire à des extinctions ou à des retours de flamme. Elles causent ainsi une usure prématurée des chambres de combustion, et dans des cas extrêmes, leur destruction. Ces instabilités de combustion sont largement étudiées, mais restent très difficiles à prévoir car elles font intervenir de nombreux phénomènes physiques multi-échelles (aérodynamique, chimie, acoustique, ...). Elles résultent principalement d'un couplage résonant entre la dynamique de la combustion et l'acoustique du système. Les mécanismes fondamentaux sont maintenant bien connus. La dynamique de la combustion dans des flammes turbulentes est de mieux en mieux maîtrisée, tandis que la structure du champ acoustique peut désormais être calculée dans les géométries complexes des chambres de combustion modernes. Les principaux mécanismes de couplage ont eux aussi été identifiés : le dégagement de chaleur instationnaire est une importante source de bruit et donc d'ondes de pression, qui peuvent interagir avec l'écoulement en amont de la flamme pour générer des perturbations dans la composition du mélange réactif. Les conditions aux limites acoustiques du système déterminent la structure du champ de pression acoustique dans l'installation, ainsi que les flux acoustiques entrants et sortants. Ces flux doivent être pris en compte pour évaluer le taux de production de l'énergie acoustique dans le système, au même titre que le terme source dû à la combustion. Ce taux permet de déterminer le développement potentiel d'une instabilité de combustion thermo-acoustique. Malgré leur importance, les conditions aux limites sont peu prises en compte et leur influence peu étudiée. Elles sont en effet difficiles à mesurer voire à contrôler sur une installation industrielle. L'objectif de ce travail est donc de répondre à ce manque d'information, en étudiant sur un banc de combustion turbulente (CTRL-Z) l'influence de la condition acoustique d'entrée sur les oscillations de combustion auto-entrenues qui apparaissent dans la chambre de combustion. Un système de contrôle passif a été développé pour piloter l'impédance du système de prémélange, sans modification des conditions de fonctionnement ou de la géométrie. Ce système de contrôle d'impédance (ICS) est basé sur une utili-

sation de plaques perforées faiblement poreuses, au travers desquelles circule un écoulement. Un piston mobile permet de piloter la profondeur de la cavité résonante formée en amont des plaques, et ainsi de piloter leurs impédances. L'ICS a été conçu et testé de façon paramétrique dans un tube à impédance permettant d'atteindre des niveaux sonores élevés comme ceux rencontrés dans les régimes instables de combustion. Cette installation modulaire permet une large plage de variations de la vitesse d'écoulement à travers les plaques, de la profondeur de la cavité, ainsi que de l'amplitude et de la fréquence de la modulation acoustique. Par ailleurs, ce dispositif a permis la validation d'une méthode de mesures d'impédance, et des protocoles de reconstruction des vitesses et flux acoustiques à partir des signaux de fluctuation de pression. L'impédance de plaques perforées de différentes porosités a ainsi été mesurée à la fois pour de faibles et de forts niveaux d'excitation acoustique, et un critère de transition entre les régimes linéaire et non-linéaire a été déterminé. L'ICS a été optimisé pour permettre un contrôle de son coefficient de réflexion de 0 à 1 sur une plage de fréquence (100 à 1000 Hz) couvrant la gamme des instabilités thermoacoustiques classiques et pour des niveaux d'amplitude de perturbations de 100 à 150 dB. L'ICS est utilisé pour contrôler l'impédance au niveau de l'entrée du système de prémélange du banc CTRL-Z, en amont de la zone de combustion. Cette installation pré-existante, présentant de fortes instabilités basses fréquences a été équipée d'un système de mesures acoustiques détaillées non seulement dans la chambre de combustion mais aussi dans le système de prémélange. La méthode de mesure d'impédance a donc pu être utilisée in-situ pour obtenir la valeur du coefficient de réflexion de l'ICS à la fréquence de l'instabilité principale. Les résultats sont comparés avec succès aux données obtenues dans le tube à impédance, validant ainsi la méthode de mesure pour des environnements bruyants. L'analyse spectrale des fluctuations de pression et de dégagement de chaleur en fonction de l'impédance d'entrée démontre une réduction du niveau d'oscillation pouvant atteindre 20 dB. Ces résultats sont confirmés par une estimation au premier ordre d'un bilan d'énergie acoustique prenant en compte le terme source dû à la combustion ainsi que les flux acoustiques en amont et aval de la zone de flamme. Ce bilan démontre par ailleurs l'importance du flux amont, du même ordre de grandeur que le terme source, et souligne la nécessité de prendre en compte ces flux pour déterminer correctement le taux de croissance de l'énergie. Pour conclure, une analyse de la structure modale du banc CTRL-Z a été réalisée, théoriquement, puis expérimentalement dans des cas non-réactifs afin de déterminer l'origine des modes d'instabilités mesurés et pour examiner les conditions nécessaires au bon fonctionnement de l'ICS.

Abstract

Combustion instabilities induced by a resonant flame-acoustic coupling are commonly observed in most applications of combustion from gas turbines to domestic or industrial boilers. These oscillations are detrimental by nature, and are still very difficult to predict at the design stage of a combustor. They imply numerous physical phenomena at multiple scales. They mainly result from a resonant coupling between the unsteady combustion and the acoustics of the system. The basic driving and coupling mechanisms have been largely studied: acoustics in complex geometries and combustion dynamics of turbulent swirled flames are now reasonably well understood. However the effects of the acoustic boundary conditions on the system stability are much less studied, as they are uneasy to access or to control in facilities. They are nonetheless of prime importance as they determine the acoustic fluxes at the inlets and outlets of the combustor, as well as the preferential eigenfrequencies of the system. The main objective of this study is to investigate experimentally the influence of the inlet boundary condition of a generic turbulent burner on the observed self-sustained thermoacoustic oscillations. To carry out this investigation, a passive control solution has been developed. An innovative use of perforated panels with bias flow backed by tunable cavities allows to control the acoustic impedance at the inlet of a turbulent lean swirled-stabilized staged combustor (CTRL-Z facility).This impedance control system (ICS) has been initially designed and tested in a high load impedance tube. This facility also allowed to develop a robust impedance measurement technique, along with experimental protocols to measure acoustic velocities and fluxes. The acoustic response of perforates in both the linear and non-linear regimes was investigated as function of the plate porosity, bias flow velocity, back-cavity depth and incident pressure wave amplitude and frequency. The transition between the linear regime and the detrimental non-linear regime has been linked to the perforates geometrical and operational parameters. As a result the ICS enables control of its acoustic reflection coefficient from 1 to 0 in a large frequency range, 100 to 1000 Hz, for low and large incident pressure amplitudes (from 100 to 150 dB). The ICS, once implemented on the CTRL-Z facility, allowed to passively control the inlet boundary condition of the combustion rig. The impedance measurement technique was successfully used in harsh combustion situations, with high noise levels, to obtain in-situ measurements of the ICS impedance. Spectral analysis of the pressure and heat-release rate fluctuations demonstrated damping of the main self-sustained oscillation by up to 20 dB. A quantitative estimation of the acoustic energy balance was then obtained, highlighting the importance of the inlet acoustic flux. In this configuration, this term is of the same order of magnitude as the driving Rayleigh source term. Finally, an acoustic analysis of the combustion rig was led to determine the nature of the observed combustion instabilities modes and examine conditions required for an effective use of the ICS.

Objectives and outline

This investigation concerns the influence of acoustic boundary conditions on self-sustained longitudinal thermoacoustic oscillations encountered in lean premixed combustion systems. Using an experimental analysis, a passive control solution is developed that provides a tunable impedance to the premixer inlet of a swirled burner. This system is used to damp self-sustained thermoacoustic oscillations. The main objectives of this work are now detailed and the contents of the manuscript is outlined.

Predicting unstable operation is a major objective in the design of new generation combustors. This requires experimental, theoretical, and numerical developments. The problem involves multiple physical phenomena and a wide range of time and spatial scales. It is at stake since the first observations of such detrimental regimes in the 1960's. Combustion dynamics and acoustics are strongly coupled and represent key elements in the analysis of combustor stability and performance. In the present work, specific experimental procedures have been developed to analyze the role of acoustic boundary conditions on these combustion oscillations. These boundaries do not only modify acoustic reflections and participate to noise production, but they can also affect the flame dynamics. The main objectives of the work are as follows:

- Provide an adaptive control system for the inlet acoustic boundary condition of a lean premixed swirled burner,
- Conduct a parametric investigation of the influence of this boundary on self-sustained combustion oscillations, using detailed acoustic measurements,
- Evaluate an acoustic energy budget by taking into account the combustion source term and acoustic losses at the terminations,
- Develop a robust passive solution to damp longitudinal self-sustained combustion oscillations generating high sound level amplitudes.

The development of this passive control solution has also led to the investigation of the acoustic properties of perforated plates in both linear and non-linear regimes. A criterion is derived that allows to design efficient perforates, even at high sound pressure levels.

The manuscript begins with a review of background material in the fields of combustion instabilities and passive control methods (chapter 1).
The swirl-stabilized staged lean combustion rig used in this work is then presented in chapter 2, along with its associated optical diagnostics. Particle Image Velocimetry was used to measure the velocity fields in the flame region. Chemiluminescence measurements were set up to estimate the heat-release rate and derive a quantitative evaluation of the energy source term in the facility. Acoustic measurements are described in chapter 3. A high load impedance tube, used for acoustic characterization of bias flow perforates, is detailed along with the Two Microphone Method which provides the acoustic impedance measurements either in the

impedance tube or in the combustion rig. This chapter also considers the protocols and post-processing methods implemented to measure the acoustic fluxes and velocities in both facilities.
Chapter 4 deals with the acoustics of perforated plates backed by resonant cavity, in presence of bias flow. Two models selected in the literature are first presented, which describe the acoustic properties of low porosity perforated plates under low and high amplitude incident pressure perturbations. The linear acoustic model, valid for small sound levels, is used to design a set of perforated plates with specific acoustic properties, that are parametrically tested in the impedance tube. The influence of the Sound Pressure Level (SPL) is then investigated and experimental data are compared to the second model to highlight a transition criterion between the two regimes. As a conclusion, an Impedance Control System is designed that provides a tunable acoustic impedance using low porosity bias flow perforates backed by cavity of adjustable depth.

Chapter 5 exposes the implementation of the Impedance Control System (ICS) at the premixer inlet of the combustion rig. The influence of the inlet impedance on self-sustained combustion oscillations of large amplitude is investigated in different regimes, and an important reduction of 10 to 20 dB of the thermoacoustic oscillation amplitude is demonstrated. The chemical source term and the acoustic fluxes at the premixer inlet and chamber outlet are then evaluated to derive a first order approximation of the acoustic energy balance in the combustion rig as a function of the premixer inlet impedance.

Finally chapter 6 describes the acoustic characterization that was led to determine the origin of the different resonances observed in the combustion rig. A model is first proposed for propagation of acoustic longitudinal plane waves in a simplified geometry of the rig composed of two coupled acoustic cavities. The experimental protocol used to measure the response of the rig to external acoustic forcing is described. Results are then compared to the model predictions to link the acoustic resonances measured in cold gas and reactive configuration to the test rig acoustic modes. The structure of the main instability mode is also investigated.

Contents

List of Figures

List of Tables

Nomenclature

Roman Symbols

a	Hole radius [mm]
C	Coherence function
c	Sound celerity [m.s^{-1}]
D	Premixer inner diameter [mm]
d	Hole spacing [mm]
e	Acoustic energy density [J]
f	Frequency [Hz]
H	Microphones transfer function
$\mathcal{H}$	Hilbert transform
He	Helmholtz number
I	Light intensity emitted by the flame [A.U]
$\mathcal{I}$	Acoustic intensity [Pa.m.s^{-1}]
k	Wavenumber [m^{-1}]
K_R	Rayleigh conductivity
L	Back-cavity depth [mm]
$\dot{m}_f$	Fuel massflow rate [g.s^{-1}]
$\dot{m}_{a,t}$	Total air mass flow [g.s^{-1}]
$\mathbf{n}$	Outward pointing normal vector
p	Pressure [Pa]
P	Thermal power [W]
p_{ref}	Reference pressure [Pa]
P_{xx}	Power spectral density of real signal x
P_{xy}	Cross-spectral density between signals x and y
Q	Heat-release [W]
Q	Resonance parameter
$\dot{q}$	Heat-release rate [W.m^2.s^{-1}]
R	Acoustic reflection coefficient
s	Microphone spacing [m]
St	Strouhal number
t	Plate thickness [mm]
T	Period of combustion oscillation [s]
T	Temperature [K]
u	Velocity [m.s^{-1}]
U	Mean bias flow velocity [m.s^{-1}]
Uj	Mean axial velocity
Vj	Mean radial velocity
V	Combustor volume [m^3]
Z	Acoustic impedance [kg.m^{-2}.s^{-1}]
Z_0	Characteristic impedance[kg.m^{-2}.s^{-1}]

Greek Symbols

α	Fuel staging [%]
α_{ac}	Acoustic absorption coefficient
γ	Specific heat ratio
δ	End correction [mm]
Δh_f^0	Propane heating value [J.g^{-1}]
ζ	Specific impedance
η	Effective compliance
λ	Wavelength [m^{-1}]
μ	Dynamic air viscosity [kg.m^{-1}.s^{-1}]
ρ	Density [kg.m^{-3}]
σ	Plate porosity
Σ	Combustor control surface [m^2]
Φ	Equivalence ratio
Φ_{ac}	Acoustic flux [W]
ω	Pulsation [Hz]

Superscripts

$\prime$	Fluctuating component of velocity
*	Excited state of species D
o	TMM original configuration
s	TMM switched configuration

Subscripts

0	Mean value of quantity A
1	Fluctuating part of quantity A
C	Combustor
P	Premixer

Complex Numbers

Im	Imaginary part
Re	Real part

Acronyms

ICS	Impedance Control System
PMT	Photomultiplier Tube
SPL	Sound pressure level [dB]
STFT	Short-Time Fourier Transform
TMM	Two-Microphone Method

Chapter 1

Background

This chapter begins with a general discussion on combustion instabilities. Current interest is mainly focused on gas turbines but there are many other systems which develop such instabilities. Hence the concepts developed in the present document can also be useful in other applications such as ramjets, industrial boilers, processes involving radiant burners, amongst others. This section (1.1) is terminated with a discussion of the Rayleigh criterion. Section 1.2 then focuses on an acoustic energy balance which extends the Rayleigh criterion as it takes into account acoustic energy fluxes at the system terminations. The third section (1.3) is devoted to active control methods. It is shown that much of the existing work has relied on closed loop schemes with modulation of the air or fuel injections. Passive control methods are then briefly reviewed in section 1.4. These techniques essentially increase the level of damping in the system. A special type of device consists of perforated plates traversed by a mean flow. Damping in this case is related to energy dissipation by vortex shedding. This concept is discussed in section 1.5 and explored in the rest of the document. It is shown that these so-called bias flow perforates can be used as a control scheme to reduce or eliminate acoustically coupled combustion instabilities.

1.1 Combustion instabilities in gas turbines

Evolution of gas turbines technology, either terrestrial or airborne, has been driven in the last two decades by more and more stringent regulations concerning pollutant emissions, and a need to improve fuel consumption efficiency. The enforcement of the Clean Air Act policy on NOx emissions has led to very efficient stationary gas turbines. The CAEP/6 regulations of the International Civil Aviation Organization (ICAO) which also strictly limit the particle emissions from aircraft engines, has been enforced in January 2008. Gas turbine combustion has evolved from conventional Rich-burn Quick-quench Lean-burn (RQL) combustors, where high operating power parts of the cycle are responsible for most of the NOx emission, to Lean Premix Combustion (LPC) which drastically reduces the amount of particles generated in the process, from 200 ppm down to less than 10 ppm in the most advanced systems. This is synthesized by Correa (1998) who considers modern combustion technologies and the influence on NOx formation, and also addresses the role of air staging and premixing. These two tech-

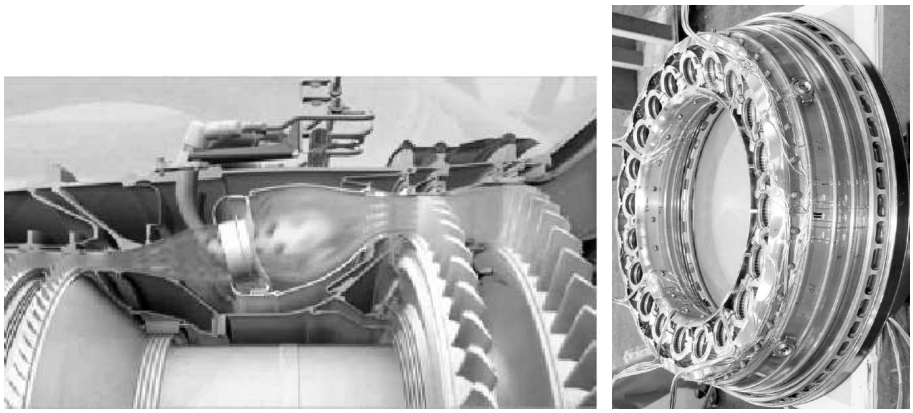

Figure 1.1: General Electric TAPS combustor as an example of lean premixed radially staged combustor. From General Electrics. (Left) Sideview of the annular combustor, with the flow sketched from the intake (left) to the distributors (right). (Right) View of the full TAPS combustion chamber.

nological developments are required to run lean burners in their largest operating range.
Premixing the reactants ensures fuel equivalence ratio uniformity in the flame region. However it also promotes flame flashback into the injection system. It is therefore important to carefully design the injectors to eliminate possible flashback by flame propagation in wakes, boundary layers or induced by vortex breakdown. Recent studies, such as Nauert et al. (2007) have demonstrated that the latter is the prevailing source of flashback in modern swirled stabilized without centerbodies. The occurrence of flashback is still difficult to predict as the triggering mechanisms are not yet clearly identified. Thibaut and Candel (1998) propose a first numerical approach of the flashback with comparison to experiments for a backward facing step and a sudden expansion geometries. Advances in numerical simulations may now give access to detailed information on this phenomenon in more complex configurations as demonstrated for example by Sommerer et al. (2004), who present a comparison between CFD calculation and experimental observations of flashback in a lean premixed combustor.
The air and fuel staging allows to operate near the lean limit in a wide range of loads by gradually reducing the fuel injection, while preventing flame extinction. This staging is often obtained by concentric air injections, to reduce the size of the burner. Furthermore the central flame can be used as a richer pilot flame to stabilize the main premixed flame near its lean extinction limits or during temporary bursts. Recent investigation on this staging technology can be found in Ballester et al. (2008), where the distributions of temperature and species have been measured in different regimes. Barbosa et al. (2009) present an extensive study of the staging effect on the flame structure in a multipoint swirled burner comprising a pilot flame. As a result, aircraft engines have evolved from rich-burning single annular combustors, developed in the seventies, to double annular combustors radially staged and, since the mid nineties, to combustors with staging and premixing inside the swirler, as reviewed by Mongia (2004) for example. This technology, referred as TAPS (Twin Annular Premixing Swirler) by General Electric, allows to reduce the levels of NOx and unburnt hydrocarbon production and has been tested on CFM56 and Genx class engines (figure 1.1) (Mongia 2004).

On stationary ground based gas turbines the staging is often achieved axially as burner injectors can generally be much longer than in aircraft engines. This also allows to enhance

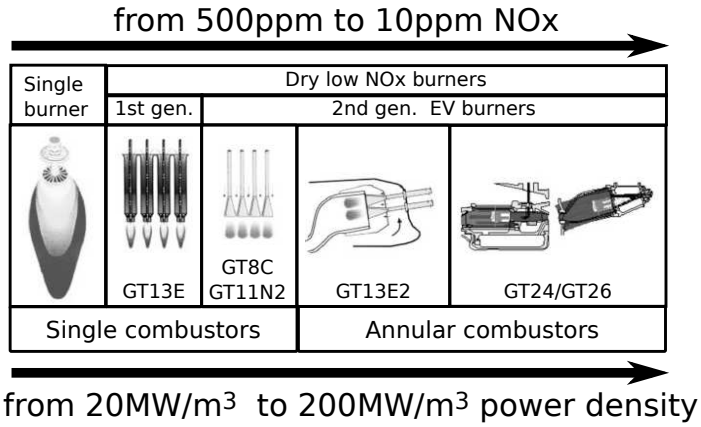

Figure 1.2: Evolution of the Alstom Gas Turbine technology, from Dobbeling et al. (2007).

the fuel and air mixing in the burner. Dobbeling et al. (2007) present the design evolution of stationary gas turbines in the last twenty five years with the example of the Alstom group. This historical review clearly illustrates the evolution from single burner technology to the current sequential combustion systems used in annular combustors designed for low levels of pollutants emission. This is illustrated in figure 1.2. The EV burner class is an example of such axial staging and premixing in industrial combustors. This system has been the focus of many investigations. Hubschmid et al. (2008) present some of the most up-to-date results on this configuration. This type of design allows short mixing lengths and promotes the existence of a strong swirling motion.

Swirl stabilized combustion is widely used in gas turbines and a recent review on the role of this swirl has been carried out by Syred (2006). With this concept, a strong radial circulation of the fresh reactants is created which, combined with the axial flow propagation, promotes an helical motion (Gupta et al. 1984). This will first increase the mixing length for the reactants before entering the combustion chamber. This motion also promotes the formation of a central negative axial pressure gradient. A zone of reverse axial velocities appears in the center of the swirl, where active recirculation of heat and chemical species help flame establishment and stabilization. This process is sketched in figure 1.3. In this Central toroidal Recirculation Zone (CRZ), the turbulent flame velocity can indeed match the low flow velocities. Furthermore the CRZ carries back hot combustion products toward the base of the flame and facilitates ignition. Finally swirling motion creates compact flame regions, which is useful especially in airborne engines to reduce the combustor length. As a consequence, most of the modern gas turbines exhibit a strong swirling vortex core in the center of the flame region, as imaged by Anacleto et al. (2002) in figure 1.4. Associated to this CRZ, a precessing vortex core (PVC) is often observed in non reactive configurations. The occurrence of the PVC during combustion is more difficult to document and is mainly a function of the fuel injection location, equivalence ratio and confinement (Syred 2006). The flame structure and associated velocity fields in a swirl-stabilized burner have recently been investigated by Stohr et al. (2008) using stereo-PIV and Laser Induced Fluorescence, which highlighted the presence of a helical precessing vortex core during combustion.

This swirl also influences flame stabilization as investigated by Bernier et al. (2000). Lean Premixed Combustion is indeed quite sensitive to operating conditions. Operating close to

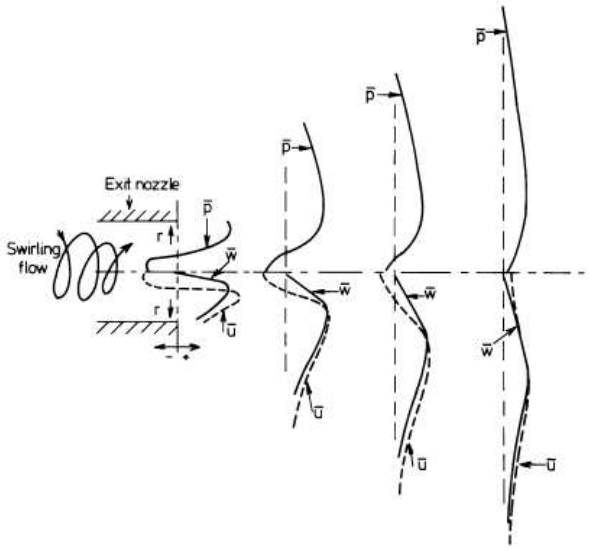

Figure 1.3: Schematic diagram of processes leading to CRZ formation, from Syred (2006): (1) a tangential velocity profile creates a centrifugal pressure gradient and sub-atmospheric pressure near the central axis; (2) the axial decay of tangential velocity causes decay of radial distribution of centrifugal pressure gradient in axial direction; (3) thus, an axial pressure gradient is set up in the central region towards the swirl burner, causing reverse flow.

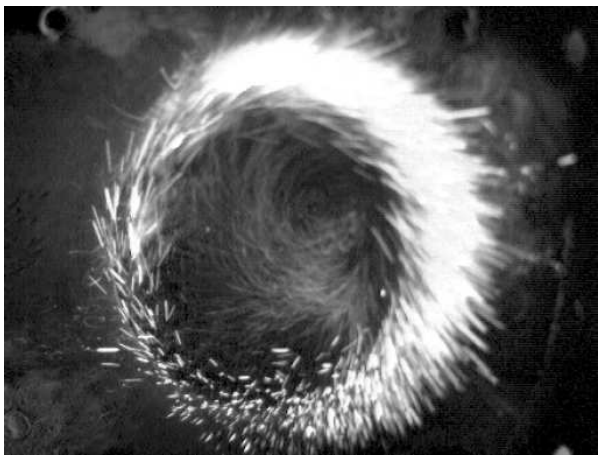

Figure 1.4: Sample images of a PVC generation for a swirl number of $S = 1.26$. Visualization by aluminum particles at Re = 19000 in a plane across the vortex axis, from Anacleto et al. (2002).

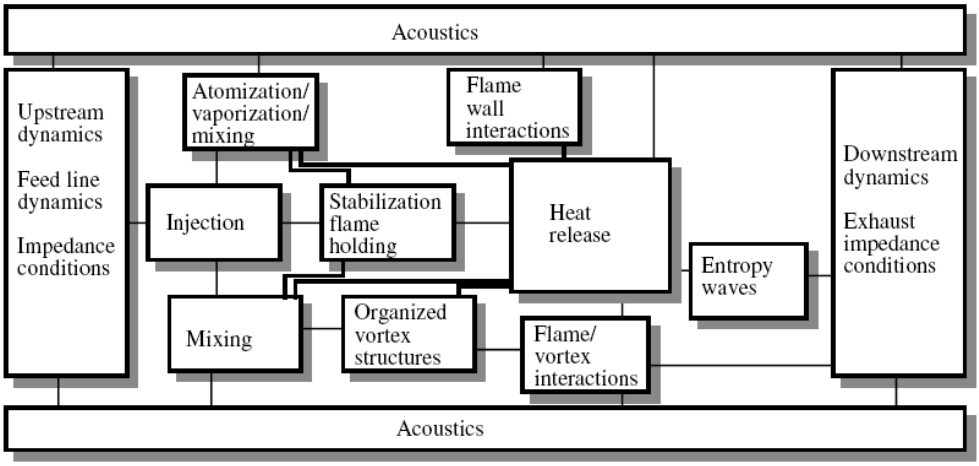

Figure 1.5: Basic interactions leading to combustion instabilities, from Candel (2002).

the lean limit implies that slight changes in the injection conditions can quickly result in lean blow-out (Nair and Lieuwen 2005). It is known that LPC is prone to the development of combustion instabilities (see for example Dowling and Stow (2003)). These instabilities produce large synchronized pressure oscillations which may reach a few percent of the operating pressure (Keller 1995). These oscillations increase heat fluxes to the chamber walls thus reducing the lifetime of the combustor, increase the production of pollutants, and lead to structural damages and, in some extreme cases, destruction of parts of the turbine.

Combustion instabilities were observed in liquid rocket motors in the early 60's (Crocco 1951). They have been one of the major issues in combustion research since then, undergoing numerous investigations. Combustion instabilities were observed in industrial furnaces (Putnam 1971), in ramjets (Hedge et al. 1987; Samaniego et al. 1993) or in afterburners (Bloxsidge et al. 1988). Many reviews have been published, see for example the collective work recently gathered by Lieuwen and Yang (2006). These unstable regimes result from interactions between system acoustics and unsteady combustion and involve many dynamical phenomena, such as the burner acoustics, the fuel evaporation and mixing processes, the flame dynamics and its interaction with vortices and walls amongst others, as reviewed by Candel (1992, 2002), Culick (2006) and Dowling and Morgans (2005). Figure 1.5 presents some of the physical processes involved in the development of combustion instabilities. In many practical configurations, thermoacoustic oscillations are generated by driving process that cause perturbations in the reactants, yielding fluctuations of the heat-release rate. This unsteady heat-release is an efficient acoustic source (Dowling et al. 1985) which generates pressure waves propagating in the system. A feedback mechanism then couples the perturbations to the driving process and leads, for some conditions, to the growth of an instability. As only acoustic waves can propagate in the up and downstream directions, they are the main feedback path. Acoustics is thus the main source of the resonant coupling with the unsteady heat-release.

Fluctuations of heat-release rate produces sound pressure waves radiated in the combustion chamber and constitute the retroaction mechanism. The feedback mechanisms involve other potential sources, as pressure fluctuations may not directly act on the combustion process. Acoustic wavelengths are indeed in most situations much greater than the flame thickness

(McIntosh 1991). Pressure fluctuations induce velocity and fuel equivalence ratio variations which, in turn, act on the heat-release rate, by stretching the flame surface, shedding vortices in the fresh gases or creating local mixture inhomogeneities, as reviewed by Ducruix et al. (2003). Self-sustained combustion oscillations usually develop from perturbations of small amplitudes (Lieuwen and Yang 2006) but may also result from the nonlinear triggering by finite level perturbations (Noiray et al. 2008b). It is thus relevant to investigate the dependence of the flame response to the level of incident perturbations (Balachandran et al. 2005; Durox et al. 2009). Combustion dynamics may not solely respond nonlinearly to flow perturbations. The flow and the boundaries may also feature non-linear responses when the oscillation level increases.

Non-linear response of the combustor boundaries will have a profound impact on the feedback loop. In practical applications, combustor walls often feature collections of perforations with multiple orifice sizes conveying a bias flow. These perforations are used for wall cooling and for dilution of hot combustion products within the chamber. Recent simulations indicate that these perforations influence the burner stability (Nicoud et al. 2007). The response of these perforations yet largely deviate from linear theoretical predictions (Howe 1979) when the amplitude of the incident pressure perturbations increases. This was demonstrated by Ingard and Ising (1967) for a single orifice submitted to external forcing by a piston. This phenomenon was also highlighted with perforates in a lab scale combustor by Tran et al. (2008). Nonlinearity of the flame response has been modelled by Dowling (1999) for velocity perturbations, later extended by Morgans and Stow (2007) to account for other types of flow perturbations. The nonlinear dynamics of an unstable burner has been experimentally determined by (Noiray et al. 2008b), in a configuration gathering many nonlinear phenomena such as hysteresis, frequency shifting or mode switching.

Unsteady perturbations in the fuel or air feeding lines may also produce nonlinear flow response in the fresh stream. This can take the form of large scale coherent structures shed at the injector lips and conveyed by the mean flow to the flame front (Poinsot et al. (1987), Wu and Kung (2000), Spencer et al. (2008)). The differential response of the fuel and air feeding lines to pressure oscillations also induces a periodic release of reactants inhomogeneities as explained by Lieuwen and Zinn (1998) and Sattelmayer (2003). The influence of the flame shape has recently been highlighted by Durox et al. (2009). The role of lateral flame confinement has been stressed out by Birbaud et al. (2007). It is shown that the nonlinear response of the flame depends on its interaction with the walls. Flame dynamics is also sensitive to the input level of perturbations. Balachandran et al. (2005) presented experimental results linking the nonlinear response of the heat-release rate of a lean premixed flame to the inlet velocity amplitude, equivalence ratio and forcing frequency.

The complexity and the nonlinearity of this flame-acoustic coupling has hindered the development of a general tool to predict the occurrence and growth of thermoacoustic instabilities, and to estimate oscillation levels at limit cycles. As a result, predictive methods have been derived for only a small number of simple and well controlled configurations such as obtained by Noiray et al. (2008b) in the case of multiple flames anchored on a grid. These authors propose a method based on the flame describing function, a generalization of the flame transfer function, and demonstrate that it can be used to retrieve most of the nonlinear features of their experiment. In most situations, a criterion, originally derived by Rayleigh (1878) is used to determine the nature of the observed oscillations: when heat-release rate fluctuations occur in phase with pressure oscillations in the system, a thermoacoustic resonant coupling is likely to develop. This criterion was used by many authors to detect thermoacoustic coupling in their lab-scale combustors. It is a necessary, yet insufficient condition to observe the devel-

opment of combustion instabilities. Unfortunately it can only be evaluated a posteriori, when the instability is set. Mathematically, it is often expressed as follow:

$$\frac{1}{T}\int_T\int_V p_1\dot{q}_1 dvdt > 0 \tag{1.1}$$

where p_1 represents pressure fluctuations, and $\dot{q}_1$ heat-release rate (per unit volume) oscillations, integrated over the combustion volume V and over a period of oscillation T.

Indeed this criterion, despite its common use, does not account for many physical processes, such as the energy losses inside the volume and at the volume boundaries, which may prevent the instability growth. This Rayleigh integral represents only one of the terms of a global acoustic energy budget. It is better to use more complete formulations as discussed in many classical studies such as the works of Cantrell et al. (1963) focused on rocket engines, of Chu (1965) for more general applications, and of Morfey (1971) which includes non uniform flows effect. These works were completed by further studies by Myers (1991), Dowling (1992), Nicoud and Poinsot (2005) and Giauque et al. (2007). The acoustic energy balance is also investigated by Durox et al. (2008), who established a budget for an experiment where multiple flames oscillate at limit cycle.

1.2 Acoustic energy balance

The concept of acoustic energy is first introduced for low Mach non-reacting flows. Equations of linear acoustics are derived from the main conservation equations (mass, momentum and energy), in the absence of volume forces, heat sources, mean flow and with negligible viscous forces. Flow perturbations are considered isentropic. In addition, quantities are decomposed into a mean component, denoted by subscript 0, and an acoustic component, marked by subscript 1, such that the acoustic part is much smaller than the mean value. Pressure is decomposed as $p = p_0 + p_1$, velocity as $\mathbf{u} = \mathbf{u}_0 + \mathbf{u}_1$ and density as $\rho = \rho_0 + \rho_1$. Classical equations of mass, momentum and energy can be combined to derive two equations describing acoustic waves propagation(Rienstra and Hirschberg 2006):

$$\frac{1}{c_0^2}\frac{\partial p_1}{\partial t} + \rho_0 \nabla\cdot\mathbf{u}_1 = 0 \tag{1.2}$$

$$\rho_0\frac{\partial \mathbf{u}_1}{\partial t} + \nabla p_1 = 0 \tag{1.3}$$

These two equations are combined to obtain the wave equation:

$$\nabla^2 p_1 - \frac{1}{c_0^2}\frac{\partial^2 p_1}{\partial t^2} = 0 \tag{1.4}$$

They can also be combined by multiplying eq. 1.2 by ρ_1/ρ_0, taking the scalar product of eq. 1.3 with $\mathbf{u}_1$ and summing the results:

$$\frac{\partial}{\partial t}\left(\frac{1}{2}\rho_0\mathbf{u}_1^2 + \frac{1}{2}\frac{p_1^2}{\rho_0 c_0^2}\right) + \nabla\cdot(p_1\mathbf{u}_1) = 0 \tag{1.5}$$

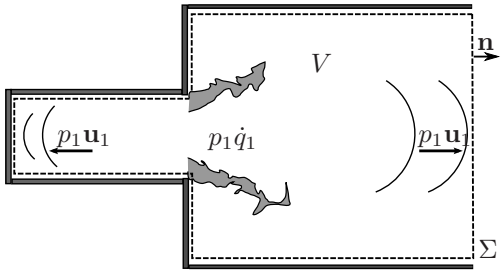

Figure 1.6: Illustration of the source term and acoustic fluxes.

For a quiescent non reacting flow, the acoustic energy density $e = \rho_0 \mathbf{u}_1^2/2 + p_1^2/2\rho_0 c_0^2$ only varies because of acoustic fluxes $p_1\mathbf{u}_1$ at the system boundaries.
In the presence of a reacting flow, the situation becomes more complicated because the unsteady combustion is also a source of noise. One obtains (Dowling (1992)):

$$\frac{\partial e}{\partial t} + \nabla \cdot (p_1 \mathbf{u}_1) = \frac{\gamma - 1}{\rho_0 c_0^2} p_1 \dot{q}_1 \tag{1.6}$$

where γ is the heat capacity ratio. Extensive work has been done to derive expressions of the acoustic energy density and fluxes including mean flow effects. Cantrell et al. (1963) have provided one of the first discussions upon the form of the growth rate for energy perturbations for a mean isentropic and irrotational flow. The definition of acoustic energy and flux in various types of flows has also been investigated by Candel (1975).
In the absence of mean flow, they derived a simple expression of the total energy E growth rate as the ratio of the acoustic fluxes integrated over the control surface Σ divided by the first order approximate of the acoustic energy density e over the volume V:

$$\frac{\langle dE/dt \rangle_T}{\langle E - E_0 \rangle_T} = -2 \frac{\left\langle \int_\Sigma p_1 \mathbf{u}_1 \cdot \mathbf{n} d\sigma \right\rangle_T}{\left\langle \int_V e dv \right\rangle_T} \tag{1.7}$$

where the acoustic energy density e, the pressure p_1 and acoustic velocity fluctuations $\mathbf{u}_1$ are integrated over a volume V delimited by a control surface Σ, with a normal vector $\mathbf{n}$ pointing outward of the surface, as illustrated in figure 1.6. Brackets denote time averaging over a period of oscillation.

In the presence of a mean flow, acoustic perturbations are convected, and therefore the acoustic energy cannot be constructed from first order perturbations (Landau and Lifshitz 1987). Cantrell et al. (1963) derived another expression for the growth rate of energy perturbations, relating it to first order acoustic variables and mean flow field. Morfey (1971) proposed a comprehensive analysis of the transport of energy disturbances in more general flows, in the absence of combustion nonetheless. Dowling (1992) extended his formulation to take combustion into account, while Myers (1991) developed an exact solution for arbitrary disturbances in a steady flow, without any assumption on the linearity of the disturbances. Giauque et al. (2007) also propose a recent extension of the work of Myers, including species and heat-release terms to take combustion into account. However in many combustion systems, the flow Mach number remains very small, and approximate forms of acoustic energy with

no mean flow can be used. These developments led to an extended version of the Rayleigh criterion which accounts for acoustic losses in the system. Chu (1965) proposed such an extension of the classical Rayleigh criterion, recently completed by Nicoud and Poinsot (2005). This formulation accounts for entropy fluctuations and therefore makes use of the temperature instead of the pressure term:

$$\frac{1}{T_0}\left\langle \int_V T_1 \dot{q}_1 dv \right\rangle_T \geq \left\langle \int_\Sigma p_1 \mathbf{u}_1 \cdot \mathbf{n} d\sigma \right\rangle_T \tag{1.8}$$

This result is appealing in presence of entropy waves yet difficult to verify experimentally, as access to time resolved temperature fluctuations is not yet achievable.
In the case of a combustion instability with no mean flow nor entropy waves, where thermal and viscous diffusion processes are neglected, the extended form of the Rayleigh criterion can be obtained from the expression of the acoustic energy growth rate:

$$\left\langle \frac{\partial E}{\partial t} \right\rangle_T + \left\langle \int_\Sigma p_1 \mathbf{u}_1 \cdot \mathbf{n} d\sigma \right\rangle_T = \left\langle \int_V \frac{\gamma - 1}{\gamma p_0} p_1 \dot{q}_1 dv \right\rangle_T \tag{1.9}$$

Once the limit cycle of oscillation is reached, the acoustic energy E remains constant and therefore the two sides are in balance. An instability is thus likely to grow when these terms are out of balance:

$$\int_V \frac{\gamma - 1}{\gamma p_0} p_1 \dot{q}_1 dv \geq \int_\Sigma p_1 \mathbf{u}_1 \cdot \mathbf{n} d\sigma \tag{1.10}$$

The left hand side term is the classical expression of the Rayleigh criterion, which must overcome the energy losses by acoustic fluxes (right hand side term) for an instability to develop. Only acoustic losses at boundaries have been taken into account, for simplicity. Additional dissipation terms, accounting for all other sources of losses in the volume, have been discarded. There are no contributions of acoustic fluxes at the chamber and premixer walls since the acoustic velocity vanishes at these locations. They can however be significant at the inlet and outlet boundaries of the system and must be taken into account to determine the onset of instabilities.
The different terms defining the acoustic energy balance are not often evaluated. Recent developments of Large Eddy Simulation allowed Giauque et al. (2007) to propose a numerical evaluation of this extended criterion in a turbulent lean premixed combustor. In practice, it is still a challenging task. The Rayleigh criterion is often involved in experimental studies, but most discussions remain qualitative. Pressure and heat-release rate fluctuations are measured over the whole flame region by microphones and photomultipliers, and the phase of the correlation between these signals is easily evaluated. Such integrated measurements, based on spontaneous emission from radicals such as CH^*, are yet difficult to calibrate to obtain quantitative heat-release rate estimates (Price et al. 1969). The increasing sensitivity of modern cameras now allows to map this Rayleigh term on the flame zone and to detect preferential instability region within the combustion zone as demonstrated by Samaniego et al. (1993). More recently Balachandran et al. (2005) used this method combined with laser induced fluorescence to estimate the local heat-release rate of a turbulent flame submitted to velocity fluctuations. This was also employed by Meier et al. (2007) to investigate the time evolution

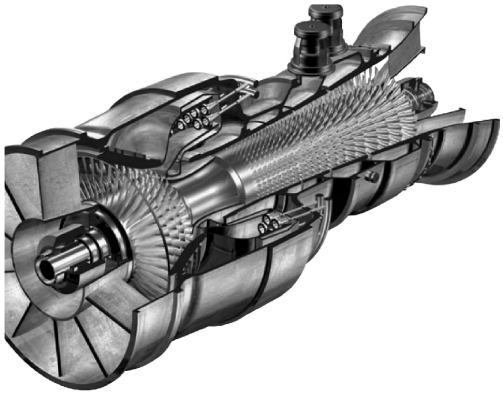

Figure 1.7: Schematic of a full scale gas turbine, illustrated with Alstom GT13E2 model equipped with EV burners (center), for an acoustic energy budget and determination of real acoustic boundary conditions. From Alstom commercial leaflet.

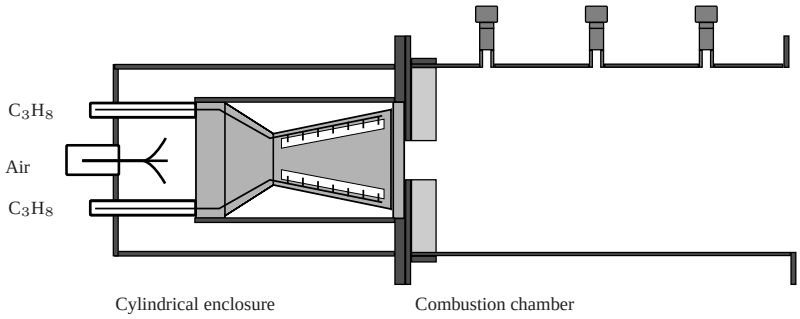

Figure 1.8: Laboratory installation for EV burner characterization at lab. EM2C (Dioc 2005).

of a thermoacoustic pulsation and highlight the feedback mechanism.

A complete experimental evaluation of the different terms appearing in the acoustic energy balance has recently been achieved by Durox et al. (2008). Many studies have focused on the effect of flow perturbations on flame response, but much less attention has been paid to the influence of the acoustic boundary conditions, mainly because they are difficult to measure and to control in practical configurations. The schematic view of an Alstom GT13E2 complete gas turbine (figure 1.7) clearly illustrates the complexity of the situation. This gas turbine is equipped with the previously mentioned EV burners, visible in the center of the turbine. The environment of the burner is therefore quite different from the installation for laboratory testings, such as used by Dioc (2005) and sketched in figure 1.8. Terminations differs from those found in practice inducing a distinct acoustic environment.
These acoustic boundaries are however of prime importance as they determine the acoustic field in the system and therefore the resonances at which thermoacoustic oscillations may occur. They also constitute potentially important energy loss terms that may be sufficient to prevent the onset of instabilities. Boundary conditions represent one of the main differences between test rigs and complete industrial facilities. As an example, the turbine distributor of a gas turbine is usually considered to operate as a choked boundary condition for the down-

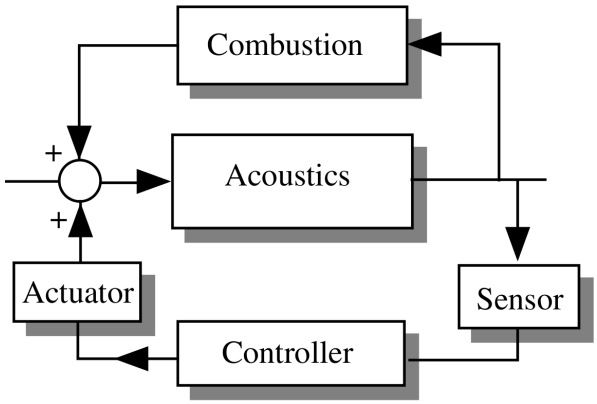

Figure 1.9: General principle of active control of instability, from (Candel 2002)

stream termination of the combustion chamber, while lab test rigs rarely feature this kind of exhaust. This mismatch between test rig and industrial gas turbine acoustic boundary conditions limits the value of the combustion instabilities investigations led in laboratories. A stable burner may well be more unstable once included in an industrial system. Active control has recently been applied by Bothien et al. (2008) using loudspeakers to modulate the downstream acoustic field of a burner in order to reproduce a large range of exhaust boundary conditions. The importance of these boundary conditions also implies that combustion instabilities cannot be eliminated solely by design of the burner itself.
Because of the lack of models accounting for these acoustic boundary conditions, no general tool has been developed to predict the occurrence of combustion instabilities.There are however a variety of methods which can be used to limit the consequences of instabilities either by active or passive control. While active control solutions usually aim at modifying the feedback loop to hinder the resonant coupling between unsteady combustion and system acoustics, passive control methods are in general used to damp the resonant acoustic modes. A brief overview of these methods is proposed in what follows.

1.3 Active control systems

Active combustion control designates methods that use a feedback loop between a sensor and an actuator to ensure a stable combustion regime, as sketched in figure 1.9. The concept was originally proposed in the 1950's by Tsien (1952). At that time, technology was not available to demonstrate practical feasibility of active control. This was later carried out by, for example, Poinsot et al. (1992) who successfully implemented a closed loop actuation with loudspeakers of the fuel injection lines, effectively reducing the amplitude of unstable pressure fluctuations by an important factor, as illustrated in figure 1.10. At the same period, Bloxsidge et al. (1988) achieved active suppression of low frequency reheat buzz in ducts, using a choked plate and an oscillating centerbody to modify the upstream condition. McManus et al. (1993) provided a review of active control methods applied to combustion instabilities. This has been updated by Dowling and Morgans (2005), amongst others.
One of the main difficulty in active control is to create sufficiently large input levels to over-

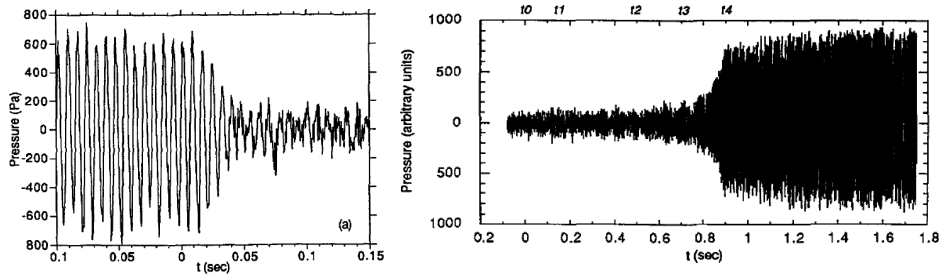

Figure 1.10: Active control of combustion instability from Poinsot et al. (1992). (Left) The control system is switched on at $t = 0$. The pressure trace clearly show a strong damping of the instability. (Right) The active control system is turned off at $t = 0$. Pressure signal indicates clearly that the system reaches a limit cycle of oscillation when active control is off.

come the large pressure oscillations generated by the combustion instabilities. The actuation device must create significant modulations of the control parameters. An efficient method is to use actuation of the fuel and air injections (Bernier et al. 2003), by periodic modulation or by use of secondary jets as proposed by Hathout et al. (2000). Cohen et al. (2008) have recently implemented fuel modulation in a sector combustor, obtaining $6\,\mathrm{dB}$ noise reduction. Conrad et al. (2007) use intermittent modulation of the liquid fuel injectors to modify the spray properties and thus the combustion regime. Tachibana et al. (2007) have thoroughly investigated active control by secondary fuel injection, examining the influence of the fuel bypass percentage, the injector geometry and injection angle.

Another promising method is to act on the boundary conditions. In laboratory test rigs, the active modulation of the acoustic boundary conditions by loudspeakers has also been investigated, see amongst others the work of Paschereit et al. (2000), and recently of Bothien et al. (2008). Such acoustic modulation is convenient for preliminary studies as it is easily implemented. In addition, it gives access to the jump conditions between acoustic perturbations on each side of the combustion region, which can be used to evaluate the flame response (Polifke and Lawn 2007) and build models that are in turn used in feedback algorithms. Such flame response models may prove useful when active control systems are to be implemented in complete systems. Most of the studies are indeed carried out on single burners, where longitudinal modes are dominant, while modern combustors are annular chambers where transverse acoustic instabilities may occur, as shown for example by Morgans and Stow (2007).
Initially, active control was mostly based on closed-loop systems which require accurate actuators and control loops. Richards et al. (2007), amongst others, have shown that open-loop algorithms, which are easier to implement, can also be effective control solutions.

In any case, active control requires accurate sensors in the combustion zones. Docquier and Candel (2002) provide a complete review on sensors applied to modern gas turbines to optimize the system performances. Monitoring the unsteady pressure is easily achieved, but is not sufficient to detect instabilities. In-situ measurements of the heat-release rate are now made possible thanks to the optic fiber technology. Sanz et al. (2008) describe some modern sensors for gas turbine monitoring and address the issue of their calibration through a extensive experimental investigation.

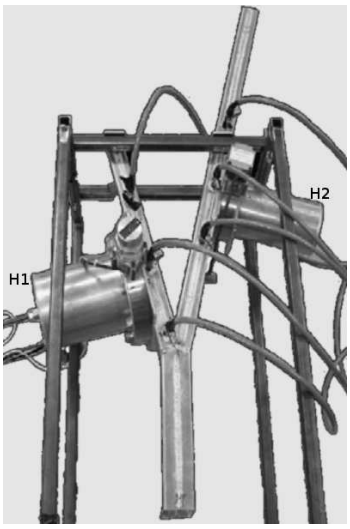

Figure 1.11: Helmholtz resonators (H1 and H2) on a Y-shaped Rijke tube, from Zhao and Morgans (2008).

Despite all these recent developments, active control remains a complex solution to implement on industrial facilities. It requires adequate sensors submitted to harsh environments in the combustion chamber along with robust actuators on the injection lines, such as fast-response valves. Loudspeakers remain a laboratory scale implementation. In addition, one of the main drawbacks of active control is that in case of system failure, a burner becomes quickly unstable. This is illustrated in figure 1.10 where the pressure amplitude quickly reaches a limit cycle once the active control system is deactivated (Poinsot et al. 1992). Passive methods may be more robust and some have already proved their efficiency in real configurations.

1.4 Passive control systems

Passive methods mainly consists in the optimal placement of damping devices like quarterwave resonators (Richards and Robey 2008), Helmholtz resonators (Bellucci et al. 2004), or perforated panels (Melling 1973). Such dampers are designed to absorb acoustic energy at a single given frequency. In systems featuring several unstable modes, or prone to frequency shifting, multiple devices must be incorporated, as shown by Zhao and Morgans (2008) using two Helmholtz resonators.

Passive control may also be achieved through careful design of the injectors and their positioning in the burner, as reported by Steele et al. (2000). In the case of annular combustors, where transverse acoustic modes may couple the response of the different injectors, Richards and Robey (2008) propose to prevent such coupling by tuning each injector impedance with quarterwave resonators placed on the fuel lines (figure 1.12). A different approach, using staggered constrictions, was taken by Noiray et al. (2008a) to create phase mismatches between adjacent flames in order to break the coherent coupled response of a set of flames.

The main drawback of acoustic resonators is their space requirement in the combustion chamber. It is difficult to add the large volumes required by Helmholtz resonators in existing systems. The test setup of Zhao and Morgans (2008) reported in figure 1.11 illustrates the size of

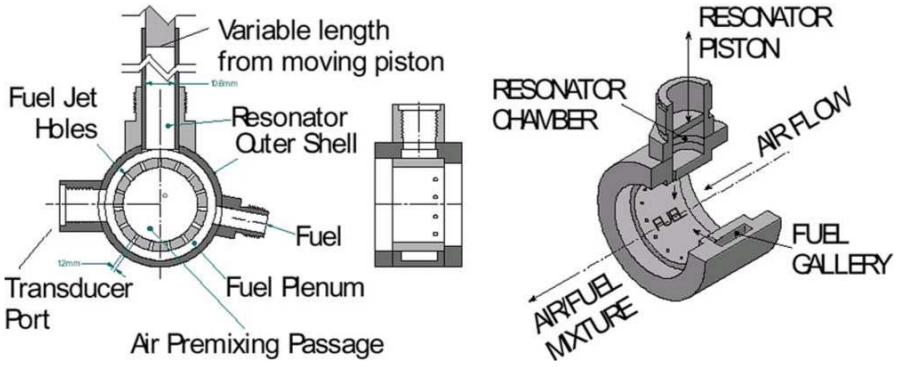

Figure 1.12: A quarter-wave resonator, with variable length $0 - 0.8\,\mathrm{m}$ and a diameter of $10.6\,\mathrm{mm}$, connected to a fuel premixer, from Richards and Robey (2008).

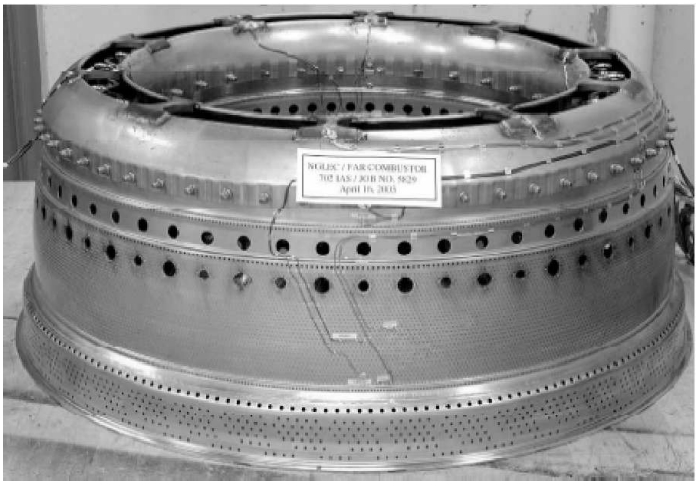

Figure 1.13: GE gas turbine combustion chamber with lateral perforations for film cooling and air dilution.

a Helmholtz resonator. Tuning the volume of the fuel injection line, as proposed by Richards and Robey (2008), may also have detrimental side-effects as the positioning of the injectors also affects the flame dynamics. In contrast, perforated panels are widely used in aircraft engines casing (Hughes and Dowling 1990) and in mufflers (Munjal 1987). Furthermore, many perforations are also present inside combustion chambers for film cooling and secondary air injection for dilution of the hot combustion products as illustrated in figure 1.13. Perforated panels have thus potential for passive control of instabilities in combustion chambers and are examined in the following section.

1.5 Perforated plates for acoustic damping

Acoustic damping by perforated plates has been the focus of numerous studies, because of the large number of parameters and configurations involved. Many models are therefore available

in the literature, yet no universal modelling has emerged. While the model of Melling (1973) considers the effect of the dissipative acoustic layer in each perforation, the semi-empiric model obtained by Narayana Rao and Munjal (1986) is limited to the case of a grazing flow. A more general framework has been set by Howe (1979), who demonstrated that the vortex-shedding, that takes place at the edges of an aperture, is responsible for significant acoustic damping, in the case of a single aperture in an infinite plane. Bechert (1980) has shown that the efficiency of this vortex shedding is dramatically increased in the presence of a bias flow through the apertures and by the use of a resonant cavity behind the perforate. These results were later confirmed by Forster and Michel (2003). Based on these developments, Hughes and Dowling (1990) designed efficient screech noise absorbers. In its initial form, the model of Howe discards the influence of the plate thickness and is limited to infinitely thin plates. Luong et al. (2005) proposes a theoretical extension to account for this parameter, while Jing and Sun (2000) have investigated this issue numerically, and Celik et al. (2005) present experimental data. In many applications, perforated panels are used to reduce, and even cancel noise in a narrow frequency range. Attempts were made to widen this frequency range by multiplying the number of panels (Lee and Kwon 2004) or by actively controlling the back-cavity depth (Congyun et al. 2005).

Most studies have focused on linear acoustic interaction with the perforates, when the pressure perturbation amplitude reaches only small levels. However, large amplitude of pressure oscillations are typical of combustion instabilities and may imply non-linear acoustics (Culick 1994). The effect of high amplitude pressure waves in perforates is less documented. Cummings and Eversman (1983) propose a theory for this non-linear behavior in the absence of mean flow. Amongst the first experimental studies of such interactions, the work of Ingard and Ising (1967) is one of the most extensive. They obtained a semi-empirical model to account for the influence of the sound pressure level on the acoustic impedance of an orifice. Dragan and Lebedeva (1998) have also highlighted these nonlinear interactions experimentally, while Jing and Sun (2002a) use numerical methods to determine the influence on vortex-shedding. There is yet no complete model accounting for both linear and non-linear acoustic interaction, and no transition criterion between these regimes has been derived to the author knowledge. For an application to the damping of combustion instabilities, this is an important lack which has to be addressed to allow efficient perforate design.

The current study tackles this issue and a design solution of such perforates is proposed, based on experimental data gathered in both acoustic regimes.

Chapter 2

Turbulent combustion rig and associated optical diagnostics

This chapter describes the turbulent combustion rig used in this work, along with the two optical diagnostics set up to investigate the flow aerodynamics and the combustion process Section 2.1 presents the lean premixed burner which has been adapted for detailed acoustic measurements inside its premixer. Its operating principle is briefly presented along with the regimes used for the study. Then the technical aspects of the apparatus (ICS) designed to control the premixer inlet acoustic condition are described in section 2.2. The flowfield aerodynamics has been investigated using high-speed Particle Image Velocimetry, with a focus on the influence of the ICS. The technique is described in section 2.3. Finally, chemiluminescence measurements of spontaneous radical emissions used to study the heat-release process are described in section 2.4. This technique is well documented in the literature, therefore emphasis is made on the method that allows to link the radical emission to the flame heat-release rate and eventually to obtain a quantitative evaluation of this chemical source term.

2.1 Swirl-stabilized staged lean premixed combustor

2.1.1 Description

The EC2 combustor photographed in 2.1 was designed by François Lacas and Nathalie Dioc (2005). It has been thoroughly studied and its behavior is well documented. It features a lean partially premixed staged injection system, stabilized by swirl, illustrated in figure 2.2. The premixer is composed of two identical stages described below.

Air is fed into each stage through a circular manifold in which a swirler is inserted. This swirler comprises a hollow cylinder with large lateral openings, through which air is injected in the inner premixer channel. Inside these rectangular openings, four injectors (1 mm-diameter) deliver gaseous propane perpendicularly to the air flow. This cross-flow configuration enhances fuel-air mixing. The tangential air injections create a strong swirl motion (swirl number estimated above 0.6 (Dioc 2005)) in the $D = 30\,\text{mm}$ diameter inner channel.

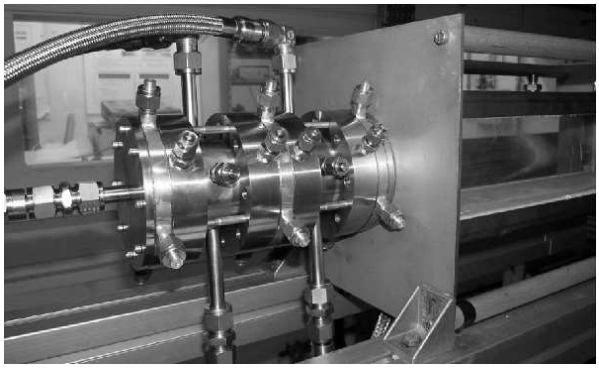

Figure 2.1: Photography of the EC2 premixer

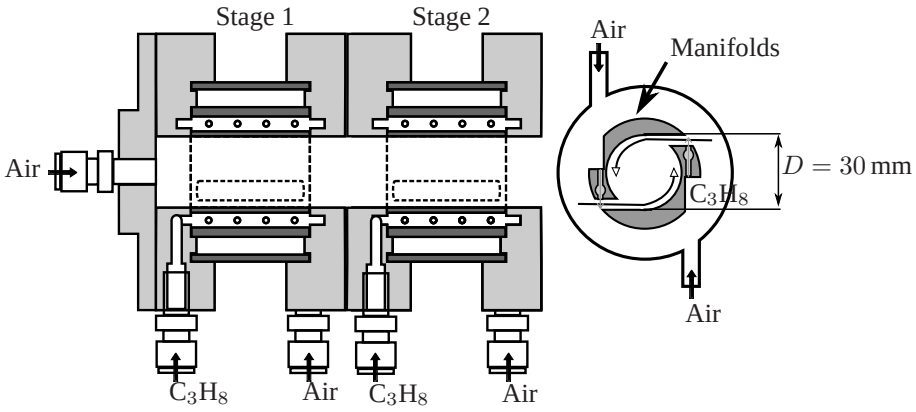

Figure 2.2: Schematic view of the original version of the premixer.

A precessing vortex core (PVC) is therefore promoted which results in a short flame, typical of swirl-stabilized configurations (Syred (2006)). For the regimes studied in the current work, the flame is compact, about $10 - 15$ cm long, and its base is located inside the premixer. An axial air injection avoids flame flashback, which may damage the injectors. This axial flowrate corresponds to a small fraction of the total tangential massflow ($\simeq 2.5\%$). The premixer is connected to a rectangular combustion chamber, with a high expansion ratio (> 14). This chamber is made of two quartz windows for flame visualizations, and two refractory concrete plates (top and bottom) which can be equipped either with small quartz windows for laser measurements, or with transducer ports for acoustic measurements. The exhaust, which represents the downstream boundary condition of the chamber, is a square open end. Hot gases flow out of the facility and are collected by a large funnel connected to a chimney. In the low frequency range considered in this study ($100 - 1000$ Hz) only longitudinal pressure perturbations are to be envisaged because of the chamber dimensions (50 cm total length with a square test section of 10×10 cm^2) and acoustic pressure can be assumed roughly uniform in a given section. The premixer was slightly modified to add access ports for acoustic and flow measurements. Three new sections, 10 mm thick, were added: one at each end plus one between the two stages. They are thus spaced by 10 cm. Each section has four radial ports, which can be used to insert microphones, hot-wire probes or thermocouples inside the premixer channel. The combustion chamber and the premixer are equipped with microphones. All these sensors are flush-mounted on calibrated water-cooled waveguides (see section 3.1.2). The premixer is equipped with four microphones, and the chamber with three microphones. Microphone M1, located farthest upstream of the flame and closest to the upstream boundary condition, always measures the highest Sound Pressure Level. As a consequence, this SPL is used as a reference SPL in the combustion facility. It must be noted that the location of microphone M1 is not a constant pressure antinode with frequency, and hence the reference SPL is only a qualitative indicator.
The updated schematic of the combustor, indicating positions of the pressure transducers is given in figure 2.3, at scale with a flame OH-PLIF snapshot. This snapshot shows the extent of the flame relatively to microphone M5, and also confirms that the flame base is not anchored at the section change but inside the premixer channel. The original premixer inlet condition is also depicted. It consists in a $12''$ air inlet plugged in the center of a rigid plate.
The different operating regimes investigated in this work are now described.

2.1.2 Combustor operating regimes

This configuration features strong combustion instabilities depending on the fuel staging ratio α, defined as the ratio of the fuel massflow in the stage furthest from the chamber (stage 1) to the total fuel massflow injected (see figure 2.2 and Dioc (2005)):

$$\alpha = \frac{\dot{m}_{f,1}}{\dot{m}_{f,1} + \dot{m}_{f,2}} \tag{2.1}$$

These instabilities are characterized by intense acoustic levels within the chamber and the premixer, and important noise radiation. Large fluctuations of the heat-release rate, characterized by strong oscillations of the light intensity emitted by the flame, are also observed. An example of such fluctuations is given by imaging the flame with a standard CCD camera, in figure 2.4. Four successive images were acquired in the nominal operating conditions described below. The flame shape is typical of swirl-stabilized systems. It is also clear that the flame shape

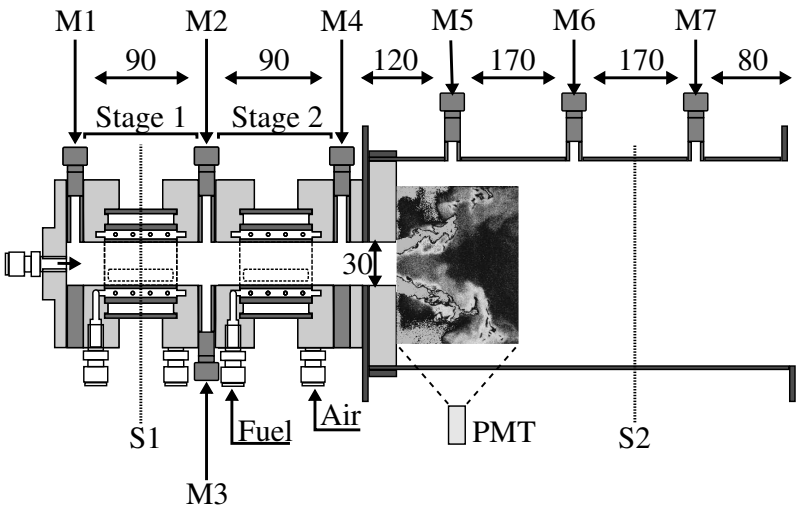

Figure 2.3: Schematic of the combustion bench. The flame snapshot illustrates the scale of the flame, and its position relatively to the microphones and PMT collection zone. Distances are given in mm.

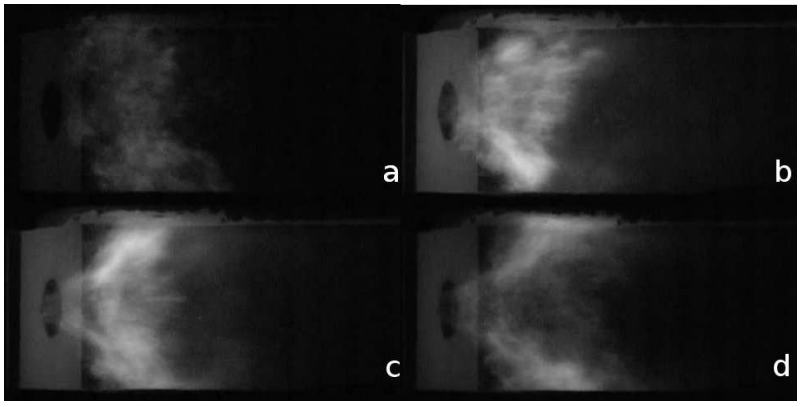

Figure 2.4: Instantaneous flame images in the nominal operating regime, obtained with a CCD camera.

Parameter	Unit	Min.	Max.	Operating	Leaner	Richer
Total air mass flow	Nm^3h^{-1}	30	60	41.15	41.15	41.15
$\dot{m}_{a,t}$	$g.s^{-1}$	10.75	21.5	14.74	14.74	14.74
Staging α	-	0	1	0.145	0.32	0.50
Total equivalence ratio Φ_t	-	0	1	0.81	0.72	0.87
Thermal power P	kW	17	59	32.29	28.2	35.3
Reynolds number Re	-	22000	44000	32000	32000	32000

Table 2.1: Combustion bench operating range

and light emissions vary strongly during a cycle.
The regime studied corresponds to an air injection in each stage of $\dot{m}_{air} = 7.1 \pm 0.1\,g.s^{-1}$ and a propane total massflow rate of $\dot{m}_f = 0.76 \pm 0.02\,g.s^{-1}$ with a staging of $\alpha = 14.5\%$. The global equivalence ratio is fixed to $\Phi = 0.82$, when perfectly mixed gases are assumed. The facility operating range is detailed in table 2.1. This particularly unstable regime is described by Dioc (2005). A flame image obtained by Planar Laser Induced Fluorescence (PLIF) on the OH^* radical is provided at scale with the burner geometry in Figure 2.3. One can clearly identify the flame position with respect to the microphone locations and its spatial extension. Two other regimes have also been explored in this study, one on the lean side and the other characterized by a richer fuel equivalence ratio. Their characteristics are also gathered in table 2.1.
Examples of evolutions of the PSD measured in the facility are reported in figure 2.5 for the $\Phi = 0.82$ operating regime. A strong peak can be observed at $f = 288\,Hz$ on every sound power spectrum, as well as on the heat-release rate fluctuation spectrum obtained from chemiluminescence fluctuations measurements. This combustion instability corresponds to pressure fluctuations in the whole facility of up to $p_1 \simeq 200\,Pa$.
The premixer inlet boundary condition has been replaced by the Impedance Control System (ICS) used to provide an adaptive impedance condition. Technical aspects of this system are now described. Detailed description of its principle are presented in chapter 4, while results of its implementation are presented in chapter 5.

2.2 Impedance Control System (ICS)

The premixer inlet adaptive impedance system (ICS) is composed of a perforated plate of low porosity (below 10%) and a piston sliding in an airtight cylindrical casing, as sketched in figure 2.6a. The perforated plate is placed at the inlet of the premixer channel. The ICS is designed such that changing the back-cavity depth does not result in adding a length to the inner premixer channel, that would simply shift the combustor eigenfrequencies. Tuning the cavity depth rather implies a modification of the perforated plate impedance as is described in chapter 4. The influence of the premixer inlet impedance on the resonance frequencies of the combustion rig point is investigated in chapter 6. The sliding piston has an hollow shaft and partially hollow head, to enable air injection through the perforate. The hollow part of the head is covered by a sinter bronze plate inserted in a thick metal plate covering the rest of the head surface, as illustrated in figure 2.6b. This provides a flat rigid surface. The sinter bronze

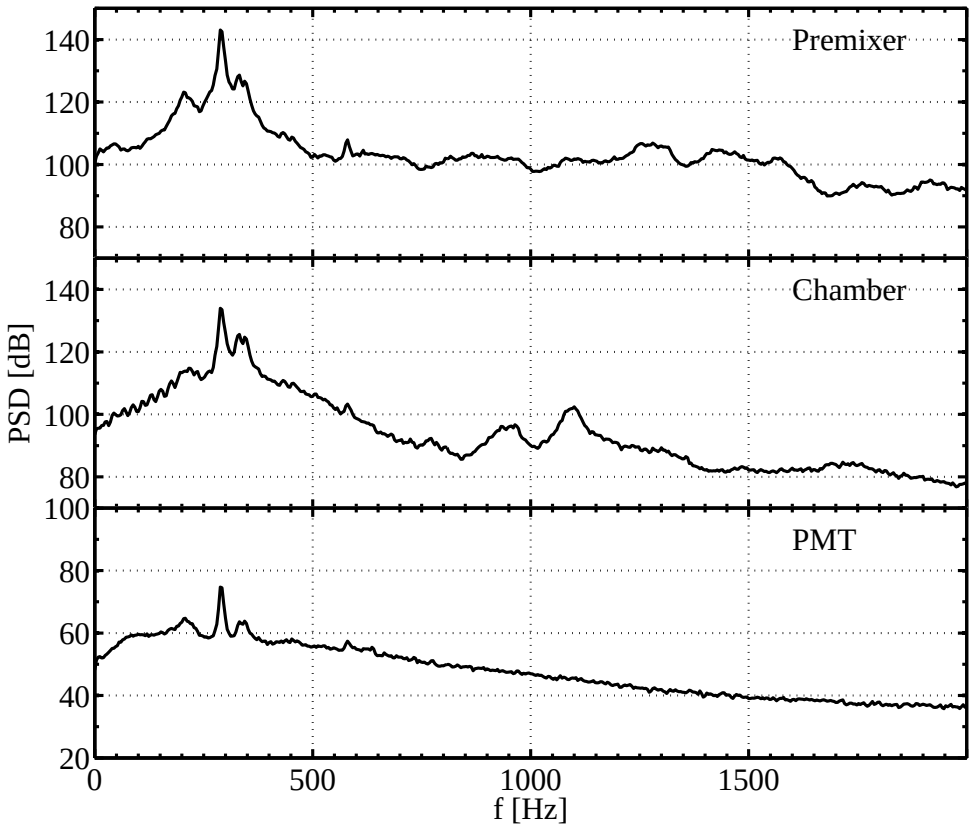

Figure 2.5: Power Spectral Densities in the combustion facility at the operating regime. A low frequency instability peak emerges at $f = 288\,\text{Hz}$ in the premixer channel (top), inside the combustion chamber (middle) and on the chemiluminescence emission signal from the flame (bottom) indicating heat-release rate oscillations synchronized with large pressure fluctuations.

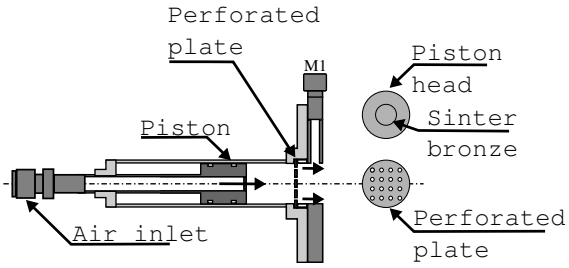

(a) Schematic of the ICS, with details of the perforated plate geometry and of the piston head.

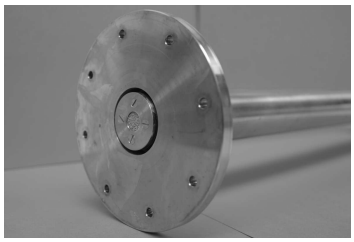

(b) Piston head and casing as installed on the combustion facility. Head diameter is $D = 30\,\text{mm}$.

Figure 2.6: Adaptive impedance control system (ICS) schematic (a) and photo (b).

is a slightly absorbing material from the acoustic point of view. However its surface is small enough to assimilate the piston head to a perfectly reflecting plate. On the fly measurements of the reflection coefficient will confirm this assumption. The cylindrical casing and the piston shaft provides a displacement up to $50\,\text{cm}$.
Once set up on the combustor, the perforated plate is located $1.5\,\text{cm}$ upstream of the first microphone port. This device can be envisaged as a passive control system. The piston is shifted manually, which cannot be done during firing tests for obvious safety reasons. The cavity backing the perforated plate may be considered as decoupled from the premixer inner channel thanks to the low plate porosity. When the piston is shifted, there is no modification of the inner geometry of the facility. The influence of the ICS on the flow aerodynamics is now investigated using Particle Image Velocimetry.

2.3 Flow aerodynamics by Particle Image Velocimetry

Particle Image Velocimetry (PIV) is a non intrusive optical technique which allows measurements of two-dimensional velocity fields, see Adrian (2004) for a review. It consists in illuminating a slice of a flow field seeded with tracer particles and recording two successive image of the light scattered by the particles. The most common PIV setups make use of a laser to illuminate the flow and of cameras to record images pairs. Lasers provide a high energy density beam which is easily reshaped in a planar slice using a set of cylindrical lenses. The displacement of the tracers can then be computed through an analysis of the images. With reliable flow tracers, the flow velocity at a particle location is equal to the particle velocity. This velocity is thus retrieved from the measured displacement δx and the imposed time delay between the laser exposures δt :

$$v\,(x,t) = \frac{\delta x}{\delta t} \tag{2.2}$$

where the particle displacement must be small enough to neglect the potential contribution of particle acceleration. Furthermore, a tracer particle must meet several requirements to accurately reproduce the local flow velocity :

- it should not perturb the flow,
- its inertia should be very low such that it induces a minimal velocity lag,

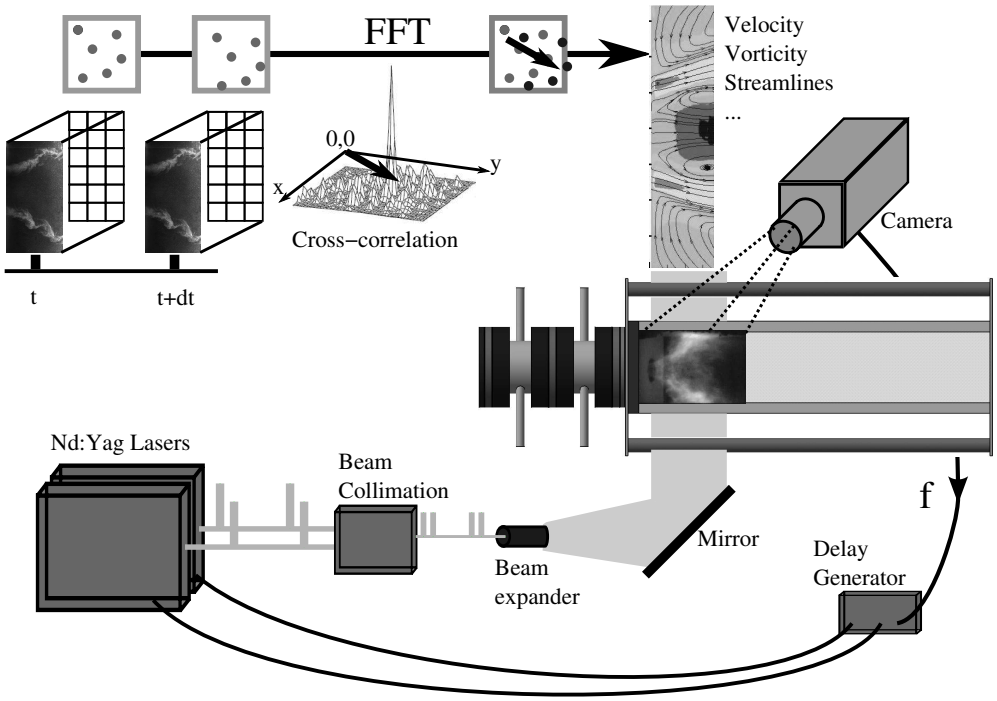

Figure 2.7: Schematic of the PIV acquisition system and of the post-processing principles.

- it should ensure homogeneous flow seeding in time and space,
- it should scatter light efficiently.

To limit flow perturbations, particle density should be low and their diameter should be much smaller than the size of the typical turbulent structures. Small diameters are also needed for an accurate estimation of the local flow velocity. However, the choice of the particle size results of a trade-off between this ability to follow the flow and their efficiency in scattering light. From Mie theory, particle diameter should be chosen of the order of magnitude of the wavelength of the incident light. Particles most commonly used have a diameter of about a micrometer to allow the use of lasers in visible wavelengths. Finally the tracers mass density controls the ability to homogeneously seed a flow containing vortical structures.
Within the frame of PIV in combustion, the nature of the particles also plays a key role on the results. Liquid seeding tracers (like oil droplets) will only allow measurements in the unburnt fresh gases. Refractory solid particles with melting points higher than the flame temperature will obviously allow measurements in both fresh and burnt gases.

2.3.1 PIV setup

A High Speed Particle Image Velocimetry (HSPIV) technique was used to measure velocity fields both in reactive and non-reactive cases (see Barbosa et al. (2009) for more details on this system). Figure 2.7 sketches the acquisition setup and the post-processing principles. The combustion chamber is equipped with rectangular quartz windows ($25 \times 120\,\mathrm{mm}^2$) in the bottom and top concrete plates, through which a vertical laser sheet crosses the combustion chamber, downstream the injection plane. Two *Quantronix* Nd:YAG laser beams are colli-

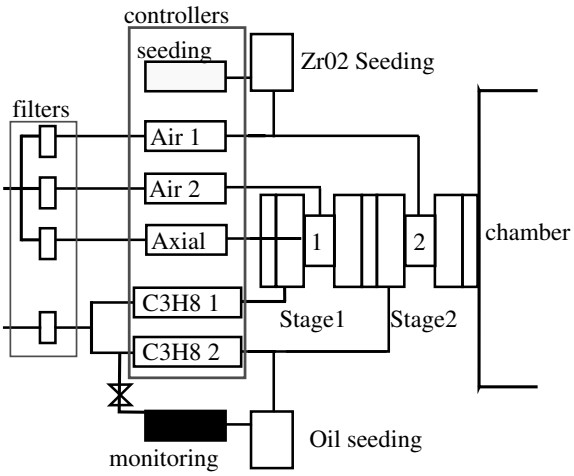

Figure 2.8: Schematic of the feeding lines of the combustion bench, with the two seeding setups for oil and particle seeding. Air, fuel and particles seeded flow massflow rates are controlled by massflow meters. Oil seeded massflow rate is controlled by a valve and measured with a flowmeter. Air flowmeters **Air1** and **Air2** and propane flowmeters **C3H8 1** and **C3H8 2** feed stages 1 and 2 respectively, while **Axial** flowmeter provides the axial air injection.

mated along the same trajectory such that the shooting rate can reach up to $20\,$kHz. The laser sheet ($0.3\,$mm thick and $90\,$mm wide) is generated by a set of *Melles Griot* cylindrical lenses. Images are recorded on a CMOS sensor by a *Photron* high speed camera equipped with a $105\,$mm *Nikon* lens. The camera, operating at $24\,$kHz controls a pulse delay generator, which triggers alternatively each laser, operating at $12\,$kHz with a time delay of $\delta t = 6\,\mu$s. At such acquisition rates, images are limited to $128 \times 512\,$pixels^2. Flow was seeded either with paraffin oil in non reactive cases, or with solid white particles of zirconium dioxide ZrO_2 in reactive configurations. Zirconium dioxide has a melting point higher than typical adiabatic flame temperatures of common hydrocarbon fuels. The schematic of the tracer seeding setup is presented in figure 2.8. The main characteristics of the different tools are gathered in table 2.2. Paraffin oil was chosen for its mean particle diameter and ease of use. It was used to seed the propane injection line of the second stage, as only a small amount of particles was needed to achieve homogeneous seeding. The propane massflow was replaced by the equivalent air massflow rate to conduct these non reactive experiments. Part of this massflow was bypassed via a valve and injected in a *Dantec* fog generator. The seeded flow is then mixed with unseeded air flow and fed to the premixer. In the reactive case, the amount of particles required to achieve sufficient seeding was much higher. Therefore, the air injection of the first stage was used in this case. Part of the airflow was bypassed via a massflow controller into a homemade powder seeding generator. Its operating principle is based on the creation of a cyclone inside an enclosure containing the particles. At the center of the box, and of the cyclone, a small exhaust collect a flow seeded with the smallest particles, as the large ones are ejected from the cyclone. This massflow is then mixed with the unseeded airflow and injected into the premixer.

Equipment	Manufacturer	Type	Characteristics
Lasers	Quantronix	Nd:Yag	$\lambda = 532\,\text{nm}$ Pulse duration: $160\,\text{ns}$ Energy per pulse: $60\,\text{mJ}$ Frequency: max.$20\,\text{kHz}$
Camera	Photron	Fastcam APX	10bit monochrome CMOS $1024 \times 1024\,\text{pixels}^2$ at $2\,\text{kHz}$
Lens	Nikon	Nikkor	$105\,\text{mm}$, $\text{F}/1.8$
Parrafin oil	Dantec		Mean diameter: $1.6\,\mu\text{m}$ Density: $0.8\,\text{gcm}^{-3}$
Zirconium oxide	Fischer Chemical	Z/1850/50	Melting point: $2715\,^{\text{o}}\text{C}$ Density: $5.89\,\text{gcm}^{-3}$

Table 2.2: PIV diagnostic tools characteristics.

2.3.2 PIV post-processing

The PIV technique is based on a statistical approach to obtain the most probable displacement of a group of particles. The groups are determined by subdividing the images in small interrogation windows. Cross-correlation of corresponding windows is then performed on the image pairs using Fast-Fourier Transform. The distance of the cross-correlation peak to the origin gives the most probable displacement of the particles within the interrogation window. The correlation noise is due to the mean background intensity of the images and to marginal and random matching of particles. The amplitude of the correlation peak relatively to the noise level allows evaluation of the reliability of the correlation. It can be improved on the one hand by enhancing the raw image quality (by optimizing the light scattering, enhancing the contrast and laser light uniformity for example) and, on the other hand, by interrogation window displacements (Westerweel et al. (1997)) and distortions, to increase the number of matching particles between image pairs (Scarano and Riethmuller (2000), Nogueira et al. (2001)). For each case presented in this work, 12000 image pairs were acquired, for a total duration of $1\,\text{s}$. These $12\,\text{bits}$ Tiff image pairs were processed with the *Dantec* Flow-Manager adaptive cross-correlation software (Dantec 1998). A Fast-Fourier algorithm, combined with interrogation window displacements and distortions and subgrid interpolation is used to determine the velocity field. Square 8×8 interrogation windows were used with a 25% overlap.

2.3.3 Aerodynamic characterization of the ICS

In the nominal operating regime, it has been checked that the ICS adapted at the premixer inlet has no influence on the velocity field in the flame region, that is stabilized at the exhaust of the premixer channel, using the HSPIV protocol. Several back-cavity depths were set with the sliding piston, and 6200 image pairs were recorded, corresponding to an acquisition duration of $1\,\text{s}$. The time delay was set to $6\,\mu\text{s}$. The image field is a rectangular vertical window centered on the premixer symmetry axis, representing a field of view of $512 \times 256\,\text{pixels}^2$, which corresponds to a $70 \times 31\,\text{mm}^2$ region. Classical post-processing was carried out on interrogation windows of $8 \times 8\,\text{pixels}^2$ interrogation windows. The mean velocity fields were obtained

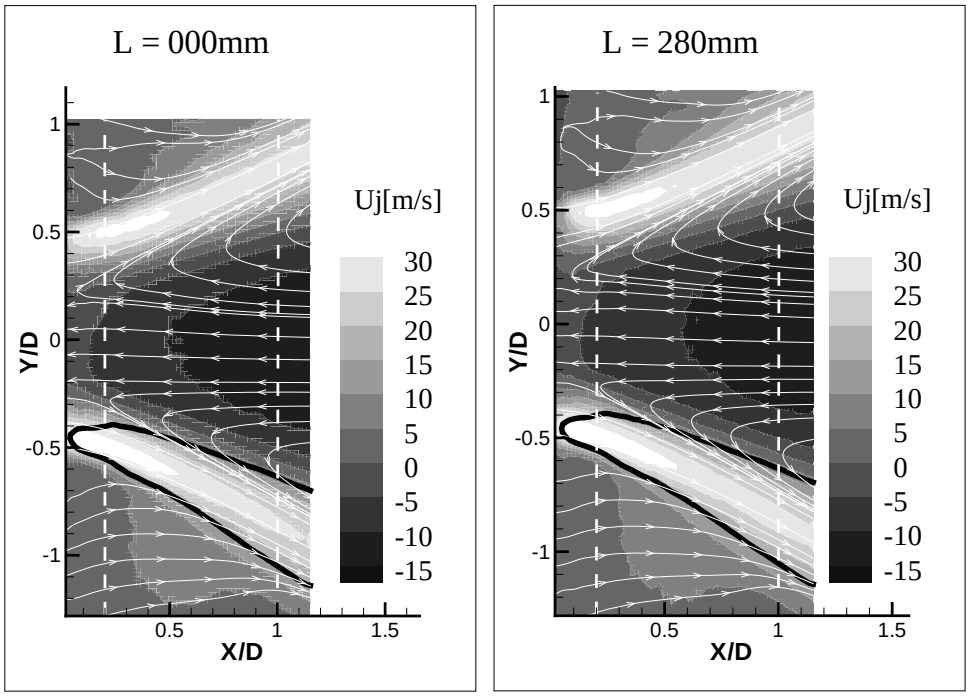

(a) $L = 000\,\text{mm}$. (b) $L = 280\,\text{mm}$

Figure 2.9: Mean velocity fields, colored by the axial velocity amplitude, in the symmetry plane at the premixer exhaust for two different back cavity depths, $L = 0$ (a) and $L = 280\,\text{mm}$ (b) in the nominal combustion regime. The black contour indicates a zone of negative radial velocity. White lines are velocity streamlines. Dimensions were divided by the premixer channel diameter $D = 30\,\text{mm}$ and the zero is set at the premixer axis of symmetry.

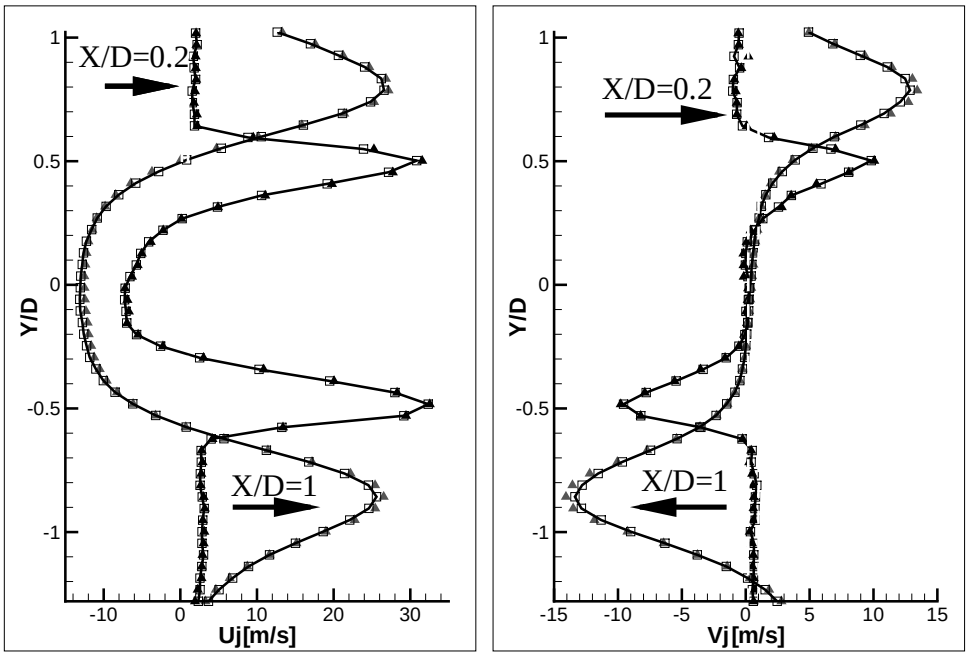

(a) Mean axial velocity profiles.

(b) Mean radial velocity profiles

Figure 2.10: Mean velocity profiles extracted at $x/D = 0.2$ (black) and $x/D = 1$ (grey). Solid line and square symbols represent the configuration with no back-cavity ($L = 0$ mm), while triangles plot the results for $L = 280$ mm.

by averaging all the acquired sequences. The mean axial velocity Uj for two back-cavity depths $L = 0$ mm and $L_{opt} = 280$ mm are compared in figures 2.9. As will be shown in the following, L_{opt} represents the optimal cavity depth to minimize the ICS reflection coefficient around $f = 288$ Hz.Dimensions were divided by the premixer channel diameter $D = 30$ mm. The amplitudes and structures of the mean axial velocity fields are quite similar in both cases. The black contour determines a region of the flow which corresponds to a negative radial velocity. This zone is located at the same position in both cases. Finally the streamlines are almost identical.

Two velocity profiles were extracted for further comparisons, at $x/D = 0.2$ and $x/D = 1$. The influence of the two cavity depths on these profiles is plotted for the mean axial Uj and radial Vj velocities in figures 2.10a and 2.10b respectively. Symbols differentiate the cavity depths (squares mark the case $L = 0$, triangle the case $L = 280$ mm). Colors indicate profile location (black corresponds to $x/D = 0.2$, grey to $x/D = 1$). The profiles obtained for $L = 0$ mm and $L = 280$ mm are perfectly superimposed at both locations. Further results concerning the velocity fluctuations are provided in figures 2.11a and 2.11b. Profiles of axial fluctuating velocities at $x/D = 0.2$ and $x/D = 1$ are compared in the two situations, $L = 0$ mm and $L = 280$ mm. The relative difference between the velocities fluctuations levels at $L = 0$ mm and $L = 280$ mm is also evaluated at the same locations and given in appendix A. Changing the back-cavity depth from $L = 0$ mm to $L = 280$ mm results in a $5\,\%$ decrease of

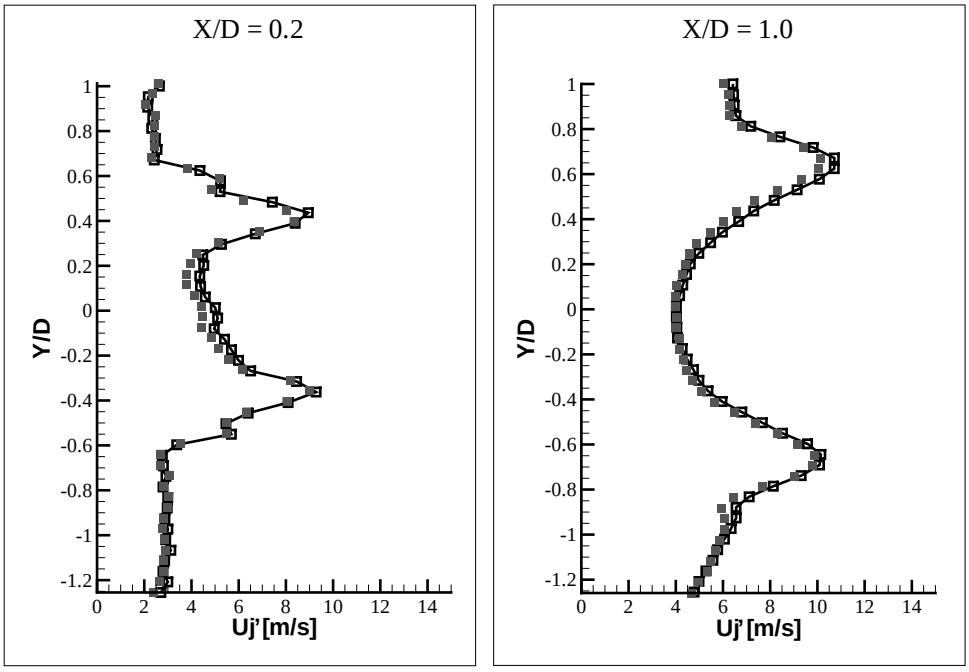

(a) $X/D = 0.2$. (b) $X/D = 1$.

Figure 2.11: Axial fluctuating velocity profiles extracted at $x/D = 0.2$ (a) and $x/D = 1$ (b). Solid line and square symbols represent the configuration with no back-cavity ($L = 0$ mm), while grey squares plot the results for $L = 280$ mm.

the fluctuating velocities, either axial or radial. The maximal amplitude of the axial fluctuating velocity is about $Uj' = 9\,\mathrm{ms}^{-1}$, and $Vj' = 5\,\mathrm{ms}^{-1}$ for the radial velocity. As a consequence, the slight difference in the fluctuating amplitudes between the two situations is not significant and it may be assumed that the premixer inlet impedance has a weak influence on the velocity fluctuations.
Since the ICS is designed to have a strong influence on the acoustic field in the combustion rig, it was expected to observe this effect directly on the fluctuating velocity fields, which contain the acoustic contribution. This is obviously not the case. It may be due to high levels of velocity fluctuations associated with aerodynamic processes such as the inner precessing vortex core rotation which may dominate the acoustic contribution. This assumption should be further investigated with dedicated experiments.

2.3.4 Evaluation of the Strouhal number at the premixer outlet

Using the mean velocity fields from PIV, it is possible to evaluate a Strouhal number St characterizing the flow oscillating mechanisms, based on the premixer channel diameter D, the instability frequency f and the measured velocity Uj:

$$\mathrm{St} = fD/U_j \tag{2.3}$$

A classical investigation reported by Crow and Champagne (1971) indicates that the response of a circular turbulent jet to a pure tone excitation reaches a maximum for a jet Strouhal number equal to $\mathrm{St} = 0.3$. However, for a free jet (Crow and Champagne 1971), the Strouhal number corresponding to the vortex passage frequency is equal to $\mathrm{St} = 0.45$. This preferred mode Strouhal number depends to some extent on the initial conditions and background noise level and takes values from 0.2 to 0.64 according to Gutmark and Ho (1983).
The Strouhal number in the present configuration is calculated making different hypothesis on the flow structure, at the frequency of the main instability peak $f = 272\,\mathrm{Hz}$. One considers first a circular jet of diameter equal to the premixer inner channel $D = 30\,\mathrm{mm}$. The mean flow velocity is computed from the massflow conservation in the channel, $Uj \simeq 16.5\ \mathrm{ms}^{-1}$. This yields a Strouhal number of $\mathrm{St} = 0.49$, quite close to the value of the preferential mode for a free jet (Crow and Champagne 1971). However, from the mean velocity fields obtained by HSPIV, it can be noted that the flow pattern is closer to an annular jet of hydraulic diameter $D = 3\,\mathrm{mm}$ than to a free circular jet. The mean flow velocity at the basis of this annular jet is measured at $Uj = 30\ \mathrm{ms}^{-1}$ (figure 2.9), resulting in a much lower Strouhal number $St = 0.0272$. Such low value would discard the influence of the unsteady processes in the observed instability. The presence of a large central recirculation zone on the velocity field could be assimilated to a virtual bluff-body and therefore the instability may be due to the shear layer existing in its wake. In such situation, the Strouhal number would equal $\mathrm{St} = 0.22$, based on the diameter of the CRZ $D = 24\,\mathrm{mm}$ and the velocity obtained by PIV $Uj = 30\ \mathrm{ms}^{-1}$. With such an assumption, the observed combustion instability could be linked to a Strouhal number within the commonly accepted range (Gutmark and Ho 1983). The instability frequency would then be the preferential mode linked to the wake of the CRZ. These results are gathered in table 2.3.
The estimated Strouhal numbers span over a wide range of values and may not provide a direct link between the observed instability frequency and the flow features. In his review upon the influence of the precessing vortex core, Syred (2006) gathered Strouhal numbers for various situations, as a function of the Swirl number, the equivalence ratio or the confinement amongst other. Results spans from 0.005 to more than 2 and appears mainly linked to the

Configuration	Velocity Uj [ms^{-1}]	Distance D[mm]	St
Massflow conservation	16.5	30	0.49
Annular jet from PIV	30	3	0.0272
Wake with jet velocity from PIV	30	24	0.22

Table 2.3: Evaluation of flow Strouhal numbers at $f = 272$Hz.

Swirl number. This investigation on the flow Strouhal number in the current facility would thus require further investigation to yield conclusive results.
This study of the aerodynamics of the flame region confirms that the ICS placed at the premixer inlet has a weak influence on the velocity field. Its effects are therefore expected to be only of acoustic nature. In addition to the HSPIV technique, the heat-release rate fluctuations were measured to study the combustion process, determine the nature of the observed instabilities and eventually measure the Rayleigh source term in the facility. This measurement technique is now presented.

2.4 Heat-release rate measurements

Radical	Transition	λ [nm]
OH*	$\mathrm{A}^2\Sigma^+ \rightarrow \mathrm{X}^2\Pi$ (1-0)	282,9
	$\mathrm{A}^2\Sigma^+ \rightarrow \mathrm{X}^2\Pi$ (0-0)	308,9
CH*	$\mathrm{B}^2\Sigma^- \rightarrow \mathrm{X}^2\Pi$	387,1
	$\mathrm{A}^2\Delta^+ \rightarrow \mathrm{X}^2\Pi$	431,4
C_2^*	$\mathrm{A}^3\Pi\mathrm{g} \rightarrow \mathrm{X}^3\Pi_\mathrm{u}$ (Swan)	516,5

Table 2.4: Main transitions and associated wavelength of the three main species observed in industrial hydrocarbons flames. Adapted from Docquier et al. (2000).

In lean premixed flames, the natural chemiluminescence results from the radiation of intermediate excited species D^*, in the reaction region. These excited species are destroyed either by collisions or by spontaneous emission. In the latter case, a photon of energy $\mathrm{h}\nu$ is emitted : $\mathrm{D}^* \rightarrow \mathrm{D} + \mathrm{h}\nu$, where h is the Planck constant and ν is the photon frequency. This frequency corresponds to the energy difference between the excited state (D^*) and the ground state (D). Each molecule emits a radiation which is characteristic of its electronic structure. It is known that the emission intensity from OH^*, CH^*, and $\mathrm{C2}^*$ in hydrocarbon flames can be used to observe the location of the primary combustion region. This property has been used extensively in combustion studies. Poinsot et al. (1987) were probably the first to report instantaneous phase conditioned maps of free radicals emissions. This was used to examine a vortex-driven acoustically-coupled instability of a multiple injector combustor. The main transitions and the corresponding emitted wavelengths of the three radicals are summarized in table 2.4. The chemiluminescence from these three excited radicals is commonly used to measure aspects of combustion. For a recent analysis see Schefer (1997) who has shown that their emissions coincide with the reaction zone. The emission intensities have indeed been

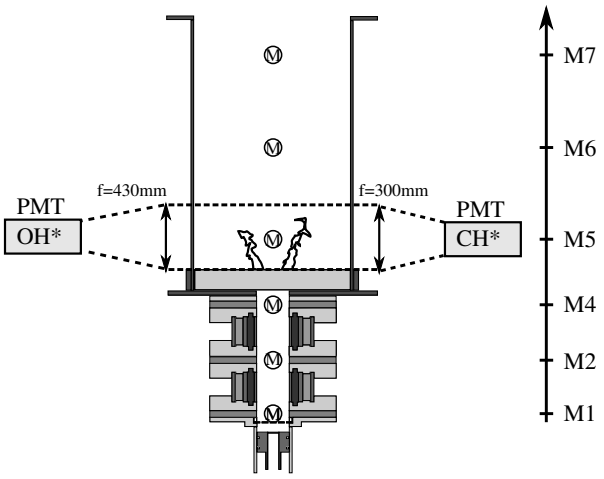

Figure 2.12: Technical arrangement used to monitor the spontaneous emissions of the OH^* and CH^* excited radicals. Microphone ports and numbering is also indicated.

Equipment	Manufacturer	Type	Characteristics
Photomultiplier tubes	Electron Tubes	9124QB	Spectral range: $160 - 680$ nm
CH^* filter		9605	Bandwith: $\lambda = 430 \pm 10$ nm
OH^* filter		9352	Bandwith: $\lambda = 310 \pm 30$ nm
Lens	Melles & Griot	Quartz	Focal length: $f = 430$ mm
			Diameter: 15 cm
Lens	Melles & Griot	Quartz	Focal length: $f = 300$ mm
			Diameter: 15 cm

Table 2.5: Heat release diagnostic tools characteristics.

correlated to the equivalence ratio in various conditions. Higgins et al. (2001) and Docquier et al. (2002) have used the OH^* and CH^* emissions to infer the equivalence ratio of premixed fuel-lean methane/air flames at atmospheric and elevated pressures. They used integrated measurements to collect the whole flame light emissions. In other studies, Kojima et al. (2000) have used spatially resolved measurements in the reaction zone of a laminar premixed rich methane/air flame. It is commonly accepted that in well controlled configurations, radical light emissions of a laminar premixed flame are proportional to, and in phase with, its heat-release rate (Walsh et al. 1998; Schuller et al. 2002). In turbulent, partially premixed lean system, such a proportionality is more difficult to establish.

2.4.1 Chemiluminescence measurements

The spontaneous emission of radicals CH^* and OH^* has been measured using *Electron Tubes* fused silica PhotoMultiplier Tubes (PMT) equipped with specific filters in the arrangement depicted in figure 2.12. One PMT was equipped with a very narrow band pass filter to detect CH^* radical, and the second was focused on the OH^* radical. Figures 2.13a and 2.13b show

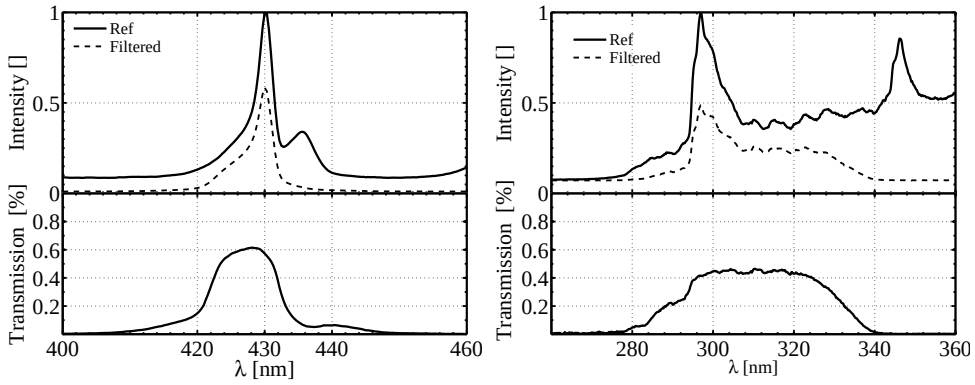

(a) CH^* filter. (b) OH^* filter.

Figure 2.13: Characteristics of the filters used for chemiluminescence measurements. Top graphs present the normalized intensity (dashed line) obtained by filtering a given signal (solid line). Bottom graphs indicate the filter bandwith and transmission percentage.

the characteristics of the CH^* and OH^* filters. The bandwith and transmission percentage of each filter was measured using a spectrometer and a given reference signal. This reference signal and the filtered signal are presented, normalized by the peak amplitude of the reference. The OH^* filter has a large bandwith about 60 nm and a low transmission about 40% while the CH^* filter is very narrow (10 nm) and has a better transmission (around 60%). A better signal to noise ratio and a greater signal dynamic are thus expected from the PMT equipped with the CH^* filter.

The photomultiplier tube is an extremely sensitive light detector providing a current output proportional to the collected light intensity I. Large area light detection, high gain and the sensitivity to detect a few photons are the key advantages of this tube. The experimental arrangement is sketched in figure 2.12, and the characteristics of the setup are gathered in table 2.5. Two PMT were positioned on each side of the combustion chamber, and large quartz lenses were used to collect the global light emission from the combustion volume and focus it on the PMT sensitive element. Measurements were realized in a dark room resulting in a minimal background noise measured by both PMT. They are thus providing a signal proportional to the global emission in the flame region, I_{CH^*} and I_{OH^*} respectively. PMT signals are composed of a mean continuous voltage, and a fluctuating component. Therefore, the spontaneous emission of radical D can be decomposed as $\mathrm{I}_{D^*} = \mathrm{I}_{0,D^*} + \mathrm{I}_{1,D^*}$. Examples of raw chemiluminescence signals are presented in figures 2.14a and 2.14b for a stable (left) and for an unstable regime (right). The associated Power Spectral Densities (PSD) are also plotted in figures 2.14c and 2.14d. In both cases, there is a mean component due to the average light emission of the flame. During the unstable regime, very large fluctuations of the radicals spontaneous emission are measured by the PMT indicating large variations of the heat-release rate. In figure 2.14b, the PMT response exhibits bursts and almost sinusoidal fluctuations. The associated power spectral analysis (figure 2.14d) highlights the presence of a fundamental mode and its first harmonic associated with these oscillations, at $f = 272\,\mathrm{Hz}$ and $f = 544\,\mathrm{Hz}$ respectively.

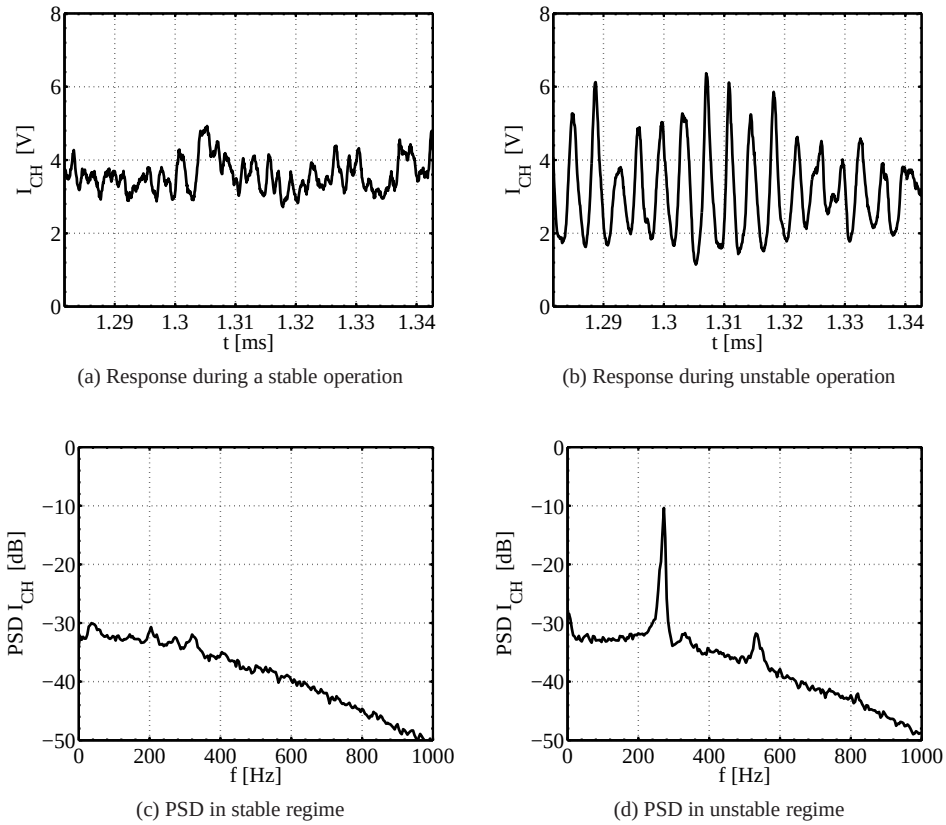

(a) Response during a stable operation

(b) Response during unstable operation

(c) PSD in stable regime

(d) PSD in unstable regime

Figure 2.14: Raw PMT time traces and PSD signals of the CH^* chemiluminescence measured during stable and unstable combustion regimes.

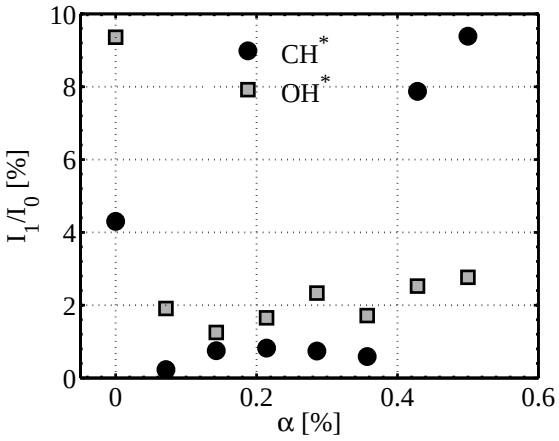

Figure 2.15: Influence of the fuel staging α on the PMT response, for a fixed total fuel equivalence ratio $\Phi = 0.81$.

2.4.2 Heat-release rate estimation

The combustion bench is a turbulent, partially premixed lean combustor. It is commonly considered that the light emission collected from the flame is proportional to the heat-release rate in perfectly premixed systems. This relationship is yet mostly used to examine the phase of the heat-release rate with respect to the pressure fluctuations in the flame region. The Rayleigh criterion indicates that combustion instabilities are promoted if pressure fluctuations, p_1, and heat-release rate fluctuations, $\dot{q}_1$, locally oscillate in phase. This is mathematically expressed by:

$$\int_T p_1 \dot{q}_1 dt \; > \; 0, \tag{2.4}$$

To obtain quantitative results, a relationship must be established between the heat-release rate within the combustion chamber and the chemiluminescence signal. Therefore a calibration of the PMT response (I) was carried out as a function of the fuel massflow rate $\dot{m}_f$, the global equivalence ratio Φ and the fuel staging α: $\mathrm{I} = g\left(\alpha, \Phi, \dot{m}_f\right)$.

The influence of the fuel staging is first investigated to determine the quality of the fuel-air premixing. The ratio of the fluctuating to the mean component of the PMT response $\mathrm{I}_1/\mathrm{I}_0$ varies very few for moderate values of the staging α, as presented in figure 2.15 for the two radicals emissions investigated. The variation reaches 10% in extreme cases, when there is no staging or in strongly unstable conditions, when $\alpha \geq 50\%$. These staging are largely out of the scope of this study where the reference regime corresponds to a staging of $\alpha = 14.3\%$. It is thus assessed that the fuel staging has no influence on the chemiluminescence response, fuel and air are considered as perfectly premixed before combustion, around the nominal operating conditions.
In a second set of experiments, the influence of the fuel massflow rate was investigated for three different equivalence ratios $\Phi = 0.75, 0.81 \,\mathrm{and}\, 0.93$. At each equivalence ratio, linear relationships were observed between the PMT mean value and the massflow rate, as illustrated

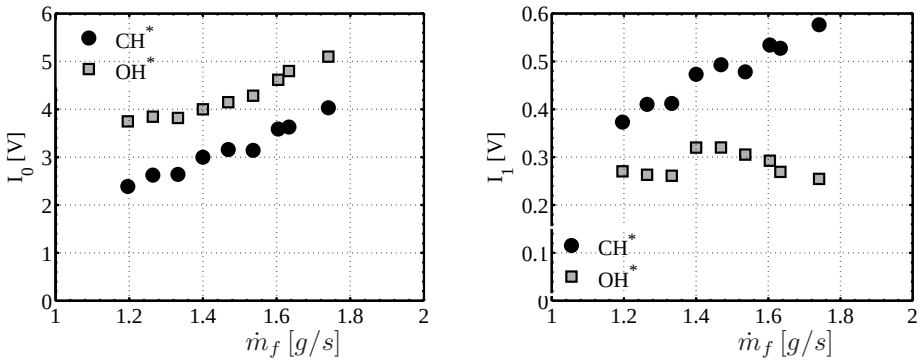

(a) PMT Mean intensity I_0 (b) PMT RMS intensity I_1

Figure 2.16: Evolution of the PMT response with fuel massflow rate for an equivalence ratio of $\Phi = 0.81$. Black circles mark the CH^* radical, grey squares correspond to the OH^* radical.

in figure 2.16a for the particular case of a global equivalence ratio of $\Phi = 0.81$. The fluctuating component exhibits also a clear proportionality with the fuel massflow rate in the case of the CH^* radical, while the OH^* radical present a very weak dependence on this parameter (fig. 2.16b). The response obtained with the OH^* radical has a weaker dynamic which may be due to the larger bandwith of the filter resulting in a broader background noise and to its low transmission coefficient.
For a given global equivalence ratio, the PMT response is found to verify a linear relationship with the fuel massflow rate injected in the premixer:

$$\mathrm{I} = a\left(\Phi\right)\dot{m}_f + b\left(\Phi\right) \tag{2.5}$$

The non dimensional ratio of the fluctuating component to the mean PMT response can then be constructed :

$$\frac{I_1}{I_0} = \frac{\dot{m}_{f,1}}{\dot{m}_{f,0} + b/a} \simeq \frac{\dot{m}_{f,1}}{\dot{m}_{f,0}} \simeq \frac{\dot{Q}_1}{\dot{Q}_0} \tag{2.6}$$

In a first approximation, $b/a \leq \dot{m}_f$. The PMT response is therefore only a function of the massflow rate and its fluctuations. For the reference equivalence ratio used in this work $\Phi = 0.81$, this approximation leads to an overestimation error of $\approx 20\%$ of the non-dimensional ratio $\frac{\dot{Q}_1}{\dot{Q}_0}$.

2.5 Evaluation of the Rayleigh source term

There is no direct access to quantitative measurements of the unsteady heat-release rate $\dot{q}$, but this term can be deduced from the optical measurement of the flame light intensity detected

Φ	a	b	b/a
0.75	5.18	0.59	0.11
0.81	2.95	1.17	0.39
0.93	8.67	3.73	0.43

Table 2.6: Coefficients of the linear relationship 2.5 for the different fuel equivalence ratio.

by the photomultiplier tubes. The objective is to measure the Rayleigh source term:

$$\mathcal{S} = \left\langle \int_V \frac{\gamma - 1}{\gamma p_0} p_1 \dot{q}_1 dv \right\rangle_T \tag{2.7}$$

where $\langle X \rangle_T = \frac{1}{T} \int_T X dt$ denotes the mean value over a period of combustion oscillations.
The flame is compact with respect to acoustic wavelengths at stake; its spreads in the combustion chamber over a typical length of $10\,\text{cm}$, while the acoustic wavelength associated to the main instability ($f \approx 280\,\text{Hz}$) in the hot gases ($c_0 \approx 700\,\text{m.s}^{-1}$) corresponds to $\lambda = c_0/f \approx 2.3\,\text{m}$. Pressure fluctuations can thus be assumed to be uniform over the whole flame region and are monitored by a single pressure sensor placed above the flame (microphone M5 in figure 2.12). Furthermore, the PMT provides an integrated measurement over the whole flame volume, as large collection lenses were used. If it is assumed that γ and c_p are constant over the flame region, the unsteady source term can be rewritten as :

$$\mathcal{S} = \left\langle \int_V \frac{\gamma - 1}{\gamma p_0} p_1 \dot{q}_1 dv \right\rangle_T = \left\langle \frac{\gamma - 1}{\gamma p_0} p_1 \int_V \dot{q}_1 dv \right\rangle_T = \left\langle \frac{\gamma - 1}{\gamma p_0} p_1 \dot{Q}_1 \right\rangle_T \tag{2.8}$$

where capital letter Q indicates the volume integrated value of the unsteady heat-release rate $\dot{q}$. Assuming that all fuel is burnt, the mean heat release rate $\dot{Q}_0$ can be estimated from the fuel massflow rate and the fuel heating value : $\dot{Q}_0 = \dot{m}_f \Delta h_f^0$. The source term can be expressed as:

$$\mathcal{S} = \frac{\gamma - 1}{\gamma p_0} \dot{m}_f \Delta h_f^0 \left\langle \frac{p_1 \dot{Q}_1}{\dot{Q}_0} \right\rangle_T \tag{2.9}$$

Finally, using equation 2.6, the Rayleigh source term can be evaluated from experimental data as follow :

$$\mathcal{S} \simeq \frac{\gamma - 1}{\gamma p_0} \frac{\dot{m}_f \Delta h_f^0}{I_0} \langle p_1 I_1 \rangle_T \tag{2.10}$$

where γ is the heat capacity ratio, p_0 the mean pressure, $\dot{m}_f$ is the total fuel massflow injected, Δh_f^0 is the propane heating value and $\mathrm{I} = \mathrm{I}_0 + \mathrm{I}_1$ is the total light emissions from the flame collected by PMT.

Concluding remarks

A lean premixed swirled stabilized burner, designed and extensively studied in a previous Ph.D (Dioc (2005)), has been slightly modified to allow acoustic measurements inside the

premixer itself. The premixer inlet boundary condition of this burner has also been equipped with a passive impedance control system (ICS) that provides an tunable acoustic impedance boundary condition. PIV was used at high repetition rate to give access to instantaneous velocity field in the combustion chamber and check that this system does not modify the aerodynamic behavior of the original burner. The heat-release rate measurements were used classically to qualitatively evaluate the Rayleigh criterion. A complete protocol was also setup to obtain first-order quantitative estimations of this energy source term. This represent the first step for the experimental evaluation of the acoustic energy balance. The second step is to evaluate the acoustic fluxes at the inlet and outlet of the domain, to take into account the losses that are discarded in the simple formulation of the Rayleigh criterion. This evaluation was achieved using microphones to measure acoustic pressures and is presented in chapter 3. This facility is drawn side by side in figure 2.17 with the high load impedance tube that has been used to test and validate the ICS. This impedance tube can reproduce the geometry of the premixer, thanks to the airflow injections, its tunable nature that allows to position microphones freely and the loudspeaker that simulates the flame sound production. The inner diameter of the two benches are relatively close (30 mm for the premixer tube and 50 mm for the impedance tube respectively), ensuring good similarity. Therefore, the results obtained with perforated plates in the impedance tube facility may be easily transposed to the combustion bench. This impedance tube facility, along with the different protocols for acoustic measurements are presented in the following chapter.

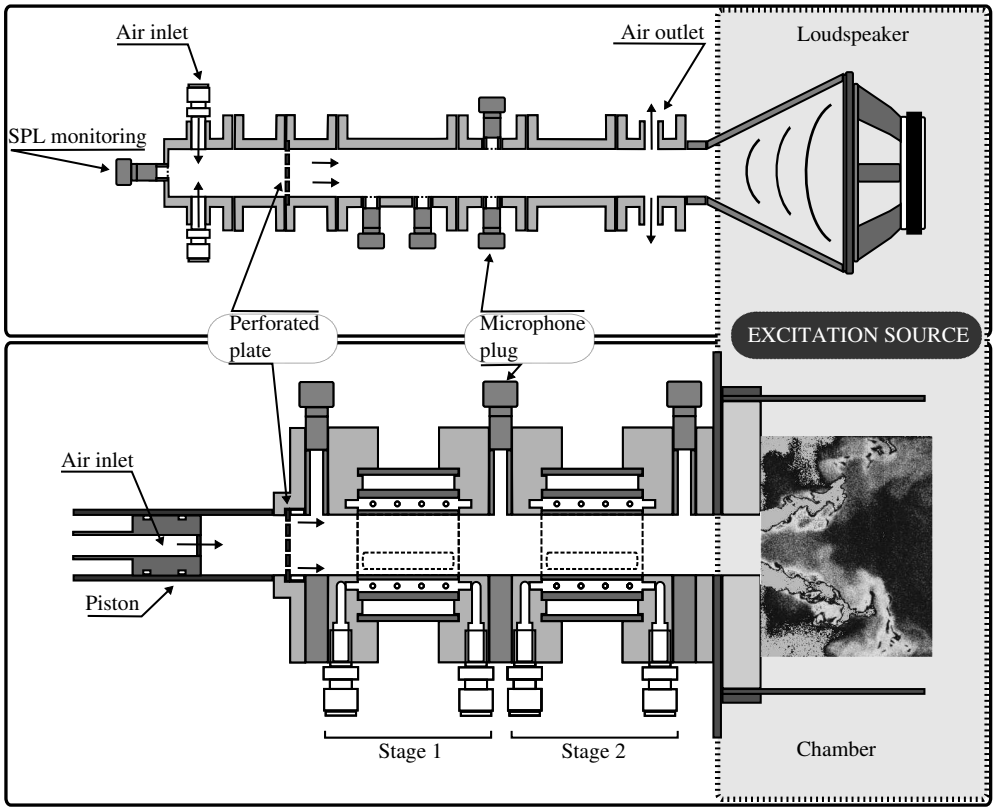

Figure 2.17: Impedance tube (top) used to characterize the ICS in cold flow experiments under external forcing with a loudspeaker, and CTRL-Z facility (bottom) where the ICS is adapted at the premixer inlet for reactive flow experiments with the flame as unique sound source. The geometrical arrangement is very similar, with the same flow direction.

Chapter 3

Acoustic measurement and impedance tube

Acoustic pressure measurement using microphones is a widely used technique in combustion dynamics studies, as the amplitude of pressure fluctuations is an indicator of the combustion stability and of the noise radiated by the flame. The key definitions concerning acoustic pressure are first recalled along with the description of a waveguide technique used to carry out measurements in the combustion chamber (section 3.1). Measurement techniques and protocols were developed and benchmarked in a high load impedance tube which is presented in section 3.2. A two-microphone method (TMM) used in this study to retrieve the acoustic impedance of the combustor terminations is then described in section3.3. This method is extensively used in the impedance tube to investigate the response of perforated plates. In addition, methods were developed to measure acoustic fluxes and reconstruct the acoustic velocity from pressure measurements. These methods are described in section 3.4.

3.1 Acoustic pressure measurements

The basic principles of sound measurements are briefly introduced in this section. The textbook of Morse and Ingard (1987) is a key reference for more advanced considerations. The Microphone Handbook published by Brüel & Kjaer is also an interesting source for technological aspects on acoustic pressure transducers.

3.1.1 Definitions

The sound pressure at a given location is frequently measured as the difference between the instantaneous pressure and the ambient mean pressure. The unit of sound pressure p_1 is the Pascal (Pa). The Sound Pressure Level (SPL) is defined by $\mathrm{SPL} = 20 \log p_1/p_{ref}$, in decibels (dB), where the reference value p_{ref} for Sound Pressure Level is $p_{ref} = 20\,\mu$Pa.
A root-mean-square value (RMS) of $p_1 = 1\,$Pa corresponds to a SPL of $94\,$dB. The lowest

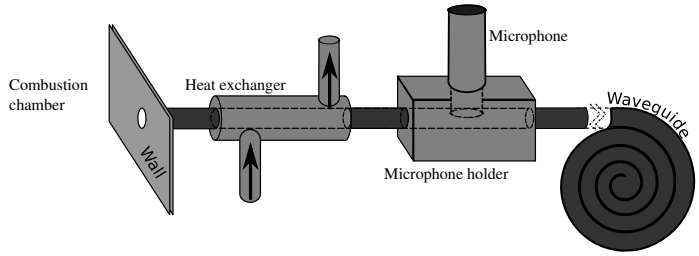

Figure 3.1: Schematic of the water-cooled waveguide used during firing test to protect the microphones.

audible sound, threshold of hearing, corresponds approximately to a sound pressure equal to p_{ref}, while the threshold of pain corresponds to a RMS value of $p_1 = 100\,\text{Pa}$.

Microphones are divided into two categories. Free-field microphones are used very far from the source, or in anechoic rooms, i.e. in situations where sound waves propagate freely without any reflection. Pressure-field microphones, as used in this study, are designed to allow measurements at distances much smaller than the acoustic wavelengths of interest, in cavities or close from the sources. A microphone is composed of a pressure-sensing condenser and a preamplifier, connected to a signal conditioner. The condenser measures the local pressure by the displacement of a diaphragm, and converts it into a voltage output. The preamplifier is an impedance converter between the high impedance microphone and its cable. A low output impedance is necessary to drive long signal cables. At the end of the line, the signal conditioner converts the analog input into a conditioned analog signal to be digitized using an Analog/Digital board. This conditioner controls the sensitivity and the gain of the microphone sensor. The sensitivity is the ratio of the output voltage to a given input pressure and is expressed in Volt per Pascal. This is the key parameter for measurements, which requires careful calibration. These calibrations are performed with Sound Level Calibrators which deliver a reference signal of given amplitude and frequency, e.g. $1\,\text{Pa}$ at $1\,\text{kHz}$.

3.1.2 Wall pressure measurements in harsh environments

The main characteristics of the pressure acquisition tools used in this study are gathered in table 3.1. The same equipment was used for all measurements, either in the impedance tube or in the combustion chamber. In the former situation, the microphones are flush-mounted at the inner wall surface, while in the latter, they are used with water-cooled waveguides to protect them from hot gases, particles and corrosive gases.
These waveguides are composed of a very long tube to limit acoustic reflections (the waveguide itself, of $4-5\,\text{m}$) with open end, a heat exchanger used to cool down the hot gases and a holder in which the microphone is inserted perpendicularly to the waveguide so that its membrane is flush-mounted on an aperture in the tube. This arrangement is illustrated in figure 3.1. The inner diameter of all tubing and connections is kept constant from the combustion chamber to the end of the waveguide to prevent occurrence of spurious interactions between waves, with a value of $6\,\text{mm}$. This method obviously introduces a time lag, which duration can be simply determined from the distance between the waveguide inlet at the chamber wall to the actual microphone position in the waveguide, taking the sound celerity of the gases filling the

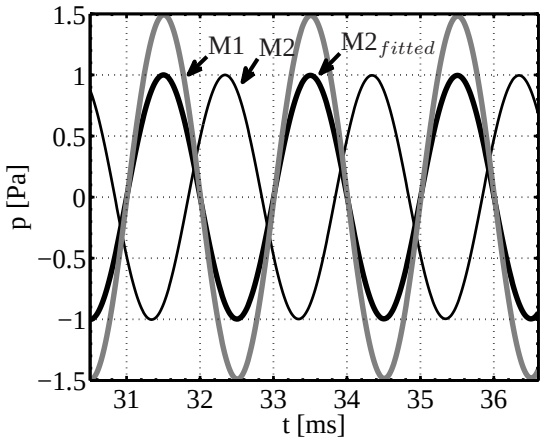

Figure 3.2: Example of correction of the waveguide induced time lag on the microphones signals, for an excitation frequency $f = 500\,\text{Hz}$. Grey line plots signal from M1, which amplitude was increased to differentiate it from thick black line representing the corrected signal M2$_{fitted}$. Thin black line represents the original signal from M2.

tube into account. This time delay and the phase difference between microphones signals used with and without waveguides has been verified in the impedance tube for clod flow conditions. A microphone M1 is directly flush-mounted on the test section, facing a second microphone M2 installed in a waveguide. They are then simultaneously submitted to a sinusoidal excitations. The original pressure signal of M2 is delayed to take into account the propagation in the waveguide, resulting in a signal M2$_{fitted}$. Temporal evolutions of the three pressure signals are reported in figure 3.2 for an excitation at $f = 500\,\text{Hz}$. In the non-corrected situation, M1 and M2 are almost in phase opposition while once corrected M1 and M2$_{fitted}$ are correctly in phase.It was also checked in the impedance tube that using a waveguide induces only a time delay and no change in the microphone response in amplitude. For hot flow conditions, a preliminary analytical modelling of the temperature gradient has shown that a negative gradient may result in a slight amplitude amplification of the waves, without effect on their phase. This amplification rate also appears to be constant in the low frequency range ($100 - 1000$ Hz). It must be kept in mind that the signals actually measured are of very large amplitude, especially in the unstable regimes. The instability peaks are furthermore largely dominant above the rest of the signal, most often by more than 10 dB (see figure 2.5). Therefore, the presence of the heat exchanger is estimated to yield only to small overestimation of the acoustic pressure in the combustion chamber, compared to measurements in the premixer.

The sensitivity was checked individually for each microphone using a reference source (Sound Level Calibrator). Then all microphones were simultaneously submitted to same acoustic forcing, in the impedance tube, to reduce the remaining gain and phase mismatches.

Equipment	Type	Characteristics
Microphone	4938	Pressure-field $1/4$ inch Sensitivity: 1.6 mV/Pa Frequency: $4 - 70000$ Hz Dynamic Range: $30 - 172$ dB Temperature: -40 to $300\,^{o}$C
Preamplifier	2670	$1/4$ inch Phase linearity: $\leq \pm 1\,^{o}$ below 100 kHz Signal attenuation: ≤ 0.4 dB
Nexus conditioner	2690-A-0F4	
Sound Level Calibrator	4231	Reference signal: 94 and 114 dB at 1kHz

Table 3.1: Acoustic diagnostic tool characteristics. All devices are manufactured by Brüel & Kjaer

3.2 High load impedance tube facility

A modular impedance tube was set up to allow pure acoustic measurements and validation of acoustic measurements protocols prior to their use in the combustion facility.

3.2.1 Setup description

The facility, sketched in figure 3.3, is composed of a high-efficiency loudspeaker controlled by a signal generator. The loudspeaker is connected to the test section by a conical adaptation piece. Its diameter and sensitivity allows very large forcing amplitudes, resulting in Sound Pressure Levels from 90 up to 150 dB in the test section, for frequencies between 50 and 2000 Hz. The test section is composed of cylindrical tubes, with an inner diameter $D = 50$ mm, joined together with seals. This device is air-tight, with a constant inner diameter and it is also highly modular. Samples to be tested are placed in between tubes, and their distance to the loudspeaker membrane can be adjusted by addition of tubing. A minimal distance of 1 m is kept between the loudspeaker membrane and the microphones ports to ensure plane wave propagation, and reduce spurious noises that may arise in the conical adaptation. Above the samples, the setup is equipped with special sections with flow injection ports from on top of the facility. Air, controlled by a massflow meter, can be injected using 4 to 8 radial injection ports. The test section can thus be fed with an uniform flow, which exits the impedance tube by two radial exhaust ports located above the loudspeaker casing. Bulk flow velocities inside the setup range from 0 to 10 ms^{-1} at room temperature.
The impedance tube is closed on its top by a rigid plate. This closed end therefore corresponds to a pressure antinode independent of the frequency. The reference Sound Pressure Level in the impedance tube is hence measured by a microphone MSPL, flush-mounted at the geometric center of this plate. The rigid plate is placed just above the air injections in order to limit the minimal depth of the cavity backing the samples to 30 mm. This depth can be increased by the addition of tubing of various lengths. These tubing present the key advantage to cover a wide range of use. In addition to their different lengths, they are equipped with radial, flush-mounted, $1/4$ inch microphone holders. This tunable facility can thus be used in

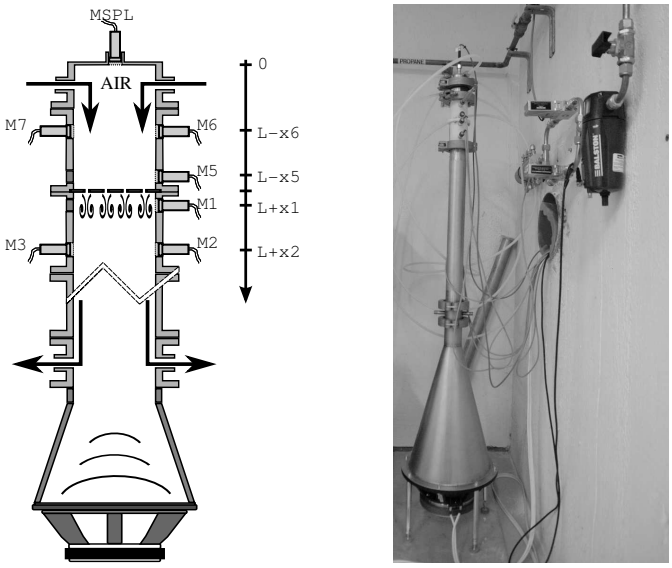

(a) (b)

Figure 3.3: (a) Schematic view of the impedance tube facility, with flow and arrangement of microphones. MSPL is used to monitor the SPL in the facility. (b) Experimental setup, with air inlets connected to a massflow meter and a Balstom filter.

many different configurations for acoustic measurements. Finally, the whole setup is placed on vibration absorbing pads.
In the situation depicted in figure 3.3, the microphone M1 is located very close to the sample (9 mm), while microphones M2 and M3 are 10 cm below. The microphone M2 can be switched with microphone M1 to reduce phase mismatches when measuring impedances, while M3 remains in place and serves as a reference to obtain the coherence function between microphones. All microphones are connected to an Analog/Digital acquisition board. Signals are digitized using a specific *Labview* program. The characteristics of the electronic devices of the facility are gathered in table 3.2.

3.2.2 Benchmarking

This facility has been tested in well-controlled configurations to ensure the check quality and accuracy of the measurement techniques.

Loudspeaker signal

Acoustic properties of the loudspeaker are first characterized by placing two microphones M1 and M2 facing each other above the loudspeaker membrane (fig.3.4a). Power spectra and coherence function between these microphones were then measured. It was verified that the peak of these functions at the modulation frequency is at least 40 dB higher than the background noise level and other harmonic peaks (fig. 3.4b,3.4c) in the frequency range of interest $[100 - 1000]$ Hz.

Equipment	Manufacturer	Type	Characteristics
Loudspeaker	B& C Speakers	12PE32	Response: $50 - 4000$ Hz Sensitivity: 101.5 dB
Function generator	Fluke	PM 5138A	Range: 0.1 mHz to 10 MHz
A/D Acquisition board	National Instrument	BNC2090 PCIMIO16E4	22 inputs Sampling frequency : 250 kHz Resolution: 12 bits
Amplifier	Power Sound	LS 600	Power: 300 W

Table 3.2: Impedance tube apparatus characteristics

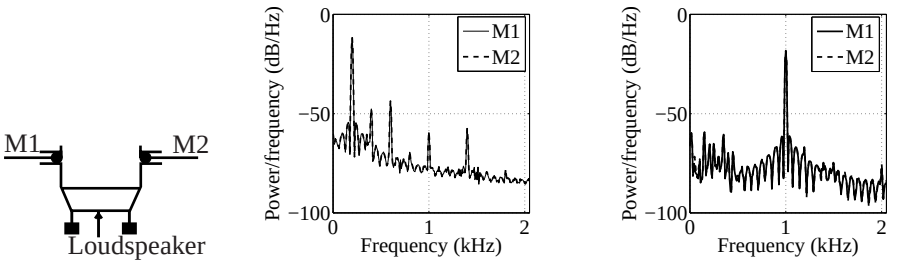

(a) Setup (b) Power spectrum at 200 Hz (c) Power spectrum at 1000 Hz

Figure 3.4: Characterization of the driver unit. (a) experimental setup, (b) and (c) power spectra with microphones M1 (full lines) and M2 (dashed lines). Spectra are almost superimposed.

The performances of the loudspeaker being assessed, the characteristics of the full facility are benchmarked in two well-defined acoustic configurations corresponding to open and closed ends.

Closed end tube

The first test is conducted with the tube closed by a rigid wall. One introduces a vertical ascending axis which originates at the loudspeaker membrane ($x = 0$). The rigid wall which closes the tube is located at a distance $x = L$ (fig. 3.5). Using the signal synthesizer, the loudspeaker membrane generates a sinusoidal velocity excitation of the form $u_1(x = 0) = U_0 \sin(\omega t)$ on the air column. The rigid wall at the termination imposes $u_1(x = L) = 0$. Theses boundary conditions determine a longitudinal acoustic pressure field of the form :

$$p_1(x,t) = Z_0 U_0 \frac{\cos(k(L-x))}{\sin(kL)} \cos(\omega t) \tag{3.1}$$

where $Z_0 = \rho_0 c_0$ is the characteristic impedance of air. Using two microphones flush-mounted at the surface of the tube, microphone M1 located at a distance l from the termination, and microphone M2 at distance $l - s$, the ratio of acoustic pressure at these locations

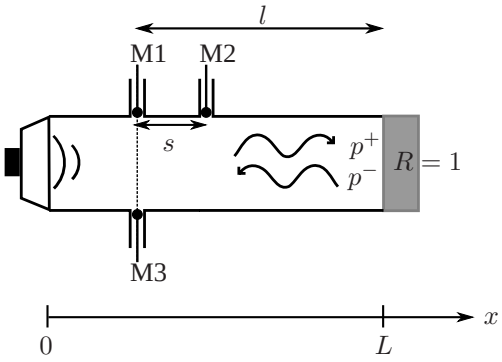

Figure 3.5: Closed end tube benchmark.

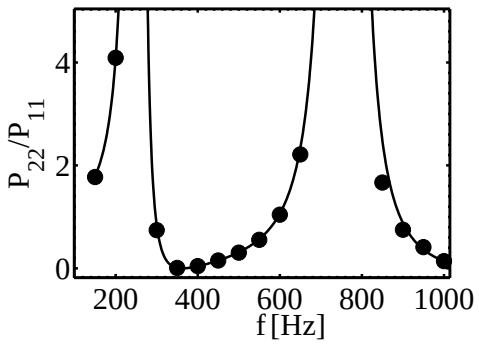

Figure 3.6: Power Spectral Density as a function of frequency for a closed-end tube. The solid line indicates previsions, dots correspond to experimental data obtained with a moderate SPL of 100 dB.

verifies:

$$\frac{p_1(\text{M2})}{p_1(\text{M1})} = \frac{p_1(L-l+s)}{p_1(L-l)} = \frac{\cos k\,(l-s)}{\cos kl} \tag{3.2}$$

This ratio does not depend on the total tube length L, which does not need to be accurately measured. It is however sensitive to the microphones separation distance s. Power Spectral Densities were measured at different forcing frequencies and compared to predictions in figure 3.6:

$$\frac{P_{22}}{P_{11}} = \left(\frac{\cos k\,(l-s)}{\cos kl}\right)^2 \tag{3.3}$$

Excellent agreement is found in the whole frequency range $100 - 1000$ Hz.

Equation 3.1 indicates that there should be no source of time-shift between the two pressure measurements. It was indeed checked that pressure signals in the tube are either perfectly in

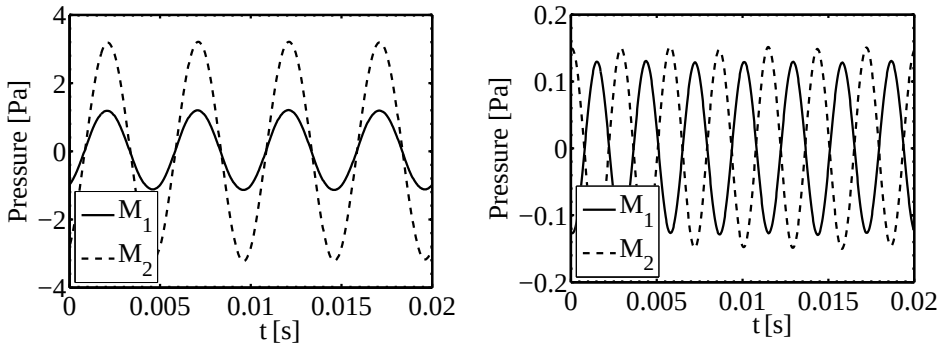

(a) Modulation frequency 200 Hz (b) Modulation frequency 350 Hz

Figure 3.7: Examples of the pressure signals measured in the impedance tube closed with a rigid wall for various modulation frequencies. Only two situations can be observed (a) in phase or (b) in phase opposition.

phase or in phase opposition (figure 3.7), depending on the sign of the ratio $\cos k\,(L-x)$ $/\sin(kL)$.
It is easily checked that with such pressure field, the impedance at the closed end goes to infinity as expected, which implies that the reflection coefficient tends towards unity, $R(L) = 1$. An incident wave is totally reflected by a perfectly rigid wall, with the same phase and amplitude, whatever the amplitude is. The eigenmodes of this setup with a closed end are of halfwave type:

$$f_n = 2n\frac{c}{4L} \tag{3.4}$$

The resonances are sharply located at the predicted frequencies when the tube is much longer than twice its diameter (Morse and Ingard (1987)). For a tube of total length $1\,\mathrm{m}$ with an inner temperature $T = 291\,\mathrm{K}$, eigenmodes have been measured at $f = 170$, 340, 511, 669 and $825\,\mathrm{Hz}$. These values are relatively close to the theoretical predictions: $f_{theo} = 171$, 342, 514, 684 and $855\,\mathrm{Hz}$.
The case of a open pipe is now considered.

Unflanged pipe

For a tube with an open termination and without mean flow, it is known that the acoustic pressure node is not located exactly at the exhaust ($x = L$) but at a distance δ from the tube exhaust (see for example Levine and Schwinger (1948)). This distance, called end-correction, is defined by $\delta = 8r/3\pi$, where r is the pipe radius (see for example Rienstra and Hirschberg (2006)). It corresponds to the inertia of the air column at the exhaust of the tube which is set in motion by the acoustic waves. The acoustic boundary conditions in this configuration are fixed by:

$$u_1(x=0) = U_o\cos(\omega t) \tag{3.5}$$
$$p_1(x=L+\delta) = 0 \tag{3.6}$$

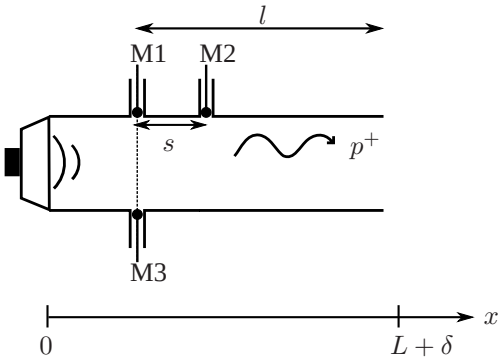

Figure 3.8: Open tube

The specific impedance at a position x can then written :

$$\frac{Z(x)}{Z_0} = i \tan\left(k(L+\delta-x)\right) \tag{3.7}$$

The impedance Z equals 0 when $x = L + \delta$. This implies that the reflection coefficient at the tube exhaust is $R = -1$, and corresponds to a constant modulus equals to unity and a constant phase equals to $-\pi$ in the whole frequency range. The eigenmodes in this configuration are of quarterwave type, which eigenfrequencies are defined by:

$$f_n = (2n+1)\frac{c}{4(L+\delta)} \tag{3.8}$$

3.3 Impedance measurements

In addition to the sound pressure measurements used to investigate combustion oscillations, microphones were also used to measure acoustic impedances of different devices.

3.3.1 Impedance and reflection coefficient

The acoustic impedance is a measure of the resistance of a surface, or a medium, to the motion induced by an incident pressure wave. It is defined as the ratio of the acoustic pressure to the local velocity, in the frequency domain :

$$Z\left(x\right) = \frac{p_1\left(x,\right)}{\mathbf{u_1}\left(x,\right)\cdot\mathbf{n}} \tag{3.9}$$

at a point x on a surface S with the unit normal vector $\mathbf{n}$ pointing into the surface. The real part of Z is called the resistance, and its imaginary part the reactance. The characteristic impedance is a property of the medium, defined by the product of the medium density and the sound celerity, $Z_0 = \rho_0 c_0$. The specific impedance is the ratio of the acoustic impedance to

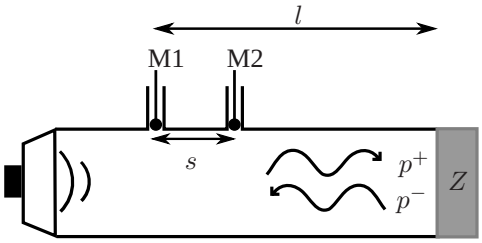

Figure 3.9: Setup for the two-microphones technique

the characteristic impedance $\zeta = Z/Z_0$. The reflection coefficient R is defined as the ratio of the reflected to incident pressure waves on a surface S. An incident pressure wave of amplitude p^+ is reflected by an obstacle surface into a wave of amplitude p^-, leading to $R = p^+/p^-$. The reflection coefficient can classically be linked to the specific acoustic impedance by the relationship:

$$R = \frac{\zeta - 1}{\zeta + 1} \tag{3.10}$$

In order to measure the acoustic impedance, the acoustic pressure and velocity must be determined. The most straightforward technique would be to use simultaneously a pressure microphone and hot-wire anemometry for example. However, impedances can also be determined using two microphones. The technique is based on the developments of Chung and Blaser (1980) which has been formalized in an ISO norm (ISO 10534-2). This two-microphone method (TMM) is well-known and only its key features will be presented here. Recent reviews were completed by Dalmont (2001) and Jones and Stiede (1997), and an interesting uncertainty analysis on this technique was carried out by Schultz et al. (2002).

3.3.2 The two-microphone method

In the configuration given in figure 3.9, the specific acoustic impedance at the distance l from the first microphone M1 (the second, M2, located at the distance $l - s$ from the same cross-section) is given by :

$$\zeta = \frac{Z}{\rho_0 c_0} = i\frac{H_{12}\sin(kl) - \sin(k[l-s])}{\cos(k[l-s]) - H_{12}\cos(kl)} \tag{3.11}$$

where c_0 is the speed of sound in the tube, k the wavenumber and H_{12} the transfer function between the two microphones, at the forcing frequency. The transfer function between microphones M1 and M2 is defined as the ratio of the cross power spectral density between M1 and M2 P_{12} to the power spectral density of M1 P_{11}: $H_{12} = P_{12}/P_{11}$. The microphones should be set close enough from the boundary condition to be characterized to avoid transmission loss, but not too close to avoid near field effects.

3.3.3 Microphone spacing and position influence

The interspace between microphones M1 and M2 defines the maximal frequency at which the impedance can be measured. It should be chosen such that $s \leq c_0/2f_{max}$, where f_{max} is

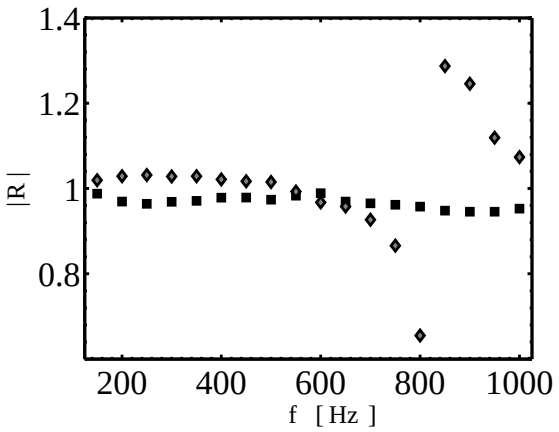

Figure 3.10: Measurements of the reflection coefficient modulus $|R|$ of a closed-end tube for two different microphones interspaces. Black squares correspond to a separation distance of $s = 10.5$ cm, gray diamonds of $s = 20$ cm.

the highest frequency to be investigated. For a 1 kHz maximum frequency, $s \leq 17$ cm and this fixes the largest interspace between microphones M1 and M2 for accurate measurements. The second spacing limitation is due to the minimal wavelength to be characterized, as this will fixed the position of the first pressure node within the setup from the impedance location. For a harmonic modulation at 1000 Hz, this distance equals 34 cm and sets a maximum for l. Furthermore, the microphone M1 should be placed far enough from the loudspeaker at a location where the wavefield has become plane. This distance was chosen greater than $L \geq 1$ m in the impedance tube. Figure 3.10 illustrates the limitation due to the microphone interspace s. In the configuration depicted, the reflection coefficient of a rigid wall is measured for two different interspace values, $s = 10.5$ cm and $s = 20$ cm. This reflection coefficient should be equal to unity for all frequencies, as measured with $s = 10.5$ cm. With $s = 20$ cm, the measured reflection coefficient deviates from unity for frequencies above 750 Hz. Using the relationship $s \leq c_0/2f_{max}$, the predicted maximal frequency at which impedance can be correctly measured is $f = 800$ Hz. It can be concluded that with an interspace $s = 10$ cm correct measurements of the impedance can be achieved in the whole range of interest $100 - 1000$ Hz.

3.3.4 Accuracy improvements

In their definition of the technique, Chung and Blaser (1980) recommend to switch the two microphones and acquire signals in both configurations. Indeed, a correct calibration both in amplitude and phase of each microphone is fundamental for the accuracy of the technique. Whereas calibration in amplitude is easy, calibration in phase is much more challenging. By switching the microphones, errors due to calibration mismatches are minimized. As an example, the gain and phase of the reflection coefficient of a close-end tube are plotted against frequency for three different configurations (fig.3.11). Squares indicate the original configuration, with M1 at distance l from the termination and M2 at $l - s$. Diamonds indicate the switched configuration, with M1 at $l - s$ from the termination and M2 at l. The solid line represent the final value of the reflection coefficient. The continuous line is obtained by

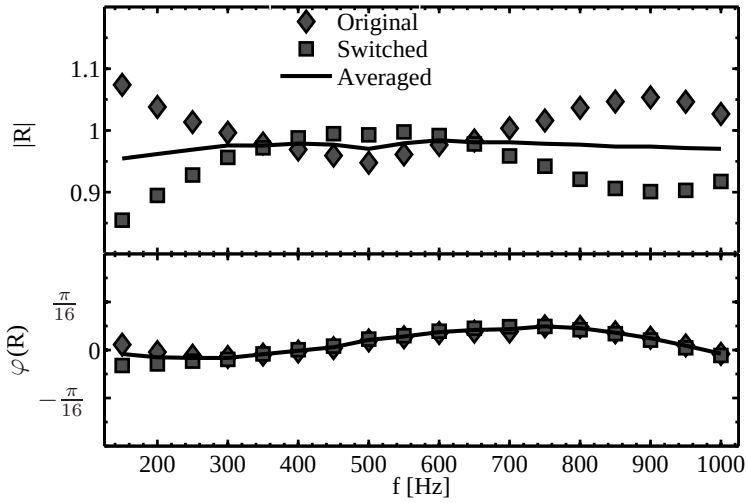

Figure 3.11: Effect of the microphone switching on the impedance measurements accuracy. Squares indicate the original configuration, with M1 at distance l from the termination. Diamonds indicate the switched configuration, with M1 at $l - s$ from the termination and M2 at l. The solid line represent the final value of the reflection coefficient.

combining the two previous data sets and computing the arithmetic mean value H_{12} of the transfer functions obtained in each configuration. This post-processing technique clearly reduces errors due to calibration mismatches and position uncertainties. This technique allows an accurate reconstruction of the reflection coefficient, almost equal to unity at all frequencies. It should be noted that the phase φ of the reflection coefficient has been plotted in a narrow range $[-\pi/16, \pi/16]$.

As high background noise levels are expected in turbulent flow conditions, a third microphone M3 was used to improve the signal to noise ratio. This reference microphone is set at the same distance l from the sample as the farthest microphone, and remains fixed. The arrangement is sketched in figure 3.12. Coherence functions between microphone signals at the driving frequency are calculated in the original (^{o}) and switched (^{s}) configurations. This yields a

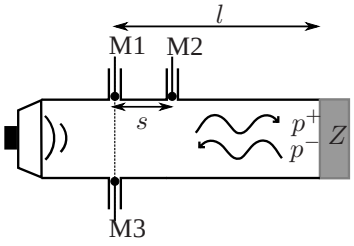

Figure 3.12: Microphones arrangement used for the TMM method with an additional reference microphone M3.

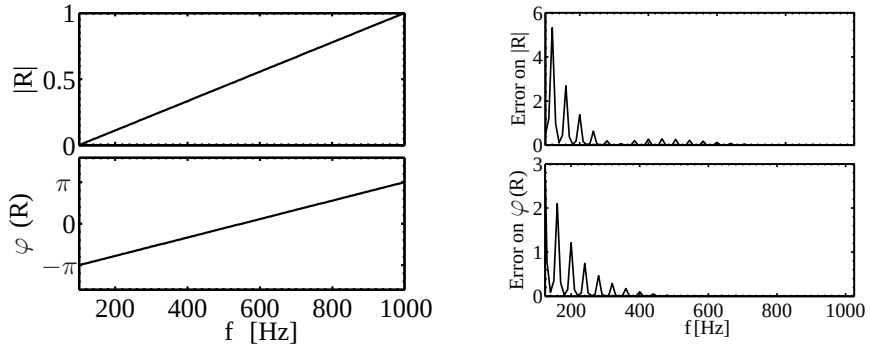

(a) Evolution of the synthetic reflection coefficient (b) Error percentages between exact and calculated reflection coefficient

Figure 3.13: Error induced by the impedance measurement post-processing technique.

coherence factor defined by:

$$C^{o,s} = C_{23}^{o,s} / C_{12}^{o,s} C_{31}^{o,s} \tag{3.12}$$

where $C_{i,j} = |P_{i,j}|^2/(P_{ii}P_{jj})$ denotes the coherence function evaluated between microphones i and j ($i, j = 1, 2, 3$) in each configuration. For pure tone noise, this coherence factor equals unity. Using the microphone switching technique and a third reference microphone drastically reduces measurement errors, especially for those in noisy conditions as in the combustion chamber. The final transfer function H_{12} in equation 3.11 is obtained from :

$$\mathrm{H}_{12} = [C^o \mathrm{H}_{12}^o C^s \mathrm{H}_{12}^s]^{1/2} \tag{3.13}$$

3.3.5 Benchmarking the post-processing tools

Data are processed with Matlab using a Welch periodogram method with Hanning windows (Oppenheim and Schafer 1975). A total of $N = 32768$ data points were acquired at a sampling frequency of $f_s = 16384$ Hz. Transfer functions in the original H_{12}^o and the switched configurations H_{12}^s were computed. The mean H_{12} was then calculated and used to determine the reflection coefficient using equation 3.11. The algorithm was tested with synthetic signals for increasing values of the reflection coefficient R. The difference between the exact imposed reflection coefficient and the results of the post-processing algorithm based on the TMM is plotted in figure 3.13. The largest deviations occur for very low values of the reflection coefficient modulus. Maximum error reaches 5% at $f = 100\,\mathrm{Hz}$ where $|R| \simeq 0$. This difference rapidly decreases with increasing modulus values. This processing method has been validated. Other tests were also performed with noisy signals and similar conclusions were drawn.

Termination	Total length [cm]	δ [cm]	L [cm]	s [cm]	f_s [Hz]	N
$Open$	145	2.1	24	10.5	32768	32768
$Close$	145	0	24	10.5	32768	32768

Table 3.3: Measurement parameters.

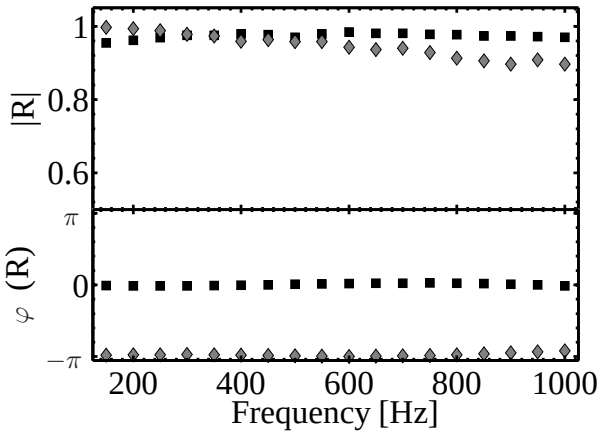

Figure 3.14: Reflection coefficient for two different terminations. Black squares correspond to a closed end termination $R = 1$, gray diamonds to an open end termination $R = -1$.

3.3.6 Tests on generic configurations

The TMM and the post-processing tools were then tested in simple configurations corresponding to an open and a closed end ducts. Distances and sampling parameters for these tests are given in table 3.3. Modulus and phase of the reflection coefficient R measured in these configurations are plotted in figure 3.14. Value for the modulus $|R|$ of the closed-end tube is just below unity and almost constant in the whole frequency range, as expected for this reference case. Differences between theoretical predictions and measured values may be attributed in this case to the acquisition and processing technique. However, the relative error remains below 5%. For the open-end tube case, the gain slightly decreases with increasing frequency in agreement with results found in the literature (e.g Morse and Ingard (1987)). Phases in both cases are also in agreement with theoretical predictions.

All these tests validate the technical arrangement and the post-processing tools as an efficient method to measure acoustic impedances.

3.4 Acoustic intensity and particle velocity reconstructions

Combined analysis of acoustic pressure and chemiluminescence emissions within the combustion rig enables access to the Rayleigh criterion A global acoustic energy balance however requires the evaluation of acoustic fluxes at the inlet and outlet of the domain. Simultaneous

measurements of acoustic pressure and acoustic velocity are thus also needed. In the combustion facility, optical velocity measurements such as LDV could not be performed in the premixer channel, because there is no optical access and are quite uneasy to obtain at the chamber exhaust, because of the hot combustion products. It was not possible to use hot-wire anemometry in the premixer, because it was technically difficult to introduce this fragile probe in the system. The evaluation of acoustic velocity and fluxes thus solely relies on pressure measurements and are now described, first in the frequency domain, then in the time domain.

3.4.1 Acoustic intensity estimation

$$\frac{\partial \mathbf{u_1}}{\partial t} = -\frac{1}{\rho_0}\nabla p_1 \tag{3.14}$$

A budget for the acoustic momentum, eq. 3.14, yields a direct relationship between velocity and pressure in a region with no mean flow and no acoustic source term. One considers the case of two closely spaced pressure sensors measuring 1D stationary harmonic sound waves at the same frequency f. The separation distance δx in the direction of propagation is assumed to be much smaller than the wavelength: $\delta x \ll \lambda$. If x_1 denotes the position of the first pressure sensor and $x_2 = x_1 + \delta x$ the second one, an approximation of equation 3.14 can be made in the frequency domain:

$$\hat{u}_1\left(\frac{x_1+x_2}{2}\right) \approx -i\frac{\hat{p}_1(x_2)-\hat{p}_1(x_1)}{\rho_0\omega\delta x} \tag{3.15}$$

This yields a first order estimate of the Fourier transform of the velocity fluctuation at $x = (x_1 + x_2)/2$. Similarly, the Fourier transform of the pressure $\hat{p}_1$ midway of the two pressure sensors can be interpolated :

$$\hat{p}_1\left(\frac{x_1+x_2}{2}\right) \approx \frac{\hat{p}_1(x_2)+\hat{p}_1(x_1)}{2} \tag{3.16}$$

Using this procedure, the acoustic intensity $\mathcal{I} = \frac{1}{T}\int_T p_1 u_1 dt$ can be evaluated in the frequency domain.

An expression of the acoustic intensity was nonetheless derived by Chung (1978) as follow:

$$\begin{aligned}
\mathcal{I} &= \frac{1}{T}\int_T [p_1\mathbf{u}_1]\,dt \\
&= \frac{1}{4T}\int_T [(\hat{p}_1+\hat{p}_1^*)(\hat{\mathbf{u}}_1+\hat{\mathbf{u}}_1^*)]\,dt \\
&= \frac{1}{2T}\int_T [\mathrm{Re}(\hat{p}_1\hat{\mathbf{u}}_1)+\mathrm{Re}(\hat{p}_1\hat{\mathbf{u}}_1^*)]\,dt
\end{aligned} \tag{3.17}$$

Using expressions (3.15) and (3.16) in (3.17), one obtains :

$$\begin{aligned}
\mathcal{I} &= \frac{1}{2\rho_0\omega\delta x}\frac{1}{T}\int_T [-\mathrm{Re}\left(\hat{p}_1(x_1)\right)\mathrm{Im}\left(\hat{p}_1(x_1)\right) \\
&+ \mathrm{Re}\left(\hat{p}_1(x_2)\right)\mathrm{Im}\left(\hat{p}_1(x_2)\right)+\mathrm{Im}\left((\hat{p}_1(x_1)\hat{p}_1^*(x_2)\right)]\,dt
\end{aligned} \tag{3.18}$$

For a stationary, ergodic signal A with a zero mean value, $\int_T \mathrm{Re}(\hat{A})\mathrm{Im}(\hat{A})dt = 0$. The acoustic intensity can thus be expressed as a function of the cross-spectral density between the pressure fluctuations $p_1(x_1)$ and $p_1(x_2)$:

$$\mathcal{I} = \frac{\mathrm{Im}(P_{p_1(x_1),p_1(x_2)})}{2\rho_0\omega\delta x} \tag{3.19}$$

As a result, it is possible to directly estimate the acoustic intensity $\mathcal{I}$ in a plane midway of two microphones using the cross-spectral density between their corresponding sound pressure signals. With a sensor spacing δx small compared to the acoustic wavelength, for a 1-D plane wave sound field inside a duct, the acoustic flux Φ_{ac} can thus be obtained by considering that the acoustic intensity is constant over the whole cross-section of surface Σ:

$$\Phi_{ac} = \frac{\mathrm{Im}(P_{p_1(x_1),p_1(x_2)})}{2\rho_0\omega\delta x}\Sigma \tag{3.20}$$

It has been shown that the acoustic intensity $\mathcal{I}$ and flux Φ_{ac} can be reconstructed from the signals of two microphones for a one-dimensional field with no source terms in between the sensors. It is also possible to evaluate the acoustic velocity in the frequency domain with this method (eq. 3.15). However, the measured pressure signals $p_1(x_1,t)$ and $p_1(x_2,t)$ are not analytic. It is therefore not possible to reconstruct the time evolution of the particle velocity $u_1(x,t)$. The method used to obtain the evolution of the particle velocity in the time domain is now explained.

3.4.2 Reconstruction of the particle acoustic velocity in time domain

Because of the multiplication by $i = \sqrt{-1}$ in equation 3.15, inverse Fourier transform cannot be used to retrieve the time evolution of the particle velocity. Only analytical signals can be used, as causality is required for such reconstruction (Rienstra and Hirschberg 2006). An analytical representation of a real signal $y(t)$ can be obtained by using the Hilbert transform, as presented by Oppenheim and Schafer (1975) for example:

$$y_a(t) = y(t) + i\mathcal{H}\left(y(t)\right) \tag{3.21}$$

where $\mathcal{H}$ indicates the Hilbert transform, and $y_a(t)$ the analytical representation of $y(t)$. The original real signal $y(t)$ is simply the real part of the analytical representation. The Hilbert transform itself is defined as the Cauchy principal value (P.V.) of the convolution of a signal with the Hilbert function $1/\pi t$:

$$\mathcal{H}(y) = \frac{1}{\pi}\text{P.V.}\int_{-\infty}^{+\infty}\frac{y(\tau)}{t-\tau}d\tau \tag{3.22}$$

This corresponds to a 90^{o} phase shift of the real signal in the complex plane, having the same magnitude and frequency content. The Hilbert transform is linked to the Fourier transform by the sign function **sgn**:

$$\hat{\mathcal{H}}(y)(\omega) = (-i\mathbf{sgn}(\omega))\hat{y}(\omega) \tag{3.23}$$

where $\hat{\mathcal{H}}$ is the Fourier transform of $\mathcal{H}$ and

$$\mathbf{sgn}(x) = \begin{cases} -1 & \text{if } x < 0 \\ 0 & x = 0 \\ 1 & x > 0 \end{cases}$$

From the definition of the sign function, it follows that the Fourier transform of a analytical signal is a one-sided spectrum, where only positive frequencies are present. This property is used in *Matlab* to evaluate the Hilbert transform. The coded function does indeed compute first the FFT of the input signal, then set to zeros the coefficients corresponding to negative frequencies. Finally an inverse Fourier Transform is applied to the resulting signal. Hilbert transforms are often used to create amplitude envelope followers for narrowband signals.
The Hilbert transform is used to build analytical signals from the real pressure signals measured at x_1 and x_2 in equation 3.15: $p_a(x_1) = p_1(x_1,t) + i\mathcal{H}\left(p_1(x_1,t)\right)$ and $p_a(x_2) = p_1(x_2,t) + i\mathcal{H}\left(p_1(x_2,t)\right)$ respectively. Equation 3.14 can then be approximated in the complex domain using these analytical expressions:

$$\begin{aligned} \frac{\partial \mathbf{u_1}}{\partial t} &= -\frac{1}{\rho_0}\nabla p_1 \\ -i\omega u_a &\simeq \frac{-1}{\rho_0}\frac{p_a(x_2) - p_a(x_1)}{\delta x} \\ u_a &\simeq \frac{-i}{\rho_0 \delta x \omega}\left(p_a(x_2) - p_a(x_1)\right) \end{aligned} \tag{3.24}$$

The r.h.s term of equation 3.24 can be rewritten as:

$$-i\frac{p_a(x_2) - p_a(x_1)}{\rho_0 \omega \delta x} = \frac{1}{\rho_0 \omega \delta x}\left(\mathcal{H}(p_1(x_2)) - \mathcal{H}(p_1(x_1)) + i\left(-p_1(x_2) + p_1(x_1)\right)\right) \tag{3.25}$$

Using the definition of the Hilbert transform, it can be observed that the imaginary part in equation 3.25 is the Hilbert transform of the real part:

$$-p_2 + p_1 = \mathcal{H}\left(\mathcal{H}(p_1(x_2) - \mathcal{H}(p_1(x_1))\right) \tag{3.26}$$

Introducing $\Delta = \mathcal{H}(p_1(x_2)) - \mathcal{H}(p_1(x_1)) = \mathcal{H}(p_1(x_2) - p_1(x_1))$, equation 3.24 yields:

$$u_a = \frac{1}{\rho_0 \delta x \omega}\left[\Delta + i\mathcal{H}\left(\Delta\right)\right] \tag{3.27}$$

It is thus assessed that the acoustic velocity has an analytical expression, and is therefore causal. As a result the real velocity signal can be reconstructed by extracting the real part of u_a

$$u_1 = \mathrm{Re}(u_a) = \frac{\mathcal{H}(p_1(x_2) - p_1(x_1))}{\rho_0 \omega \delta x} \tag{3.28}$$

It can be checked that the Fourier transform of equation 3.28 verifies equation 3.15 using the relationship 3.23 between the Fourier and Hilbert transforms.
The algorithm was first tested on synthetic harmonic signals to validate the reconstruction methodology. For harmonic signals of angular frequency $\omega = 2\pi f$ and imposed amplitude A, the acoustic pressure and velocity can classically be written as :

$$p_1(x,t) = A\cos(\omega\,(t - x/c)) \tag{3.29}$$

$$u_1(x,t) = \frac{A}{\rho_0 c_0}\cos(\omega\,(t - x/c)) \tag{3.30}$$

Using the transformation defined by equation 3.28 with the form of the pressure field in eq. 3.30 yields:

$$\mathcal{H}(p_1(x_2) - p_1(x_1)) = \mathcal{H}\left(-2A\sin\left(\omega t - k\frac{x_1+x_2}{2}\right)\sin\left(k\frac{\delta x}{2}\right)\right) \tag{3.31}$$

$$= 2A\sin\left(k\frac{\delta x}{2}\right)\cos\left(\omega t - k\frac{x_1+x_2}{2}\right) \tag{3.32}$$

Therefore the acoustic velocity at the mid-location is given by:

$$u_1\left(\frac{x_1+x_2}{2}\right) = \frac{2A\sin\left(k\frac{\delta x}{2}\right)}{\rho_0\omega\delta x}\cos\left(\omega t - k\frac{x_1+x_2}{2}\right) \tag{3.33}$$

$$= \frac{A\sin\left(k\frac{\delta x}{2}\right)}{\rho_0 c_0 k\delta x/2}\cos\left(\omega t - k\frac{x_1+x_2}{2}\right) \tag{3.34}$$

$$\simeq \frac{A}{\rho_0 c_0}\cos\left(\omega t - k\frac{x_1+x_2}{2}\right) \tag{3.35}$$

since for $\delta x \ll \lambda$, one can develop $\sin\left(k\frac{\delta x}{2}\right) \simeq k\delta x/2$. Figure 3.15 shows an example reconstruction for such signals. The time evolution of the acoustic pressure as expressed in equation 3.30 is computed with a forcing frequency $f = 200$ Hz and an amplitude $A = \rho_0 c_0$, at two locations x_1 and x_2 spaced by $\delta x = 10$ cm. The acoustic velocity is reconstructed using Hilbert transform (symbols) and compared to the theoretical expression in eq.3.30: $u_1(x_1 + \delta x/2, t) = \cos(\omega(t - (x_1 + \delta x/2)/c_0))$, plotted by the solid line. In the case of standing waves, the reconstruction procedure is quite efficient.

Concluding remarks

Microphones data are extensively used to measure acoustic pressure and therefore investigate combustion instabilities. A classical impedance measurement technique was adapted to provide accurate measurements of the acoustic reflection coefficient. Data processing tools were presented that allow the direct quantitative evaluation of the acoustic fluxes and particle velocity. Used in conjunction with photomultipliers, they give access to an experimental estimation of the acoustic energy balance in a combustor. These various methods can be applied in a well controlled environment such as in an impedance tube, but also in dire conditions encountered in combustion chambers. They are efficient and accurate, as successfully demonstrated in various test cases. An experimental facility has been set up for this study: a highly modular

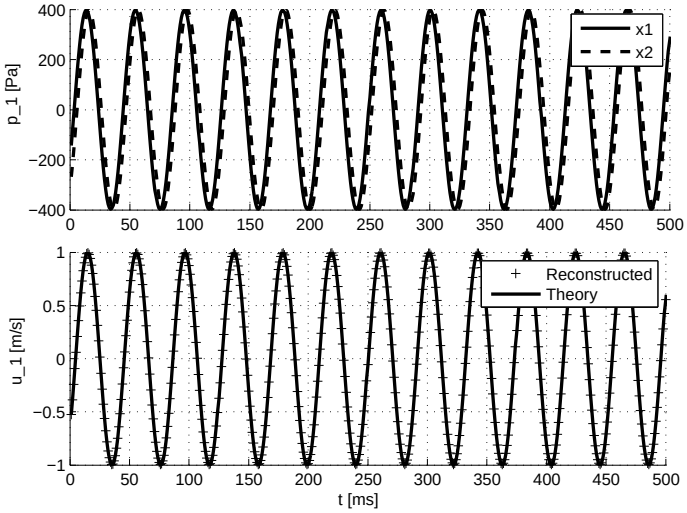

Figure 3.15: (Top) Synthetic pressure signals of given amplitude ρc_0 with a forcing frequency $f = 200\,\text{Hz}$ detected by two virtual pressure sensors spaced by $\delta x = 10\,\text{cm}$. (Bottom) Reconstructed velocity $(+)$ vs. theoretical waveform $(-)$ at the middle point location. The reconstructed velocity amplitude equals unity as predicted.

impedance tube was used to benchmark all the acoustic protocols and to lead the investigation on the acoustic response of perforated plates.

Chapter 4

Acoustic control with perforates

Perforated panels with bias flow are used effectively to damp acoustic waves, and have been the focus of many studies. The current work makes use of perforates of fixed geometry submitted to a wide range of incident pressure amplitudes, as encountered during combustion oscillation. It is shown in section 4.1 that two models can be used to describe the acoustic response of perforates of low porosity over a large amplitude dynamics. Then a parametric experimental investigation is carried out to measure the influence of the plate design on its acoustic damping properties. For low pressure perturbation amplitudes, the acoustic response of the bias flow perforates is independent of the incident level. A linear model describes the plates response in this regime, and was used to design the perforates geometry (section 4.2). When the pressure amplitude takes large values, the response becomes nonlinear and a second model is proposed to predict the acoustic behavior of the perforated plate under large SPL in section 4.3. A transition criterion between these two regimes is finally proposed, based on the plate geometry.

4.1 Models analysis for the acoustic response of bias flow perforates

Several models are available in the literature to describe the characteristic response of perforates, based either on theoretical developments (Melling (1973), Howe (1979)), or built on semi-empirical formulations (Narayana Rao and Munjal (1986)). Given the wide range of parameters which characterize this technology, the models are usually adapted to a given configuration, and no general theory has emerged. For example, Narayana Rao and Munjal (1986) obtained an effective empirical model yet limited to the case of grazing flows, but including porosity and plate thickness effects. Melling (1973) proposes a complete framework for low and high amplitude interactions, which is based on an integration of the Navier-Stokes equations and takes into account the dissipative acoustic layer in the perforations. However this model does not take into account acoustic dissipation at the perforations outlet which were identified as the main source of sound absorption for thin perforates of low porosity. In this case, the vortex shedding at the aperture's rim is known to be the main acoustic dissipa-

tion source. Many models based on this mechanism rely on the original expression proposed by Howe (1979) for the Rayleigh conductivity of a single aperture traversed by a bias flow. Recent developments include the plate thickness (Jing and Sun 2000), hole shape (Randeberg 2000; Lee and Chen 2003), vena contracta (Peters et al. 1993) and grazing flow (Syed et al. 2002) effects. The presence of a resonant back cavity behind perforates has been shown to drastically improve the damping performance (Hughes and Dowling 1990; Eldredge and Dowling 2003). Recent progresses in direct numerical simulation have allowed Leung et al. (2006) to back up these results. It is shown in that reference that small apertures are effective in damping broadband noise by vortex shedding with or without mean flow. This has led to the development of perforated devices featuring a quasi-perfect non reflecting condition for specific pure tones (Hughes and Dowling 1990). Therefore, perforated panels with bias flow and back cavity are an attractive solution for acoustic damping in combustion chambers.

4.1.1 Linear modeling of a perforated plate with bias flow

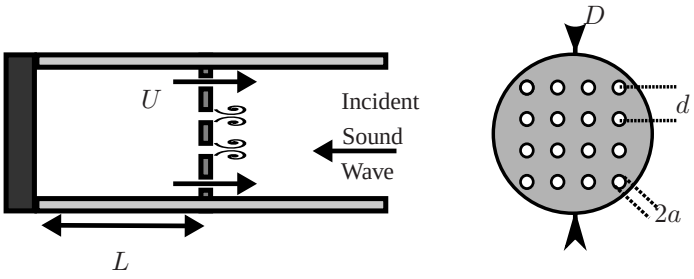

Figure 4.1: Perforated plate backed by a rigid cavity, with bias flow, submitted to normal incident pressure perturbations.

Considering plates of low porosity ($\sigma \leq 10\%$), with hole radius a and hole interspace d, compact with respect to the acoustic wavelengths of interest ($a, d \ll \lambda$), as sketched in figure 4.1, an expression for the complex reflection coefficient R at the front face of the perforated plate backed by a cavity of depth L can be obtained as a function of the perforation parameters a and d, the cavity depth L, the bias flow velocity U and the wavenumber $k = \omega/c_0$ (Hughes and Dowling (1990)):

$$R = \frac{\left(ikd^2/K_R\right) + 1 - (i/\tan(kL))}{(ikd^2/K_R) - 1 - (i/\tan(kL))} \tag{4.1}$$

where $i = (-1)^{1/2}$ and the reflection coefficient is classically defined as:

$$R = \frac{Z - \rho_0 c_0}{Z + \rho_0 c_0}$$

This expression relies on Howe's model for the Rayleigh conductivity K_R of a single aperture. Its validity is thus limited to plates with well separated apertures ($a/d \ll 1$) without any restriction for the choice of the aperture radius a or the spacing d. This conductivity is a

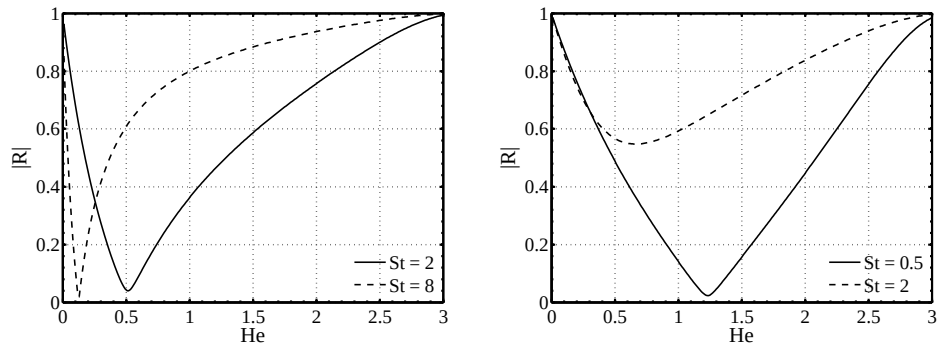

(a) $\mathrm{Q} = 1$. (b) $\mathrm{Q} = 0.5$

Figure 4.2: Evolution of the reflection coefficient modulus $|R|$ with the Helmholtz number He, for given Strouhal numbers St and resonance parameters Q.

function of the Strouhal number $\mathrm{St} = \omega a/U$ based on the bias flow velocity and the aperture radius (Howe 1979):

$$K_R(\mathrm{St}) = 2a(\Gamma - i\Delta) \tag{4.2}$$

where the real and imaginary parts Γ and Δ are fully determined by Bessel functions of the Strouhal number St (Howe 1979; Luong et al. 2005).

Using equation 4.1, it is then possible to find the roots $R = 0$ yielding conditions which maximize acoustic damping. Hughes and Dowling introduce the resonance parameter $\mathrm{Q} = k/k_{He}$ where $k_{He} = 2a/(Ld^2)$ is the frequency of the equivalent Helmholtz resonator (of volume Ld^2 and aperture diameter $2a$) and propose to find the roots of equation 4.1 by setting its value to $\mathrm{Q} = 1$. They show that this leads to the best acoustic absorption properties for well identified Strouhal $\mathrm{St} = \omega a/U$ and low Helmholtz $\mathrm{He} = kL$ numbers. A nearly perfectly non-reflecting condition can indeed be achieved using this method, but good damping properties are also limited to a narrow band around the Helmholtz resonance frequency f_{He} (see figure 4.2a). It is worth noting that this is not the unique solution to cancel the reflection coefficient in eq. 4.1. The constraint $Q = 1$ can also be released, and one can tune the different parameters of equation 4.1 to find other "off-design" optimized solutions. A trade-off between vanishing reflection for pure tones and small but non zero reflection over a wider frequency interval can also be achieved depending on the final application envisaged (figure 4.2b).

Most of the models derived from Howe's formulation are however based on linear acoustics, and this limits their validity to interactions with small amplitude pressure perturbations. In most combustion systems like those used in modern gas turbines, acoustic energy reaches high values, corresponding to pressure waves of several hundreds Pa. This implies a strong nonlinear response of the perforated plates to the incident pressure perturbations. It is found that such nonlinearities can totally cancel the damping properties of perforated plates placed in a combustion chamber (Tran et al. 2008).

4.1.2 Nonlinear interactions

Interaction of the bias flow through perforations with high intensity incident sound waves has been seldom studied. Few theoretical investigations deal with the effect of sound level amplitude. Current knowledge is mainly based on a few experimental observations available.
Cummings and Eversman (1983) developed a model to account for such high amplitude interaction with duct terminations, in absence of a mean flow. Cummings (1986) pursued this work with a numerical approach to solve the problem directly in the time domain, still in absence of a mean flow, by considering a time-varying end correction for an orifice plate. Grace et al. (1999) examine the stability of high Reynolds number grazing flows, while Luong et al. (2005) use the model of Cummings (1986) to extend the validity range of the Rayleigh conductivity expression obtained by Howe (1979). Jing and Sun (2002a) propose a discrete vortex model to simulate the vortex shedding process associated with high-intensity sound at an orifice with bias flow. The main conclusion is that the nonlinear effects mainly depend on the vortex shedding rate at the orifice edge and the convection velocity of the shed vortices, rather than on detailed interactions at the aperture's rim (Jing and Sun (2002b)). The most extensive experimental dataset, reported by Ingard and Ising (1967), corresponds to a parametric study of the effect of incident SPL on the response of a single aperture of large diameter with and without mean bias flow. A semi-empirical expression for the absorption coefficient $1-|R|^2$ is derived as a function of the plate porosity and SPL. A recent study, from Dragan and Lebedeva (1998), contains a non-dimensional transition criterion which takes into account the perforate geometry, but it does not seem to correlate with the results of Ingard & Ising.

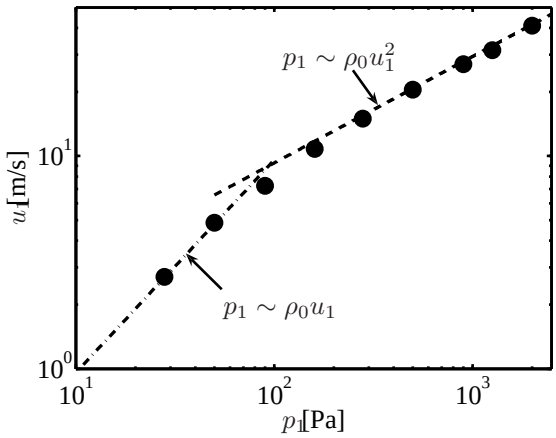

Figure 4.3: Peak velocity as a function of the pressure amplitude. Data from Ingard and Ising (1967)

Simultaneous measurements of the pressure and acoustic velocity fluctuations in an orifice have highlighted two relations between the pressure and the acoustic velocity amplitudes.
For small sound pressure levels, pressure fluctuations are proportional to acoustic velocity, $p_1 \sim \rho_0 u_1$. At higher levels, pressure is proportional to the square of the acoustic velocity: $p_1 \sim \rho_0 u_1^2$. Data collected by Ingard & Ising are shown in figure 4.3.
Ingard and Ising (1967) propose a relationship to link pressure and velocity perturbations in

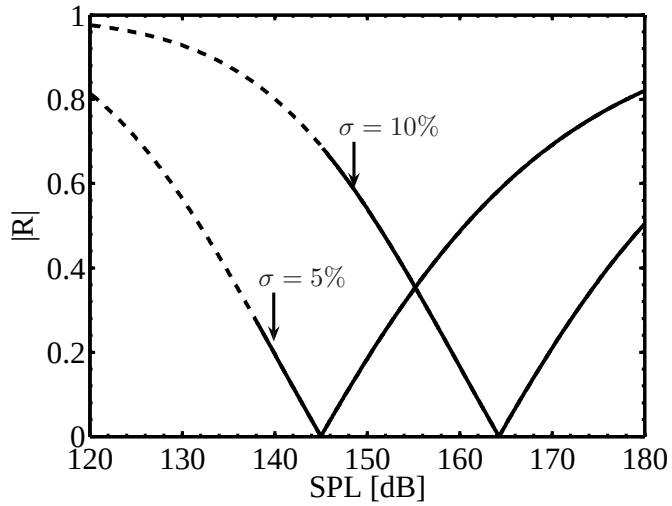

Figure 4.4: Modulus of the reflection coefficient derived from equation 4.4 as function of the incident SPL, for two plate porosities. Solid line represent the model above its lower limit ($u' \geq 10$ ms^{-1}), dashed line extends it to low SPL values.

the orifice of a perforate of porosity σ near acoustic resonance:

$$\frac{u_1}{c_0\sigma} = \sqrt{\frac{1}{4} + 2\frac{p_1}{\gamma p_0 \sigma^2}} - \frac{1}{2} \tag{4.3}$$

Introducing the quantity $\beta = p_1/\gamma p_0 \sigma^2$, they eventually derived an expression of the absorption coefficient at the resonance as a function of the driving pressure amplitude:

$$\alpha \approx 64\beta / \left(1 + \sqrt{1 + 8\beta}\right)^3 \tag{4.4}$$

Where p_0 is the ambient pressure and $\gamma = c_p/c_v$ the specific air capacity ratio. The absorption coefficient is simply a function of β, which depends on the acoustic pressure and plate porosity. The influence of plate porosity is illustrated on figure 4.4 ; the lower the porosity, the lower the SPL at which the peak absorption ($|R| = 0$) occurs.
These relationships are valid when the viscous part of the resistance is low, i.e. when the acoustic velocity is larger than a critical value u_c defined by Ingard and Ising (1967).
Empirically, they determined a threshold level equal to $u_1 \approx (1 + t/2a)\sqrt{f/2}$, where t designates the plate thickness. This limit does not take into account the influence of the aperture spacing. As a consequence, this formulation cannot be used to link the threshold between linear and nonlinear acoustic responses to the perforates geometry. The bias flow velocity that triggers the nonlinear regime highlighted by Ingard and Ising (1967) cannot be directly related to the optimal bias flow velocity that was shown to control the linear regime.

Plate	a [mm]	d [mm]	σ [%]	$U_{opt}[$ ms$^{-1}]$	N
P_4	0.5	4	4.84	9.0	121
P_5	0.5	5	2.76	5.6	69
P_6	0.5	6	1.96	4.0	49
P_7	0.5	7	1.48	3.0	37
P_8	0.5	8	1.22	2.3	25

Table 4.1: Perforated plate parameters. a: aperture radius, d: aperture interspace, σ: porosity, U_{opt}: optimal bias flow velocity and N number of apertures.

Concluding remarks on the models

The model based on the linear expression of the Rayleigh conductivity has been successfully used in the past to design effective absorbing perforated plates. This model takes into account the influence of bias flow, but does not account for nonlinear interaction with high pressure amplitudes. The semi-empirical formulation of Ingard & Ising addresses this issue and yields conditions for total sound absorption $|R| = 0$ at high SPL. These two models thus offer a rather complete framework for modeling the response of bias flow perforates submitted to a large dynamic of incident pressure perturbation levels.
Equation (4.1) is used to design a set of perforates which differ only by their aperture spacing. The effect of the orifice diameter has not been included in the present work. This limitation seems to be of lesser importance, as Ingard & Ising reported very good agreement between measurement obtained over a wide range of aperture diameters. The influence of the radius to spacing ratio and of the velocity on the acoustic damping properties is thus investigated first in the linear regime, and results are presented in the following section. It is demonstrated that these plates effectively feature large amplitude of variation of their reflection coefficient with frequency and back-cavity depth. It is possible to control their acoustic response at a given frequency by tuning the cavity depth. The influence of the bias flow velocity through the aperture is then presented, before the investigation on effects of the aperture spacing. Interactions with high amplitude pressure waves is measured with and without bias flow. Data are compared to predictions from the two models and finally a transition criterion is derived.

4.2 Acoustic response of perforated plates submitted to low SPL

The model proposed in eq. 4.1 was successfully implemented by Hughes and Dowling (1990) to design noise absorbers for gas turbines. The design of perforated plates used in the present study is hence based on this model, yet with different constraints. The aims are to define plates of low porosity which feature a large absorption bandwidth in the low frequency range (below 1 kHz) and such that their reflection coefficient can be effectively controlled by adjusting the back-cavity depth. A design rule for the aperture radius-to-spacing ratio a/d of perforates is also looked for.

Following the model of Howe (1979), the reflection coefficient of a bias flow perforate backed by a resonant back-cavity is a function of the aperture radius and spacing, the bias flow veloc-

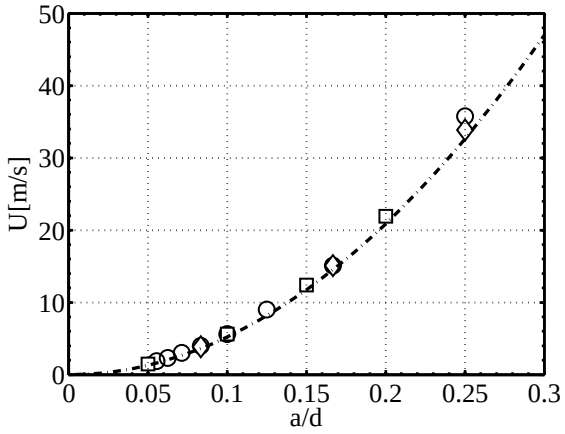

Figure 4.5: Optimal bias flow velocity as a function of a/d. Circles correspond to a variable spacing d and a constant radius $a = 0.5$ mm. Squares were obtained with a constant spacing $d = 5$ mm and diamonds with $d = 3$ mm. Dashed line plot the evolution of $U = A(a/d)^2$ with $A = 522$.

ity through these apertures, the depth of the back-cavity and the operating frequency (equation 4.1). In the low frequency range ($f \leq 1$ kHz), and for a given a/d ratio, it is possible to select a unique bias flow velocity U_{opt} which allows good damping properties. Demonstration for a given plate geometry is included in appendix B. This optimal bias flow velocity is a function of the aperture radius-to-spacing only, $U \approx A(a/d)^2$ ($A \approx 522$, figure 4.5). As a consequence, the reflection coefficient of this type of perforate with a given a/d ratio can simply be considered as a function of the cavity depth and the frequency, when operated at its optimal bias flow velocity U_{opt} .
A set of plates with constant aperture radius a and increasing apertures spacing d was thus designed. A typical geometrical arrangement is shown in figure 4.1.
Plates properties are gathered in table 4.1. For each plate, the optimal bias flow velocity U_{opt} has been computed. The plate porosity is given by $\sigma = 4Na^2/D^2$ where N is the number of holes, a the holes radius and D the plate diameter. Considering the perforations as a network of N apertures equally distributed over a square mesh, the porosity can also be expressed as $\sigma \simeq \pi a^2/d^2$, thus linking the aperture properties to the plate dimensions.
The pressure losses through the perforates were estimated using plate P4 and the database in Idel'Cik (1999). Theses perforates correspond to "thick grids "of low Reynolds number, since the ratio of their thickness to aperture hydraulic diameter is equal to unity and the Reynolds number based on the optimal bias flow velocity is $Re \simeq 560$. Such configuration yields a pressure drop coefficient $\zeta = \simeq 600$ and subsequently a pressure drop of about 10 Pa in the configuration used.

The influence of the cavity depth and forcing frequency on the reflection coefficient has been characterized for each plate in the impedance tube facility, for a fixed Sound Pressure Level of 110 dB, monitored by the microphone MSPL. Measurements were carried out with the corresponding imposed optimal bias flow velocity (table 4.1). The evolution of the modulus $|R|$ of the reflection coefficient as a function of the cavity depth L and the frequency f is

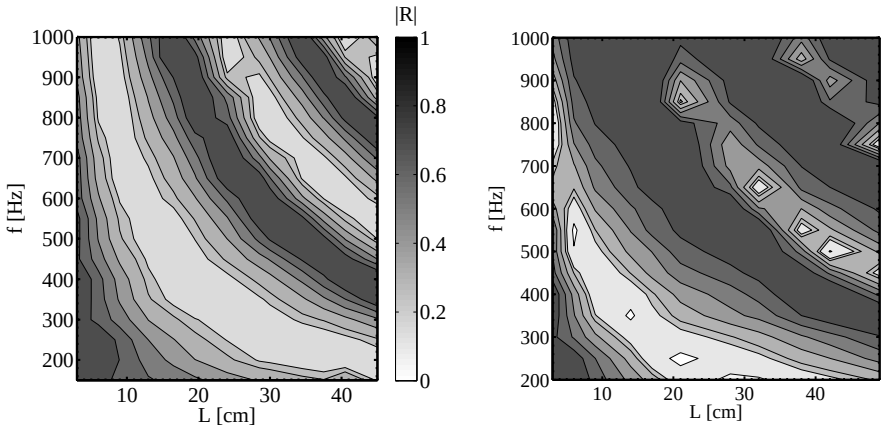

(a) Plate P_4. $U_{opt} = 9$ ms^{-1}.

(b) Plate P_8. $U_{opt} = 2.3$ ms^{-1}.

Figure 4.6: Evolution of the reflection coefficient modulus $|R|$ with cavity depth L and frequency f for plates P_4 and P_8. $U = U_{opt}$ for a constant $SPL = 110$ dB measured with MSPL.

plotted in figure 4.6a for plate P_4 and 4.6b for plate P_8. Magnitude ranges from 1 (dark zones) to 0 (white regions). It must be noted that more measurements were carried out for plate P_4 than for P_8, yielding a better resolution in figure 4.6a. Several conclusions can be drawn from such magnitude maps. First, a large amplitude of control of $|R|$ can be achieved for all frequencies considered, between 100 and 1000 Hz. Secondly, at a given forcing frequency, a smooth and gradual evolution of the modulus is achieved when the cavity depth L is varied. Finally by choosing the cavity length between $L = 5$ and $L = 45$ cm, it is possible to impose any value of the reflection coefficient within the chosen frequency range. The evolution of the reflection coefficient with respect to frequency for two cavity depths is plotted in figure 4.7. For a small depth, $L = 165$ mm, only one minimum is reached but the reflection coefficient takes small values over a wide interval ($|R| \leq 0.5$ over almost 600 Hz). By increasing the cavity depth, it is possible to set a lower reflection coefficient for two distinct frequencies, but with a steeper evolution, as the modulus reaches a maximum in between these minima. In both cases, the phase displays a sign shift when reaching the local minimum. The present study focuses on controlling the reflection coefficient modulus by varying the back-cavity depth. The phase was not controlled. One can however note that the phase smoothly evolves without abrupt changes and with a reduced amplitude of variations.
In the rest of this chapter, data are presented for a single cavity depth $L = 150$ mm for every plate unless indicated otherwise.

4.2.1 Effect of the bias flow velocity

Evolutions of the moduli and phases of the reflection coefficient for plates P_4 and P_7 with frequency are presented in figures 4.8a and 4.8b to highlight the role of the bias flow through the apertures. Model predictions are compared to measurements carried out without bias flow ($U = 0$) and with the optimal velocity through the apertures ($U = U_{opt}$). The evolution of the phase $\varphi(R)$ with frequency is globally unaffected by the presence of the bias flow and

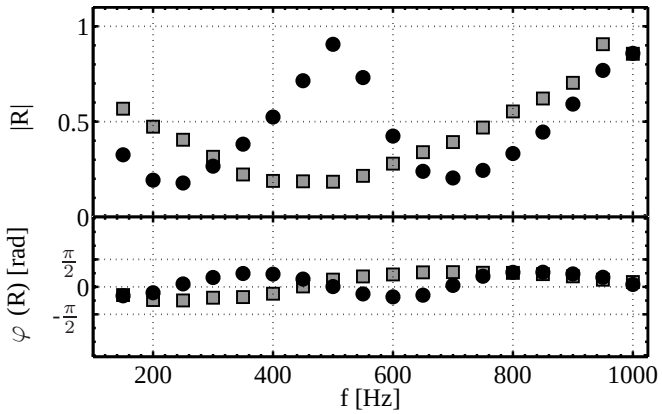

Figure 4.7: Evolution of the reflection coefficient modulus $|R|$ with the frequency f for plate P_4 for $L = 165\,\text{mm}$ (squares) and $L = 345\,\text{mm}$ (diamonds). $U = U_{opt} = 9\,\text{ms}^{-1}$ for a constant $SPL = 110\,\text{dB}$ measured with MSPL.

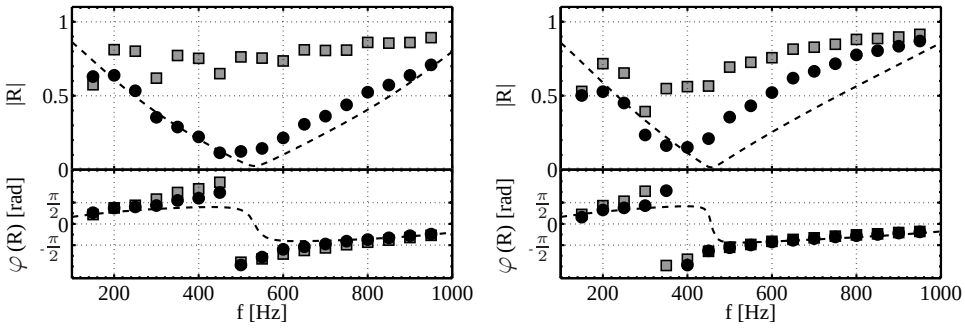

(a) Plate P_4. $U_{opt} = 9$ ms^{-1}.

(b) Plate P_7. $U_{opt} = 3$ ms^{-1}.

Figure 4.8: Effect of the bias flow velocity on the modulus $|R|$ (top) and the phase φ (bottom) of the reflection coefficient for a fixed cavity depth of $L = 150$ mm and a constant SPL of 110 dB. Model prediction for the optimal bias flow velocity U_{opt} (dashed line) is compared to measured data at same U_{opt} (black circle) and to measurements without any bias flow, $U = 0$ ms^{-1} (grey squares).

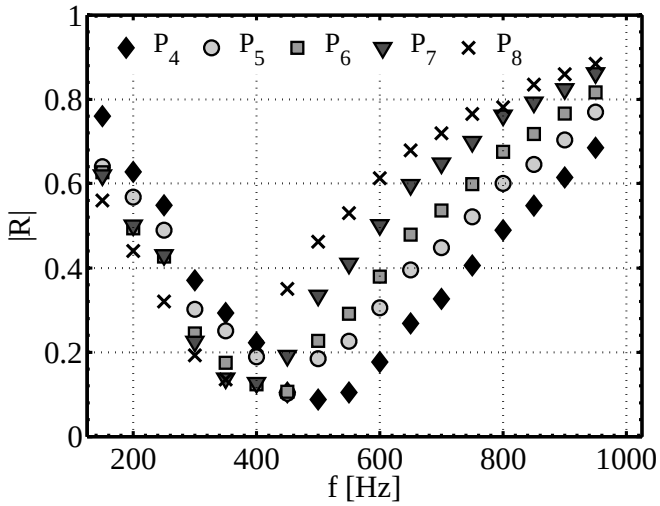

Figure 4.9: Evolution of $|R|$ with frequency f for the whole set of plates. Measurements obtained for a constant SPL of 110 dB and a cavity depth $L = 150$ mm. The optimal bias flow velocity U_{opt} was imposed for each plate.

correlates well with the model. A small difference can be observed for the frequency at which the phase transition occurs, which in practice occurs at a lower frequency than modelled.
The bias flow has a much greater influence on the modulus of the reflection coefficient. For plate P_4, the modulus $|R|$ is almost constant ($|R| \approx 0.8$) with frequency, in the absence of bias flow, while it features a large magnitude of variation once vortex shedding is promoted at the optimal Strouhal number. In this latter case, the model is suitably predictive, even though the predicted minimum is located at a slightly higher frequency than that observed. The modulus ranges smoothly from 0.15 up to 0.8. For plate P_7, similar conclusions can be drawn for the phase evolution which is well predicted. The model is less accurate in predicting the modulus evolution, especially above $f = 400$ Hz. This evolution is similar to the one observed for plate P_4: a low slope decrease followed by a low slope increase. Minima and maxima are well predicted. The main difference is the frequency at which the maximum absorption occurs.
The bias flow velocity has therefore a key influence on the modulus of the reflection coefficient for perforated plates submitted to low pressure perturbation levels ($p \approx 6$ Pa), hereby confirming the role of vortex shedding in acoustic energy absorption. Thus, the model proposed by Howe (1979) suitably predicts the phase and modulus evolutions for this kind of perforates and can be used for plate design, at least when the SPL remains small.

4.2.2 Influence of the aperture spacing

Influence of the aperture spacing on the reflection coefficient modulus was characterized at a constant SPL of 110 dB, for a fixed cavity depth $L = 150$ mm and for the corresponding optimal bias flow velocity U_{opt} of each plate. Results are gathered in figure 4.9. All these plates feature similar evolutions of the modulus $|R|$, with little effect of the aperture spacing $d = 4, 5, 6, 7, 8$ mm on the damping properties, except that the minimal reflection is shifted towards lower frequencies when the interspace d is increased. It can also be noted that the

higher the spacing, the steeper the slope of the curves. This does not interfere with the large amplitude of control of $|R|$ that is achieved, nor with the large bandwidth in which the modulus remains small: $|R| \leq 0.5$ in a band of $300\,\text{Hz}$, and $|R| \leq 0.2$ in an interval of $150\,\text{Hz}$ for all plates. The different plates have very similar behaviors. This demonstrates that the reflection coefficient can be effectively tuned by control of the cavity depth.
As a conclusion on the interaction of perforated plates with small Sound Pressure Levels, it can be noted that the model of Howe (1979), based on vortex shedding, can be used for bias flow perforates design and performance predictions. Measurements have shown, first, good agreement with the theory and, second, the key role of the bias flow through the apertures. The tested designs feature similar good performances over a wide frequency band when submitted to incident pressure perturbations of low amplitudes. The reflection coefficient of these bias flow perforates is effectively controlled by adjusting the depth of the resonant back-cavity. It was yet observed, in the literature and in this study, that, when the perturbation amplitude increases, the response of these perforates changes dramatically. For input levels similar to those measured during typical combustion instabilities (several hundreds Pascals), these perforated plates have distinct acoustic response.
A detailed analysis is thus conducted with the whole set of plates to determine the influence of the geometry and of the bias flow velocity on the acoustic response to increasing SPL. Results are compared to the nonlinear model previously described and a transition criterion between the linear and nonlinear regimes of such low porosity perforates is highlighted.

4.3 Acoustic response of perforates submitted to high SPL

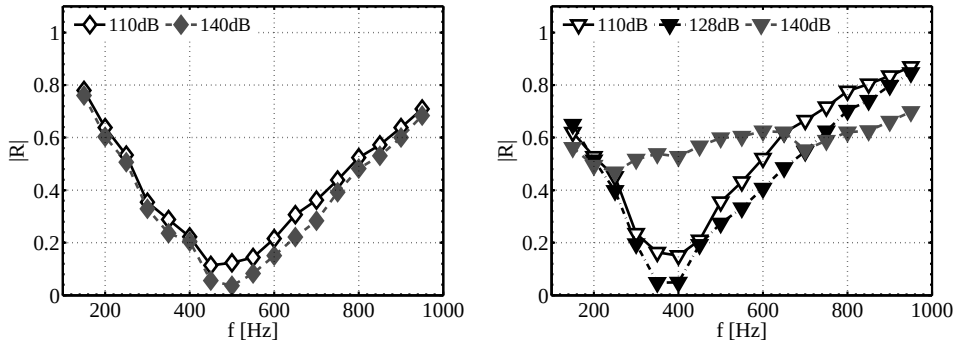

(a) Plate P4.

(b) Plate P7.

Figure 4.10: Effect of the SPL on the evolution of $|R|$ with frequency for plates P_4 and P_7, for a given cavity depth of $L = 150\,\text{mm}$, at their respective optimal bias flow velocities.

Previous studies have already highlighted the effect of pressure amplitude on the acoustic response (Ingard and Ising 1967; Dragan and Lebedeva 1998). Once reverse flow in the aperture is promoted by high incident acoustic velocities, perforates respond nonlinearly, and their performances may be severely altered. Figures 4.10a and 4.10b illustrate the influence of an increasing incident SPL for plates P_4 and P_7. Evolution of $|R|$ with frequency was measured for different forcing amplitudes $SPL = 110, 128\,\text{and}\,140\,\text{dB}$ monitored by the microphone MSPL.

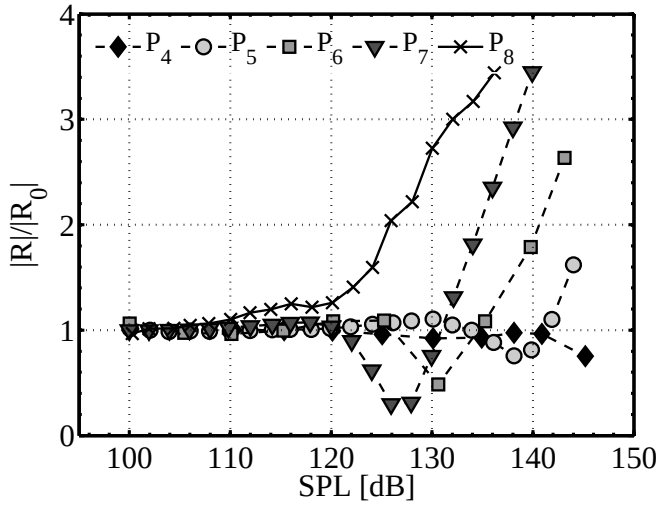

Figure 4.11: Evolution of the ratio $|R|/|R_0|$ with increasing SPL for the whole set of plates. Optimal bias flow velocity is used for each perforated plate, while cavity depth and frequency are fixed ($L = 150$ mm, $f = 400$ Hz).

With plate P_4, a forcing input lower than 140 dB does not have any influence on the reflection coefficient,which remains identical to its value at 110 dB. For a forcing of 140 dB, however, the reflection coefficient is globally lower in amplitude, especially around the resonance frequency. At $f = 500$ Hz, the modulus $|R|$ decreases from 0.12 down to 0.03.
For plate P_7, the forcing level has a strong effect on the evolution of the reflection coefficient. First, a moderate SPL increase has a positive effect. The modulus is decreased in the whole frequency range (curve at 128 dB). At the resonance frequency $f = 400$ Hz, the value drops down from 0.15 to 0.05. However, when the forcing amplitude is further increased (curve corresponding to 140 dB), the influence becomes very detrimental. The evolution of $|R|$ is flattened, approaching a constant value independent of the frequency, around $|R| \approx 0.6$. The thresholds, at which the perforates acoustic response changes, appear to be linked to the plate geometry.

4.3.1 Influence of the perforate geometry on the onset of nonlinearities

Detailed investigation was led to study the influence of the SPL on the perforate response along with the effect of the aperture radius-to-spacing ratio on the threshold levels. Measurements were made for all plates with a fixed configuration ($L = 150$ mm, $f = 400$ Hz and $U = U_{opt}$) in which $|R|$ takes small values at 100 dB. All plates then feature different moduli R_0 as could be expected from figure 4.9. The lowest values are obtained with plate P_6 and P_7, but only plate P_7 has its actual resonance frequency equal to the forcing frequency (its phase is null).
SPL is then increased up to 145 dB. Results are gathered in figure 4.11. The modulus of the reflection coefficient of each plate has been divided by its value $|R_0|$ measured for $SPL \leq 100$ dB.
Three different zones can be distinguished in this plot. First, at low SPL (globally below

120 dB), the reflection coefficient is unaffected by the perturbation level. Then, in a limited range of SPL, the modulus decreases ($|R|/|R_0| < 1$). Finally, above a second SPL threshold, the modulus takes rapidly large values. The two threshold levels are functions of the aperture radius to spacing ratio a/d. The smaller the interspace d, the higher the threshold level. In the extreme case of plate P_4, only the first threshold level could be reached at 140 dB. When the interspace is very large, with plate P_8, there is no reduction of $|R|/|R_0|$ and the acoustic response is quite distinct. Indeed, for plate P_8, the reflection coefficient only increases with SPL, first slowly up to 120 dB, then very strongly.
This dataset indicates that there are two regimes of dependence of the perforates to the SPL. In the first regime, the plate reflection coefficient is independent on the input level. In the second regime, it becomes strongly dependent on the SPL, with two successive behaviors. The threshold between these regimes is clearly linked to the plate geometry and more precisely to the a/d ratio. This preliminary result is of prime interest for design. The linear model yields perforated plates effective for moderate SPL, yet of limited performances for high SPL. This nonlinear behavior is examined more closely in the following section

4.3.2 Modelling the linear and nonlinear response of bias flow perforates

The experimental data shown in figure 4.11 are now compared to the model prediction proposed by Ingard and Ising (1967), using equation 4.4, for plates P_4, P_6 and P_7 in figures 4.12a, 4.12b and 4.12c respectively. The influence of the bias flow velocity is also investigated; data obtained without bias flow are shown (black squares) along with measurements at the optimal bias flow velocity (grey circles). Prediction using Howe's model (eq. 4.1) obtained for the optimal bias flow velocity appears as an horizontal line, since the model is independent of the SPL. The V-shaped curve is the model of Ingard & Ising.
As mentioned by the authors, the validity of their model is limited to high values of the SPL, with a threshold linked to the occurrence of flow reversal in the apertures. For each plate, equation 4.3 was used to determine the pressure amplitude corresponding to a peak-to-peak velocity in the apertures equal to the optimal bias flow velocity, $u_1 = U_{opt}$. For perturbations amplitudes larger than this threshold, flow reversal occurs in the apertures and the model of Ingard& Ising can be applied. The solid line marks the model above this lower limit, while the dashed line represents the model evolution in the low range of SPL. Finally, it should be noted that the horizontal line stops where the dashed curve ends, i.e. at the so determined lower limit.

It can first be noted that, for the three plates presented P_4, P_6 and P_7, the SPL has a strong influence not only in the presence of the optimal bias flow, but also on the evolution of the reflection coefficient in absence of bias flow. In the latter case, the regime independent of SPL is limited to very small input levels (≤ 105 dB). When the SPL is increased, $|R|$ rapidly decreases and ends up matching closely the reflection coefficient obtained with bias flow. The decreasing slope matches the nonlinear model predictions very well, for amplitude levels much smaller than the estimated threshold limit. Once this limit is reached, the acoustic responses of perforates with and without bias flow evolve identically. This indicates that the bias flow is then not the main source of energy dissipation anymore. The lower SPL threshold, estimated from the occurrence of flow reversal in the apertures, is a good indicator of the onset of the second regime. Below this value, the modulus remains independent of the SPL and is controlled by the value of the bias flow velocity. For higher SPL, the nonlinear predictions fit remarkably well with the data; the SPL at which $|R|$ is minimal is well predicted, along with

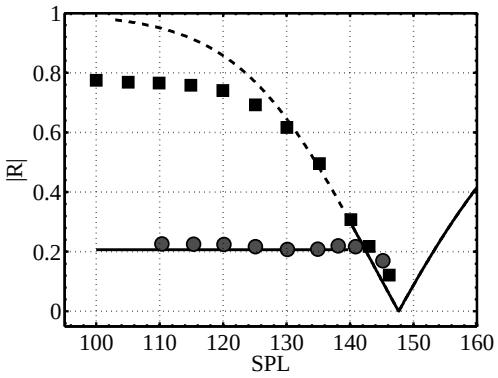

(a) Plate P4.

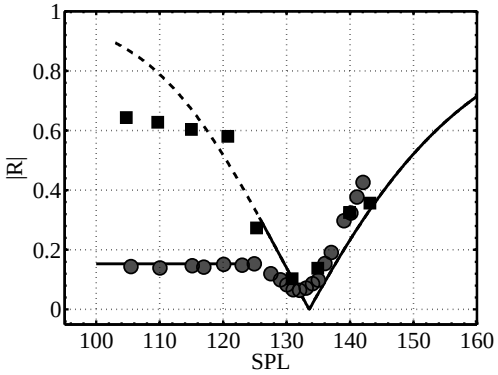

(b) Plate P6.

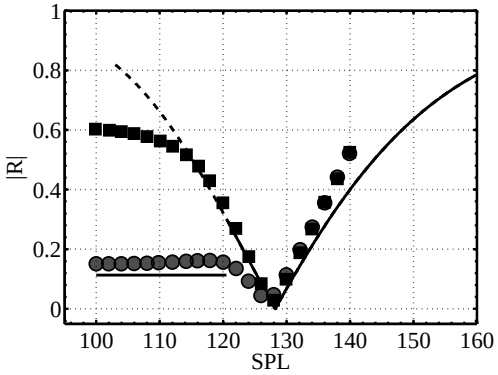

(c) Plate P7.

Figure 4.12: Evolution of $|R|$ with SPL for plates P_4,P_6 and P_7 for a fixed cavity depth $L = 150\,\text{mm}$ and an imposed forcing frequency $f = 400\,\text{Hz}$. Measurements with optimal bias flow U_{opt} (grey circles), and without bias flow (black squares) are compared with the linear and nonlinear models (lines). The nonlinear model is represented above its lower threshold limit, based on U_{opt}, by the solid curve. Dashed curve present the nonlinear model over the whole SPL range. The horizontal line is the value computed from the linear model using the optimal bias flow velocity.

the subsequent increase. Attention is drawn on the fact that the model evaluates accurately the amplitude of the modulus, measured with and without bias flow. In case of plate P_4, the SPL minimizing the modulus could not be reached due to power limitations of the loudspeaker. For the two other plates, this SPL is observed within 2 dB of the modeled value.
The two different regimes can therefore be analyzed separately. The first regime, independent of the SPL, is well predicted by the linear model of Howe (1979). The second regime is well reproduced by the nonlinear formulation of Ingard and Ising (1967). This model correctly accounts for the existence of an optimal SPL at which $|R|$ is minimal, and for the large increase of the modulus when the SPL is increased above this optimal value. The onset of flow reversal $u_1 = U_{opt}$ in the apertures is a good indicator of the transition between the two regimes.
The bias flow velocity largely enhances the damping properties of low porosity perforates plates. Small values of the reflection coefficient can indeed be reached in the bias-flow controlled regime, independently of the incident SPL. When the SPL is increased, the presence of this bias flow velocity seems to determine the onset of the nonlinear regime. Perforates used without bias flow display a nonlinear response with SPL much lower than when used with their optimal bias flow velocities. As a result it can be inferred that the bias flow velocity also extend the range of the linear domain for these perforated plates.
The response of these perforated plates is controlled by linear interactions when acoustic perturbations within the apertures are smaller that the bias flow velocity. This corresponds to a bias-flow controlled (BFC) regime, $u_1/U_{opt} < 1$. For higher SPL, the acoustic velocity may eventually overcome the bias flow velocity and flow reversal occurs within the apertures. This determines the transition to the perturbation-flow controlled (PFC) regime, $u_1/U_{opt} > 1$. The ratio between the steady mean bias flow and the acoustic velocity in the aperture appears to be the key parameter controlling the acoustic response of perforates. This acoustic velocity could not be directly measured with the current setup. This quantity is derived from acoustic pressure measurements in the next section.

4.3.3 Transition between BFC and PFC regimes

The back cavity behind the perforates can be considered as a cylindrical rigid tube closed on its rear side, considering that the lateral air injections have negligible effects on the longitudinal acoustics. The impedance Z in a section located at a distance x from the back wall is thus given by:

$$Z(x) = -i/\tan(kx)$$

The complex amplitude of velocity fluctuation at the perforated plate location can then be estimated as a function of the acoustic pressure:

$$u_1\left(L^-\right) = \frac{i}{\rho_0 c_0}\tan(kL^-)p_1\left(L^-\right)$$

The pressure level at $x = L^-$ is not known but the pressure amplitude at the back wall ($x = 0^+$) is measured by microphone MSPL and there is a simple relation between these two quantities:

$$p_1\left(L^-\right) = p_1(0)\cos kL.$$

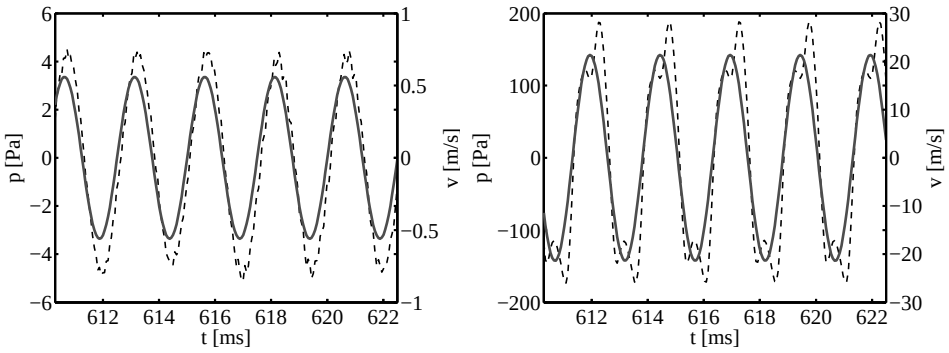

(a) Low forcing amplitude.

(b) High forcing amplitude.

Figure 4.13: Original pressure signal (dashed line) and reconstructed acoustic velocity from filtered signal (solid line) at two forcing amplitudes, 104 and 136 dB respectively.

The acoustic velocity at the perforated plate can thus be simply expressed as:

$$u_1\left(L^-\right) = \frac{i}{\rho_0 c_0} p_1(0) \sin kL \tag{4.5}$$

The acoustic velocity within the apertures can then be estimated from the acoustic velocity upstream of the plate (Noiray et al. 2008a):

$$u_1\left(L\right) \approx \frac{u_1\left(L^-\right)}{\sigma} \tag{4.6}$$

To estimate $u_1\left(L\right)$, a pressure signal, filtered at the forcing frequency f, is needed. The Hilbert transform method described in chapter 3 is used here. The raw pressure signals are distorted when the forcing amplitude is high. The filtering eliminates high order harmonics and provides a sinusoidal signal for which simple relationships exist between the root-mean-square and the peak-to-peak amplitudes. The RMS calculated from the filtered signal corresponds for most cases to 92% of the RMS of the raw pressure signal for small forcing amplitudes, with a decrease of only 10% when the forcing amplitude is multiplied by 100. Examples of reconstructed acoustic velocities are shown in figures 4.13a and 4.13b for two forcing amplitudes, 104 and 136 dB respectively.

Equation 4.6 was used to evaluate the acoustic velocity amplitude u_1 within the perforations for each plate, using the filtered pressure signal at the forcing frequency. Evolution of the reflection coefficient is then plotted versus the ratio of this acoustic velocity amplitude to the optimal bias flow velocity u_1/U_{opt} for increasing SPL. The normalized modulus $|R|/|R_0|$ evolution is plotted in figure 4.14a, R_0 being the modulus measured for small SPL.
With this new representation, it can first be noticed that all results collapse to a similar curve. For all plates, there is no evolution of the modulus at low acoustic velocities $u_1/U_{opt} \leq 1$, showing the range of the BFC regime. With increasing SPL, i.e when the perturbation velocity u_1 increases in the apertures, moduli of the reflection coefficient decrease to reach a minimum for a velocity ratio $u_1/U_{opt} \approx 2-3$, for all plates except P_8. When the perturbation velocity further increases, above $u_1/U_{opt} \geq 3$, a steep increase in the reflection coefficient occurs

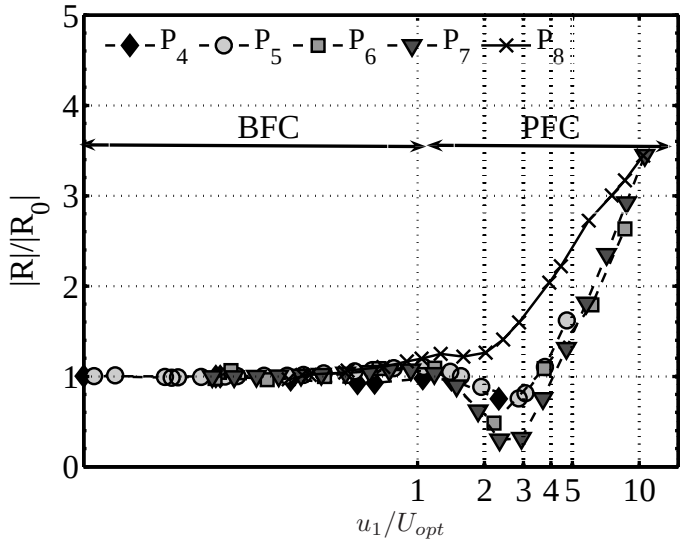

(a) Normalized gain $|R|/|R_0|$ evolution.

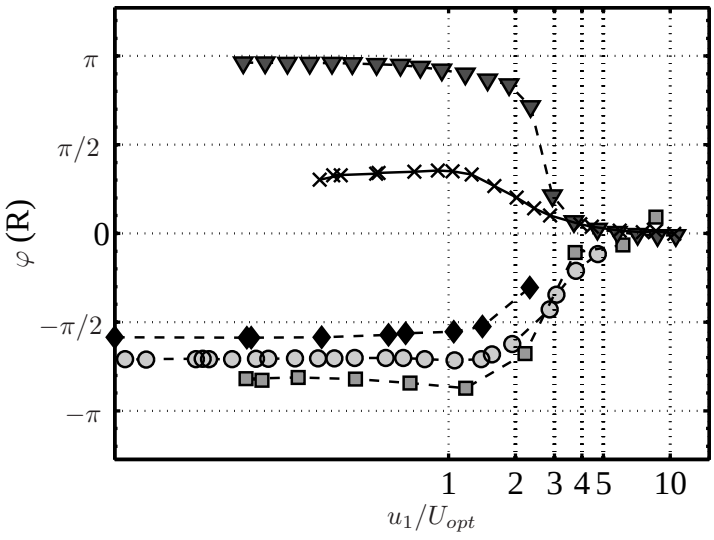

(b) Phase evolution.

Figure 4.14: Evolution of the reflection coefficient with the acoustic to bias flow velocity ratio u_1/U_{opt} for the whole set of plates. Optimal bias flow velocity is used for each perforated plate, while cavity depth and frequency are fixed ($L = 150\,\text{mm}$, $f = 400\,\text{Hz}$).

$|R| > |R_0|$. These are the two sub-regimes that compose the PFC regime. From the phase evolution in figure 4.14b it can be noted that in the PFC regime, phase of the reflection coefficient tends toward zero; the reactance vanishes and therefore the impedance becomes a pure real number when the incident SPL is high. In the BFC regime for a given plate, there is obviously no evolution of the phase.

Concluding remarks

An experimental analysis was carried out to determine the acoustic behavior of low porosity perforated plates submitted first to small pressure perturbation levels, then to perturbation levels similar to those measured during typical self-sustained combustion instabilities in practical burners. The initial objective was to design perforated plates of small diameter to be used as an impedance control system on the combustion rig. Classical acoustical analysis was carried out to design a set of perforated plates with different porosities. Amongst the key results of this first study, it was shown that, in the frequency range of interest ($100 - 1000$ Hz), an optimal bias flow velocity, function of the plate geometry, should be selected to obtain the largest amplitude of control of the reflection coefficient of perforates backed by a rigid cavity. Controlling the depth of the resonant back-cavity allows to impose distinct values of the reflection coefficient modulus, with reduced influence on the phase of the reflected pressure waves. All the designed plates feature a large amplitude of variation of their reflection coefficient modulus, from 1 to almost 0 when submitted to small SPL. However, as expected from previous investigations, the incident SPL has a strong influence on the acoustic response of the perforates associated with nonlinear response of the system. A second model, accounting for nonlinear acoustics, was successfully compared to the dataset obtained at high SPL, and allowed to link the onset of this nonlinear regime to the bias flow velocity imposed through the perforated plate.

The combination of these two models offers a complete theoretical framework for the analysis of the acoustic response of low porosity perforated plates, that was found in good agreement with the extensive experimental data collected. The linear model allows to design effective perforated plates, with an optimal bias flow velocity which largely enhances the damping properties of the system. This bias flow velocity also determines the extent of the linear response regime. Indeed, when SPL is increased, reverse flow is promoted inside the apertures of the perforated plates, and the response becomes nonlinear. The SPL threshold between the linear and nonlinear regimes is determined by the ratio of the perturbation velocity to the bias flow velocity in the orifice u_1/U_{opt}. This ratio indeed controls the acoustic response of these bias flow perforates:

- for low SPL, $u_1/U_{opt} < 1$, it is the Bias-Flow Controlled regime in which the evolution of the reflection coefficient is independent of the SPL and can be predicted by the model of Howe (1979).
- when $u_1/U_{opt} = 1$, flow reversal is promoted inside the apertures, and nonlinear response is triggered. The SPL associated to $u_1 = U_{opt}$ is therefore the upper validity limit of the BFC regime.
- at high SPL, $u_1/U_{opt} > 1$, the response of the perforates is nonlinear and is controlled by the perturbation velocity in the orifice u_1. It is the Perturbation-Flow Controlled regime, which can be modelled by the formulation of Ingard and Ising (1967).

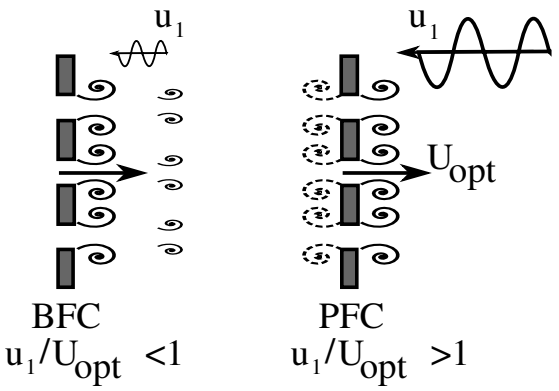

Figure 4.15: (Left) Illustration of the Bias-Flow Controlled (BFC) regime, in which vortex shedding is controlled by the optimal bias flow velocity through the perforates U_{opt}, larger than the perturbation velocity u_1. (Right) Perturbation-Flow Controlled (PFC) regime where $u_1 \geq U_{opt}$. The vortex shedding then occurs alternatively on each side of the perforates.

The vortex-shedding occurs differently in the BFC and PFC regimes, as sketched in figure 4.15. In the BFC regime, the vortex shedding is still by the steady mean bias flow as there is no flow reversal during the cycle; the vortex are shed only in the direction of the mean bias flow, i.e only on the side of the perforated plate facing the incident perturbation. In the PFC regime, when $u_1 \gg U_{opt}$, the acoustic velocity u_1 fluctuates in a quasi-sinusoidal way in the apertures, vortices are shed on both sides of the plate, alternatively during the cycle.
Such bias flow perforated plates, backed by an adjustable cavity, allow effective control of their impedance for a large dynamic of pressure fluctuation levels. An impedance control system (ICS) is thus designed and implemented at the inlet of the turbulent combustion rig, which features large combustion oscillations, to control its inlet acoustic boundary condition. The study on the influence of the ICS on these thermoacoustic self-sustained oscillations is presented in the next chapter.

Chapter 5

Control of self-sustained combustion instabilities by adaptation of the premixer inlet impedance

The Impedance Control System (ICS) is now used to control the acoustic boundary condition at the premixer inlet of the CTRL-Z combustion rig. It is first assessed in section 5.1 that the TMM impedance measurement technique can effectively be used during hot-fire test to obtain the in-situ reflection coefficient of the ICS. Section 5.2 presents the influence of the inlet acoustic reflection coefficient on self-sustained combustion instabilities. The importance of the perforates robustness to pressure amplitude is also demonstrated. Finally, an experimental evaluation of the acoustic energy balance in the facility is obtained in section 5.3 by measuring the acoustic fluxes and the Rayleigh source term. The limits of application of the ICS are then illustrated with different unstable combustion regimes (section 5.4)

The ICS is implemented on the combustion facility as presented in chapter 2 and as sketched in figure 5.1. Perforated plates, designed in chapter 4, are positioned at the inlet of the premixer line. The sliding piston is used to pilot the cavity depth. The combustion facility is equipped with microphones connected to the premixer and to the combustion chamber. Photomultiplier tubes (PMT) are installed on both sides of the chamber to collect the chemiluminescence of CH^* and OH^* radical emissions in the flame zone. Photograph 5.2 shows the full experimental arrangement, with water-cooled waveguides and light collection lenses. Perforates are placed at the rear side of the premixer inside the casing of the sliding piston, to control the reflection coefficient of this premixer. The microphones in the premixer and the chamber are flush-mounted on water-cooled waveguides so as to measure the pressure fluctuations in their respective locations according to the method described in section 3.1.2. The whole set is identically cooled and installed on waveguides of similar lengths.It was shown that this method allows correct measurement of the pressure fluctuations at the position of the inlet of the waveguide, as long as the time delay induced by the waveguide is accounted for. Microphone M1,

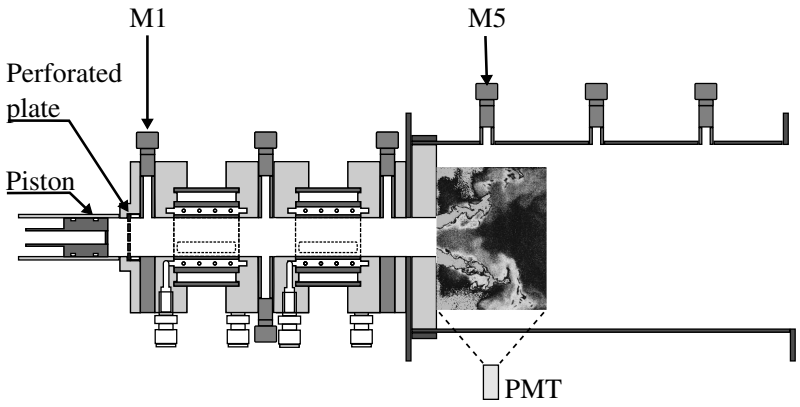

Figure 5.1: Microphones and photomultiplier arrangement for hot fire tests.

located just in front of the perforated panels is used to monitor the SPL in the facility. In the following chapter, the reported SPL is the one effectively affecting the perforated panel in the combustion setup. Two similar microphones are installed at the inner junction between the two stages of the premixer, diametrically facing each other, so as to allow the measurement of the perforates reflection coefficient in a similar way as in the High Load impedance tube (see 3.2). Then three microphones are installed in the combustion chamber, with microphone M5 in the flame region monitored by the PMT.

5.1 Measurements of the premixer reflection coefficient during hot-fire tests

When the burner is operated, the reflection coefficient R at the premixer inlet could be measured using the three microphones located inside the premixer, the flame acting as a sound source. Instead of a pure tone excitation, the source corresponds to a broadband noise dominated by a few peaks in unstable regimes. In this noisy configuration, the reflection coefficient may only be retrieved with good accuracy at the main instability frequency, when the signal to noise ratio is high. In such cases, the SPL is large, often reaching levels higher than 140 dB inside the premixer. It is known (chapter 4) that such high SPL have a strong influence on the response of perforated plates. The aim of this section is to check that the TMM can still be used during hot fire tests to perform on-the-fly measurements of the premixer inlet impedance in such harsh environment. Tests were carried out in the nominal regime described in table 2.1 of chapter 2. Measurements with the ICS equipped with plate P4 are plotted in figure 5.3 for the frequency $f = 272$ Hz corresponding to the main oscillation peak of the unstable regime studied here.

Measurements during firing tests (white symbols) are compared to those obtained in the impedance tube for a constant SPL of 110 dB (black symbols) and to the theoretical predictions (solid line). It was previously shown that the SPL has a very little influence on the plate response below 140 dB, see figure 4.11. Without back cavity ($L = 0$ cm), the reflection coefficient modulus is slightly lower than unity as would be expected for a rigid wall perfectly reflecting waves. This may be due to the airflow through the perforations that may attenuate incident acoustic waves or to the small cavity apertures in the perforated plate that may scatter

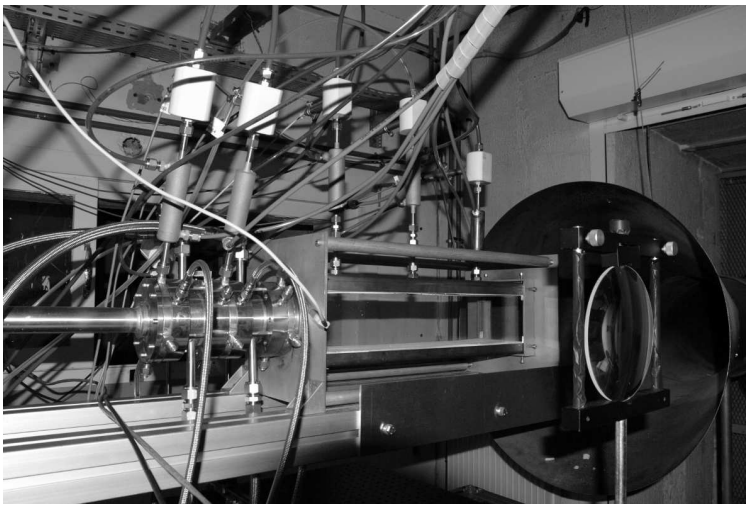

Figure 5.2: Combustion facility, fully equipped with watercooled microphones flush-mounted on waveguide (on top of the chamber and premixer) and photomultipliers tubes with collection lenses. The combustion chamber exhausts in a large funnel connected to a chimney.

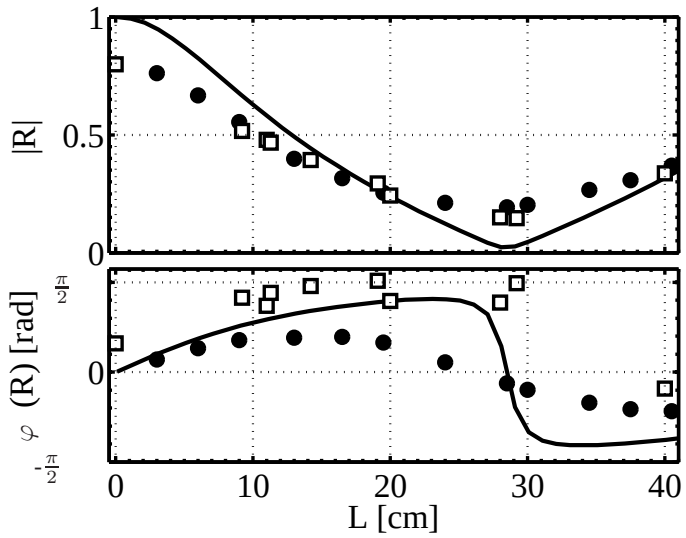

Figure 5.3: Comparison of the reflection coefficient measured inside the premixer at $f = 272$ Hz (white symbols) during firing operations, with model predictions (line) and measurements in an impedance tube at SPL=110 dB (black circles).

sound and thus results in a slightly reduced value of the reflection coefficient modulus. At the instability frequency, $f = 272$ Hz, on-the-fly measurements of the modulus of the reflection coefficient are reduced from $|R| = 0.8$ to $|R| = 0.15$ when the cavity depth is augmented from $L = 0$ to 28 cm. When the depth is increased beyond this value, the modulus increases again. These results are consistent with experimental data gathered in the impedance tube and

with the model predictions (figure 5.3). Evolutions of the modulus and phase are similar and the cavity depth minimizing the modulus of the reflection coefficient can be well predicted using either the model or the impedance tube data.
There is more dispersion on the phase φ of the reflection coefficient between the model predictions, the impedance tube data and the measurements in the combustion facility. Phase values corresponding to small values of the modulus are subjected to uncertainties because of poor signal to noise ratio obtained at these operating conditions in the combustion facility. Except for these points, the global trend of the phase is however correctly predicted. These tests indicate that the reflection coefficient can be accurately measured during hot-fire tests with a large broadband noise and validate the efficiency of the proposed system to pilot the premixer inlet acoustic boundary condition. It also validates the multiple possibilities of the impedance control system (ICS), which can be applied in cold flow and hot-fire setups. Extensive data obtained in the impedance tube can be used to estimate the cavity depth to be set in the combustion facility in order to impose a specific value of the reflection coefficient modulus in a desired frequency range.

The TMM was also implemented in a combustion setup of smaller power, where measured impedances were successfully compared to theoretical predictions. In the geometry depicted in figure 5.4, the objective is to measure the reflection coefficient $\mathrm{R}_{PF} = A^-/A^+$ of a system composed of a perforated plate and a set of laminar conical flames anchored to the plate. This system is now active, as flames may generate noise and thus may lead to reflection coefficients greater than one. The perforated plate has an high porosity (34%), with regularly spaced 2 mm-diameter apertures. A methane and air mixture is fed radially at the basis of a tube, above a loudspeaker which is used to modulate the acoustic field and impose the amplitude of velocity fluctuations at the perforations outlet, which are monitored by the hot wire probe located just below the perforated plate.

The reflection coefficient of the perforated plate has first been measured in a non reactive case, plotted in figure 5.5. The modulus remains below unity, and tends to decrease with frequency in a way similar to the response of an unflanged pipe. However the phase evolves with frequency with an almost $90^{\,\mathrm{o}}$ shift from 100 to 1000 Hz. The reflection coefficient measured by the TMM in the reactive case is then compared to a predictions obtained by Noiray (2007).
Measurements presented in figure 5.6a were obtained with a modulation level of $u_1/u_0 = 0.2$. Measurements of the reflection coefficient of the perforated plate inside the burner are very close to the predictions in terms of modulus and phase. It is shown in particular that the modulus is greater than one approximately between 500 and 800 Hz. A reflection coefficient greater than unity implies that flames reflect acoustic waves A^- with a larger amplitude than the incident perturbation A^+.
In figure 5.6b, the forcing amplitude is twice greater, $u_1/u_0 = 0.40$. Measurements extend to a wider frequency band than the model predictions. Experimental results are still in good agreement with the predictions in terms of modulus and phase. In this active configuration, the TMM was successful in retrieving the acoustic reflection coefficient.

The impedance control system (ICS) is now used to modify the premixer inlet boundary condition to analyze its influence on combustion instabilities. In the nominal unstable operating regime, well organized self-sustained oscillations of high amplitude are observed. Therefore

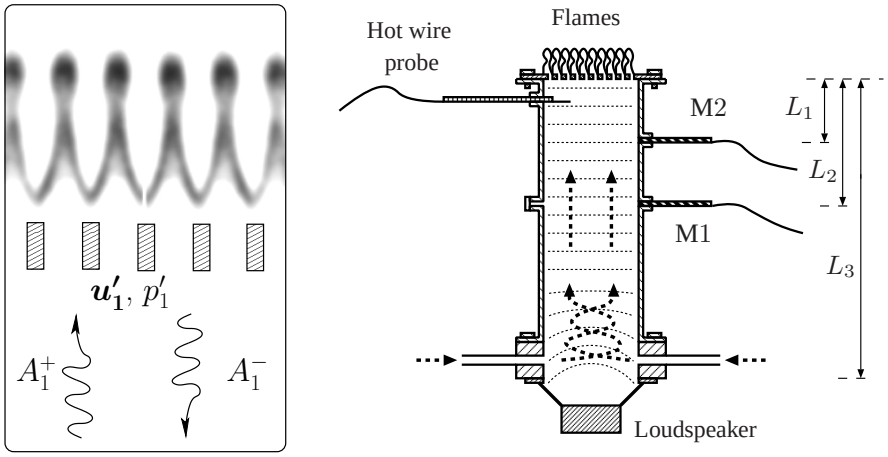

(a) Schematic view

(b) Experimental setup

Figure 5.4: (a) Schematic representation of the perforated plate - flames couple with annotations used to model the acoustic reflection coefficient R_{PF}. (b) Experimental setup used to measure the reflection coefficient R_{PF} of the perforated plate - flames couple. Courtesy of Noiray (2007).

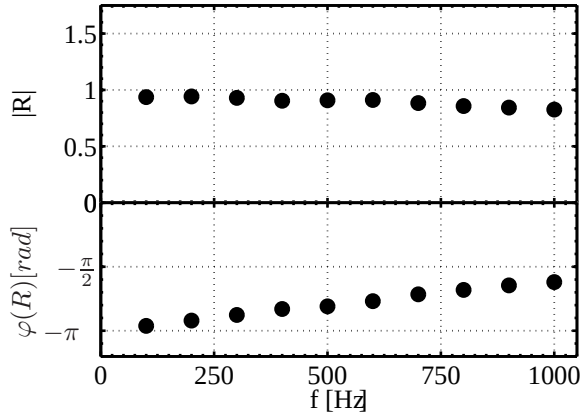

Figure 5.5: Acoustic reflection coefficient of the perforated plate of figure 5.4, in a non reactive case.

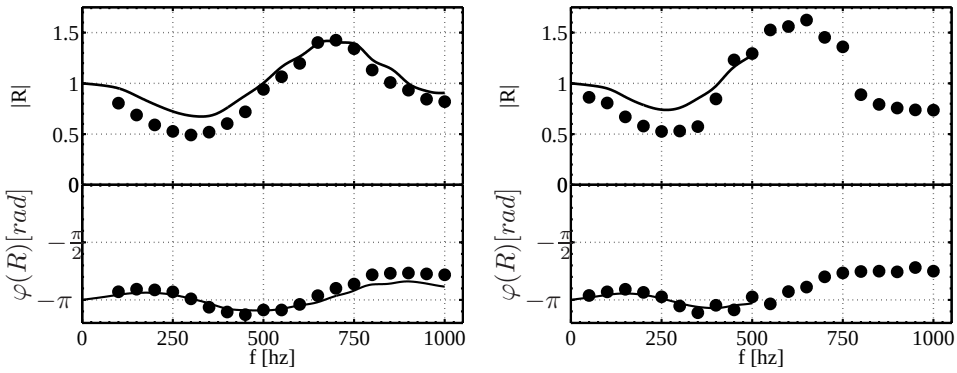

(a) $u_1/u_0 = 0.20$ (b) $u_1/u_0 = 0.40$

Figure 5.6: Comparison of the theoretical predictions (solid line) from the FTF model of Noiray (2007) with experimental data obtained by the TMM (circles) for the reflection coefficient of the perforated plate with anchored flames.

plate P4, which features a robust response to incident pressures up to 145 dB, is used for the main study. However the influence of the plate design is first illustrated, by using plate P8 instead of P4 at the rear side of the premixer.

5.2 Control of combustion instabilities with the ICS

5.2.1 Influence of the plate design: Plate P8

The acoustic investigation in the impedance tube has demonstrated that at low SPL, plate P8 and P4 feature similar behavior. The evolution with cavity depth of the reflection coefficient of the ICS equipped with either plate is quite similar at a given frequency, as illustrated in figure 5.7 for $f = 300$ Hz and a constant SPL of 110 dB. This investigation has also shown that plate P8 quickly reaches its non-linear response regime, for a SPL about 115 dB. Hot fire measurements of the reflection coefficient of the ICS with P8 were carried out and confirmed previous results: for a large SPL (around 140 dB), this plate exhibits a constant reflection coefficient whatever the cavity depth of the ICS, as plotted in figure 5.8.
Figure 5.9 presents the evolutions of the Power Spectral Densities (PSD) of the acoustic pressure in the premixer and in the chamber, along with the PSD of the heat-release rate, obtained for distinct back-cavity depths of the ICS. These depths were chosen using data measured in the impedance tube under a small SPL (110 dB), for which they correspond to three distinct reflection coefficient moduli : $|R| = 0.87$, 0.61 and 0.16, as illustrated in figure 5.7. During firing tests in the explored regime, the main instability peak is measured at $f = 300$ Hz and reaches 142 dB inside the premixer. This instability frequency is slightly different than that observed in the nominal regime ($f \simeq 270$ Hz). It is however associated to the fundamental mode of the premixer. These experiments were amongst the first conducted, and the combustion chamber had to be rebuild before conducting experiments with the ICS equipped with plate P4. It is observed that changing the ICS cavity depth does not affect the combustion instability significantly. This directly results from the fact that plate P8 features a quasi-constant

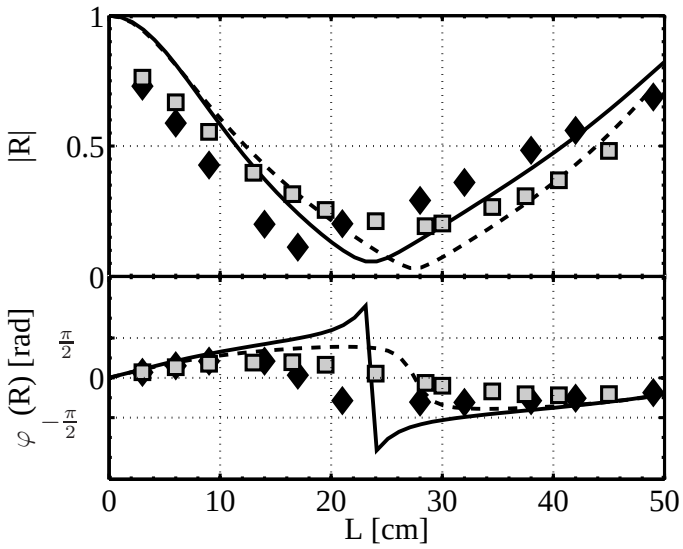

Figure 5.7: Evolution of the reflection coefficient with the cavity depth, for plates P4 (squares) and P8 (diamonds) for a SPL of $110\,\mathrm{dB}$. Data obtained in the impedance tube with a forcing frequency of $f = 300\,\mathrm{Hz}$ is compared with the linear model (dashed and solid lines for P4 and P8 respectively).

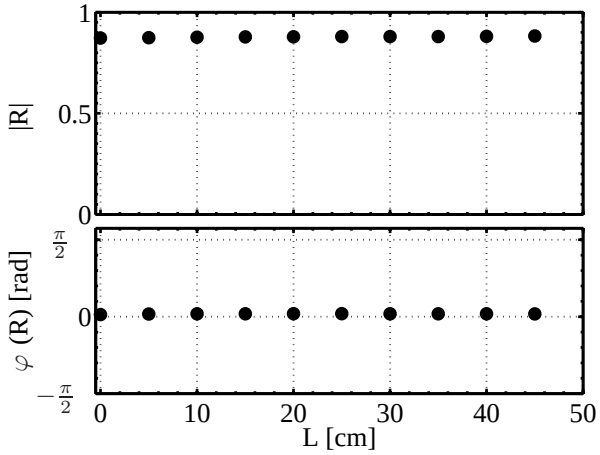

Figure 5.8: On-the-fly measurements, on the combustion rig, of the reflection coefficient of plate P8 for various cavity depths of the ICS and a SPL $\geq 140\,\mathrm{dB}$.

reflection coefficient at high SPL.
These results with plate P8 confirm that the perforate geometry is of key importance, as it defines the efficiency range in term of incident pressure fluctuation amplitude that can be damped. The investigation is from now on carried out with plate P4, which should be very robust to incident SPL.

5.2.2 Influence of the premixer inlet impedance

The ICS is used to control the modulus of the reflection coefficient at the oscillation frequency $f = 272$ Hz of the main instability using plate P4 at the rear side of the premixer. By varying the cavity depth of the ICS, the modulus of the reflection coefficient can be set to distinct values $|R| = 0.8, 0.65,$ and 0.25, measured at $f = 272$ Hz for SPL lower than 145 dB. A difference is observed between the dominant frequency measured with P8 and with P4. It has been checked that it is not due to the plate itself, but rather to the combustion chamber. Tests with P8 were realized with a combustion chamber that ended severely damaged and had to be rebuild for the tests with P4. As a consequence, the wear of the concrete plate, and the air tightness of the whole chamber are different between the tests and may account for a fraction of the frequency shift. Another source of frequency shift of about 4 to 8 Hz between tests was observed depending on the local weather conditions. This must also be taken into consideration in the interpretation of these differences.
Figure 5.10 shows the Power Spectral Densities (PSD) of the fluctuating pressure signals measured by the microphones M1 located inside the premixer, M5 located directly above the flame, and CH^* radical spontaneous emission measured by the PMT, in the arrangement shown in figure 5.1.

During these experiments, it was noticed that there is no significant effect of distinct moduli on the PSDs for frequencies higher than $f = 600$ Hz, which are thus not shown in the following figures. Setting the ICS back cavity depth to zero ($L = 0$ cm), combustion is strongly unstable and characterized by large coherent cyclic pulsations at $f = 272$ Hz. The unsteady flame motion is illustrated by the five consecutive snapshots ($\delta t = 160\,\mu$s) obtained by high speed tomography in figure 5.11.
This regime corresponds to the reference case (black line in fig. 5.10) obtained with $L = 0$ cm, characterized by a reflection coefficient modulus $|R| = 0.8$. A strong pressure peak is measured in the premixer and in the combustion chamber. In addition, a cyclic fluctuation of the light emitted by the flame is observed by the PMT, with a main frequency peak at $f_1 = 272$ Hz (figure 5.10, bottom). It is found that this frequency peak is also present in the signals measured by all microphones, confirming a strong acoustic-flame coupling. The fluctuations amplitude reaches 138 dB inside the premixer and 132 dB inside the combustion chamber. The first harmonic of the fundamental oscillation frequency is also present in the PSDs at $f_2 = 544$ Hz.
When the modulus $|R|$ is reduced to smaller values $|R| = 0.65$ and 0.25 by changing the ICS cavity depth, a large reduction of the amplitudes of the PSD is observed for almost all frequencies comprised between 0 and 600 Hz. The lower the reflection coefficient, the lower the fluctuations amplitude in the premixer and the chamber. This effect is emphasized at the main instability frequency $f_1 = 272$ Hz. In the premixer, the level drops down from 138 dB in the reference regime to 122 dB for $|R| = 0.65$ and to 109 dB for $|R| = 0.25$, corresponding to a damping of 29 dB. In the chamber, the nominal peak amplitude reaching 132 dB at $f_1 = 272$ Hz is lowered by 23 dB by the ICS when the modulus is reduced to $|R| = 0.25$. A

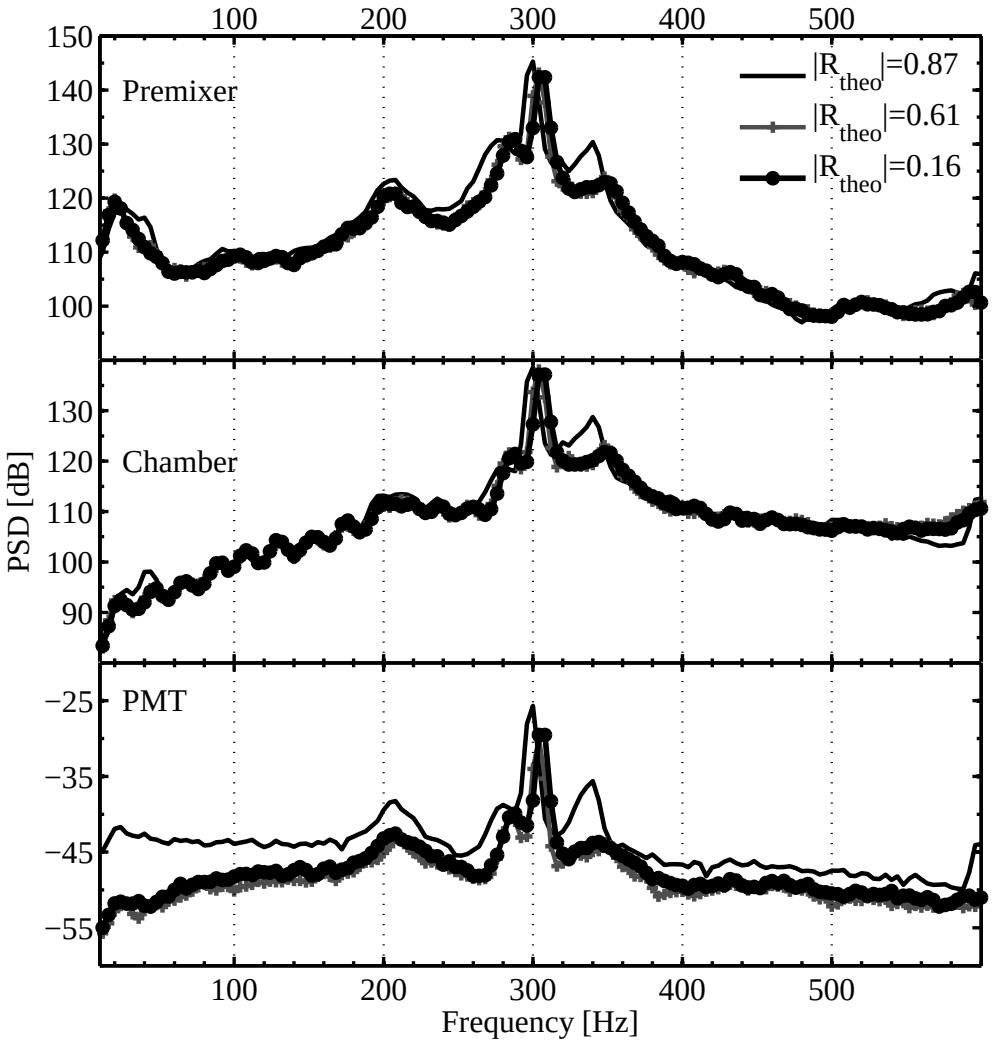

Figure 5.9: Power Spectral Densities (PSD) of the pressure signal recorded inside the premixer (top), inside the combustion chamber (center) and the CH^* fluctuations (bottom) for three different values of the reflection coefficient modulus of the ICS with P8. The theoretical values of reflection coefficient were measured for the frequency of the instability peak at $f = 300$ Hz in the impedance tube , for a SPL of 110 dB.

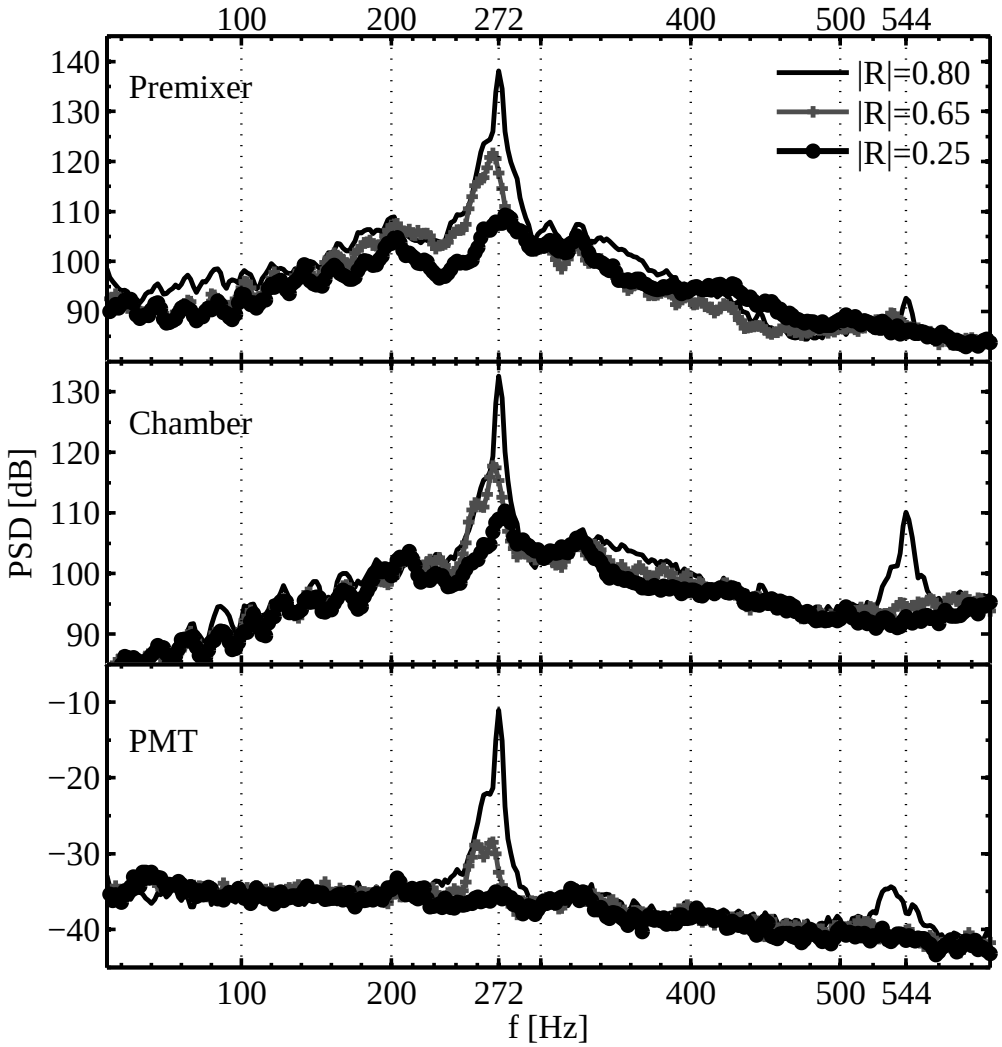

Figure 5.10: Power Spectral Densities (PSD) of the pressure signal recorded inside the premixer (top), inside the combustion chamber (center) and the CH^* fluctuations (bottom) for three different $|R|$. The reflection coefficient of plate P4 was measured on-the-fly at the instability frequency $f = 272$ Hz and matches data obtained for a SPL of 110 dB in the impedance tube.

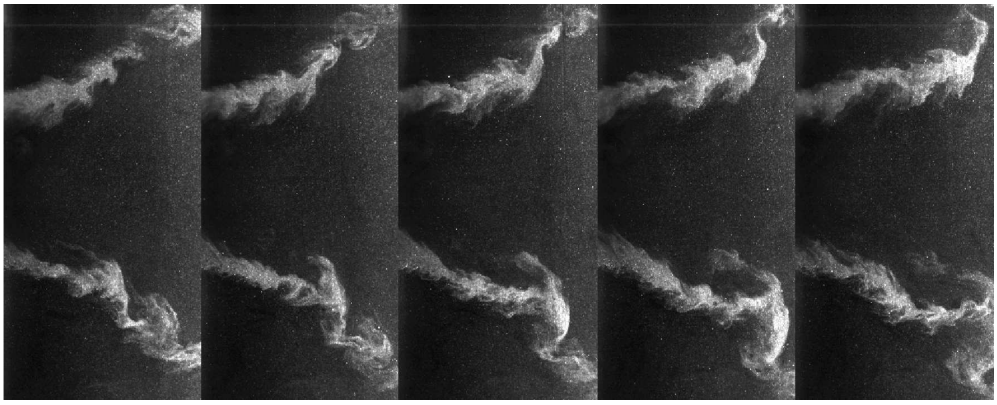

Figure 5.11: Five consecutive snapshots, obtained from high speed tomography, separated by $\delta t = 160\,\mu$s, in the nominal unstable regime. Sampling frequency is $f = 6250$ Hz.

24 dB reduction is also observed in the signal measured by the PMT when $|R|$ is decreased to 0.25. This attenuation effect is also visible for the harmonic at $f_2 = 544$ Hz, which is totally damped when $|R| \leq 0.65$. It should be noted that no resurgence of other frequencies is observed during these experiments, as sometimes observed with other passive control systems (see for example Noiray (2007)).
The amplitude of the PSD peaks of the fluctuating light emission (i.e. the heat-release rate) and pressure signals, measured in the system, is thus directly controlled by the value imposed to the modulus of the premixer inlet reflection coefficient. In the most favorable case, corresponding to $|R| = 0.25$, the initial instability at $f = 272$ Hz is completely damped when using the ICS with a back-cavity depth of 28 cm. This result highlights the importance of the acoustic boundary conditions on the flame-acoustic coupling. It also stresses the sensitivity of the flame to perturbations originating from the fresh reactants zone.

5.3 Analysis of the acoustic energy balance

The influence of the premixer impedance on the amplitude of both the pressure and heat-release rate fluctuations has been described in the previous section. This effect is now examined by considering the balance of acoustic energy. This requires an evaluation of the Rayleigh source term and of the acoustic fluxes crossing the boundaries. The local balance of acoustic energy density, $e = p_1^2/(2\rho_0 c_0^2) + \rho_0 u_1^2/2$, may be cast in the form:

$$\frac{\partial e}{\partial t} + \nabla \cdot (p_1 \mathbf{u_1}) = \frac{\gamma - 1}{\gamma p_0} p_1 \dot{q}_1 \tag{5.1}$$

where p_1, u_1 and $\dot{q}_1$ designate the acoustic pressure, acoustic velocity and heat-release rate fluctuations respectively. Assuming a combustor of volume V delimited by a surface Σ, undergoing combustion oscillations with a period of oscillation $T = 2\pi/\omega$, this expression can be integrated over the whole volume and over a period of oscillations to obtain:

$$\left\langle \frac{\partial E}{\partial t} \right\rangle_T = \left\langle \int_V \frac{\gamma - 1}{\gamma p_0} p_1 \dot{q}_1 dv \right\rangle_T - \left\langle \int_\Sigma p_1 \mathbf{u_1} \cdot \mathbf{n} d\sigma \right\rangle_T \tag{5.2}$$

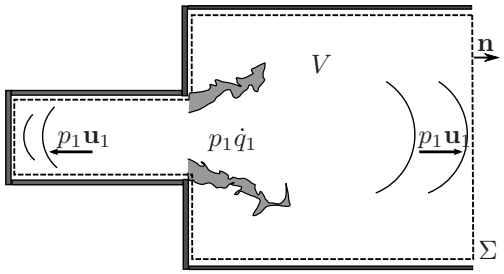

Figure 5.12: Illustration of the source term and acoustic fluxes.

where $\langle x \rangle_T = 1/T \int_0^T x dt$ and E is the acoustic energy integrated over the whole combustor. The unit vector $\mathbf{n}$ is normal to the surface Σ, directed toward the outside of this surface.
At the limit cycle, there is no more variation of the acoustic energy: $\left\langle \frac{\partial E}{\partial t} \right\rangle_T = 0$ and the r.h.s terms are expected to be in balance. The acoustic source term $\mathcal{S}$ is counterbalanced by the acoustic fluxes Φ_{ac} at the boundaries of the combustor. When acoustic-structure interactions are negligible, acoustic fluxes at the combustor walls are null ($\mathbf{u_1} \cdot \mathbf{n} = 0$). This is not the case at at the inlet (1) and outlet sections (2). As a result equation 5.2 reduces to a balance between the source term $\mathcal{S} = \left\langle \int_V \frac{\gamma-1}{\gamma p_0} p_1 \dot{q}_1 dV \right\rangle_T$ and the acoustic fluxes at the combustor terminations $\Phi_{ac} = \left\langle \int_\Sigma p_1 \mathbf{u_1} \cdot \mathbf{n} d\Sigma \right\rangle_T$:

$$\mathcal{S} = \Phi_{ac}^1 + \Phi_{ac}^2 \tag{5.3}$$

In this expression, Φ_{ac}^1 designates the acoustic flux at the premixer inlet and Φ_{ac}^2 at the combustion chamber exhaust.

5.3.1 Evaluation of the Rayleigh source term

The Rayleigh source term appears as the only source of acoustic energy. In the chapter dedicated to optical measurements of the heat-release rate (chapter 2), it has already been shown that under certain assumptions (perfect premixing, lean regime) it is possible to estimate this source term quantitatively with photomultiplier tubes. PMT provide integrated measurements of the light emission from the flame which is proportional to the heat-release rate. Capital letter $\dot{Q}$ indicates the volume integrated value of the unsteady heat-release rate $\dot{q}$, and I is the associated integrated light emission collected by the PMT. Assuming that all fuel is burnt, the mean heat release rate $\dot{Q}_0$ can be estimated from the fuel massflow rate and the fuel heating value: $\dot{Q}_0 = \dot{m}_f \Delta h_f^0$. The Rayleigh source term can be expressed as:

$$\mathcal{S} = \frac{\gamma - 1}{\gamma p_0} \dot{m}_f \Delta h_f^0 \frac{\langle p_1 I_1 \rangle_T}{I_0} \tag{5.4}$$

The cross-spectral density CPSD ($P_{p,I}$) is computed between the pressure fluctuations measured by microphone M5 and the heat-release rate fluctuations measured by the PMT. In the reference case ($|R| = 0.8$), there is a strong correlation between these two quantities at the instability frequency $f = 272\,\text{Hz}$. The phase of the CPSD equals $-60\,^{\text{o}}$. The qualitative Rayleigh criterion states that combustion instabilities may occur when the phase of the cor-

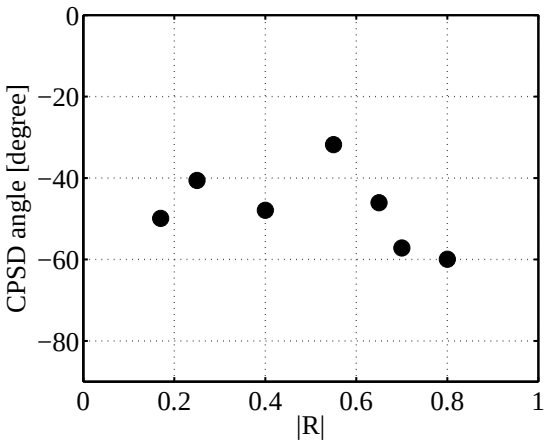

Figure 5.13: Evolution of the phase of the CPSD between the pressure and heat-release rate at the instability frequency, with the reflection coefficient, for plate P4.

relation lies between -90 and $+90\,^{\circ}$. The cross-spectral density confirms that the main instability frequency results from a flame-acoustic coupling, and that it satisfies the qualitative Rayleigh criterion.
The influence of the premixer inlet impedance on the phase of this CPSD, at the main instability peak, is presented in figure 5.13. There is little influence of the premixer inlet impedance on this phase, which remains low, around $45\,^{\circ}$.
As it has little effect on the phase of the pressure to heat-release rate correlation, the ICS does not seem to act on the flame-acoustics phase matching condition, but rather on the level of the acoustic fluxes. The reduction of these fluxes may damp the fluctuation levels inside the chamber and the premixer, which in turn attenuates the instability.

5.3.2 Acoustic fluxes and energy balance

The ICS barely affects the phase coupling between the unsteady heat-release rate and pressure fluctuations. The amplitudes of different terms appearing in the acoustic energy balance (eq. 5.4) can be evaluated at the instability frequency, and compared for different premixer inlet impedances. It was shown in chapter 2 that the constants in the Rayleigh source term formulation can be experimentally evaluated to determine this term quantitatively in Watts. The protocol to obtain the acoustic fluxes from pressure measurements located at x_1 and x_2 respectively was also presented in chapter 3:

$$\mathcal{S} = \frac{\gamma-1}{\gamma p_0}\dot{m}_f \Delta h_f^0 \frac{\langle p_1 I_1\rangle_T}{I_0} \tag{5.5}$$

$$\Phi_{ac} = \frac{\mathrm{Im}(P_{p_1(x_1),p_1(x_2)})}{2\rho_0\omega\delta x}\Sigma \tag{5.6}$$

where $P_{p_1(x_1),p_1(x_2)}$ designates the cross spectral density between two pressure measurements from microphones separated by a distance $\delta x = x_2 - x_1$. In the control surface Σ between these two sensors, there should be no source term and the acoustic field must be one-

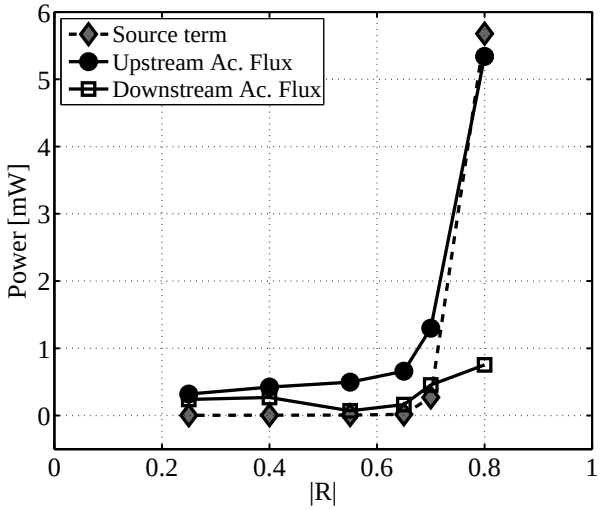

Figure 5.14: Evolutions of the acoustic fluxes (solid lines) in sections S_1 (circles) and S_2 (squares) and of the source term (diamonds) with the modulus $|R|$ of the premixer inlet reflection coefficient.

dimensional. The acoustic fluxes were thus evaluated in the premixer, upstream of the flame region, and at the chamber exhaust, in the hot combustion products.

The estimates of the source term and acoustic fluxes are plotted in figure 5.14 for different values of the modulus $|R|$ of the reflection coefficient. As already mentioned, the reference case corresponding to a "hard "reflection condition $|R| = 0.8$ is obtained for a cavity depth set to zero ($L = 0$ cm) and corresponds to the unstable regime with a strong oscillation peak at $f = 272$ Hz. When the cavity length L is increased, the modulus of the reflection coefficient $|R|$ is reduced at the premixer inlet. As a consequence, the inlet premixer and burner outlet acoustic fluxes, Φ^1_{ac} and Φ^2_{ac}, are modified. Except when the inlet reflection coefficient takes small values ($|R| = 0.25$) where both fluxes are of the same order, the inlet flux always exhibits larger values than the outlet flux, $\Phi^1_{ac} > \Phi^2_{ac}$. This result was expected, since the burner outlet corresponds to a nearly open acoustic termination. In this situation, the acoustic flux would be zero for a zero mean flow. The outlet flux remains small $\Phi^2_{ac} \sim 0$ except for highly unstable regimes ($|R| = 0.8$), where large structures may be convected outside the burner and produce perturbations of the outlet acoustic flux. Such results confirm the predominant role of the premixer inlet acoustic boundary condition in this burner. Acoustic fluxes $\Phi_{ac} = \Phi^1_{ac} + \Phi^2_{ac} \simeq \Phi^1_{ac}$ remain essentially controlled by the inlet premixer impedance $Z_1 = (1+R)/(1-R)$ which determines $\Phi^1_{ac} = 1/(\mathrm{Re}[Z_1]) \left(p^1_{rms}\right)^2 S_1$, where p^1_{rms} is the root mean square pressure fluctuation at the plane location S_1.
The source term $\mathcal{S}$ which feeds acoustic energy into the system is now examined. It takes vanishingly small values for premixer inlet reflection coefficient moduli lower than $|R| < 0.65$ and notably increases for larger values of $|R|$. The global trend corresponds to the one observed for the inlet flux, $\mathcal{S} \sim \Phi^1_{ac}$. It was observed in figure 5.10 that a minimal reflection coefficient led to a suppression of the instability at $f = 272$ Hz. This is confirmed by the global evolution of $\mathcal{S}$. With some caution due to the crude assumptions used for these esti-

mations, a quantitative analysis may also be carried out. The production of acoustic energy $\mathcal{S} > \Phi^1_{ac}$ exceeds the inlet flux only for $|R| = 0.8$ and remains lower $\mathcal{S} < \Phi^1_{ac}$ for lower values $|R| < 0.75$. The unbalanced difference $\Phi^1_{ac} - \mathcal{S}$ can be significant. This might be attributed to non linear phenomena of exchange of acoustic energy to other frequencies, which might explain the larger value $\mathcal{S} > \Phi^1_{ac}$ for $|R| = 0.8$ with a transfer of acoustic energy from the fundamental $f_1 = 272$ Hz to the first harmonic at $f_2 = 544$ Hz (figure 5.10). Terms neglected in the acoustic budget might also partly explain this difference.
Modifying the premixer inlet acoustic boundary condition can be used to control the acoustic flux incident on the flame from the burner inlet. This may also affect the acoustic flux at the burner exhaust, but only for highly unstable regimes. As the burner is open to atmospheric conditions, the stability of this turbulent combustor is solely controlled by the premixer inlet boundary condition. Controlling this boundary condition is an efficient way to control combustion instabilities in this system because (1) the inlet acoustic flux is entirely viewed by the flame (2) intense acoustic fluxes can be concentrated on a small section area (3) flames are known to be very sensitive to slight modifications of dynamics of the fresh reactive flow. Without any apparent effect on the coupling mechanism itself, as the heat-release rate and acoustic pressure fluctuations remain in phase, the oscillation level can be significantly lowered to prevent the onset of oscillations.

5.4 Control of different combustion regimes

All the results presented in this report were obtained in the nominal regime, which was well documented by Dioc (2005). Investigations were yet lead in other regimes, in terms of equivalence ratio, fuel staging or thermal power. The ICS is a robust solution that can efficiently limit the growth of combustion instabilities as long as they are (1) controlled by the flame-acoustic coupling and (2) sensitive to modifications of the premixer acoustics. A second example of such a self-sustained regime, in addition to the reference case, is now presented. For a fuel staging of $\alpha = 32\%$, an equivalence ratio $\Phi = 0.72$ and a thermal power of $29\,$kW, the control system equipped with P4 was used to damp the combustion instability that occurs in these operating conditions. Figure 5.15 presents the evolution of the PSD for the pressure and heat-release fluctuations. The ICS allows a reduction of $20\,$dB in the premixer and $12\,$dB in the chamber and totally damps this instability. This was checked for many other regimes by varying the three control parameters.

There are however other types of unstable regimes for which the ICS cannot damp the main instability. In these regimes, the instability arises at frequencies very close to those associated with the rotation of the precessing vortex core, i.e. around $330 - 350\,$Hz. The fundamental mode associated with the chamber length is also expected around $f = 326\,$Hz (see chapter 6). An example of such regime is plotted in figure 5.16. This regime corresponds to a staging of $\alpha = 50\%$, a fuel equivalence ratio of $\Phi = 0.87$ and a thermal power of $35\,$kW. It is strongly unstable, with a self-sustained oscillation occurring at $f = 336\,$Hz. In this configuration, acting on the premixer inlet impedance has almost no effect on the instability, except a slight shift of the main instability peak.

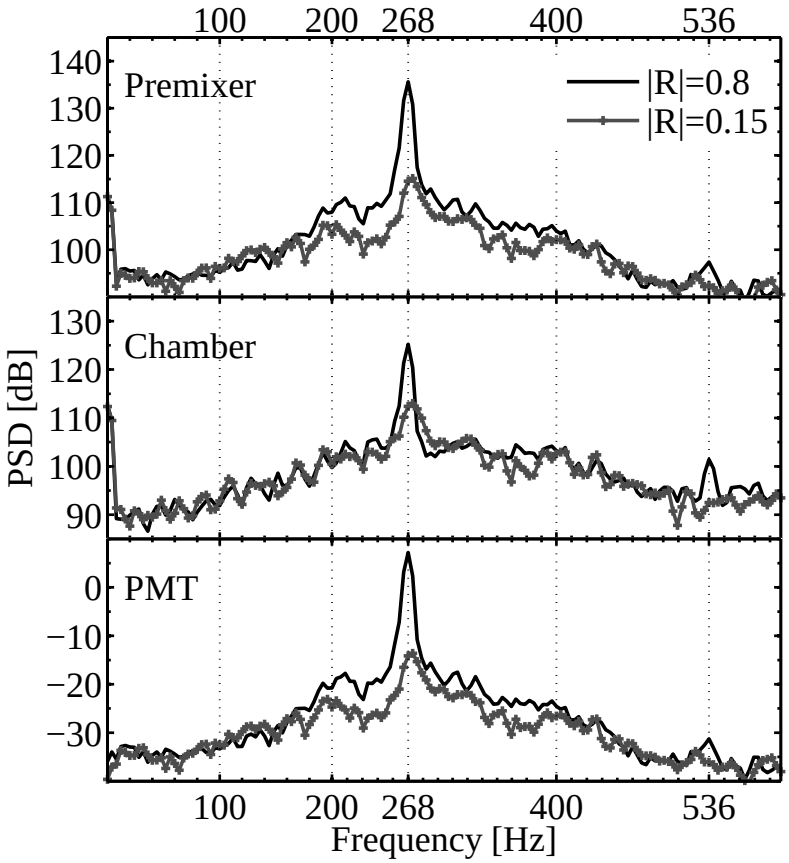

Figure 5.15: PSD of the pressure signal and the CH^* fluctuations for two different $|R|$ of plate P4 for a staging of $\alpha = 32\%$, an equivalence ratio $\Phi = 0.72$ and a thermal power of $29\,\mathrm{kW}$.

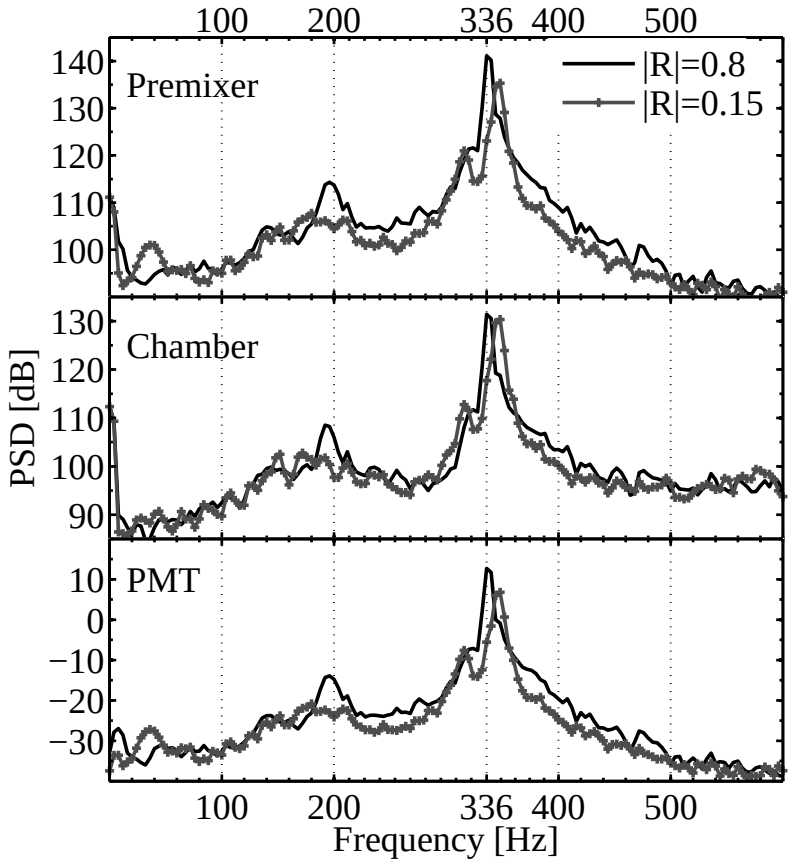

Figure 5.16: PSD of the pressure signal and the CH^* fluctuations for two different $|R|$ of plate P4 for a staging of $\alpha = 50\%$, an equivalence ratio $\Phi = 0.87$ and a thermal power of $35\,\mathrm{kW}$.

Concluding remarks

This chapter is concerned with the implementation of the impedance control system (ICS) on the combustion rig. It is first shown that the two-microphone method (TMM) can be applied to reactive configurations to measure impedances. The impedance of the ICS, obtained in combustion, was successfully compared to data obtained with acoustic forcing in the impedance tube and to theoretical predictions. The TMM was also applied to another facility to measure the impedance of active elements. Results were again in agreement with model predictions.
Then the ICS was used to impose various acoustic boundary conditions at the premixer inlet of the combustion rig experiencing strong self-sustained combustion oscillations. Imposing low moduli of the premixer inlet reflection coefficient efficiently damps these thermoacoustic oscillations, reducing their amplitude by 20 dB in the premixer and 10 dB in the combustion chamber. Further study of the phase of the acoustic to heat-release rate correlation shows little influence of the ICS. An acoustic energy balance is finally estimated, taking into account the Rayleigh source term and the acoustic fluxes at the premixer inlet and at the chamber outlet. It is shown that the acoustic flux in the premixer is of the same order of magnitude as the Rayleigh source term, and can even overcome this source, reducing hitherto the level of oscillations. In the nominal regime, the ICS is an effective control solution that can almost cancel the main combustion instability. This is achieved when the outgoing energy flux in the premixer matches the level of the Rayleigh source term, and when the flame is essentially sensitive to perturbations in the fresh reactants,and also to the structure of the acoustic field in the premixer.
Further investigation is led in the following chapter to determine the origin of the main unstable mode, along with the structure of the pressure distribution in the combustion rig.

Chapter 6

Characterization of the combustion rig acoustics

The swirled burner features a set of unstable combustion modes below 1 *kHz. The oscillation frequency depends on the flow regime and the thermal power. It was shown that when the oscillation frequency is lower than* 300 *Hz, the acoustic-combustion coupling is very sensitive to acoustic losses at the premixer inlet. However, when the instability frequency lies around* 340 *Hz, a modification of the premixer inlet acoustic boundary condition has almost no influence on this self-sustained oscillation. It is thus valuable to analyze the acoustic modal structure of the combustion facility to determine the frequencies associated with the main modes. A one-dimensional acoustic model of the burner geometry is first presented in section 6.1. It consists in a coupled cavity problem where the first cavity represents the premixer and the second corresponds to the combustion chamber. It takes into account the influence of the premixer inlet acoustic boundary condition and of the section discontinuity between the cavities. The influence of a temperature difference between the cavities is also envisaged. This analysis provides asymptotic solutions in limiting cases, and allows a parametric investigation when solved numerically. The acoustic response of the combustion rig is then characterized experimentally in non-reactive configurations using a frequency sweeping method and the pressure distribution is compared with the theoretical modes (section 6.2). The influence of the premixer feeding lines on the modal structure is also considered. The acoustic response of the burner in the reference reactive case is then investigated in section 6.3. Finally, the structure of the main instability mode is reconstructed from pressure measurements throughout the facility and compared to the proposed model predictions.*

Foreword: Specific notations are introduced in this chapter to designate acoustic eigenfrequencies of the n-th eigenmode obtained by different means. These notations are introduced within the text. However they are all gathered here as a specific nomenclature to ease the reading.

- f_P^n and f_C^n designate theoretical asymptotic solutions based on the premixer and combustion chamber lengths respectively. $f_P^n = (2n+1)c_P/4L_P$ and $f_C^n = (2n+1)c_C/4L_C$,

- f^n_{PC} designate theoretical eigenfrequencies of the coupled-cavities (premixer-chamber) modes,
- f^n_{rig} designates peak frequencies measured in the combustion rig, in isothermal non-reactive experiments.

6.1 Acoustic analysis of the modal structure of the combustion rig

A one-dimensional model of the combustion rig is developed that takes into account the premixer inlet impedance, the influence of the area expansion ratio between the premixer and the chamber and of the temperature change on the modal structure for longitudinal acoustic waves. The objective is first to analyze the distribution of the eigenfrequencies and the structure of the associated modes in the combustion facility. A second objective is to investigate modifications induced by the presence of the feeding lines and by the presence of the hot gases produced by combustion.

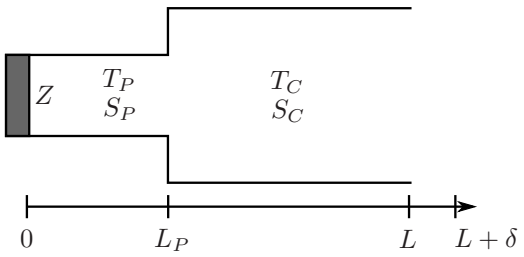

Figure 6.1: Acoustic model of the combustor composed of two cylinders with distinct physical properties and cross-sections. P denotes the premixer and C the combustion chamber.

The combustor is decomposed into two one-dimensional elements, the premixer tube and the combustion chamber, labelled by the P and C subscripts respectively (figure 6.1). The premixer length is $L_P = 23.5\,\text{cm}$ and the combustor's is $L_C = 49\,\text{cm}$ corresponding to a total length $L = L_P + L_C = 72.5\,\text{cm}$. The system is bounded by an acoustic impedance $Z(x = 0^+) = Z$ at the premixer inlet, which models the ICS effect and by the atmospheric pressure p_a at the chamber outlet $p(x = L + \delta) = p_a$, where δ is the end-correction for a flanged pipe (Ingard 1953). For low Mach flow numbers, this can be modelled by $\delta = 8r/3\pi \simeq 0.85r$, where r is the pipe radius. The chamber has a square section of $10\,\text{cm}$ breadth. Assuming an equivalent circular surface area results in an end-correction $\delta \approx 4\,\text{cm}$. To simplify notations, this end-correction is added to the chamber length in the following developments: $L_C = L_C + \delta$, resulting in an updated total combustor length $L \simeq 76.5\,\text{cm}$. The premixer and the chamber feature distinct geometries and are fed with gases with different properties. The premixer has a complex geometry with several radial manifolds for air and propane and an external plenum, which may influence the acoustics. These connections are not taken into account in the present model and the premixer is modelled by a pipe of radius $r_P = 1.5\,\text{cm}$ and a cross-section S_P where air has a temperature T_P and a celerity c_P. The chamber is a rectangular duct of square section S_C with a breadth l_C where air has a temperature $T_C \geq T_P$ and a celerity $c_C \geq c_P$. In this simple acoustic model, only air is considered and the effect of combustion is modelled by a temperature difference between the

fresh reactants at T_P and the burnt gases at T_C. The air characteristic impedance is defined by $Z_P = \rho_P c_P$ in the premixer and $Z_C = \rho_C c_C$ in the chamber.

Pressure p and velocity u are decomposed into mean (p_0, u_0) and fluctuating (p_1, u_1) components. Harmonic decomposition is applied to the fluctuating part such that $p_1(x,t) = \mathrm{Re}\left(\hat{p}(x)\,\mathrm{e}^{-i\omega t}\right)$, where Re is the real part of the complex number in parenthesis.
The influence of the mean flow is assumed to be negligible as the flow Mach number $M = u/c_0$ remains small. An estimation of the velocity based on PIV measurements indicates a maximum value of about 30 ms^{-1}, resulting in a flow Mach number $M \simeq 0.09$ at the premixer inlet and an attenuation factor of $1 - \sqrt{1-M^2} = 0.38\%$ (Munjal 1987). This attenuation is not taken into account in what follows.

The cut-off frequencies, below which only plane waves propagate, for a cylindrical duct of radius r_P and for a rectangular duct of larger side dimension l_C are respectively given by:

$$f_{cut,P} = \frac{1.84 c_P}{\pi r_P} \tag{6.1}$$

$$f_{cut,C} = \frac{c_C}{2 l_C} \tag{6.2}$$

In the chamber, plane wave propagates below $f_{cut,C} = 1710\,\mathrm{Hz}$ for cold gases at $T_C = 300\,\mathrm{K}$ and $f_{cut,C} = 3882\,\mathrm{Hz}$ for hot gases at $T_C = 1500\,\mathrm{K}$. In the premixer where reactants remain at $T_P = 300\,\mathrm{K}$ the cut-off frequency limit is $f_{cut,P} = 6676\,\mathrm{Hz}$. For the low frequencies of interest in this study, i.e. below 1 kHz, only plane waves must be considered. A plane wave decomposition into forward and backward traveling waves leads to:

$$\hat{p}_P(x) = A^+\,\mathrm{e}^{ik_P x} + A^-\,\mathrm{e}^{-ik_P x} \tag{6.3}$$

$$Z_P \hat{u}_P(x) = A^+\,\mathrm{e}^{ik_P x} - A^-\,\mathrm{e}^{-ik_P x} \tag{6.4}$$

$$\hat{p}_C(x) = B^+\,\mathrm{e}^{ik_C(x-L_P)} + B^-\,\mathrm{e}^{-ik_C(x-L_P)} \tag{6.5}$$

$$Z_C \hat{u}_C(x) = B^+\,\mathrm{e}^{ik_C(x-L_P)} - B^-\,\mathrm{e}^{-ik_C(x-L_P)} \tag{6.6}$$

The wavefield must comply with the boundary conditions at the premixer inlet and chamber outlet, along with the continuity of pressure and volume flow rate fluctuations at the junction between the two sections:

$$Z = Z(x=0) = \hat{p}_P(0)/\hat{u}_P(0) \tag{6.7}$$

$$\hat{p}_C(L) = 0 \tag{6.8}$$

$$\hat{p}_P(L_P) = \hat{p}_C(L_P) \tag{6.9}$$

$$S_P \hat{u}_P(L_P) = S_C \hat{u}_C(L_P) \tag{6.10}$$

where the inlet impedance Z is characterized by the reflection coefficient $R = (Z/Z_P - 1)/(Z/Z_P + 1)$. The outlet condition corresponds to a pressure node because the chamber is open to the quiescent atmosphere.

Non trivial solutions for this set of equations are determined by the characteristic polynomial:

$$\begin{aligned}\mathcal{D} &= (1+\Xi)\left[\mathrm{e}^{i(k_P L_P + k_C L_C)} + R\,\mathrm{e}^{-i(k_P L_P + k_C L_C)}\right] \\ &+ (1-\Xi)\left[\mathrm{e}^{i(k_P L_P - k_C L_C)} + R\,\mathrm{e}^{-i(k_P L_P - k_C L_C)}\right] \end{aligned} \tag{6.11}$$

where the parameter Ξ takes into account the influence of the area expansion ratio and of the temperature difference between the premixer and the combustion chamber:

$$\Xi = \frac{S_P Z_C}{S_C Z_P} = \frac{S_P \bar{\rho}_c c_c}{S_C \bar{\rho}_p c_p} = \frac{S_P}{S_C}\sqrt{\frac{T_P}{T_C}} \tag{6.12}$$

The roots of the dispersion relation $\mathcal{D} = 0$ yield the eigenfrequencies as functions of the parameter Ξ, the system lengths L_P and L_C and the reflection coefficient R at the premixer inlet. The corresponding pressure distributions define the acoustic modes of the system. Assuming a forward pressure amplitude $A^+ = 1$, it is then possible to determine the structure of the acoustic pressure in the premixer and the combustion chamber:

$$\hat{p}_P(x) = \mathrm{e}^{ik_P x} + R\,\mathrm{e}^{-ik_P x} \tag{6.13}$$

$$\begin{aligned}\hat{p}_C(x) &= \frac{1}{2}\left[(1+\Xi)\left[\mathrm{e}^{i(k_P L_P + k_C(x-L_P))} + R\,\mathrm{e}^{-i(k_P L_P + k_C(x-L_P))}\right]\right. \\ &+ \left.(1-\Xi)\left[\mathrm{e}^{i(k_P L_P - k_C(x-L_P))} + R\,\mathrm{e}^{-i(k_P L_P - k_C(x-L_P))}\right]\right]\end{aligned} \tag{6.14}$$

It is straightforward to check that equations 6.13 and 6.14 satisfy the set of boundary conditions 6.7 - 6.10.

The dispersion relation $\mathcal{D} = 0$ can be solved analytically in some cases where Ξ takes vanishing small values, which are first considered. The influence of the parameter Ξ on the modal structure is then investigated numerically.

6.1.1 Modal structure of the acoustic pressure in the CTRL-Z combustor

The dispersion relation is solved for a set of conditions corresponding to:

- Two constant values of the premixer inlet reflection coefficient,
  1. A perfectly reflecting inlet $R = 1$, where the relation 6.11 simplifies to :

$$\cos(k_P L_P)\cos(k_C L_C) - \Xi \sin(k_P L_P)\sin(k_C L_C) = 0 \tag{6.15}$$

  2. An anechoic inlet $R = 0$, where this relation becomes:

$$\cos(k_C L_C) - i\Xi \sin(k_C L_C) = 0 \tag{6.16}$$

- Two temperature distributions,
  1. The case of a uniform temperature in the system at $T_P = T_C = 300\,\mathrm{K}$ for which the parameter Ξ equals the area ratio, $\Xi = S_P/S_C$. This corresponds to the non-reactive configurations explored
  2. The case where the premixer reactants are fresh at $T_P = 300\,\mathrm{K}$ and the combustion chamber is filled with uniform hot gases at $T_C = 1500\,\mathrm{K}$. This case approximates the nominal reactive configuration, where $\Xi = 0.44 S_P/S_C$.

- Two expansion ratio between the premixer and the chamber cross-sections,
  1. A single tube of length L comprising the premixer and the chamber with a constant section, $S_P = S_C$. This configuration is used to validate the dispersion relation 6.11.
  2. The second configuration explored fits the expansion ratio between the premixer inner channel and the chamber of the actual combustion rig, $S_P/S_C = 0.07 \ll 1$.

The different expressions obtained for the eigenfrequencies are gathered in table 6.1, where Ξ takes vanishing small values. Numerical values for the two first eigenfrequencies f^0 and f^1 are computed in each case. The combustion chamber temperature is taken equal to $T_C = 1500\,\mathrm{K}$ in the reactive case. The flame temperature for a propane air mixture equivalence ratio of $\Phi = 0.8$ is about $1800\,\mathrm{K}$. Flame was shown to be compact (chapter 2) and extends at a maximum of $10\,\mathrm{cm}$ inside the $50\,\mathrm{cm}$ long combustion chamber. Measurements with a thermocouple in the last section of the chamber were performed in the reactive configuration. The temperature of the hot gases in this region was found about $T_C \simeq 1300\,\mathrm{K}$. A temperature of $1500\,\mathrm{K}$ appears as a reasonable good average for the following calculations in reactive cases.

The case of a single closed-open tube of length $L = L_P + L_C$ (table 6.1, A1), is used to check the validity of the general form of the dispersion relation $\mathcal{D} = 0$ and serves as a reference case. Eigenfrequencies take in this case the classical form of quarterwave modes ($f_L^n = (2n+1)c/4L$). In the case of an anechoic inlet (table 6.1, A2), any frequency propagates freely in the pipe.

The actual burner geometry features an important area expansion ratio $S_P/S_C \ll 1$ between the premixer and the chamber, leading to small values of Ξ independently of the temperature distribution (cases B1 to B4).

- With a fully reflective inlet $R = 1$ and a uniform temperature distribution (B1), eigenfrequencies are decoupled and can be associated either with the premixer length L_P ($f_P^n = (2n+1)c/4L_P$) or with the chamber length L_C ($f_C^n = (2n+1)c/4L_C$). Theses eigenfrequencies correspond to quarterwave modes associated with each element separately considered as isolated closed-open tubes, which are obtained when Ξ takes vanishing small values. It is shown that the two first eigenmodes feature well separated eigenfrequencies: $f_C^0 = 163\,\mathrm{Hz}$ and $f_P^0 = 369\,\mathrm{Hz}$ when both temperatures are equal, $T_P = T_C = 300\,\mathrm{K}$. When $T_C = 1500\,\mathrm{K}$ and $T_P = 300\,\mathrm{K}$, these eigenfrequencies are $f_C^0 = 364\,\mathrm{Hz}$ and $f_P^0 = 369\,\mathrm{Hz}$.
- When the premixer inlet features an anechoic termination $R = 0$, corresponding to cases B3 and B4, the system acoustics behave like an open pipe (the premixer) connected to a very large volume (the chamber). As a consequence, any frequency may propagate freely in the premixer tube and there is no modal structure associated with the premixer length. The eigenfrequencies are those of the combustion chamber, which are of quarterwave type. Their frequencies are a function of the sound celerity and therefore of the gas temperature T_C, $f_C^n = (2n+1)c_C/4L_C$ with $c_C = \sqrt{\gamma r T_C}$.

This acoustical analysis shows that the eigenfrequencies of the combustor are linked to quarterwave modes associated either with the premixer or to the combustion chamber length in the limit cases of small values of the parameter Ξ. With a fully reflective premixer inlet ($R = 1$), the modal structure is a combination of the quarterwave modes of the premixer and of the chamber. When the inlet is replaced by an anechoic termination ($R = 0$), only quarterwave modes of the chamber remain. The presence of hot gases in the chamber raises the sound celerity and thus increases the eigenfrequencies of the chamber to values close to those of the premixer.

-	R	$T[\mathrm{K}]$	Ξ	$\mathcal{D}$	$f^n[\mathrm{Hz}]$	$f^0[\mathrm{Hz}]$	$f^1[\mathrm{Hz}]$
A1	1	$T_P = T_C = 300$	1	$\cos kL$	$f_L^n = (2n+1)\frac{c}{4L}$	$f_L = 113$	339
B1	1	$T_P = T_C = 300$	$\ll 1$	$\cos kL_P \cos kL_C$	$f_P^n = (2n+1)\frac{c}{4L_P}$	$f_P^0 = 369$	
					$f_C^m = (2m+1)\frac{c}{4L_C}$	$f_C^0 = 163$	$f_C^1 = 489$
B2	1	$T_P = 300$	$\ll 1$	$\cos k_P L_P \cos k_C L_C$	$f_P^n = (2n+1)\frac{c_P}{4L_P}$	$f_P^0 = 369$	
		$T_C = 1500$			$f_C^m = (2m+1)\frac{c_C}{4L_C}$	$f_C^0 = 364$	$f_C^1 = 1093$
A2	0	$T_P = T_C = 300$	1		-	-	
B3	0	$T_P = T_C = 300$	$\ll 1$	$\cos kL_C$	$f_C^n = (2n+1)\frac{c}{4L_C}$	$f_C^0 = 163$	$f_C^1 = 489$
B4	0	$T_P = 300$	$\ll 1$	$\cos k_C L_C$	$f_C^n = (2n+1)\frac{c_C}{4L_C}$	$f_C^0 = 364$	$f_C^1 = 1093$
		$T_C = 1500$					

Table 6.1: Analytical evaluation of the eigenfrequencies and dispersion relation equations as functions of the reflection coefficient R at the premixer inlet, the temperatures of the premixer T_P and of the chamber T_C and for two limit values of the area expansion ratio Ξ.

6.1.2 Influence of the area expansion ratio

Solutions of the dispersion relation $\mathcal{D} = 0$ are now envisaged numerically for finite values of the parameter Ξ in the isothermal configuration. In this case, the eigenfrequencies of the coupled cavities cannot be anymore identified as quarterwave modes of either the premixer or the chamber and are noted f_{PC}^n.

The case of a premixer inlet reflection coefficient $R = 1$ is first examined. The evolution of the three first eigenfrequencies $f_{PC}^{n=0,1,2}$ is presented in figure 6.2 using black solid lines. In this figure, frequencies are normalized by the value $f_L = 113\,\text{Hz}$ which corresponds to the frequency of the quarterwave mode of a single tube of total length $L = L_P + L_C$, obtained when $\Xi = 1$. Horizontal dashed-dotted lines in this figure correspond to the fundamental f_L and its first harmonics $3f_L$ and $5f_L$. Dashed lines indicate the fundamental f_C^0 and the first harmonic f_C^1 modes associated with the combustion chamber length, and the fundamental mode f_P^0 associated with the premixer length.
When the parameter Ξ is reduced, the area expansion ratio between the premixer and the combustion chamber increases. The fundamental oscillation frequency f_{PC}^0 deviates from the quarterwave mode f_L associated with the total length when $\Xi = 1$ to reach the frequency f_C^0 of the first quarterwave mode associated with the combustion chamber length when $\Xi = 0$. In the meantime, the first harmonic frequency f_{PC}^1 deviates from the eigenfrequency of the first harmonic $3f_L$, when $\Xi = 1$ to reach the eigenfrequency associated with the quarterwave mode of the premixer f_P^0 for $\Xi = 0$. The second harmonic f_{PC}^2 decreases from the third harmonic $5f_L$ associated with the single tube to reach the values of the first harmonic f_C^1 associated with the chamber length. It can be noted that the two first eigenfrequencies f_{PC}^0 and f_{PC}^1 increase with decreasing Ξ, while the third f_{PC}^2 decreases with decreasing Ξ. Once Ξ is lower than 0.8, the area change is important enough to deviate the eigenfrequencies from the harmonics associated with the total length $f_L^n = (2n+1)c/4L$.

The actual complexity of the premixer inner geometry is not considered in the developed model. The parameter Ξ takes only into consideration the cross-section of the premixer channel S_P. In the combustor setup, the parameter Ξ takes thus a small value $\Xi = 0.07$ in non reactive isothermal configurations. Eigenfrequencies f_{PC}^n in this case are thus very close to those determined analytically in case B1 (table 6.1). It will however be shown that the air and fuel manifolds connected to this channel modify the system eigenfrequencies. The presence of these manifolds can be considered, in a first approximation, by increasing the surface area S_P to include the open area from these manifolds. The exact inner geometry is sketched in figure 6.3. Fuel and air, fed in the external plenum, enter the premixer channel through two lateral rectangular slits. Taking into account these additional open sections yields to an area expansion ratio $S_P/S_C = 0.22$. The expected eigenfrequencies in this situation are then those of coupled-cavities modes (figure 6.2).

The three first eigenfrequencies $f_{PC}^{n=0,1,2}$ are summarized in table 6.2, for a premixer inlet reflection coefficient $R = 1$. Frequencies are given for three values of the area expansion ratio: 0, 0.07 and 0.22. When the premixer inlet is anechoic, $R = 0$, the eigenfrequencies correspond only to those associated with the chamber length, $f_C^m = (2m+1)c_C/4L_C$ and depend only on the gas temperature T_C. There is no effect of the area ratio S_P/S_C except when $S_P = S_C$, which corresponds to case B2 where all frequencies propagate.

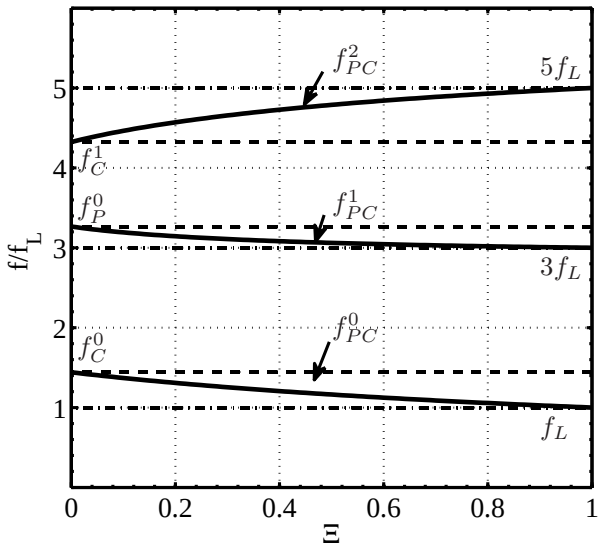

Figure 6.2: Evolution of the three first eigenfrequencies f^n_{PC} with the parameter Ξ for an isothermal configuration $T = 300\,\mathrm{K}$. Frequencies are normalized by $f_L = 113\,\mathrm{Hz}$, the frequency of the quarterwave mode of the pipe of length $L = L_P + L_C$.

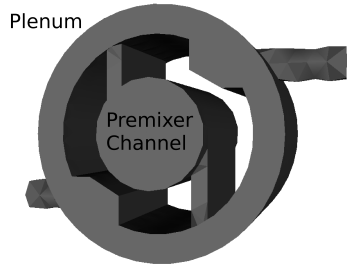

Figure 6.3: Premixer inner volume in which fluids flow. Air is fed into the plenum which is connected to the premixer channel by two rectangular slits in which fuel is injected. Courtesy of M. Leyko (Cerfacs).

	$T_C = 300\,\mathrm{K}$			$T_C = 1500\,\mathrm{K}$		
Ξ	f^0_{PC}	f^1_{PC}	f^2_{PC}	f^0_{PC}	f^1_{PC}	f^2_{PC}
0.00	163	369	489	364	369	1093
0.07	157	363	500	326	408	1050
0.22	146	354	519	294	439	1028

Table 6.2: Theoretical eigenfrequencies computed with $T_P = 300\,\mathrm{K}$ and $R = 1$, for the three values of Ξ considered in this study.

6.1.3 Influence of the temperature ratio

Solutions of the dispersion relation $\mathcal{D} = 0$ are now envisaged with emphasis on the effect of setting different temperatures in the premixer and the combustion chamber. The influence of the temperature ratio T_P/T_C is examined for a fixed expansion ratio $S_P/S_C = 0.07$ in figure 6.4a and for $S_P/S_C = 0.22$ in figure 6.4b. The evolutions of the eigenfrequencies of the three first modes f^0_{PC}, f^1_{PC}, and f^2_{PC} are plotted as functions of T_P/T_C with solid lines in figures 6.4. Evolutions of these eigenfrequencies are compared to evolutions of asymptotic solutions, which are calculated using the analytical expressions of the quarterwave modes eigenfrequencies of the chamber $f^0_C = c_C/4L_C$ and of the premixer $f^0_P = c_P/4L_P$ obtained when $\Xi = 0$ (cases B1 and B2). The influence of temperature on these solutions is taken into account only through the sound celerity. The premixer temperature is kept constant at $T_P = 300\,\mathrm{K}$, resulting in a constant value $f^0_P = 369\,\mathrm{Hz}$ (fig. 6.4 horizontal dashed line). The chamber temperature is increased from $T_C = 300\,\mathrm{K}$ to $T_C = 2000\,\mathrm{K}$. The associated eigenfrequency therefore also increase when T_P/T_C is reduced: $f^0_C = \sqrt{\gamma r T_C}/4L_C$ (dashed-dotted line, fig. 6.4).
It can be noted in figure 6.4 that asymptotic solutions cross at $T_C = 1540\,\mathrm{K}$. For chamber temperature higher than $1540\,\mathrm{K}$, $f^0_C > f^0_P$. When solving the exact dispersion relation, this frequency crossing does not occur, and the mode initial hierarchy remains the same $f^2_{PC} > f^1_{PC} > f^0_{PC}$ for all temperatures. The fundamental f^0_{PC} increases with the chamber temperature, following the asymptotic solution f^0_C. When the temperature is further increased, it tends toward the asymptotic eigenfrequency associated with the premixer quarterwave mode f^0_P. In the meantime, the second eigenmode f^1_{PC} shifts slowly towards frequencies higher than f^0_P, reaching values associated with the chamber asymptotic quarterwave mode f^0_C.
In the practical configuration, the average chamber temperature is estimated around $T_C = 1500\,\mathrm{K}$ yielding to the eigenfrequencies gathered in table 6.2, computed for $S_P/S_C = 0.07$ and 0.22 for the three first eigenmodes.

It was shown that the modal structure is very dependent on the area expansion ratio between the premixer and the combustion chamber. For a very large section difference between the premixer and the combustion chamber ($S_P/S_C = 0.07$), the modal structure is governed by almost uncoupled eigenfrequencies associated either with the premixer or with the chamber lengths. These eigenfrequencies correspond to quarterwave modes of isolated open-closed cavities in an isothermal configuration. When the open area of the premixer manifolds is taken into account ($S_P/S_C = 0.22$), the theoretical eigenmodes f^n_{PC} of the combustion rig corresponds to coupled-cavities modes, and cannot be associated with quarterwave modes. When the chamber temperature is increased, the eigenfrequencies of the modes associated with the combustion chamber f^0_{PC} and f^2_{PC} are strongly increased, while the eigenmode associated with the premixer f^1_{PC} evolves much less.
It was also shown that the reflection coefficient at the premixer inlet essentially controls the presence of the eigenmodes within the premixer, with no influence on the combustion chamber acoustics, when the area expansion ratio is large. When this inlet is set anechoic, no modes propagates in the premixer, but this has a priori no influence on the eigenfrequencies of the combustion chamber.
These predictions are compared in the next section to experimental data obtained by external acoustic forcing of the facility with a loudspeaker in the absence of combustion.

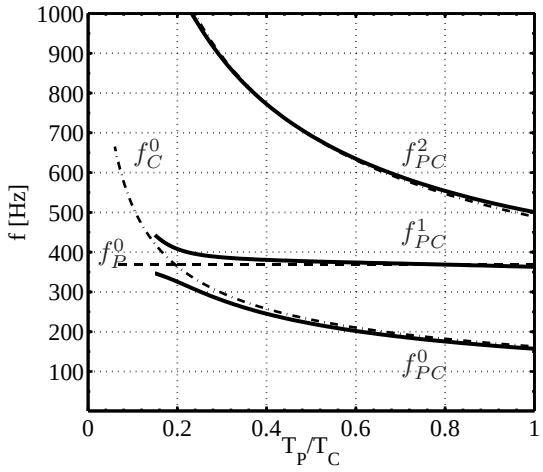

(a) $S_P/S_C = 0.07$

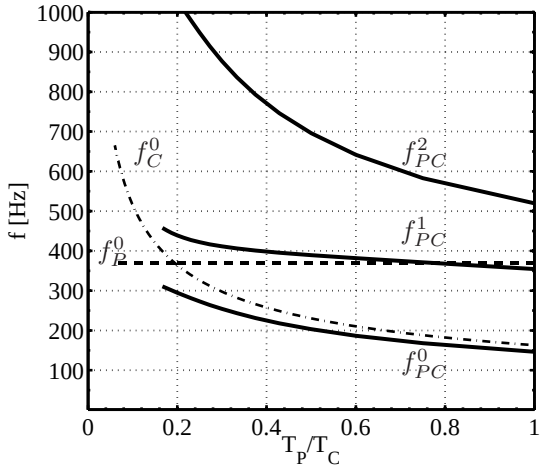

(b) $S_P/S_C = 0.22$

Figure 6.4: Evolution of the three first eigenfrequencies (solid lines) with the temperature ratio compared with theoretical evolutions of the quarterwave mode associated with the chamber $f_C^0 = c_C/4L_C$ (dot-dashed line) and with the premixer $f_P^0 = c_P/4L_P$ (horizontal dashed line), for a fully reflective inlet $R = 1$.

6.2 Acoustic characterization of the facility: isothermal experiments

An experimental characterization of the acoustic signature of the combustion rig is now undertaken in cold flow configurations. Results are compared to model predictions. Influences of the manifolds and of the airflow injection are first examined.

6.2.1 Experimental protocol for external forcing

The acoustic response of the combustion facility to external forcing using a loudspeaker has been investigated in three different configurations sketched in figure 6.5. These experiments were carried out to determine the influence of the premixer complex geometry on the combustion rig modal structure. Tests were made first without air and fuel manifolds connected to the premixer channel (6.5a). These feeding lines constitute a complex network of ducts and volumes connected radially to the premixer inner channel, and are used to convey the fresh reactants. Tests were then conducted with connected manifolds (6.5b), without and with airflow injection. In this last case, the massflow injected through the manifolds equals the one used for the nominal reactive case.

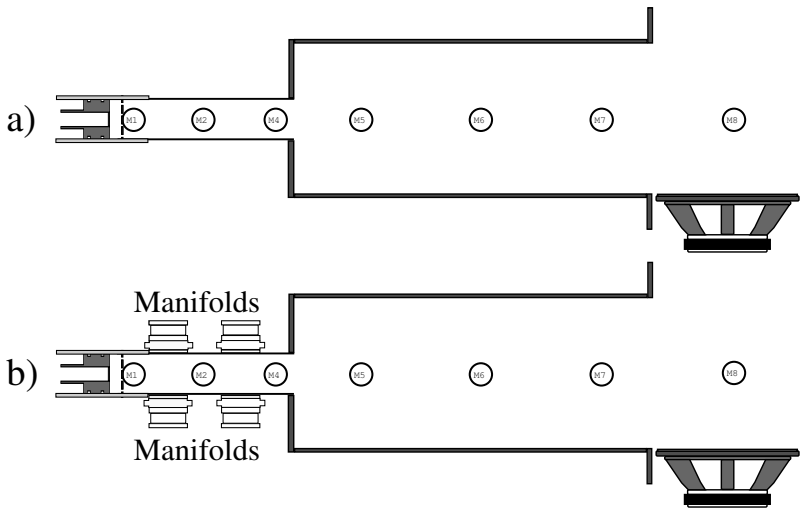

Figure 6.5: Two different configurations of the combustion facility used for acoustic characterization by external forcing. a) Air manifolds disconnected. b) Air and fuel manifolds connected to the premixer channel, tested with and without massflow injection.

These experiments were made in non-reactive isothermal configurations with the same model of loudspeaker used in the impedance tube facility. Pressure signals were recorded by eight microphones M1 to M8, positioned in the premixer and the combustion chamber as indicated in figure 6.5. Microphone M8 is placed outside the chamber,above the center of the loudspeaker, at the same height as the chamber microphones to measure the direct response of the loudspeaker. The input forcing sound level was not kept constant in these experiments throughout the frequency range explored. However care was taken to impose the same input

voltage amplitude to the loudspeaker for each forcing frequency during all tests. Results presented here yield quantitative information only when compared to each other. The rest of the setup is identical to that presented for the impedance tube facility (see chapter 3). A signal generator is used to sweep frequencies in the range $100 - 1000$ Hz. Frequency sirens were preferred to harmonic excitations for these experiments. This last method provides good statistical convergence of the signal but require a very large number of acquisitions to achieve a correct frequency sampling on such a frequency span. The latter method is now briefly described. Frequencies are swept from $f_{initial}$ to f_{final} with a siren signal of duration T_{siren} and a linear growth rate $\tau^{-2} = (f_{final} - f_{initial})/T_{siren}$. The frequency response measured by the eight microphones M1 to M8 is computed using Short-Time Fourier Transform (STFT). Considering a signal sampled at a frequency f_s with a total number of samples MN, decomposed into M windows of N samples each, the frequency resolution of the Fourier analysis is $\Delta f = f_s/N$. Each window has a time duration N/f_s, during which the forcing frequency should stay constant to perform correct Fourier analysis. To ensure this condition, the increase of forcing frequency during the sweep over the window must be smaller than the frequency resolution of the FFT over the same window. This yields the following condition:

$$\tau^{-2}\frac{N}{f_s} \leq \Delta f \tag{6.17}$$

However if the frequency growth rate is smaller than the frequency resolution, $\tau^{-2} < \Delta f^2$, the frequency increase from the Fourier analysis over M windows, $M\Delta f$, is greater than the frequency increase T_{siren}/τ^2 of the forcing siren. Combining these two conditions, the growth rate of the siren should be chosen equal to the square of the frequency resolution to perform a correct Fourier analysis with this type of modulation:

$$\tau^{-2} = \Delta f^2 \tag{6.18}$$

In addition, the Shannon theorem must be fulfilled. The sampling frequency must be chosen at least twice greater than the highest forcing frequency, $f_s > 2f_{final}$. A good representation of the signal amplitude requires more sampling points. It is suitable to acquire at least 10 points per period. This yields a condition on the sampling frequency: $f_s \geq 10 f_{final}$. The total number of samples is linked to the frequency resolution:

$$MN = \frac{f_s}{\Delta f^2}(f_{final} - f_{initial}) \tag{6.19}$$

The higher the sampling frequency and/or the lower the spectral resolution, the higher the number of points to be acquired. Finally to make use of FFT algorithms, the sampling frequency and the number of samples should be powers of two. In practice, a single frequency sweep from $f_{initial} = 100$ to $f_{final} = 1000$ Hz implies a sampling frequency of $f_s = 16384$ Hz. If a frequency resolution of $\Delta f = 4$ Hz is expected, this implies a siren duration $T_{siren} = 56.25$ s and a total number of samples $MN = 921600$ per channel. This amount of data is too high for the analog-to-digital board that equips the acquisition system. As a result, the 900 Hz frequency span was swept by two overlapping sirens with identical acquisition parameters. The first siren $S1$ spans from 98 to 578 Hz and the second $S2$ from 538 to 1018 Hz. They both have a frequency growth rate of $\tau^{-2} = +16$ Hz.s^{-1} for a duration

Siren	$f_{initial}$ Hz	f_{final} Hz	τ^{-2} Hz/s	T_{siren} s	f_s Hz	Δf Hz	Number of samples
S1	98	578	16	30	16384	4	491500
S2	538	1018	16	30	16384	4	491500

Table 6.3: Siren parameters

$T_{siren} = 30\,\mathrm{s}$. A total of 491500 samples were therefore digitized from each microphone output, with a resolution of $\Delta f = 4\,\mathrm{Hz}$. These various parameters are gathered in table 6.3. Lowering the sampling frequency f_s has only a weak influence on the total number of samples to record. Reducing the frequency resolution Δf is more efficient, but might lead to losses of some important dynamics.

An example of results obtained with the first siren $\mathrm{S1}$ is presented in figure 6.6. The frequency evolution with time is plotted on top. Evolution of the pressure fluctuations measured by microphone M8 placed directly above the loudspeaker. The responses recorded by M1 in the premixer channel and M5 in the combustion chamber are plotted as a function of time. The top graph shows that the amplitude of the forcing signal is not constant with frequency. The modulation level is lower than $20\,\mathrm{Pa}$ over the whole frequency span. Below $200\,\mathrm{Hz}$, corresponding to times shorter than $10\,\mathrm{s}$, the forcing level is weak. It can yet be seen that the response measured by microphone M1 in the premixer features large oscillations, with a signal to noise ratio sufficient to detect preferential frequencies. In all the following graphs, data have been normalized by the signal measured by microphone M8.

6.2.2 Influence of the premixer air and fuel manifolds

The influence of the air and fuel manifolds is now investigated. These manifolds consist in the cylindrical enclosure in which reactants are fed as shown in figure 6.3. The premixer channel is located in the center of these manifolds and is connected by two radial rectangular slits through which air and propane are injected. These manifolds are not taken into account in the model developed in the previous section 6.1. A crude approximation is to include the associated open surface of the plenum into the calculation of S_P. As presented previously, the area expansion ratio then increases from $\Xi = 0.07$, when only the premixer channel cross-section is considered, to 0.22 when the air and fuel manifolds area is included. This is equivalent to replacing the value of the inner channel diameter of $30\,\mathrm{mm}$ by $53\,\mathrm{mm}$.

The signature of the combustion facility is first characterized with these manifolds disconnected from the premixer channel; the slits were filled with dense metallic foam, taped inside the inner channel with rigid aluminium tape. The premixer channel is then of constant section, acoustically disconnected from the plenum. The premixer inlet impedance control system (ICS) is used with plate P4 to set different values of the reflection coefficient R and to study modifications of the acoustic response. Figure 6.7 shows the acoustic response of the facility at the different microphone locations M1, M2, M5, M6 and M7 (see figure 6.5 for microphones positions). The evolution of the reflection coefficient at the premixer inlet is plotted as a function of frequency in the top graph. Two cases are presented, one where the reflection coefficient is maximum (dashed line) obtained without back-cavity ($L = 0$) and a

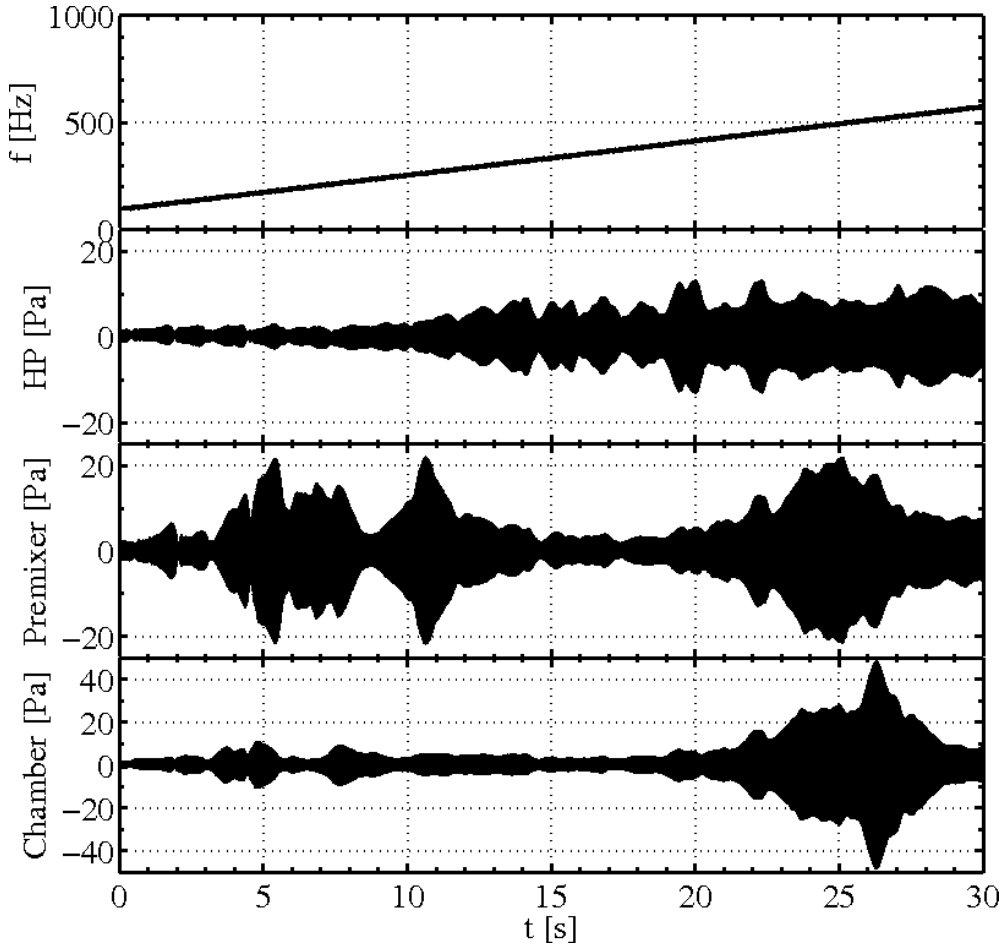

Figure 6.6: Example of the siren forcing signal used for acoustic characterization of the combustion rig. The top graph shows the frequency evolution with time imposed by the signal generator. The second graph corresponds to the temporal signal measured by microphone M8 located directly above the loudspeaker. The two last graphs show the response signals in the premixer (M1) and the combustion chamber (M5) respectively.

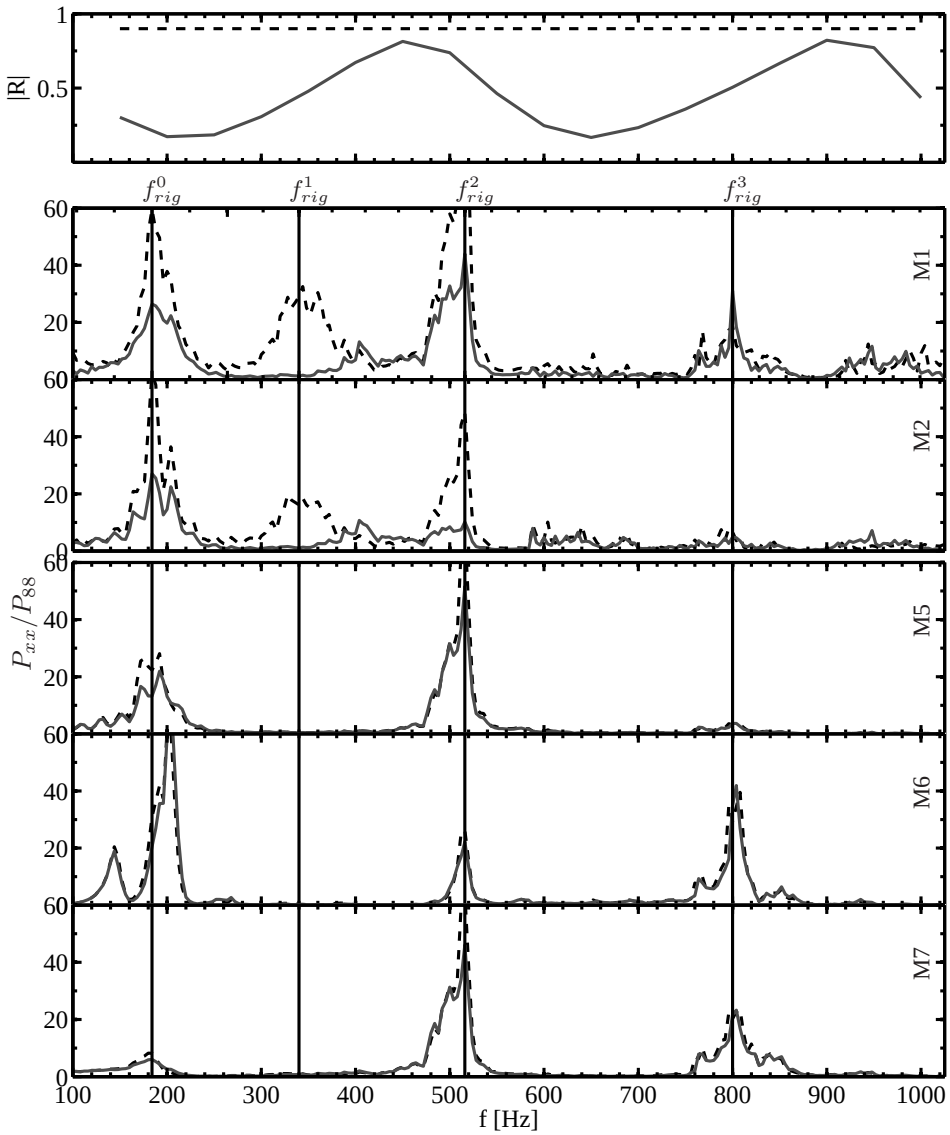

Figure 6.7: Acoustic signature of the combustion facility equipped with the ICS and plate P4, for two impedance conditions at the premixer inlet. Air and fuel manifolds are disconnected from the inner channel. Top graph: evolution of $|R|$ of plate P4 with frequency. Other graphs show from top to bottom the power spectral densities P_{xx} of the signals measured by microphones M1 to M7 downstream of the perforated plate normalized by the power spectral density P_{88} of the signal measured by M8. $L = 0$ (dashed line), $L = L_{opt} \simeq 35\,$cm (solid line).

Manifolds	Ξ		Premixer				Chamber		
		f^n_{rig}	0	1	2	3	0	2	3
Disconnected	0.07	Exp	184	340	516	800	184	516	800
Disconnected	0.07	Model	157	363	500	815	157	500	815
		f^m_{PC}	0	1	2	3	0	2	3
		f^n_{rig}	0	1	2	3	0	2	3
Connected	–	Exp	184	270	516	800	184	516	800
Connected	0.07	Model	157	363	500	815	157	500	815
Connected	0.22	Model	146	354	520	812	146	520	812
		f^m_{PC}	0	1	2	3	0	2	3

Table 6.4: Eigenfrequencies detected in the premixer and the chamber f^n_{rig} with and without air and fuel manifolds and a premixer inlet reflection coefficient $|R| = 1$. Data are compared to theoretical predictions, and associated with theoretical modes f^m_{PC}.

second situation (solid line) where the reflection coefficient reaches a minimum at $f \simeq 200$ Hz and $f \simeq 550$ Hz. It is worth noting that in the model proposed in section 6.1, the reflection coefficient was assumed to be constant over the whole frequency range, a condition which cannot be achieved in practice.
The two upper spectral densities in figure 6.7 are measured inside the premixer, and the three others are measured inside the combustion chamber. Four frequency peaks emerge from the background noise in the premixer: $f^n_{rig} = 184, 340, 516$ and 800 Hz. They are indicated in the figure by vertical solid lines. A double peak structure is detected around $f^0_{rig} \simeq 184 - 200$ Hz. The peak at 184 Hz is strong in the premixer, but is overcome by the peak at 200 Hz in the chamber. The small peak at $f^1_{rig} = 340$ Hz is not detected in the chamber. These frequencies are close within 20 Hz to the predicted eigenfrequencies obtained with $S_P/S_C = 0.07$ (table 6.4). Indeed, the fundamental is predicted at $f^0_{PC} = 157$ Hz and the first harmonic at $f^1_{PC} = 363$ Hz. Differences may be attributed to the details of the real geometry which is more complex than that being modelled. The third harmonic is detected at $f^2_{rig} = 516$ Hz. This peak is very strong in the whole facility. Lastly, the peak at $f^3_{rig} = 800$ Hz can be associated with the fourth harmonic predicted f^3_{PC}. These results are gathered in table 6.4.

The influence of the premixer inlet reflection coefficient is noticeable in the spectra measured in the premixer. The energy content within the peaks is reduced when the reflection coefficient is low. The pressure peaks at $f^0_{rig} \simeq 184 - 200$ Hz and at $f^2_{rig} = 516$ Hz are strongly attenuated in this situation. The eigenmode at $f^2_{rig} = 516$ Hz is also damped inside the combustion chamber. It was noticed that beyond $f = 600$ Hz, a poor signal to noise ratio is obtained for the measurements in the premixer, albeit the signal is strong inside the chamber. The large area reduction between the chamber and the premixer seems to act as a low-pass filter for the external acoustic excitation from the loudspeaker located at the exhaust of the chamber.

The structure of the three first eigenmodes is now investigated and compared to theoretical predictions of the pressure distribution, calculated with $\Xi = 0.07$. For such a low area expansion ratio, the theoretical eigenfrequencies are very close to the asymptotic solutions

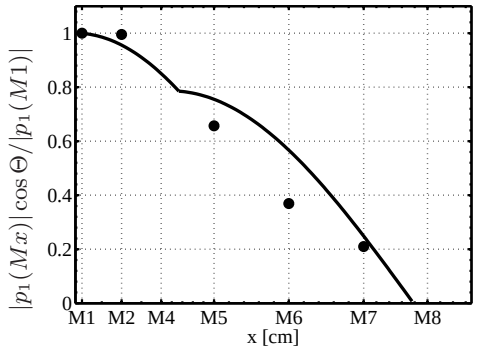

(a) Structure of the first mode measured at $f^0_{rig} = 184\,\text{Hz}$ (circles), compared with prediction at $f^0_{PC} = 157\,\text{Hz}$ (line).

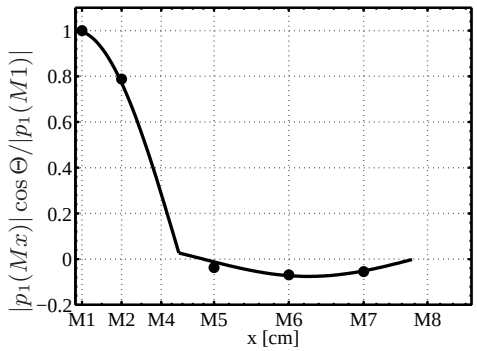

(b) Structure of the second mode measured at $f^1_{rig} = 340\,\text{Hz}$ (circles), compared with prediction at $f^1_{PC} = 363\,\text{Hz}$ (line).

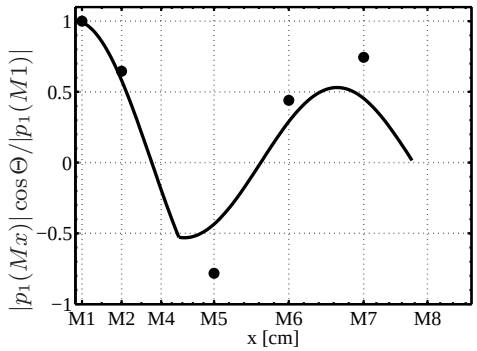

(c) Structure of the third mode measured at $f^2_{rig} = 516\,\text{Hz}$ (circles), compared with prediction at $f^2_{PC} = 500\,\text{Hz}$ (line).

Figure 6.8: Comparison between the measured pressure shapes (circles) and the theoretical predictions (lines) calculated with $T_P = T_C = 300\,\text{K}$, $\Xi = 0.07$ and $R = 1$ for the three first detected eigenmodes in the case of disconnected manifolds.

.

calculated with $\Xi = 0$ in the dispersion relation $f^0_{PC} \simeq f^0_C$, $f^1_{PC} \simeq f^0_P$. Results are plotted in figure 6.8 for the three first eigenmodes : $f^0_{rig} = 184\,\text{Hz}$, $f^1_{rig} = 340\,\text{Hz}$ and $f^2_{rig} = 516\,\text{Hz}$. The absolute pressure amplitude measured by microphone Mx $|p_1(Mx)|$ is normalized by the pressure amplitude measured by M1 $|p_1(M1)|$. It is then multiplied by the phase of the cross-correlation between microphones Mx and M1 at the frequency of interest $\Theta = \arg(P_{x,1}(f))$ to obtain the shape of the pressure distribution in the facility. Microphone M1 is used as a reference since it is always located very close to a pressure antinode. The predicted eigenmode structures fit correctly the observed pressure distribution, especially for the second mode f^1_{rig}. It can thus be concluded that the three measured frequency peaks $f^{n=0,1,2}_{rig}$ corresponds to the three predicted eigenfrequencies $f^{m=0,1,2}_{PC}$ when $\Xi = 0.07$, which also closely follow the asymptotic values f^0_C, f^0_P and f^1_C obtained for uncoupled cavities, when $\Xi = 0$.

The air and fuel manifolds are then reconnected to the premixer channel. The acoustic responses with and without air and fuel manifolds are plotted together in figure 6.9 for a back cavity depth set to zero corresponding to an almost perfectly reflecting premixer inlet ($R \simeq 1$). The three eigenfrequencies f^n_{rig} detected when the manifolds are disconnected are indicated by vertical solid lines in the figure. An additional frequency peak is measured when the manifolds are connected to the premixer channel $F^1_{rig} = 270\,\text{Hz}$, indicated by a vertical dashed line. The influence of these air and fuel manifold is noticeable on the acoustic signature of the premixer (M1 and M2). The frequencies of the peaks at f^0_{rig} and f^2_{rig} are almost unchanged when manifolds are connected but the peak at f^3_{rig} disappears because the signal to noise ratio above $600\,\text{Hz}$ becomes very low. One can also observed that the second pressure peak at $f^1_{rig} = 340\,\text{Hz}$ disappears and that a new peak is detected at $F^1_{rig} = 270\,\text{Hz}$ when manifolds are connected. A first assumption is that this is the result of a frequency shifting of the second eigenmode, induced by the presence of the feeding lines. Inside the combustion chamber, it can be noticed that when the manifolds are connected, there is very little signal below $400\,\text{Hz}$. The first eigenmode f^0_{rig} and the new mode at F^1_{rig} are barely visible. The manifolds have no influence on the other eigenfrequencies f^2_{rig} and f^3_{rig}.

The detected frequency peaks are compared to theoretical predictions, computed with an augmented area ratio $S_P/S_C = 0.22$ and a constant temperature $T_P = T_C = 300\,\text{K}$ in table 6.4. Increasing the area expansion ratio has only a limited influence on the theoretical eigenfrequencies of the coupled-cavities modes. Indeed, the first mode is predicted at $f^0_{PC} = 146\,\text{Hz}$, which is a bit lower than that measured $f^0_{rig} = 184\,\text{Hz}$. The eigenmodes at f^2_{PC} and f^3_{PC} are predicted within $10\,\text{Hz}$ of their actual values. The second mode is however predicted at $f^1_{PC} = 354\,\text{Hz}$, and the model fails to predict the new peak frequency $F^1_{rig} = 270\,\text{Hz}$. To determine the nature of this pressure peak F^1_{rig}, the structure of the pressure distribution of the three first detected peaks (f^0_{rig}, F^1_{rig} and f^2_{rig}) is compared to the theoretical predictions at $f^{n=0,1,2}_{PC}$ in figure 6.10. Predictions are presented for two values of the area expansion ratio $S_P/S_C = 0.07$ and 0.22 to further examine the influence of this ratio. The structure of the mode associated with the first pressure peak $f^0_{rig} = 184\,\text{Hz}$ is first presented in figure 6.10a. As explained in section 6.2.1, the external modulation below $200\,\text{Hz}$ resulted in low signal to noise ratio in the combustion chamber. This may account for the discrepancy observed between measurements (circles) and theoretical shapes (lines). However the phase difference between the pressure signals in the premixer and the chamber is well retrieved, and this first peak can be associated with the first coupled-cavities eigenmode f^0_{PC}. The mode associated with the second frequency $F^1_{rig} = 270\,\text{Hz}$ is compared to predictions at $f^1_{PC} \simeq 354 - 363\,\text{Hz}$

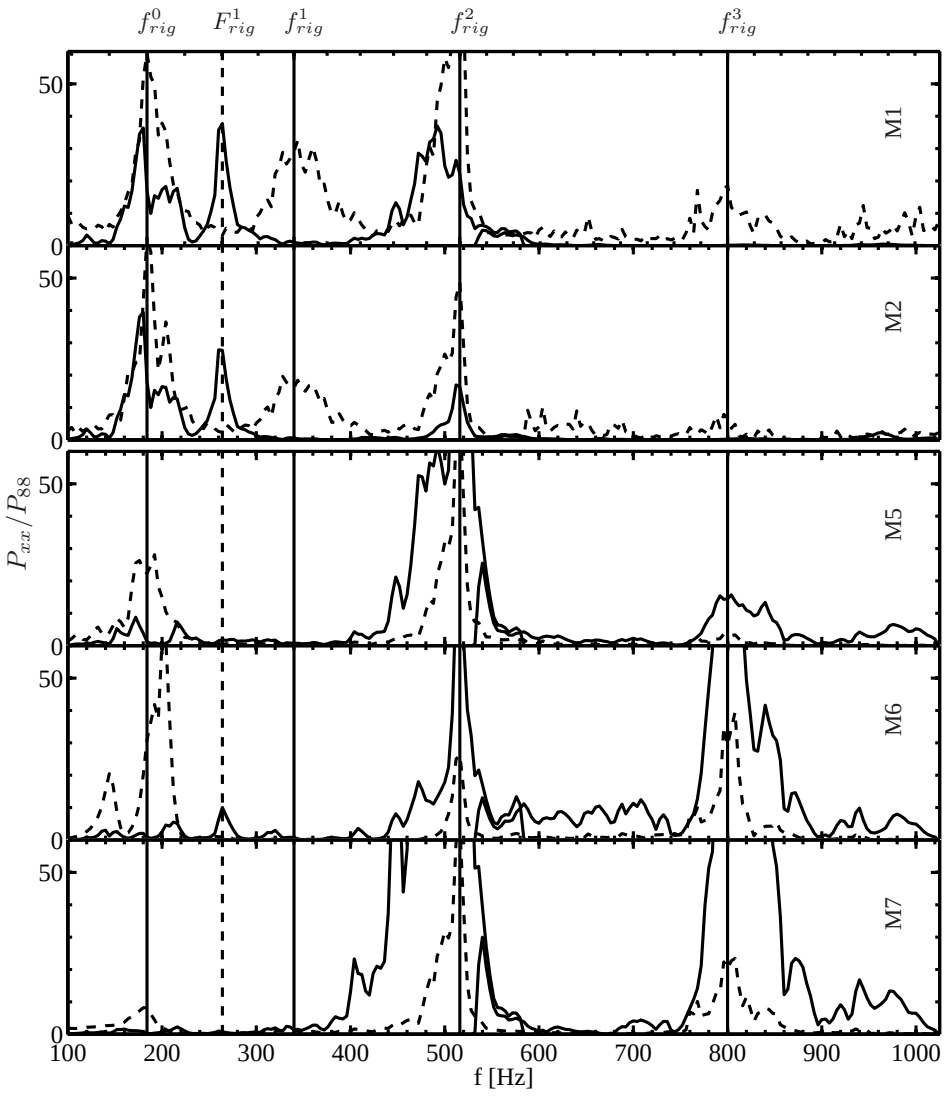

Figure 6.9: Comparison between the acoustic response of the combustion facility with (solid line) and without air and fuel manifolds (dashed line) connected to the premixer channel, for a back cavity depth set to zero ($R \simeq 1$).

in figure 6.10b. Even though the eigenfrequency is not correctly predicted, the theoretical pressure distribution fits correctly experimental data. This confirms that this frequency F^1_{rig} may be associated with the second eigenmode f^1_{PC}. When air and fuel manifolds are connected, the mode shifts from $f^1_{rig} = 370\,\text{Hz}$ to $F^1_{rig} = 270\,\text{Hz}$ but keeps the same structure. Finally figure 6.10c compares predictions at $f^2_{PC} = 500 - 519\,\text{Hz}$ with experimental data at $f^2_{rig} = 516\,\text{Hz}$. The predicted structure follows the evolution of the measured pressure distribution, linking this frequency f^2_{rig} to the third eigenmode of the coupled-cavities configuration. It can be noted that the area expansion ratio has only a weak influence on the predicted pressure distribution and eigenfrequencies in all cases investigated.

In conclusion, the four dominant peak frequencies that were experimentally observed could be associated with the eigenfrequencies predicted by the model. The modes associated with the chamber $f^0_{PC} \simeq f^0_C \simeq 184\,\text{Hz}$, $f^2_{PC} \simeq f^1_C \simeq 516\,\text{Hz}$ and $f^3_{PC} \simeq f^2_C \simeq 800\,\text{Hz}$ are unaffected by the modifications of the acoustics within the premixer when the air and fuel manifolds are connected. It can also be noted that the third eigenmode $f^2_{PC} \simeq f^1_C$ appears as a preferential mode of the whole rig, while the first $f^0_{PC} \simeq f^0_C$ is rather weak. Air and fuel plenum and feeding lines strongly modify the frequency associated with the second eigenmode f^1_{PC}, yielding to an actual observed frequency $F^1_{rig} \simeq 270\,\text{Hz}$ much lower than the value $f^1_{PC} \simeq f^0_P \simeq 360\,\text{Hz}$ predicted by considering the premixer as a tube of constant cross-section. These results are gathered in table 6.4.

6.2.3 Influence of a mean flow

The influence of the air injection in the system is investigated in the absence of combustion in this part. Preliminary results, not plotted here, were obtained without external forcing by the loudspeaker, to evaluate the sole influence of the air injection in the system. These results indicate that injecting the nominal massflow rate $\dot{m}_a = 42\,\text{Nm}^3\text{h}^{-1}$ in the premixer, through the manifolds, creates a broadband low frequency background noise. This turbulent flow excites the first eigenmode f^0_{rig} but with a relatively low amplitude compared to the results obtained with external forcing. In the premixer (M1 and M2), this mode features a peak level equal to 40 [A.U]. In the chamber this level does not exceed 15 [A.U], to be compared to the few hundreds of [A.U] obtained using a loudspeaker in figure 6.11.

Effects on the acoustic response of the combustion rig of a turbulent flow circulating through the burner is now investigated using superimposed external acoustic forcing. Results plotted in figure 6.11 indicate that the main consequence of the airflow injection is a general increase of the pressure level, especially at the eigenfrequencies previously detected f^n_{rig}. This is accompanied by a low frequency broadband noise below $150\,\text{Hz}$ in the premixer. No new frequency peak is promoted. It should be noted that the pressure amplitude in the premixer (M1 and M2) is multiplied by a factor 2 by the presence of the injection. In the chamber, levels are multiplied by almost 10. The response of microphone M4, located at the junction between the premixer and the combustion chamber has been represented in the third graph. It exhibits a poor signal to noise ratio, for all frequencies, in all configurations investigated. This microphone appears to be always located near a pressure node. It can be noted that microphone M4 features an important broadband noise for frequencies higher than $200\,\text{Hz}$ when airflow is injected. This microphone is located at the exhaust of the premixer inlet, where it may measure broadband pressure perturbations associated with the turbulent flow separation in this region of abrupt geometrical change. In conclusion, the mean turbulent flow within the com-

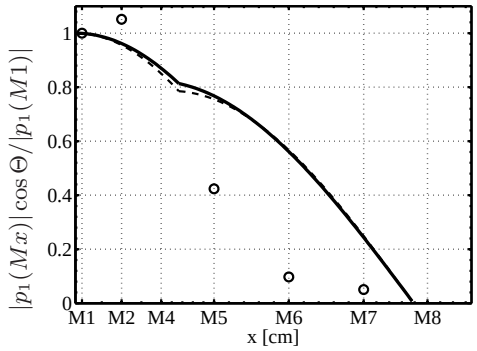

(a) Structure of the first mode measured at $f^0_{rig} = 184\,\text{Hz}$ (circles), compared with prediction at $f^0_{PC} = 157\,\text{Hz}$ ($\Xi = 0.07$, dashed line) and $f^0_{PC} = 146\,\text{Hz}$ ($\Xi = 0.22$, solid line).

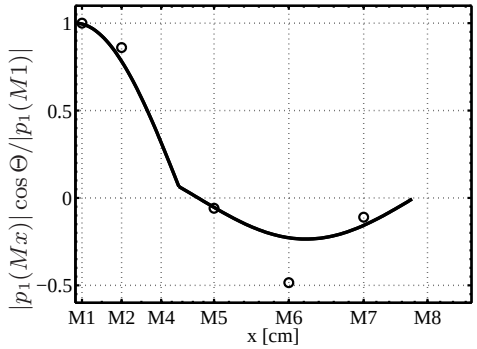

(b) Structure of the second mode measured at $F^1_{rig} = 270\,\text{Hz}$ (circles), compared with prediction at $f^1_{PC} = 363\,\text{Hz}$ ($\Xi = 0.07$, dashed line) and $f^1_{PC} = 354\,\text{Hz}$ ($\Xi = 0.22$, solid line).

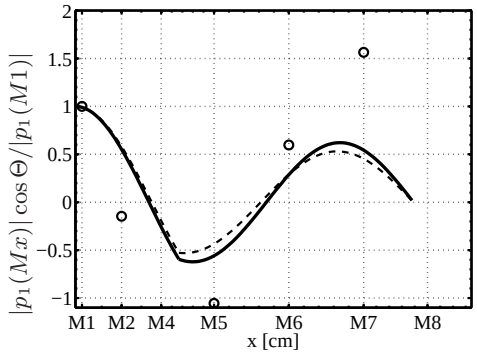

(c) Structure of the third mode measured at $f^2_{rig} = 516\,\text{Hz}$ (circles), compared with prediction at $f^2_{PC} = 500\,\text{Hz}$ ($\Xi = 0.07$, dashed line) and $f^2_{PC} = 519\,\text{Hz}$ ($\Xi = 0.22$, solid line).

Figure 6.10: Comparison between the measured pressure shapes (circles) and the theoretical predictions (lines) calculated with $T_P = T_C = 300\,\text{K}$, $\Xi = 0.07$ and 0.22 and $R = 1$ for the three first detected eigenmodes in the full configuration.

.

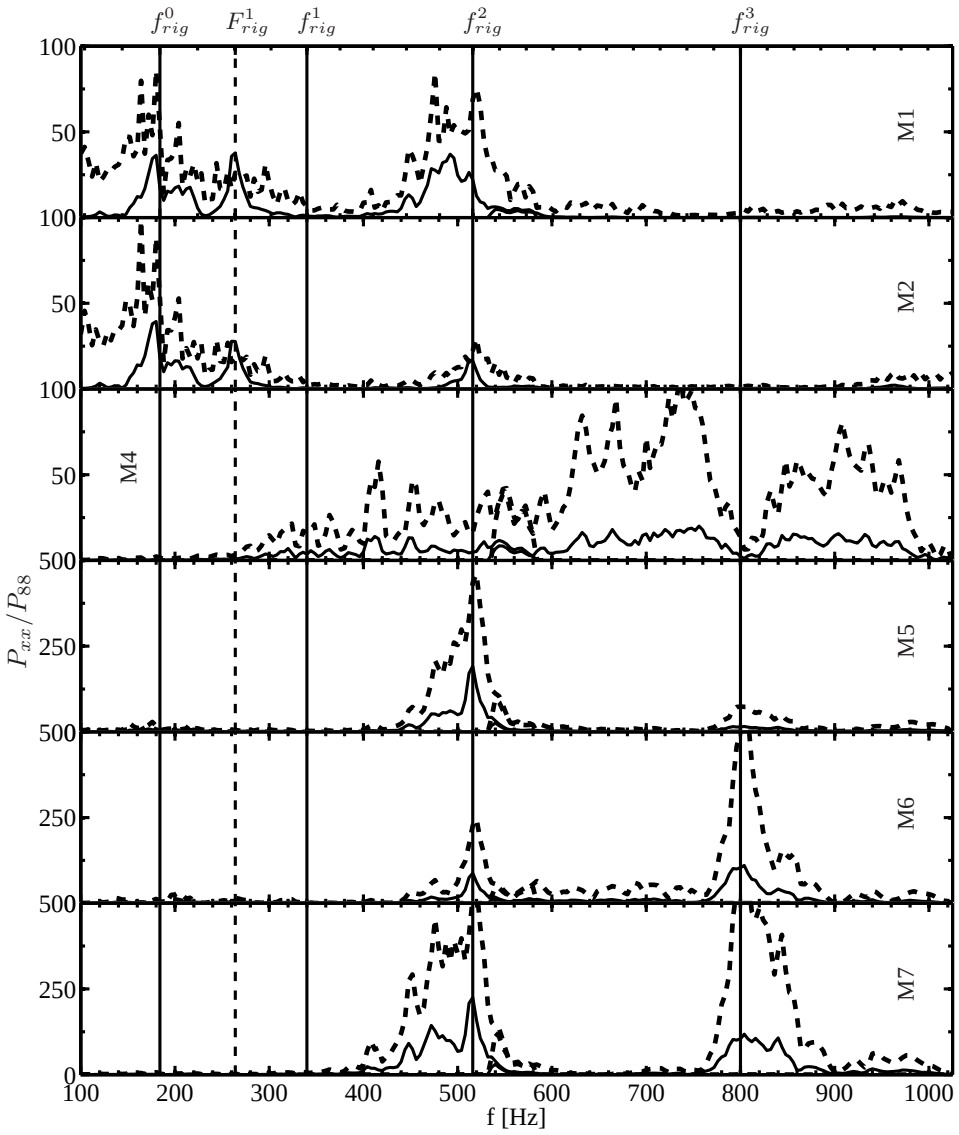

Figure 6.11: Influence of a mean flow injection on the acoustic response of the combustion facility with fully reflective inlet ($L = 0$, $|R| \simeq 1$). Solid lines indicate the case with no airflow, and dashed line the case where $\dot{m}_a = 42\,\mathrm{Nm^3h^{-1}}$ of air is injected in the combustion rig through the manifolds.

bustion rig does not modify the frequencies of the dominant modes previously observed. It also demonstrates that it was relevant to discard the mean velocity effect in the acoustic model.

This acoustic characterization by external acoustic forcing of the CTRL-Z facility, in non-reactive configurations, has highlighted effects of the airflow injection, the premixer inlet impedance and has stressed out the influence of the premixer geometry on the acoustic signature of the rig. The frequencies and structure of the main detected peaks were compared to the theoretical predictions of the model presented in section 6.1. The injection of airflow through the air and fuel manifolds does not modify significantly the frequencies of the detected peaks, either in the premixer or in the chamber, since the flow Mach number remains small. It was then demonstrated that tuning the premixer inlet reflection coefficient with the ICS effectively modifies the acoustic response of the rig, yet most significantly inside the premixer. Two configurations of the premixer were studied: (1) without air and fuel manifolds connected, and (2) the complete geometry with connected manifolds. In both cases, four pressure peaks f^n_{rig} were detected. With disconnected manifolds, the corresponding frequencies could be linked with theoretical predictions of decoupled modes, associated either with the premixer length $f^1_{rig} \simeq f^0_P = 363\,\text{Hz}$, or with the combustion chamber length $f^0_{rig} \simeq f^0_C = 157\,\text{Hz}$. The measured pressure distribution through the rig was successfully compared to the theoretical mode shapes, hence confirming the association. The presence of the manifolds does not modify the frequency of the peaks associated with the chamber ($f^0_{rig} \simeq f^0_C$, $f^2_{rig} \simeq f^1_C$ and $f^3_{rig} \simeq f^2_C$). These manifolds however induce a frequency shift of the second mode from $f^1_{rig} \simeq f^0_P = 340\,\text{Hz}$ to $F^1_{rig} = 270\,\text{Hz}$. The model cannot explain this shift, even when the area expansion ratio is increased to take into account the additional open area from the manifolds. However, the pressure distributions of the three first observed peaks f^0_{rig}, F^1_{rig} and f^2_{rig} were correctly compared to the theoretical mode shapes f^0_{PC}, f^1_{PC} and f^2_{PC}. This confirmed that the second detected peak $F^1_{rig} = 270\,\text{Hz}$ can be considered as the second eigenmode of the structure.

Such characterization could not be conducted in the reactive cases, because the combustion rig is not equipped with an actuation device powerful enough. The loudspeaker, placed at the burner outlet is not suited to withstand high temperatures. Its output power would also not be sufficient to overcome the core noise generated by the flame. Therefore the modal structure in the reactive case is examined without external forcing device, the flame being used as an internal broadband noise source.

6.3 Acoustic characterization of the facility: reactive case

Spectral analysis of the wall fluctuating pressure signals measured by M1 to M8 can be used to detect the dominant oscillation modes when the combustor is operated. The measurement setup is similar to that used in non-reactive cases. Figure 6.12 indicates the position and numbering of the different microphones used.

In the section dedicated to the control of instabilities by modification of the premixer inlet impedance, the Power Spectral Densities distributions within the premixer and the chamber were already presented. It was shown that, in these unstable regimes, the spectral response is dominated by an instability peak which lies in the low frequency range.

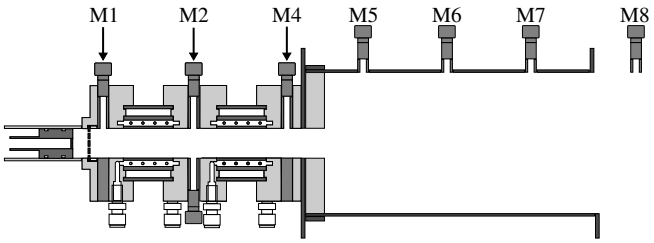

Figure 6.12: Microphones numbering starting from the perforated plate.

Figure 6.13 shows the PSD measured in the nominal regime with an equivalence ratio $\Phi = 0.82$ and a staging of $\alpha = 14.3\%$ for two values of the premixer inlet impedance. In this configuration, a strong instability occurs at $f_{inst} = 272$ Hz. Two harmonics appear at 540 and 810 Hz on the spectra.When the reflection coefficient takes low values $|R| = 0.17$, the instability is damped by 10 to 20 dB. The instability frequency can be compared to the model predictions obtained for $T_C = 1500$ K and $T_P = 300$ K, (cases B2 and B4 in table 6.1) to determine its origin.

For an area expansion ratio which takes the manifolds area into account $S_P/S_C = 0.22$, the two first eigenmodes are predicted at $f^0_{PC} = 294$ Hz and $f^1_{PC} = 438$ Hz. The third mode occurs at $f^2_{PC} = 1028$ Hz and can thus not be associated with observed pressure peaks. The first mode f^0_{PC} is close in frequency to the instability peak f_{inst}. However cold flow experiments have highlighted the fact that the model does not correctly predict the eigenfrequency of the second mode f^1_{PC} when the premixer complete geometry is considered. Therefore conclusions on the nature of the instability peak cannot be drawn only by examining the eigenfrequencies. The modal structure must be examined, as in the cold flow experiments.

The shape of the pressure distribution measured at $f_{inst} = 272$ Hz is thus compared to the model predictions in figure 6.14a for the first eigenmode f^0_{PC} and 6.14b for the second eigenmode f^1_{PC} where two values of the area expansion ratio $S_P/S_C = 0.07$ and 0.22 are considered. The first eigenmode is predicted at $f^0_{PC} = 326$ Hz for $S_P/S_C = 0.07$ and $f^0_{PC} = 294$ Hz for $S_P/S_C = 0.22$. It is clear from figure 6.14a that the pressure distribution does not reproduce the experimental observations. There is no pressure node between M4 and M5. Pressure oscillations are also predicted in phase in the premixer and the chamber, which is not observed on the combustion rig. The pressure distribution is thus compared to that of the second eigenmode predicted at $f^1_{PC} = 408$ Hz ($S_P/S_C = 0.07$) or $f^1_{PC} = 438$ Hz ($S_P/S_C = 0.22$) in figure 6.14b. Predictions are in this case in better agreement: a pressure node is calculated at the location of M4, and pressure in the chamber is in phase opposition with pressure in the premixer. As a conclusion, the measured pressure distribution at f_{inst} corresponds to the modal shape associated with the second eigenmode f^1_{PC}, which closely follows the asymptotic solution associated with the premixer fundamental $f^1_{PC} \simeq f^0_C$.

The dominant instability mode can thus be related to the second eigenmode predicted by the couple-cavities model, despite the discrepancy on the eigenfrequency. As already observed in the cold flow experiments, the presence of the air and fuel manifolds accounts for a large

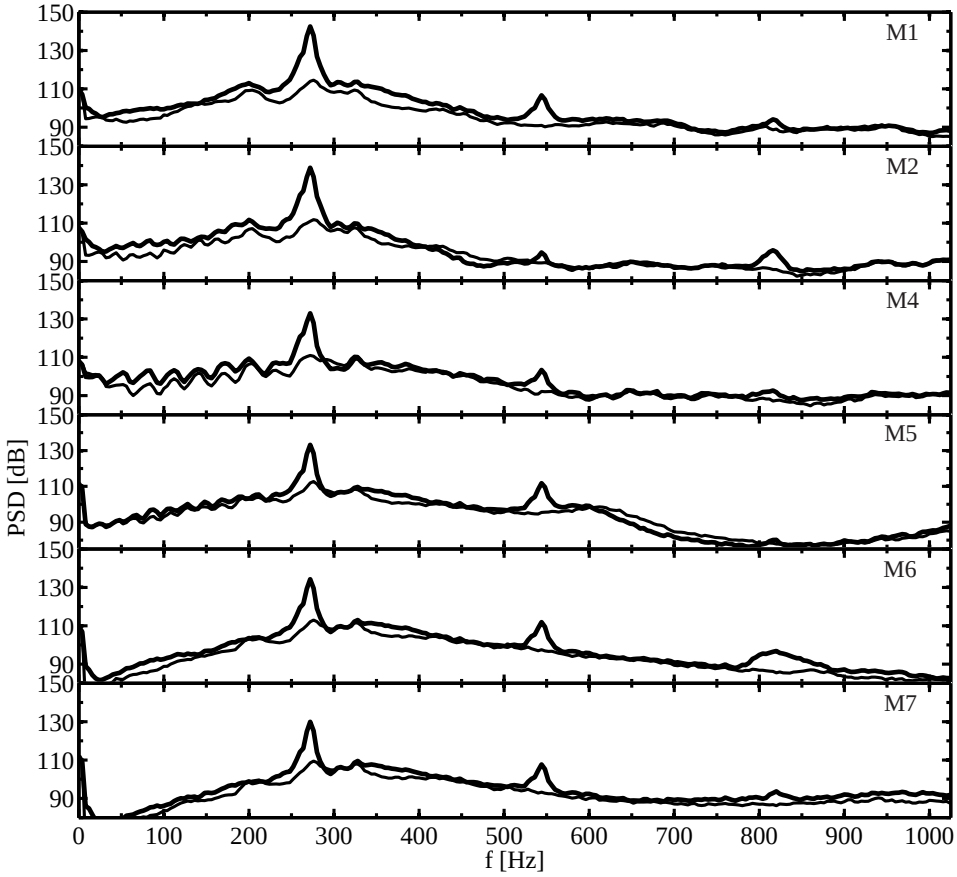

Figure 6.13: Influence of the reflection coefficient on the pressure PSD measured during combustion test i the nominal regime ($\Phi = 0.82$, $\alpha = 14.3\%$). Thick line is obtained with a maximal reflection coefficient $|R| = 0.8$ at the instability frequency $f = 270\,\text{Hz}$, thin line with $|R| = 0.17$ at same frequency.

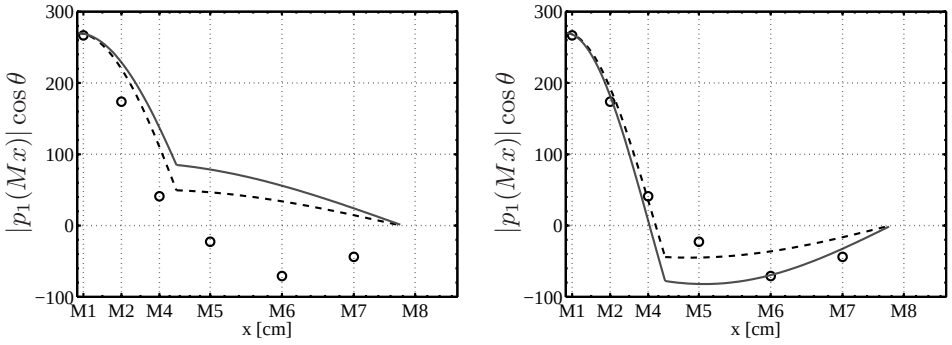

(a) Structure of the first eigenmode f^0_{PC}

(b) Structure of the second eigenmode f^1_{PC}

Figure 6.14: Comparison of the measured acoustic pressure distribution at $f_{inst} = 272\,\text{Hz}$ with the model prediction, for two values of the area expansion ratio. Symbols indicate experimental data. Dashed line indicates the predictions at $S_P/S_C = 0.07$ and the solid line at $S_P/S_C = 0.22$.

part of the frequency difference. It was shown in the parametric study of this model that this second mode is closely linked to the quarterwave mode of the premixer. This mode is quite sensitive to the premixer inlet impedance and therefore to the ICS.

The structure of the pressure distribution within the setup of the main pressure oscillation at $f_{inst} = 272\,\text{Hz}$ is now examined for two premixer inlet reflection coefficients corresponding to a soft $|R| = 0.17$ and a hard $|R| = 0.8$ boundary conditions at $f_{inst} = 272\,\text{Hz}$ in figure 6.15. The pressure amplitudes measured by each microphones are normalized by the pressure amplitude of M1, which also serves as the reference for the computation of the phase lag θ between the microphones. For an hard inlet $|R| = 0.8$, the pressure fluctuation amplitude reaches $p_1(M1) = 266\,\text{Pa}$, while for a soft inlet $|R| = 0.17$ it reaches only $p_1(M1) = 16\,\text{Pa}$. The normalized pressure distributions are similar for both premixer inlet conditions. Pressure is maximal at the premixer inlet. It steeply decreases and reaches zero between microphones M4 and M5, in the flame region. In the combustion chamber, pressure passes by a maximum, about half the absolute value measured in the premixer, in the middle of the chamber and then decreases to reach zero at the exhaust of the rig. Examination of the phase between microphones has shown that there is no noticeable effect of the ICS on the phase of the pressure distribution.
A direct consequence is that the acoustic velocity is maximum in the flame region, at the junction between the premixer and the chamber. The flame dynamics is very sensitive to velocity oscillations in that region which explains the strong flame-acoustic coupling observed at $f_{inst} = 272\,\text{Hz}$ when the premixer inlet is almost perfectly reflective. When the ICS is used to lower the value of the reflection coefficient, the amplitude of the velocity fluctuations in the flame region is also diminished, which in turn damps the instability.

As shown in the preceding chapter, it is also interesting to examine the correlation between the acoustic field and the heat-release rate fluctuations in the combustor. It was shown that the Rayleigh source term in the acoustic energy balance is proportional to such correlation:

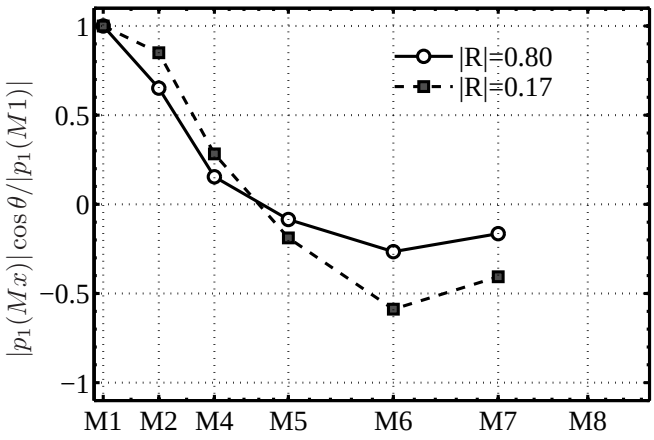

Figure 6.15: Shape of the pressure oscillation measured at $f = 272\,\text{Hz}$ for two premixer inlet boundary conditions.

$$\frac{1}{T}\int_V\int_0^T p_1\dot{q}_1 dt dv \propto \frac{1}{T}\int_0^T p_1(M5)I_1 dt$$

This is realized by computing the Cross Power Spectral Density $P_{PM,M5}$ between the pressure fluctuations in the flame region, measured by M5, and the variations of the heat-release rate estimated using photomultiplier tubes (see chapter 2 for more details on the setup). It can however be interesting to analyze this relation using the other microphones. This is achieved by computing the CPSD between the PMT and any microphone $P_{PM,Mx}$, which is then normalized by the CPSD between the PMT and M5 $P_{PM,M5}$.
The normalized CPSD amplitude $P_{PM,Mx}/P_{PM,M5}$ is plotted, at the instability frequency $f_{inst} = 272\,\text{Hz}$ in the upper graph of figure 6.16, and its phase is reported in the lower graph. Evolutions are compared for the two values of the premixer inlet reflection coefficient. As studied in chapter 5, when the combustion is unstable, the heat-release rate and the pressure oscillations in the flame region feature a phase shift lower than $90\,^{\text{o}}$, satisfying the Rayleigh criterion. For a hard inlet, $|R| = 0.80$, the phase lag in the flame region is about $60\,^{\text{o}}$ and decreases to approximately $25\,^{\text{o}}$ for a soft inlet, $|R| = 0.17$. This shift of about $30\,^{\text{o}}$ occurs on all other cross-correlations. It was However previously observed that modifications of the premixer inlet condition has no effect on the phase lag of the cross-correlation between the different microphones. Therefore, this overall shift of the curve can be attributed to the shift between microphone M5 and the PMT when the value of the reflection coefficient is lowered.

A consequence is that a modification of the premixer inlet reflection coefficient from $|R| = 0.8$ to $|R| = 0.17$ only barely modifies the phase lag between the pressure field and the unsteady combustion dynamics in the vicinity of the flame region. The Rayleigh criterion is yet always satisfied, and the damping effect can be attributed mainly to the reduction of the peak amplitude by sound absorption at the premixer inlet.

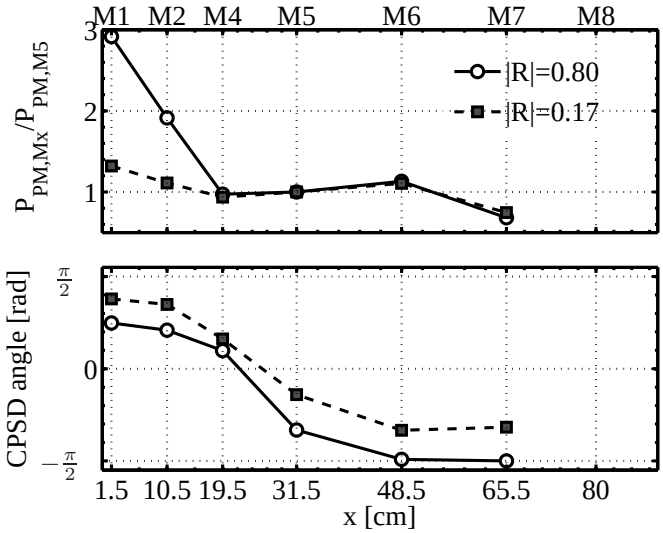

Figure 6.16: Influence of the premixer inlet impedance on the CPSD measured between the heat-release rate and the pressure fluctuations at the instability frequency $f = 272\,\text{Hz}$. (Top) Evolution of the CPSD between PMT and microphones, normalized by the CPSD between the PMT and M5 (in the flame region). (Bottom) Phase of the CPSD.

Concluding remarks

An acoustic model has been developed to determine the eigenmodes in a simplified geometry of the facility, taking into account the ICS at the premixer inlet. This model highlights the importance of the area expansion ratio between the premixer and the chamber. When this ratio is high enough, eigenmodes are decoupled and can be associated with each cavity. The predicted eigenfrequencies were then compared to the results obtained when external acoustic forcing of the combustion rig was applied in non reactive isothermal configurations. The importance of the premixer geometry was stressed out. Indeed, when the premixer is reduced to its central inner channel, eigenmodes are correctly predicted in terms of frequencies and structure. When the fuel and air manifolds are added to the premixer, the model fails to predict the observed frequency shift of the second eigenmode, from $f^1_{PC} = 370\,\text{Hz}$ to $F^1_{rig} = 270\,\text{Hz}$. However the structure of the three first detected modes f^n_{rig} was again successfully associated with the three first theoretical eigenmodes f^m_{PC}. In the reactive configuration, the pressure distribution of the main instability peak was associated with the second theoretical eigenmode f^1_{PC}. This mode is related mainly to the premixer. It was shown that the ICS has a strong influence mainly on the amplitude of the eigenmodes in the premixer only. This effect is confirmed by the acoustic model, and account for the efficiency of the ICS when the instability is driven by the acoustic mode associated with the premixer geometry.

Conclusion & Perspectives

This investigation is concerned with the influence of acoustic boundary conditions on combustion oscillations, induced by a resonant coupling between unsteady turbulent combustion and the system acoustics. Such instabilities are commonly encountered in modern lean premixed combustors and have been the subject of numerous studies because of their impact on practical systems. The phenomenon is complicated by the many different physical processes and interactions that must be taken into account.
The role of boundary conditions is less well studied experimentally, despite its assessed importance. Acoustic boundary conditions determine the structure of the acoustic field in the system. In addition, they control acoustic fluxes at the inlet and outlet of the combustion zone. The main objective of the present investigation was to examine the influence of the upstream acoustic boundary condition by developing an adaptive acoustic inlet condition, that allows investigation of self-sustained thermoacoustic oscillations in a turbulent combustor.
This was achieved by designing the Impedance Control System (ICS), a passive solution to pilot acoustic impedances in a wide range of operating conditions. An existing swirled turbulent combustion rig was modified to enable detailed measurements not only inside the combustion chamber but also inside the injection device. The ICS was implemented in the combustion rig to create the CTRL-Z facility. The influence of the acoustic inlet condition on the thermoacoustic coupling, during self-sustained cycles, was examined and an experimental evaluation of the global acoustic energy balance was obtained.

ICS and high load impedance tube

The ICS is a passive acoustic control solution based on perforated plates. It is efficient over a wide range of perturbation amplitudes, from a few Pascals ($100\,$dB) to high Sound Pressure Levels about $150\,$dB as encountered during severe combustion instabilities.
A facility was specifically developed to study and design of this ICS: the high load impedance tube. The main features of this facility dedicated to acoustic measurements are:

- Its modularity and versatility,
- Air flow injections to create uniform bias flow velocity through the perforates, from 0 to $10\,\mathrm{ms}^{-1}$ as used in the present work,
- A wide range of accessible Sound Pressure Levels, from 80 to $150\,$dB between 50 and $2\,$kHz.

This facility was also used to develop and benchmark the impedance measurement technique relying on the Two-Microphone Method (TMM). This technique was successfully used, in the

impedance tube, to measure acoustic impedances of perforates. The TMM was also effectively used to measure impedance inside the combustion rig, with the flame as unique sound source. In addition acoustic impedance of active elements (flame anchored on a plate) was experimentally retrieved with this technique and compared to model predictions.
Thanks to its modularity and its wide range of operating parameters, this impedance tube allowed extensive parametric investigation of the ICS. Perforated plates, backed by a resonant cavity, with bias flow promoting vortex shedding at the apertures rim were designed on the basis of a linear acoustic model. This model, derived initially by Howe (1979) and later improved by Hughes and Dowling (1990), was studied to find optimal solutions in extended ranges of operation. The main originalities are first the reduced perforated area available in the ICS, while the linear model was originally used to design large acoustic mufflers. Second, the ICS is an adaptive device, where piloting the back-cavity depth controls the modulus of the reflection coefficient of the perforates. In contrast, acoustic dampers usually feature fixed geometries optimized for one operating condition.
The preliminary analytical study of this linear model also highlighted, for the perforates geometry of interest in the ICS, the existence of a single optimal bias flow velocity in a wide frequency range extending from 100 to 1000 Hz. Theoretical design and results are in excellent agreement with the experimental results obtained with low levels of incident perturbations for the complete set of perforates tested. In particular, the link between the optimal bias flow velocity through the perforates and their geometry is confirmed. It was demonstrated that the ICS allows efficient control of the acoustic reflection coefficient of each perforate by piloting the back-cavity depth at low SPL. Further investigation was led to measure the behavior of the ICS with increasing SPL, eventually reaching the amplitude of pressure perturbations measured during combustion instabilities. Once reverse flow is promoted inside the apertures of the perforates, the ICS features a non-linear response to the incident perturbations, and the control capacity of the system is hindered. The experimental data at high SPL could be successfully compared to the semi-empirical non-linear model of Ingard and Ising (1967). This completes the linear model of Howe (1979), to provide a general framework for the acoustic response of the ICS in an extended range of incident SPL. Experiments indicate that a transition occurs between the linear, bias-flow controlled (BFC), regime and the non-linear, perturbation fluctuation controlled (PFC), regime. A criterion was determined as a function of the perforated plates geometry. The ICS can thus be optimized depending on the operating conditions (in terms of SPL) to remain in the BFC regime, and achieve efficient and robust acoustic control of strong combustion instabilities. This was demonstrated with the combustion rig.

Detailed instrumentation of the CTRL-Z combustion rig

The ICS was tested on a turbulent combustion rig, which features most of the characteristics of modern combustion gas turbines at a lab scale. Flame is indeed stabilized by a strong swirl and operates in lean and premixed conditions, with an axial fuel staging. This device exhibits strong combustion oscillations in most of its operation domain, depending on the fuel staging. This rig was modified to increase the number of measurements access ports in its premixer. The new rig, named CTRL-Z, is now devoted to precise acoustic measurements.
Three types of diagnostics were implemented during this work. High Speed PIV gives access to the flow dynamics during unsteady combustion cycles. It was mainly used to examine the influence of the ICS on the aerodynamics of the combustion rig. The air flow bypassed from

the main injection to feed the ICS represents only a small fraction of the total airflow and has no effect on the main flowfield. The ICS has thus solely an acoustic effect on the combustion rig.
Chemiluminescence measurements with photomultiplier tubes were also set up. In addition to classic analysis in the frequency domain of the correlation between the heat-release rate and the pressure fluctuations, a quantitative estimation of the Rayleigh source term was devised. This estimation of the main energy source term during combustion oscillations was completed by an evaluation of acoustic energy fluxes at the premixer inlet and chamber exhaust of the CTRL-Z facility. This quantitative estimate of acoustic energy fluxes was made possible by precise acoustic measurements throughout the CTRL-Z facility.
The presence of microphones inside the premixer and in the combustion chamber also allowed to characterize the shape of the acoustic pressure distribution in the facility, and thus of the main instability mode. The TMM was used during combustion tests to retrieve the impedance of the ICS, with successful comparisons with the database gathered in the high load impedance tube. As a consequence, this database and the theoretical framework can both be used to predict the acoustic response of the ICS once implemented on the CTRL-Z rig to control its inlet acoustic boundary condition.

Influence of the acoustic boundary conditions on combustion instabilities

The ICS implemented on the CTRL-Z rig was shown to effectively reduced combustion oscillations. By controlling the premixer inlet impedance to minimize the modulus of its reflection coefficient, important damping of the combustion instability was demonstrated. Despite its reduced size (30 mm-diameter), a 20 dB reduction of the main instability peak was achieved inside the premixer, yielding to a 10 dB damping in the combustion chamber. The ICS thus allows to nearby cancel instabilities occurring in the low frequency range. This first result highlights the sensitivity of the flame to the dynamics of the fresh reactants zone, and to its upstream acoustic conditions.
An experimental evaluation of the acoustic energy balance in the facility was carried out, by measuring the Rayleigh source term and the acoustic fluxes as functions of the premixer inlet reflection coefficient. The acoustic fluxes in the premixer are of the same order as the energy source term. It was shown that this term must be taken into account in the acoustic energy balance. In the unstable situation, fluxes and source terms are in balance. When the ICS is used, the acoustic energy reflected inside the premixer is diminished, which limits the amplitude of the resonant acoustic feedback. The amplitude of the acoustic energy source term thus also decreases. Eventually, with a minimal ICS reflection coefficient, acoustic fluxes in the premixer appear to overcome the source term, therefore totally cancelling the growth of the instability.
It has however been observed that the efficiency of the ICS is dependent on the main combustion instability mode. The ICS is efficient for instabilities observed around 280 Hz, while it has no effect for instabilities observed around 320 Hz. Therefore a study was carried out to determine the eigenfrequencies associated with the combustor geometry. An acoustic model was built which accounts for the different geometries and gases in the premixer and the chamber, as well as for the premixer inlet acoustic boundary condition. Theoretical eigenfrequencies were then compared to experimental results obtained in cold flow experiments. The modal structure of the CTRL-Z rig is composed of quarterwave type modes associated with the chamber and to

the premixer lengths. The complex geometry of the premixer results in a fundamental mode at $f = 270\,\text{Hz}$, very sensitive to the premixer inlet reflection coefficient. The modes associated to the chamber are unaffected by the premixer acoustic structure and are mostly dependent on the gas temperature; the fundamental mode of the chamber is calculated, in combustion, close to $f = 326\,\text{Hz}$. As a result, the ICS effectively controls instabilities associated to the premixer mode, and is inefficient for instabilities linked to the chamber modes, because of the CTRL-Z inner geometry.

Perspectives

The study upon the perforates acoustics has allowed to design an effective damping system, operating over a wide range of pressure levels. Yet the influence of the plate thickness and aperture diameter on this dependency to SPL needs further investigation. The plate thickness plays a role in the energy dissipation through the plate, via viscous effects in the boundary layers which develop in a thick plate (Melling 1973). It may also affect the vortex shedding at the aperture rim. Indeed an orifice in a thin plate may be considered as an unflanged aperture. In a thick plate it would be assimilated to a flanged pipe with an impact on acoustic propagation (Peters et al. 1993). The aperture diameter was not varied in this study, as it was previously stated that it is of lesser importance (Ingard and Ising 1967). However, it may be expected that small and large apertures feature different responses, depending on the frequency of the incident perturbation.

Accurate measurements of the bias flow velocity, as a function of the incident SPL, would also be of obvious interest. As apertures are small, the recent developments of micro-PIV offer an interesting solution for non-intrusive velocity measurements. The HSPIV used for measurements in combustion may also prove useful to examine the transient mechanism of vortex shedding at the aperture rim, and its interaction with incident pressure waves.

As the ICS device was developed as independently as possible from the combustion rig, it would be interesting to adapt it to other laboratory-scale facilities to further test its efficiency and robustness, and eventually implement it on a gas turbine combustor.

To pursue the experimental investigation on effects of acoustic boundary conditions on combustion dynamics, the exhaust condition from the CTRL-Z rig should be modified to vary the outlet impedance. The chamber itself is however not designed to sustain increased operating pressures, therefore it appears difficult to directly adapt the ICS at the exhaust.

The possibility to measure acoustic impedances, along with detailed meshing of the acoustic pressure field and instantaneous flowfield acquisition in the whole facility can also be used to gather an experimental database for validation of numerical combustion dynamical tools.

Finally, the possibility to suppress combustion instabilities in the CTRL-Z facility makes it suitable for investigation of combustion noise in confined configurations.

Appendix A

HSPIV

A complement to the aerodynamic study presented in chapter 2 is given in this appendix. The mean velocity fields can be found in section 2.3.3. The description of the HSPIV is provided in chapter 2. Results gathered in what follows concern the standard deviation, or RMS (Root Mean Squared), of the axial U' and radial V' velocities. Profiles are plotted in planes located at $x/D = 0.2$ and $x/D = 1.0$ (where $D = 30\,\text{mm}$ is the premixer channel diameter). The RMS profiles are plotted for two premixer inlet reflection coefficients: $|R| = 0.80$ obtained with $L = 0\,\text{mm}$ and $|R| = 0.17$ at $f = 272\,\text{Hz}$ obtained with $L = 280\,\text{mm}$. The objective is to determine whether the ICS has an influence on the aerodynamic flowfield.
As a slight difference is noticeable between the profiles for $|R| = 0.80$ and $|R| = 0.17$ on both velocities (figures A.1 and A.3 for U' and V' respectively), the relative difference between the two configurations was computed with respect to the reference case $|R| = 0.80$:

$$dU' = \frac{U'(|R| = 0.80) - U'(|R| = 0.17)}{U'(|R| = 0.80)} \tag{A.1}$$

$$dV' = \frac{V'(|R| = 0.80) - V'(|R| = 0.17)}{V'(|R| = 0.80)} \tag{A.2}$$

Profiles of these two quantities, are presented in figures A.2 and A.4 for the axial and radial velocities respectively. The average difference does not exceed 5%.

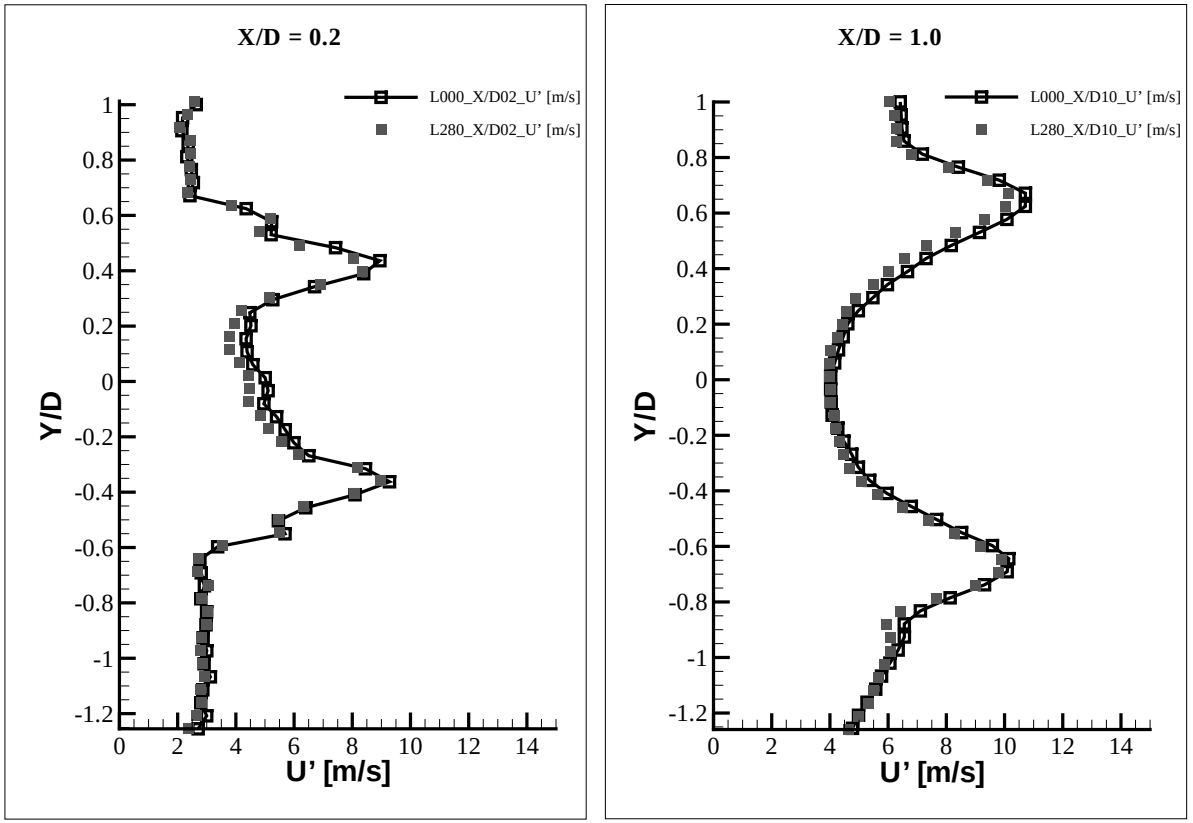

(a) $X/D = 0.2$. (b) $X/D = 1.0$.

Figure A.1: RMS of axial velocities extracted at $x/D = 0.2$ (a) and $x/D = 1$ (b). Solid black line represent the configuration with no back-cavity ($L = 0$ mm, $|R| = 0.80$), while grey squares plot the $L = 280$ mm case ($|R| = 0.17$).

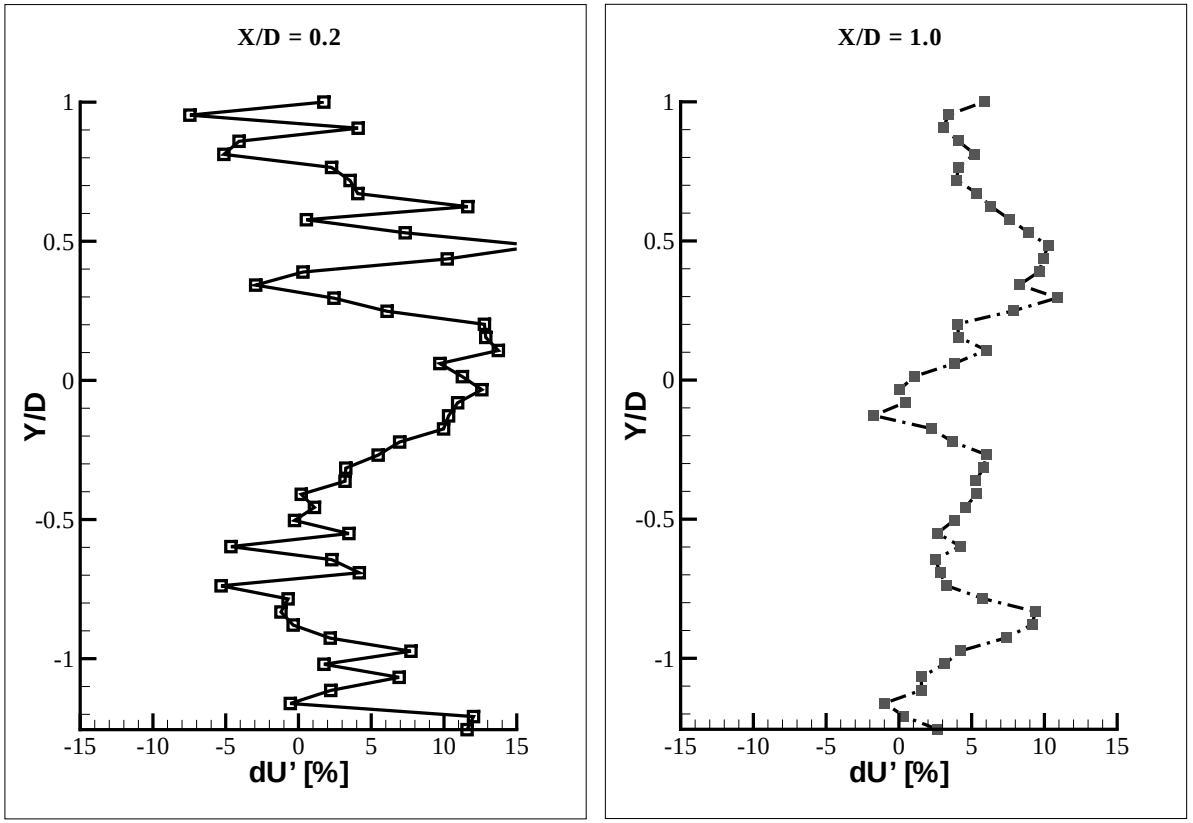

(a) $X/D = 0.2$.

(b) $X/D = 1.0$.

Figure A.2: Difference on the RMS of axial velocities dU' extracted at $x/D = 0.2$ (a) and $x/D = 1$ (b). Difference is computed between the reference case ($L = 0\,\text{mm}$, $|R| = 0.80$) and the case $L = 280\,\text{mm}$, $|R| = 0.17$, in percentage.

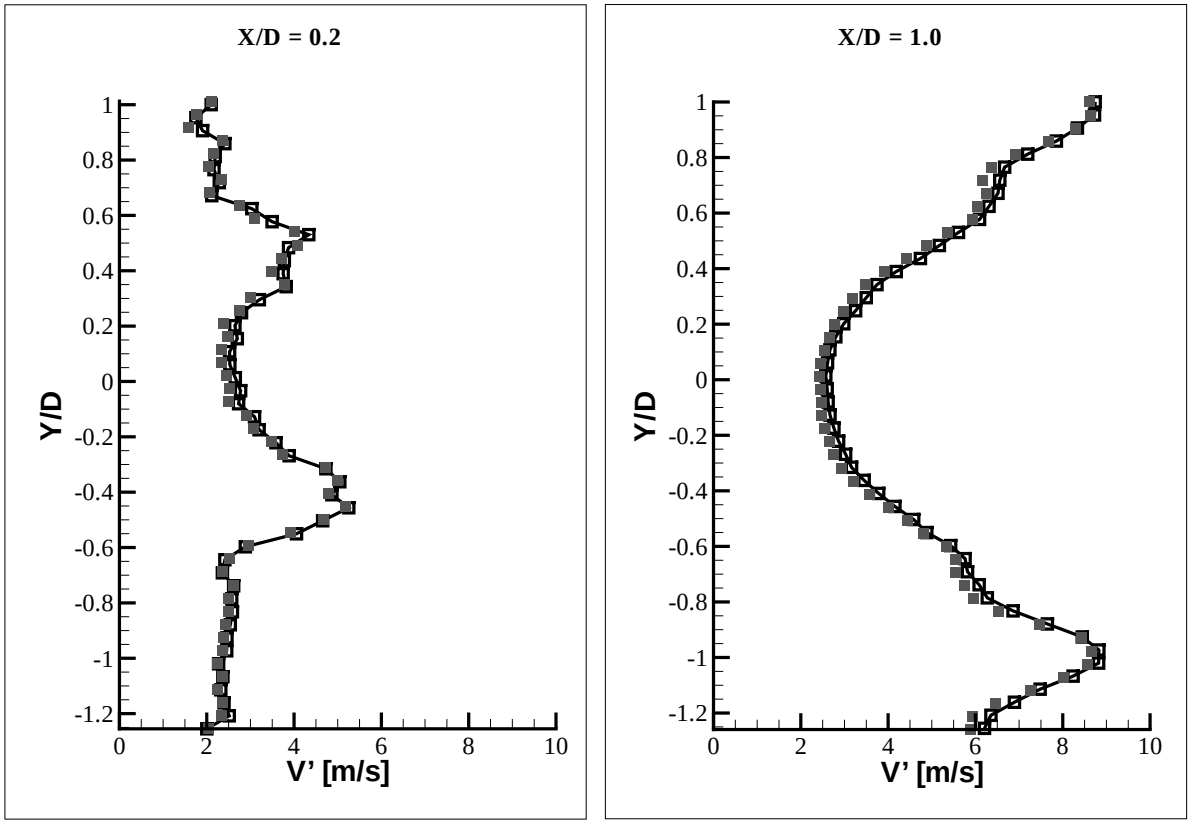

(a) $X/D = 0.2$.

(b) $X/D = 1.0$.

Figure A.3: RMS of radial velocities extracted at $x/D = 0.2$ (a) and $x/D = 1$ (b). Solid black line represent the configuration with no back-cavity ($L = 0$ mm, $|R| = 0.80$), while grey squares plot the $L = 280$ mm case ($|R| = 0.17$).

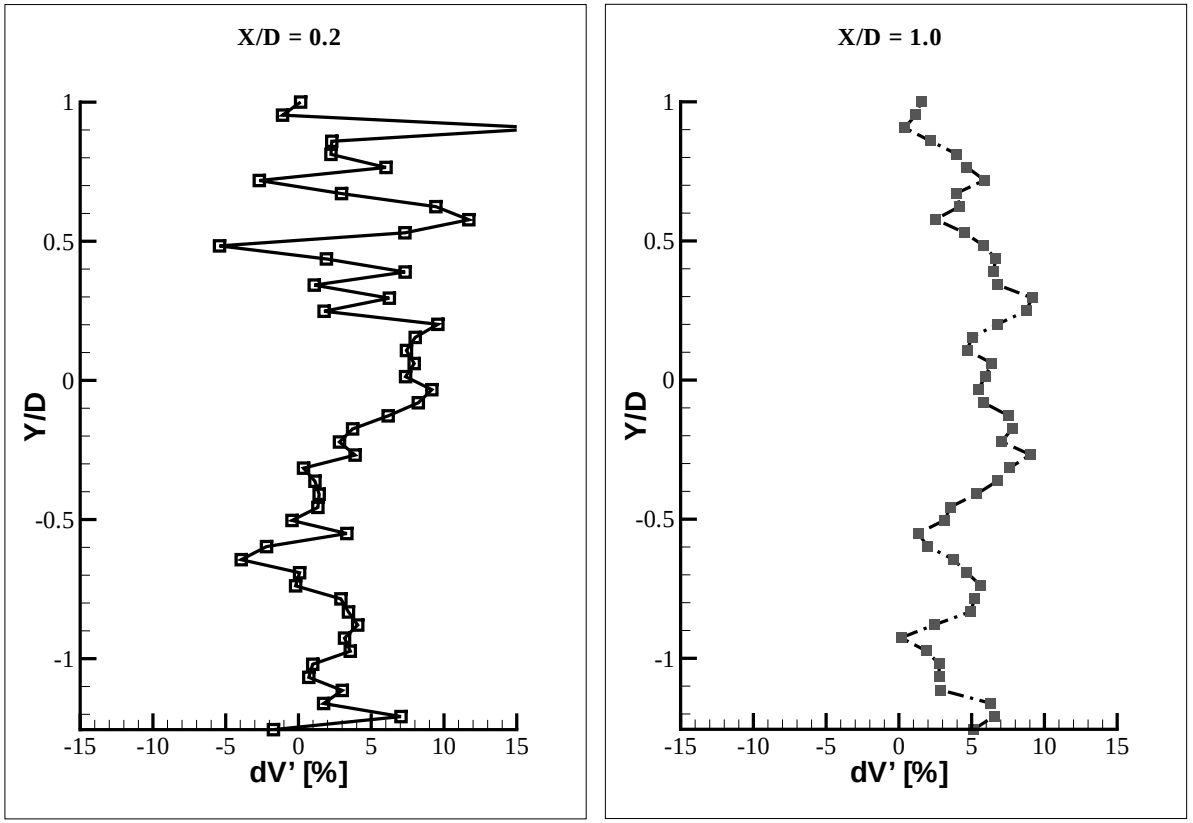

(a) $X/D = 0.2$.

(b) $X/D = 1.0$.

Figure A.4: Difference on the RMS of radial velocities dV' extracted at $x/D = 0.2$ (a) and $x/D = 1$ (b). Difference is computed between the reference case ($L = 0\,\text{mm}$, $|R| = 0.80$) and the case $L = 280\,\text{mm}$, $|R| = 0.17$, in percentage.

Appendix B

Design of perforated plate at low SPL

The theory below is adapted from the work of Hughes and Dowling (1990). The objective is to define the acoustic property of a perforated panel backed by a cavity, in order to design a system used to smoothly vary the reflection coefficient from zero to unity. This appendix is an addition to section 4 of chapter 4. It aims at giving more insight on the parametric investigation that was led on the linear model and its implication in terms of design, illustrated with the conception of plate P8.

B.1 Theory of acoustic damping by perforated panels

It is established that perforated panels can efficiently dissipate incident acoustic energy, mainly through conversion of the latter to kinetic energy by vortex shedding at the edges of the aperture. This damping is significantly increased when a mean flow is created through the apertures (Eldredge and Dowling 2003), (Hughes and Dowling 1990). Fundamentals of the theory on acoustic energy dissipation by vortex shedding can be found in the work of Melling (1973), Howe (1979) and Bechert (1980). An update of the latter has been published by Luong et al. (2005). In these theories damping is obtained by modification of the reflection coefficient of the plate due to vortex shedding.

B.1.1 Reflection coefficient of a perforated panel backed by a cavity

The geometry of interest is illustrated in figure B.1. It consists in a rigid plate in the plane $x = 0$ constituted of a uniform array of circular apertures of radius a separated by a distance d ; the aperture spacing d is much smaller than the wavelength λ of acoustic pressure oscillations. The plate is backed by a cavity formed by rigid walls such that the depth L of the cavity is much larger than the aperture radius a. A mean flow of velocity U goes through the apertures, at low Mach ($\mathrm{M} \ll 1$) but high Reynolds number ($\mathrm{Re} \gg 1$), so that viscosity is dominant only in the vicinity of the plate. Flow separation occurs at the rear part of the apertures. Shed vortices are then convected away by the uniform flow. For our purpose, only normal harmonic incident sound waves are considered and the effect of the plate thickness is not considered, so

the plate is infinitely thin.

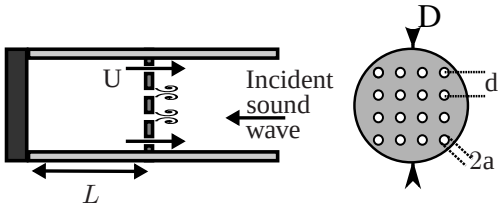

Figure B.1: Geometry of a perforated panel backed by a cavity with bias flow. $d \ll \lambda, a \ll L$. U bias flow velocity through the apertures, a aperture radius and d aperture separation distance.

The acoustic properties of the perforated panel in figure B.1 can be described by the following relation for the pressure gradient $\delta p/\delta x$ through the panel:

$$\frac{\delta p}{\delta x} = \eta \left[p\right]_{x=0^-}^{x=0^+} \tag{B.1}$$

where $[p]_{x=0^-}^{x=0^+}$ denotes the pressure jump created by the perforated panel. The effective compliance η is, in the described configuration, proportional to the Rayleigh conductivity of the circular aperture of radius a, as defined by Howe (Howe 1979) :

$$\eta = \frac{2a}{d^2}\mathrm{K_R} \tag{B.2}$$

with

$$\mathrm{K_R}\left(\mathrm{St}\right) = \gamma - i\delta \tag{B.3}$$

where γ and δ are real positive functions of the Strouhal number, $\mathrm{St} = \omega a/U$ with $\omega = 2\pi f$, given by :

$$\gamma.f\left(\mathrm{St}\right) = I_1^2\left(\mathrm{St}\right)\left[1 + \frac{1}{\mathrm{St}}\right] + \frac{4}{\pi^2}\,\mathrm{e}^{2\mathrm{St}}\cosh\left(\mathrm{St}\right)K_1^2\left(\mathrm{St}\right)\left[\cosh\left(\mathrm{St}\right) - \frac{\sinh\left(\mathrm{St}\right)}{\mathrm{St}}\right] \tag{B.4}$$

$$\delta.f\left(\mathrm{St}\right) = \left[\frac{2}{\pi\mathrm{St}}\right] I_1\left(\mathrm{St}\right)K_1\left(\mathrm{St}\right)\mathrm{e}^{2\mathrm{St}} \tag{B.5}$$

where $f\left(\mathrm{St}\right) = I_1^2\left(\mathrm{St}\right) + \frac{4}{\pi^2}\,\mathrm{e}^{2\mathrm{St}}\cosh^2\left(\mathrm{St}\right)K_1^2\left(\mathrm{St}\right)$ and I_1 and K_1 are the modified Bessel functions.
The evolutions of γ and δ are plotted against the Strouhal number in figure B.2. From the asymptotic form of the Bessel functions, the limits of $\mathrm{K_R}$ are :

$$\mathrm{K_R} \approx 1 - i/\mathrm{St} \text{ as } \mathrm{St} \to \infty \tag{B.6}$$

$$\mathrm{K_R} \approx \mathrm{St}^2/3 - i\pi\mathrm{St}/4 \text{ as } \mathrm{St} \to 0 \tag{B.7}$$

In absence of bias flow, $U = 0$ corresponding to $\mathrm{St} \to \infty$, the Rayleigh conductivity approaches unity, $\mathrm{K_R} = 1$.

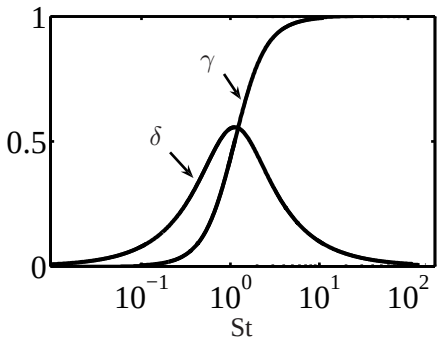

Figure B.2: Evolution of δ and γ for an infinitely thin plate

For a large distance compared to the aperture spacing, the pressure fluctuation can be written as the sum of incident and reflected plane waves:

$$p = \left[\mathrm{e}^{-ikx} + R\,\mathrm{e}^{ikx}\right]\mathrm{e}^{-i\omega t} \tag{B.8}$$

where R is the reflection coefficient at the surface of the perforated panel. Combining equations B.1, B.8 and the continuity of velocity through the apertures, the reflection coefficient can be expressed as :

$$R = \frac{(ik/\eta) + 1 - (i/\tan(kL))}{(ik/\eta) - 1 - (i/\tan(kL))} \tag{B.9}$$

where k is the wavenumber, $k = 2\pi f/c_0$, with c_0 the speed of sound.
In the absence of bias flow, $\mathrm{K_R} = 1$, it was shown that there is no absorption and the coefficient R equals 1 (Leppington and Levine 1973). With a bias flow, $\mathrm{K_R}$ is then complex, $|R| \leq 1$, and sound is absorbed by vortex shedding (Hughes and Dowling 1990).

For a normal incident sound wave at very low frequency with no bias flow, each aperture can be seen as a local Helmholtz resonator of volume Ld^2 and Rayleigh conductivity $2a$. The resonant frequency of such a resonator is given by $k^2_{helm} = \left(2a/Ld^2\right)$. Following the developments of Hughes and Dowling (1990), let's introduce two non-dimensional parameters, the Helmholtz number He and the resonance number Q such that :

$$\mathrm{He} = kL \tag{B.10}$$

$$\mathrm{Q} = \left(\frac{k}{k_{helm}}\right)^2 = \frac{k^2 d^2 L}{2a} \tag{B.11}$$

Then the reflection coefficient can be rewritten as :

$$R = \frac{\mathrm{Q}/\mathrm{K_R}\,(\mathrm{St}) - i\mathrm{He} - [\mathrm{He}/\tan(\mathrm{He})]}{\mathrm{Q}/\mathrm{K_R}\,(\mathrm{St}) + i\mathrm{He} - [\mathrm{He}/\tan(\mathrm{He})]} \tag{B.12}$$

It is a function of non-dimensional parameters only, the Strouhal number St, the Helmholtz number He and the resonance number Q.
Theoretical developments conducted by Rayleigh (1899) and Howe (1979) have led to two main results :

1. The dissipation of energy should be more efficient at low Strouhal numbers ; for low value of St, vortices can stretch far away from the aperture, and have a strong effect on the flow by blocking periodically the aperture.

2. From the theory of the Helmholtz resonator, the maximum sound absorption should occur close to the Helmholtz resonant frequency, $\mathrm{Q} = 1$.

B.1.2 Theoretical evolution of the absorption coefficient

Theoretical predictions for the absorption coefficient $\alpha_{ac} = 1 - |R|^2$ are plotted in figures B.3 and B.4 against the resonance parameter for different Helmholtz numbers He, at a Strouhal of $\mathrm{St} = 2$. It can be seen that for $He \leq \pi$ (fig. B.3, curves (-),(–),(-.)) :

1. Absorption maxima occur close to the Helmholtz resonant frequency $\mathrm{Q} = 1$.
2. Efficient sound absorption (above 50%) is achieved only for a small range of Q values. This range broadens with increasing Helmholtz number He.
3. Sound absorption is maximum for $\mathrm{He} \approx 0.3$.

Therefore, at low Helmholtz numbers, good absorption can be expected close to $\mathrm{Q} = 1$, but only in a narrow frequency range, which is fixed by the geometry of the system (from eq. (B.11)). However, for larger values of the Helmholtz number, $\pi \leq \mathrm{He} \leq 2\pi$, absorption greater than 50% can also be achieved, but at higher values of Q (fig. B.4). In this Helmholtz range, the maximum absorption is obtained for $\mathrm{He} = 3.7$, at $\mathrm{Q} = 6.4$. In figure B.4, it is also clear that the absorption maxima are much broader. A strong absorption appears also feasible in a wider frequency range. It can be concluded that, even though strong sound absorption occurs close to the Helmholtz resonant frequency $\mathrm{Q} = 1$, absorption maxima can also be found at higher values of $Q > 1$ for Helmholtz values He greater than π .

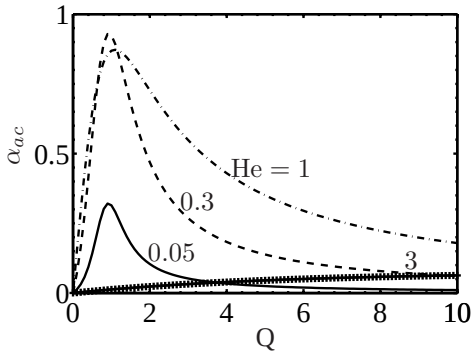

Figure B.3: Absorption coefficient for a perforated panel backed by a rigid wall with bias flow as a function of the resonance parameter Q for $\mathrm{St} = 2$ and $\mathrm{He} \leq \pi$.

The dependence on the Strouhal number of these results is further studied. The evolution of the absorption coefficient with increasing St is plotted for an Helmholtz number of 0.3 in figure B.5. The maximum absorption occurs for a Strouhal around 3 (fig. B.5, $--$). For higher St values, the maximum absorption slowly decreases, whereas it decreases quickly when the St number goes below 3. Indeed for $\mathrm{St} = 9$, the absorption is still higher than for $\mathrm{St} = 1$. It should also be noted that for a fixed Helmholtz number, the maximum absorption remains near $\mathrm{Q} = 1$ when increasing St, whereas the value of Q at the maximum continuously decreases with St. To summarize, at high Strouhal numbers, the maximum absorption remains around $\mathrm{Q} = 1$ and has a weak sensitivity to St. But at low Strouhal numbers, there is a strong dependence of the absorption to both Q and St parameters. Thus it is not sufficient to design the perforated plate by simply fixing the geometry without considering the bias flow velocity.

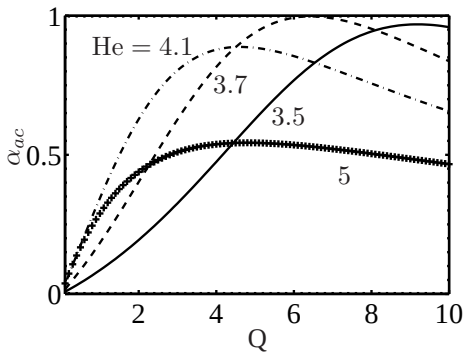

Figure B.4: Absorption coefficient for a perforated panel backed by a rigid wall with bias flow as a function of the resonance parameter Q for $\mathrm{St} = 2$ and $\mathrm{He} \geq \pi$.

In addition it seems interesting to work with low bias flow velocities U.

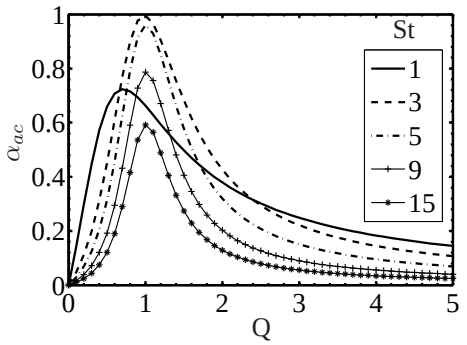

Figure B.5: Absorption coefficient for an Helmoltz number of 0.3.

To further study the effect of Q, St and He on the absorption, contours of iso-levels of the absorption coefficient α_{ac} at four different Helmholtz numbers are plotted in figure B.6. For low He ($\mathrm{He} \leq 1$), strong absorption is obtained close to $\mathrm{Q} = 1$ with a weak dependency to the Strouhal number St, thus to the velocity. For increasing He, the absorption becomes less and less dependent on the resonance parameter Q.
From this study, it appears that:

- At low He, typically below unity, the value $\mathrm{Q} = 1$ effectively locates the maximum absorption achievable.
- At higher He ($\mathrm{He} \geq 1$), the strongest absorption must be detected at other values of Q.
- In both cases, the dependency of the absorption coefficient α_{ac} to the Strouhal number is weak, and gives freedom in selecting the bias flow velocity.

In figure B.7, the resonance number has been fixed to two values : 1 and 6.4. It is clear that for the value close to the Helmholtz resonant frequency ($\mathrm{Q} = 1$), efficient absorption can be attained for a large range of Strouhal numbers St only at low Helmholtz numbers He. On the contrary, for higher values of $\mathrm{Q} > 1$, good absorption will be possible only for very few values of the pair (St, He).

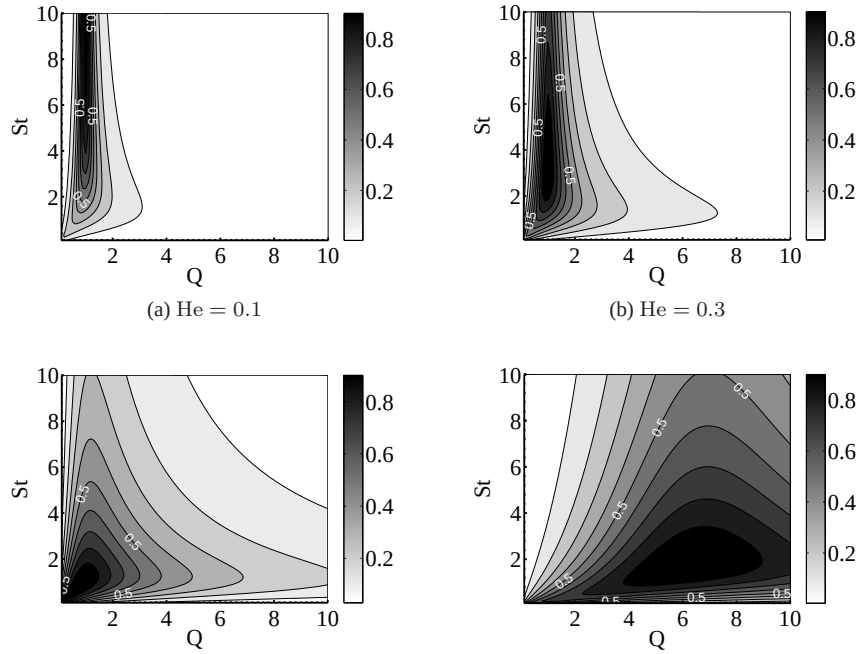

(a) He $= 0.1$ (b) He $= 0.3$

(c) He $= 1$ (d) He $= 3.7$

Figure B.6: Absorption coefficient for different Helmholtz numbers

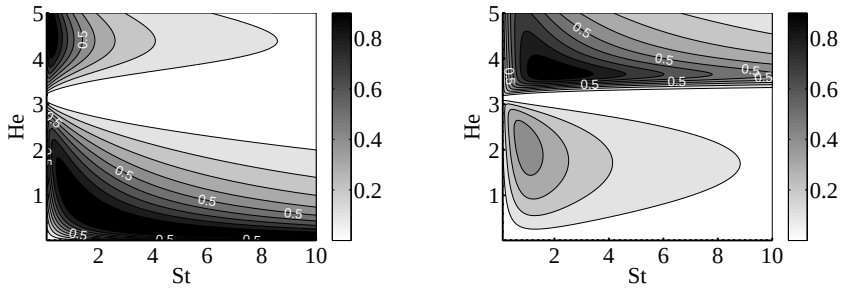

(a) Q $= 1$ (b) Q $= 6.4$

Figure B.7: Absorption coefficient $\alpha_{ac} = 1 - |R|^2$for different resonance numbers.

From there, the procedure for designing a perforated panel can be deduced : the frequency to which absorption must take place, the aperture radius and spacing must be selected first. Then the cavity depth must be chosen so that either Q ≈ 1 and He $\leq \pi$ (small depth), or Q ≥ 1 and He $\geq \pi$ (large depth) in order to achieve high absorption levels.

B.2 Control of the reflection coefficient

In the present application, the aim is not to totally cancel the reflection coefficient for a given frequency, as it is done for example by Jing and Sun (1999) and Forster and Michel (2003) .

The objective here is rather to control the reflection coefficient over a wide frequency band. Due to some geometrical limitations of the test bench used in the present study, the imposed diameter of the plate is 30 mm and it was decided to focus on the low frequencies range ($[100 - 1000]$ Hz), where first modes of unstable combustion are observed in practical systems. The aperture diameter and spacing must then be quite reduced : a diameter of $2a = 1$ mm and a spacing of $d = 8$ mm, which results in a porosity (defined as the ratio of the open to total areas) of 1.23%, were chosen. This yields to 9 holes in the plate (fig. B.8). As we are interested in attenuating a broad band of frequencies, the depth of the cavity is a design parameter.

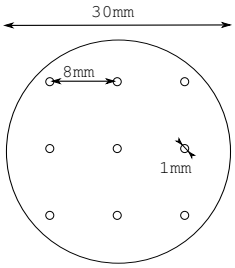

Figure B.8: Schematic of the designed plate, with $a = 0.5$ mm and $d = 8$ mm.

B.2.1 Evaluation of the feasibility

The feasibility of acoustic energy damping by the perforated panel just described must first be assessed ; the velocity range for optimal absorption must also be determined. Let us impose a resonance number equal to unity Q $= 1$. For the frequency range of interest, the depth of the cavity L then ranges from 4.6 cm to 4.6 m (figure B.9a). To attenuate in the very low frequency range, exaggerated depths are theoretically required. With a cavity length smaller than 50 cm, it is possible to work above 300 Hz.

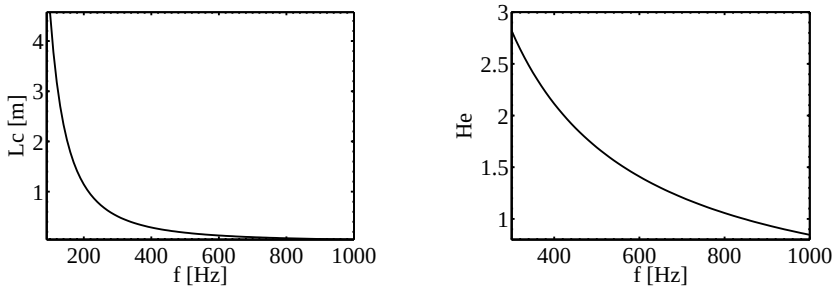

(a) Depth of the cavity

(b) Helmholtz number

Figure B.9: Q $= 1$, with $2a = 1$ mm and $d = 8$ mm

This range of cavity depth fixes the range of Helmholtz number He (fig.B.9b) between 0.84 and 3. With Q$= 1$ and this calculated range of He, the Strouhal number St giving the maximal absorption coefficient α_{ac} can be determined using results plotted in computed in figure B.7a. Absorption higher than 50% can be expected.

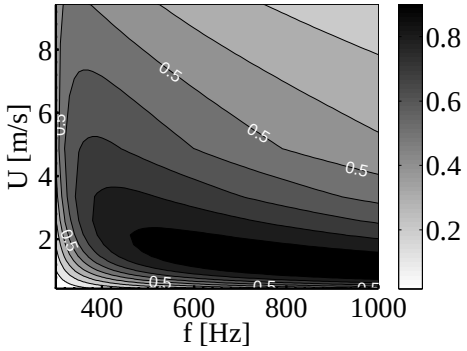

Figure B.10: Absorption coefficient as a function of the bias flow velocity U and of the frequency

These results are translated in term of velocity and frequency (fig. B.10). Maximum absorption is obtained for a bias flow velocity through the apertures around 1.7 m.s^{-1} over most of the frequency range.

B.2.2 Final design

It has been verified that such a plate can efficiently damp acoustic energy ; the preceding results are however computed with a fixed resonance number Q$= 1$, condition that may not be easy to achieve in a piratical setup. To cross-check these results and accurately design the system, the absorption coefficient is now computed without imposing any dimensionless number. The geometrical parameters of the plate are fixed ($a = 0.5$ mm, $d = 8$ mm), the cavity depth is limited to $L = 50$ cm, the frequency range is $100 - 1000$ Hz and the velocity ranges from 0 to 3 m.s^{-1}.
To accurately determine which pair (bias-flow velocity U, back-cavity depth L) maximizes the absorption coefficient α_{ac}, the latter was plotted against the former at each frequency. Maps B.11a and B.11b are examples for two frequencies 300 and 700 Hz. White lines mark the depth and velocity at which the absorption is maximal. It should be noticed that best absorption is greater than $\alpha_{ac} = 90\%$ in the whole frequency range.

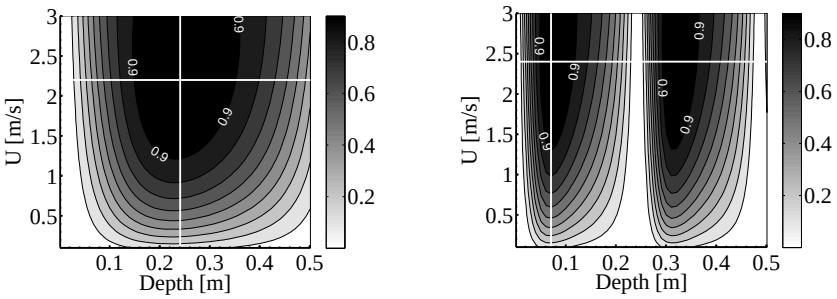

(a) Absorption coefficient at 300 Hz

(b) Absorption coefficient at 700 Hz

Figure B.11: $2a = 1$ mm and $d = 8$ mm. White lines indicates the optimal values.

Bias flow velocity U only slightly increases with frequency (fig. B.12) ; an average value of 2.3 m.s^{-1} can be chosen to achieve efficient absorption. This confirms the weak dependency on the Strouhal number St and the conclusion of Howe on the advantage of working at low St. In addition, it implies that velocity can be fixed to only one value, reducing the required degrees of freedom to the depth only. Optimal depth is also plotted as a function of frequency in figure B.12. Required depth decreases smoothly with increasing frequency. In particular it can be noted that using an adjustable system, a 50 cm maximal depth allows effectively investigation in the full frequency range of interest.

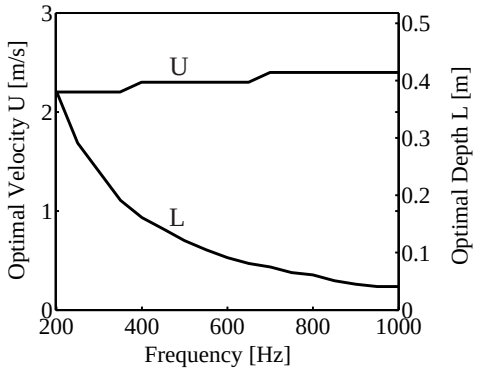

Figure B.12: Optimal velocity U and depth l for the designed plate ($2a = 1$ mm and $d = 8$ mm).

The absorption coefficient of such a setup ($a = 0.5$ mm, $d = 8$ mm and $U = 2.3$ m.s^{-1}) as a function of the frequency and the depth of the system is finally computed and plotted in fig. B.13. It can be concluded that efficient control of the reflection coefficient can be achieved. Indeed at each frequency, it is possible to control the absorption coefficient, i.e the reflection coefficient, from 0 to 1 by modifying the cavity depth L.

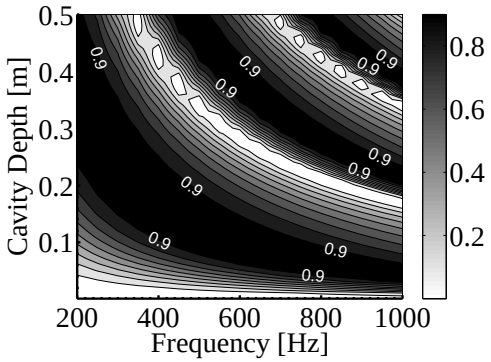

Figure B.13: Absorption coefficient for a velocity $U = 2.3$ m.s^{-1}

B.2.3 Concluding remarks

Some differences appear between the results computed with Q$=1$ and the results obtained with the variable parameters :

- The main one is the evaluation of the optimal bias-flow velocity. $U = 2.3$ instead of 1.7ms^{-1} for the plate designed at $Q = 1$. In both cases, bias flow velocity can be fixed to one optimized value in the whole range.
- Absorption levels higher than 90% are achievable (fig. B.13) in the domain instead of only 50% (fig. B.10).
- Using the second method Q, He and St optimal values are plotted as a function of frequency in figure B.14. It is shown that Q remains below unity. The Helmholtz number He is also lower than predicted for Q$=1$ (1.5 instead of 3). The Strouhal number St is also small in the whole frequency range, confirming the efficiency of the vortex shedding at low St.

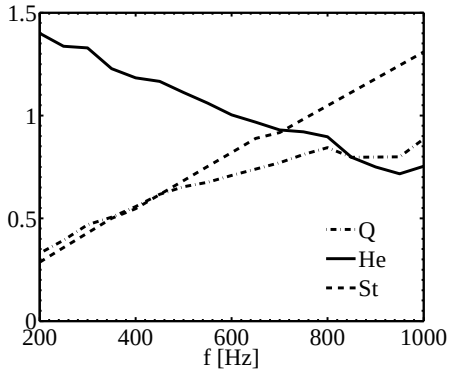

Figure B.14: Evolution of the dimensionless parameters with frequency.$a = 0.5$ mm, $d = 8$ mm and $U = 2.3$ m.s^{-1}.

Using the new design method, the range of parameters has been largely extended, as velocity, depth and frequency were not imposed ; only the radius and the spacing of the apertures were fixed, as they would be in an experiment. These parameters have been optimized. Predictions of the acoustic energy damping by the designed system (fig. B.13) are very optimistic, as complete absorption and accurate control of the reflection coefficient can be expected.

References

Adrian, R. J. (2004, July). Twenty years of particle image velocimetry. In *International Symposium on Applications of Laser Techniques to Fluid Mechanics*, Lisbon.

Anacleto, P., E. Fernandes, M. Heitor, and S. Shtork (2002, July, 8-11). Characterization of a strong swirling flow with precessing vortex core based on measurements of velocity and local pressure fluctuations. In *10th International Symposium on Applications of Laser Techniques to Fluid Mechanics*, Lisboa, Portugal.

Balachandran, R., B. O. Ayoola, C. F. Kaminski, A. P. Dowling, and E. Mastorakos (2005). Experimental investigation of the nonlinear response of turbulent premixed flames to imposed inlet velocity oscillations. *Combustion and Flame 143*(1-2), 37–55.

Ballester, J., A. Sanz, and M. A. Gonzalez (2008). Investigation of the characteristics and stability of air-staged flames. *Experimental Thermal and Fluid Science 32*(3), 776–790.

Barbosa, S., P. Scouflaire, and S. Ducruix (2009). Time resolved flowfield, flame structure and acoustic characterization of a staged multi-injection burner. *Proceedings of the Combustion Institute 32*(2), 2965 – 2972.

Bechert, D. W. (1980). Sound-absorption caused by vorticity shedding, demonstrated with a jet flow. *Journal of Sound and Vibration 70*(3), 389–405.

Bellucci, V., P. Flohr, C. Paschereit, and F. Magni (2004). On the use of Helmholtz resonators for damping acoustic pulsations in industrial gas turbines. *Journal of Engineering for Gas Turbines and Power 126*, 271–275.

Bernier, D., S. Ducruix, F. Lacas, S. Candel, N. Robart, and T. Poinsot (2003). Transfer function measurements in a model combustor: application to adaptive instability control. *Combustion Science and Technology 175*, 993–1013.

Bernier, D., F. Lacas, and S. Candel (2000, July-August). Instability mechanisms in a premixed prevaporized combustor. *Journal of Propulsion and Power 20*(4), 648–656.

Birbaud, A., D. Durox, S. Ducruix, and S. Candel (2007, January). Dynamics of confined premixed flames submitted to upstream acoustic modulations. *Proceedings of the Combustion Institute 31*(1), 1257–1265.

Bloxsidge, G. J., A. Dowling, N. Hooper, and P. Langhorne (1988, July). Active control of reheat buzz. *AIAA Journal 26*(7), 783–790.

Bothien, M. R., J. P. Moeck, and C. Oliver Paschereit (2008, December). Active control of the acoustic boundary conditions of combustion test rigs. *Journal of Sound and Vibration 318*(4-5), 678–701.

Brüel & Kjaer. *Microphone Handbook*. DK-2850 Naerum Denmark: Brüel & Kjaer.

Candel, S. (1975). Acoustic conservation principles and an application to plane and modal propagation in nozzles and diffusers. *Journal Of Sound And Vibration 41*(2), 207–232.

Candel, S. (1992). Combustion instabilities coupled by pressure waves and their active control. *Proceedings of the Combustion Institute 24*, 1277–1296.

Candel, S. (2002). Combustion dynamics and control: Progress and challenges. *Proceedings of the Combustion Institute 29*(1), 1–28.

Cantrell, R. H., R. W. Hart, and F. T. McClure (1963). Acoustic energy losses in rocket-engine cavities. *The Journal of the Acoustical Society of America 35*(5), 773–773.

Celik, E., A. C. Sever, and D. Rockwell (2005, August). Self-sustained oscillations past perforated and slotted plates: Effect of plate thickness. *AIAA Journal 43*(8), 1850–1853.

Chu, B.-T. (1965, September). On the energy transfer to small disturbances in fluid flow (Part I). *Acta Mechanica 1*(3), 215–234.

Chung, J. Y. (1978). Cross-spectral method of measuring acoustic intensity without error caused by instrument phase mismatch. *The Journal of the Acoustical Society of America 64*(6), 1613–1616.

Chung, J. Y. and D. A. Blaser (1980). Transfer function method of measuring in-duct acoustic properties. I. Theory. *The Journal of the Acoustical Society of America 68*, 907–913.

Cohen, J. M., A. Banaszuk, J. R. Hibshman, T. J. Anderson, and H. A. Alholm (2008). Active control of pressure oscillations in a liquid-fueled sector combustor. *Journal of Engineering for Gas Turbines and Power 130*(5), 051502.

Congyun, Z., H. Qibai, Z. Ming, and W. Yong (2005, September). Active absorption of perforated plate based on airflow. *Journal of Low Frequency Noise, Vibration and Active Control 24*(3), 171–180.

Conrad, T., A. Bibik, D. Shcherbik, E. Lubarsky, and B. Zinn (2007, January). Feasibility of "intermittent" active control of combustion instabilities in liquid fueled combustors using a "smart" fuel injector. *Proceedings of the Combustion Institute 31*(2), 2223–2230.

Correa, S. M. (1998). Power generation and aeropropulsion gas turbines: From combustion science to combustion technology. *Symposium (International) on Combustion 27*(2), 1793–1807.

Crighton, D. G., A. P. Dowling, J. E. Ffowcs-Williams, M. Heckl, F. G. Leppington, and J. F. Bartram (1992, November). *Modern methods in analytical acoustics. Lecture notes*, Volume 92. Springer-Verlag.

Crocco, L. (1951). Aspects of combustion instability in liquid propellant rocket motors. *Journal American Rocket Society 21*, 163–178.

Crow, S. and F. Champagne (1971). Orderly structure in jet turbulence. *Journal of Fluid Mechanics 48*(3), 547–591.

Culick, F. (1994, January). Some recent results for nonlinear acoustics in combustion chambers. *AIAA Journal 32*(1), 146–169.

Culick, F. (2006, December). Unsteady motions in combustion chambers for propulsion systems. Technical Report RTO-AG-AVT-039, NATO Research and Technology Organisation.

Cummings, A. (1986). Transient and multiple frequency sound transmission through perforated plates at high amplitude. *The Journal of the Acoustical Society of America 79*(4), 942–951.

Cummings, A. and W. Eversman (1983). High amplitude acoustic transmission through duct terminations: Theory. *Journal of Sound and Vibration 91*(4), 503–518.

Dalmont, J. P. (2001). Acoustic impedance measurement, part I : a review. *Journal of Sound and Vibration 243*, 427–439.

Dantec (1998). *FlowMap Particle Image Velocimetry Instrumentation Installation and User guide* (4th edition ed.).

Dioc, N. (2005). *Etude expérimentale des mécanismes d'instabilités dans un brûleur à injection étagée. Application aux turbines à gaz*. Ph. D. thesis, Ecole Centrale Paris, Châtenay-Malabry.

Dobbeling, K., J. Hellat, and H. Koch (2007). 25 years of BBC/ABB/Alstom lean premix combustion technologies. *Journal of Engineering for Gas Turbines and Power 129*(1), 2–12.

Docquier, N., S. Belhalfaoui, F. Lacas, N. Darabiha, and C. Rolon (2000). Experimental and numerical study of chemiluminescence in methane/air high-pressure flames for active control applications. *Symposium (International) on Combustion 28*(2), 1765–1774.

Docquier, N. and S. Candel (2002). Combustion control and sensors: a review. *Progress in Energy and Combustion Science 28*(2), 107–150.

Docquier, N., F. Lacas, and S. Candel (2002). Closed-loop equivalence ratio control of premixed combustors using spectrally resolved chemiluminescence measurements. *Proceedings of the Combustion Institute 29*(1), 139–145.

Dowling, A. and A. Morgans (2005). Feedback control of combustion oscillations. *Annual Review Fluid Mechanics 37*, 151–182.

Dowling, A. P. (1999, September). A kinematic model of a ducted flame. *Journal of Fluid Mechanics 394*, 51–72.

Dowling, A. P. and S. R. Stow (2003, Sep-Oct). Acoustic analysis of gas turbine combustors. *Journal of Propulsion and Power 19*(5), 751–764.

Dowling, A. P., J. E. F. Williams, and W. M. Wright (1985). Sound and sources of sound. *American Journal of Physics 53*(6), 604–604.

Dragan, S. P. and I. V. Lebedeva (1998, March). Absorption of high-intensity sound by a perforated panel. *Acta Physica 44*, 167–172.

Ducruix, S., T. Schuller, D. Durox, and S. Candel (2003). Combustion dynamics and instabilities: elementary coupling and driving mechanisms. *Journal of Propulsion and Power 19*, 722–734.

Durox, D., T. Schuller, N. Noiray, A. Birbaud, and S. Candel (2008, November). Rayleigh criterion and acoustic energy balance in unconfined self-sustained oscillating flames. *Combustion and Flame 155*(3), 416–429.

Durox, D., T. Schuller, N. Noiray, and S. Candel (2009). Experimental analysis of nonlinear flame transfer functions for different flame geometries. *Proceedings of the Combustion Institute 32*(1), 1391–1398.

Eldredge, J. D. and A. P. Dowling (2003, Jun). The absorption of axial acoustic waves by a perforated liner with bias flow. *Journal of Fluid Mechanics 485*, 307–335.

Forster, S. and U. Michel (2003). Experimental investigation of the dissipation of acoustic energy in perforated walls with bias flow. In C. U. Press (Ed.), *International Colloquium on Noise Control*.

Giauque, A., F. Nicoud, and M. Brear (2007). Numerical assessment of stability criteria from disturbance energies in gaseous combustion. In *13th AIAA/CEAS Aeroacoustics Conference (28th AIAA Aeroacoustics Conference) , Rome, Italy, May 21-23, 2007*, Number AIAA-2007-3425.

Giauque, A., T. Poinsot, M. Brear, and F. Nicoud (2007). Budget of disturbance energy in gaseous reacting flows. *Proceedings of the Summer Program, Center for Turbulence Research*.

Grace, S. M., T. H. Wood, and M. S. Howe (1999, June). Stability of high Reynolds number flow past a circular aperture. *Royal Society of London Proceedings Series A 455*, 2055–

+.

Gupta, A., D. Lilley, and N. Syred (1984). *Swirl flows*. Tunbridge Wells, Abacus Press.

Gutmark, E. and C.-M. Ho (1983). Preferred modes and the spreading rates of jets. *Physics of Fluids 26*(10), 2932–2938.

Hathout, J., M. Fleifil, A. Annaswamy, and A. Ghoniem (2000). Heat-release actuation for control of mixture-inhomogeneity-driven combustion instability. *Symposium (International) on Combustion 28*(1), 721–730.

Hedge, U., D. Reuter, B. Zinn, and B. Daniel (1987). Fluid mechanically coupled combustion instabilities in ramjet combustors. In *Aerospace Sciences Meeting, 25th, Reno, NV*, Number AIAA-1987-216.

Higgins, B., M. Q. McQuay, F. Lacas, and S. Candel (2001, September). An experimental study on the effect of pressure and strain rate on ch chemiluminescence of premixed fuel-lean methane/air flames. *Fuel 80*(11), 1583–1591.

Howe, M. S. (1979). On the theory of unsteady high Reynolds number flow through a circular aperture. *Proceedings of the Royal Society of London A 366*(1725), 205–223.

Hubschmid, W., R. Bombach, A. Inauen, F. Güthe, S. Schenker, N. Tylli, and W. Kreutner (2008). Thermoacoustically driven flame motion and heat release variation in a swirl-stabilized gas turbine burner investigated by lif and chemiluminescence. *Experiments in Fluids 45*(1), 167–182.

Hughes, I. J. and A. P. Dowling (1990, September). The absorption of sound by perforated linings. *Journal of Fluid Mechanics 218*, 299–335.

Idel'Cik, I. (1999). *Memento des pertes de charges*. Eyrolles.

Ingard, U. (1953). On the theory and design of acoustic resonators. *The Journal of the Acoustical Society of America 25*(6), 1037–1061.

Ingard, U. and H. Ising (1967). Acoustic nonlinearity of an orifice. *The Journal of the Acoustical Society of America 42*(1), 6–17.

Jing, X. and X. Sun (1999, novembre). Experimental investigations of perforated liners with bias flow. *The Journal of the Acoustical Society of America 106*(5), 2436–2441.

Jing, X. and X. Sun (2000, September). Effect of plate thickness on impedance of perforated plates with bias flow. *AIAA Journal 38*(9), 1573–1578.

Jing, X. and X. Sun (2002a, May). High-intensity sound absorption at an orifice with bias flow. *Journal of Propulsion and Power 18*(3), 718–720.

Jing, X. and X. Sun (2002b). Sound-excited flow and acoustic nonlinearity at an orifice. *Physics of Fluids 14*(1), 268–276.

Jones, M. G. and P. E. Stiede (1997). Comparison of methods for determining specific acoustic impedance. *The Journal of the Acoustical Society of America 101*(5), 2694–2704.

Keller, J. J. (1995). Thermoacoustic oscillations in combustion chambers of gas turbines. *AIAA Journal 33*(0001-1452), (2280–2287.

Kojima, J., Y. Ikeda, and T. Nakajima (2000). Spatially resolved measured of OH, CH and C2 chemiluminescence in the reaction zone of laminar methane/air premixed flames. In *Proceedings of the Combustion Institute*, Volume 28, pp. 1757–1764.

Landau, L. and E. Lifshitz (1987). *Fluid mechanics*. Butterworth-Heinemann.

Lee, D.-H. and Y. P. Kwon (2004). Estimation of the absorption performance of multiple layer perforated panel systems by transfer matrix method. *Journal of Sound and Vibration 278*(4-5), 847–860.

Lee, F. C. and W. H. Chen (2003). On the acoustic absorption of multi-layer absorbers with different inner structures. *Journal of Sound and Vibration 259*(4), 761–777.

Leppington, F. G. and H. Levine (1973). Reflection and transmission at a plane screen with periodically arranged circular or elliptical apertures. *Journal of Fluid Mechanics 61*, 109–127.

Leung, R. C. K., R. M. C. So, M. H. Wang, and X. M. Li (2006, February). In-duct orifice and its effect on sound absorption. *Journal Of Sound And Vibration 299*(4-5), 990–1004.

Levine, H. and J. Schwinger (1948). On the radiation of sound from an unflanged circular pipe. *Physical Review 4*, 383–406.

Lieuwen, T. and V. Yang (2006). *Combustion instabilities in gas turbine engines: operational experience, fundamental mechanisms, and modeling*, Volume 210 of *Progress in Astronautics and Aeronautics*. AIAA.

Lieuwen, T. and B. T. Zinn (1998). The role of equivalence ratio oscillations in driving combustion instabilities in low nox gas turbines. *Symposium (International) on Combustion 27*(2), 1809–1816.

Luong, T., M. S. Howe, and R. S. McGowan (2005, December). On the Rayleigh conductivity of a bias-flow aperture. *Journal of Fluids and Structures 21*(8), 769–778.

McIntosh, A. (1991). Pressure disturbances of different length scales interacting with conventional flames. *Combustion Science and Technology 75*, –.

McManus, K., T. Poinsot, and S. Candel (1993). A review of active control of combustion instabilities. *Progress in Energy and Combustion Science 19*(1), 1–29.

Meier, W., P. Weigand, X. R. Duan, and R. Giezendanner-Thoben (2007). Detailed characterization of the dynamics of thermoacoustic pulsations in a lean premixed swirl flame. *Combustion and Flame 150*(1-2), 2–26.

Melling, T. (1973). The acoustic impedance of perforates at medium and high sound pressure levels. *Journal of Sound and Vibration 29*, 1–65.

Mongia, H. (2004, Jan. 5-8). Perspective of combustion modeling for gas turbine combustors. In AIAA (Ed.), *42nd AIAA Aerospace Sciences Meeting and Exhibit, Reno, Nevada,*.

Morfey, C. (1971, January). Acoustic energy in non-uniform flows. *Journal of Sound and Vibration 14*(2), 159–170.

Morgans, A. S. and S. Stow (2007, September). Model-based control of combustion instabilities in annular combustors. *Combustion and Flame 150*(4), 380–399.

Morse, P. M. and K. U. Ingard (1987). *Theoretical Acoustics*. Number ISBN13: 978-0-691-02401-1. Princeton University Press.

Munjal, M. (1987). *Acoustics of ducts and mufflers with application to exhaust and ventilation system design*. Number ISBN: 978-0-471-84738-0. Wiley.

Myers, M. K. (1991). Transport of energy by disturbances in arbitrary steady flows. *Journal of Fluid Mechanics 226*, 383–400.

Nair, S. and T. Lieuwen (2005, January - February). Acoustic detection of blowout in premixed flames. *Journal of Propulsion and Power 21*(1), 32–39.

Narayana Rao, K. and M. L. Munjal (1986, July). Experimental evaluation of impedance of perforates with grazing flow. *Journal of Sound and Vibration 108*(2), 283–295.

Nauert, A., P. Petersson, M. Linne, and A. Dreizler (2007, July). Experimental analysis of flashback in lean premixed swirling flames: conditions close to flashback. *Experiments in Fluids 43*(1), 89–100.

Nicoud, F., L. Benoit, C. Sensiau, and T. Poinsot (2007). Acoustic modes in combustors with complex impedances and multidimensional active flames. *AIAA Journal 45*(2), 426–441.

Nicoud, F. and T. Poinsot (2005). Thermoacoustic instabilities: should the Rayleigh criterion be extended to include entropy changes? *Combustion and Flame 142*(1-2), 153–159.

Nogueira, J., A. Lecuona, and P. Rodriguez (2001). Identification of a new source of peak locking, analysis and its removal in conventional and super-resolution PIV techniques. *Experiments in Fluids 30*, 309–316.

Noiray, N. (2007). *Analyse linéaire et non-linéaire des instabilités de combustion, application aux systèmes à injection multipoints et stratégies de contrôle*. Ph. D. thesis, Ecole Centrale Paris.

Noiray, N., D. Durox, T. Schuller, and S. Candel (2008a, June 9-13, 2008). A novel strategy for passive control of combustion instabilities through modification of flame dynamics. In *ASME Turbo Expo 2008: Power for Land, Sea and Air*, Number GT2008-51520, Berlin, Germany.

Noiray, N., D. Durox, T. Schuller, and S. Candel (2008b). A unified framework for nonlinear combustion instability analysis based on the flame describing function. *Journal of Fluid Mechanics 615*, 139–167.

Oppenheim, A. and R. Schafer (1975). *Digital signal processing*. Prentice-Hall.

Paschereit, C., E. Gutmark, and W. Weisenstein (2000, June). Excitation of thermoacoustic instabilities by interaction of acoustics and unstable swirling flow. *AIAA Journal 38*(3), 1025–1034.

Peters, M., A. Hirschberg, A. J. Reijnen, and A. P. J. Wijnands (1993). Damping and reflection coefficient measurements for an open pipe at low Mach and low Helmholtz numbers. *Journal of Fluid Mechanics 256*, 499–534.

Poinsot, T., A. Trouve, D. Veynante, S. Candel, and E. Esposito (1987). Vortex-driven acoustically coupled combustion instabilities. *Journal of Fluid Mechanics 177*, 265–292.

Poinsot, T., B. Yip, D. Veynante, . Trouvé, J. Samaniego, and S. Candel (1992, jul). Active control: an investigation method for combustion instabilities. *Journal de Physique III 2*(7), 1331–1357.

Polifke, W. and C. Lawn (2007, November). On the low-frequency limit of flame transfer functions. *Combustion and Flame 151*(3), 437–451.

Price, R., I. Hurle, and T. Sugden (1969). Optical studies of the generation of noise in turbulent flames. *Symposium (International) on Combustion 12*(1), 1093–1102.

Putnam, A. A. (1971). *Combustion-driven oscillations in industry*. Number ISBN10: 0444001018. New-York: American Elsevier Pub. Co.

Randeberg, R. T. (2000). *Perforated Panel Absorbers with Viscous Energy Dissipation Enhanced by Orifice Design*. Ph. D. thesis, Norwegian University of Science and Technology, Faculty of Information Technology, Mathematics and Electrical Engineering.

Rayleigh, J. S. (1878). The explanation of certain acoustical phenomena. *Royal Institute Proceedings VIII*.

Rayleigh, J. S. (1899). *On the theory of resonance*, Volume I. Cambridge University Press.

Richards, G. A. and E. H. Robey (2008). Effect of fuel system impedance mismatch on combustion dynamics. *Journal of Engineering for Gas Turbines and Power 130*(1), 011510.

Richards, G. A., J. D. Thornton, E. H. Robey, and L. Arellano (2007). Open-loop active control of combustion dynamics on a gas turbine engine. *Journal of Engineering for Gas Turbines and Power 129*(1), 38–48.

Rienstra, S. W. and A. Hirschberg (2006). *An introduction to acoustics, extended and re-*

vised edition of IWDE 92-06. Eindhoven University of Technology.

Samaniego, J. M., B. Yip, T. Poinsot, and S. Candel (1993). Low-frequency combustion instability mechanisms in a side-dump combustor. *Combustion and Flame 94*, 363–380.

Sanz, A., J. Ballester, R. Hernandez, and L. M. Cerecedo (2008). Advanced monitoring of industrial burners based on fluctuating flame signals. *Fuel 87*(7), 1063–1075.

Sattelmayer, T. (2003). Influence of the combustor aerodynamics on combustion instabilities from equivalence ratio fluctuations. *Journal of Engineering for Gas Turbines and Power 125*(1), 11–19.

Scarano, F. and M. Riethmuller (2000). Advances in iterative multigrid piv image processing. *Experiments in Fluids 29*, S51–S60.

Schefer, R. (1997). Flame sheet imaging using ch chemiluminescence. *Combustion Science and Technology 126*, 255–270.

Schuller, T., D. Durox, and S. Candel (2002, January). Dynamics of and noise radiated by a perturbed impinging premixed jet flame. *Combustion and Flame 128*(1-2), 88–110.

Schultz, T., L. Cattafesta, T. Nishida, and M. Sheplak (2002). Uncertainty analysis of the two-microphone method for acoustical impedance testing. In *8th AIAA/CEAS Aeroacoustics Conference and Exhibit*, Breckenridge, CO; United States.

Sommerer, Y., D. Galley, T. Poinsot, S. Ducruix, F. Lacas, and D. Veynante (2004). Large eddy simulation and experimental study of flashback and blowoff in a lean partially premixed swirled burner. *Journal of Turbulence 5*.

Spencer, A., J. J. McGuirk, and K. Midgley (2008). Vortex breakdown in swirling fuel injector flows. *Journal of Engineering for Gas Turbines and Power 130*(2), 021503.

Steele, R. C., L. H. Cowell, S. M. Cannon, and C. E. Smith (2000). Passive control of combustion instability in lean premixed combustors. *Journal of Engineering for Gas Turbines and Power 122*(3), 412–419.

Stohr, M., R. Sadanandan, and W. Meier (2008). Experimental study of unsteady flame structures of an oscillating swirl flame in a gas turbine model combustor. *Proceedings of the Combustion Institute In Press, Corrected Proof*, –.

Syed, A. A., J. Yu, H. W. Kwan, and E. Chien (2002, July). The steady flow resistance of perforated sheet materials in high speed grazing flows. Technical Report NASA/CR-2002-211749, NASA, Langley Research Center, Hampton, Virginia 23681-2199.

Syred, N. (2006). A review of oscillation mechanisms and the role of the precessing vortex core (pvc) in swirl combustion systems. *Progress in Energy and Combustion Science 32*(2), 93–161.

Tachibana, S., L. Zimmer, Y. Kurosawa, and K. Suzuki (2007, January). Active control of combustion oscillations in a lean premixed combustor by secondary fuel injection coupling with chemiluminescence imaging technique. *Proceedings of the Combustion Institute 31*(2), 3225–3233.

Thibaut, D. and S. Candel (1998). Numerical study of unsteady turbulent premixed combustion. application to flashback simulation. *Combustion and Flame 113*, 51–65.

Tran, N., S. Ducruix, and T. Schuller (2008, June 9-13, 2008). Passive control of the inlet acoustic boundary of a swirled turbulent burner. In *ASME Turbo Expo 2008: Power for Land, Sea and Air*, Number GT2008-50425, Berlin, Germany.

Tsien, H. S. (1952). Servo-stabilization of combustion in rocket motors. *Rocket society Journal 22*, 256–263.

Walsh, K. T., M. B. Long, M. A. Tanoff, and M. D. Smooke (1998). Experimental and computational study of CH, CH*, and OH* in an axisymmetric laminar diffusion flame.

Symposium (International) on Combustion 27(1), 615–623.

Westerweel, J., D. Dabiri, and M. Gharib (1997). The effect of a discrete window offset on the accuracy of cross-correlation analysis of digital recordings. *Experiments in Fluids 23*, 20–28.

Wu, W.-J. and L.-C. Kung (2000, november-december). Determination of triggering condition of vortex-driven acoustic combustion instability in rocket motors. *Journal of Propulsion and Power 16*(6), 1022–1029.

Zhao, D. and A. Morgans (2008). Tuned passive control of combustion instabilities using multiple helmholtz resonators. *Journal of Sound and Vibration In Press, Corrected Proof*, –.